LEABHARLANN CHOLÁISTE NA TRÍONÓIDE, BAILE ÁTHA CLIATH | TRINITY COLLEGE LIBRARY DUBLIN
Ollscoil Átha Cliath | The University of Dublin

Terms and Conditions of Use of Digitised Theses from Trinity College Library Dublin

Copyright statement

All material supplied by Trinity College Library is protected by copyright (under the Copyright and Related Rights Act, 2000 as amended) and other relevant Intellectual Property Rights. By accessing and using a Digitised Thesis from Trinity College Library you acknowledge that all Intellectual Property Rights in any Works supplied are the sole and exclusive property of the copyright and/or other IPR holder. Specific copyright holders may not be explicitly identified. Use of materials from other sources within a thesis should not be construed as a claim over them.

A non-exclusive, non-transferable licence is hereby granted to those using or reproducing, in whole or in part, the material for valid purposes, providing the copyright owners are acknowledged using the normal conventions. Where specific permission to use material is required, this is identified and such permission must be sought from the copyright holder or agency cited.

Liability statement

By using a Digitised Thesis, I accept that Trinity College Dublin bears no legal responsibility for the accuracy, legality or comprehensiveness of materials contained within the thesis, and that Trinity College Dublin accepts no liability for indirect, consequential, or incidental, damages or losses arising from use of the thesis for whatever reason. Information located in a thesis may be subject to specific use constraints, details of which may not be explicitly described. It is the responsibility of potential and actual users to be aware of such constraints and to abide by them. By making use of material from a digitised thesis, you accept these copyright and disclaimer provisions. Where it is brought to the attention of Trinity College Library that there may be a breach of copyright or other restraint, it is the policy to withdraw or take down access to a thesis while the issue is being resolved.

Access Agreement

By using a Digitised Thesis from Trinity College Library you are bound by the following Terms & Conditions. Please read them carefully.

I have read and I understand the following statement: All material supplied via a Digitised Thesis from Trinity College Library is protected by copyright and other intellectual property rights, and duplication or sale of all or part of any of a thesis is not permitted, except that material may be duplicated by you for your research use or for educational purposes in electronic or print form providing the copyright owners are acknowledged using the normal conventions. You must obtain permission for any other use. Electronic or print copies may not be offered, whether for sale or otherwise to anyone. This copy has been supplied on the understanding that it is copyright material and that no quotation from the thesis may be published without proper acknowledgement.

The University of Dublin
Trinity College

CdTe based nanocomposite materials for biological imaging

by

Stephen J. Byrne

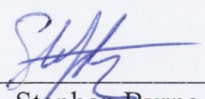
TRINITY COLLEGE
0 6 NOV 2008
LIBRARY DUBLIN

A thesis submitted to the University of Dublin, Trinity College for the degree of Doctor of Philosophy

School of Chemistry
University of Dublin
Trinity College
September 2007

Declaration

This Thesis is submitted by the undersigned to the University of Dublin, Trinity College for the examination of Doctorate of Philosophy. Except as otherwise stated, the author carried out the work described herein alone and has not submitted as an exercise for a degree to any other university.



Stephen Byrne

List of abbreviations:

AFM	Atomic force microscopy
AOT	Sodium dioctyl sulfosuccinate
BSA	Bovine serum albumin
CB	Conduction band
DAPI	4',6-diamidino-2-phenylindole
DB	Dangling bond
DCM	Dichloromethane
DLS	Dynamic light scattering
DNA	Deoxyribonucleic acid
DT	Deep trap
DTNB	5,5′-Dithiobis(2-nitrobenzoic acid)
e^-	Electron
e^- / h^+	Exciton (electron / hole pair)
EDC	1-ethyl-3-(3-dimethylaminopropyl) carbodiimide
E_g	Semiconductor band gap
ER	Endoplasmic reticulum
FRET	Fluorescence resonance energy transfer
FTIR	Fourier transform infra-red
FWHM	Full width at half maximum
H/E	Hexane / ethylacetate
h^+	Hole
HBSS	Hanks balanced salt solution
HDA	Hexadecylamine
HOMO	Highest occupied molecular orbital
HRTEM	High resolution transmission electron microscopy
IR	Infra-red
LED	Light emitting diode
LUMO	Lowest unoccupied molecular orbital
MO	Molecular orbital
MPA	Mercaptopropionic acid
MRI	Magnetic resonance imaging
MS	Mass spectra

NAC	N-acetyl-*L*-cysteine
NMR	Nuclear magnetic resonance
PAA	Poly(acrylic acid)
PBS	phosphate buffered saline
PCS	Photon correlation spectroscopy
PDDA	Poly(diallyldimethylammonium) chloride
PEG	Polyethylene glycol
PL	Photoluminescence
PMA	Phorbol-12-myristate 13-acetate
PSS	Polysodium-4-styrene sulfonate
QDs	Quantum dots
QE	Quantum efficiency
QY	Quantum yield
RDS	Royal Dublin society
RFU	Relative fluorescence units
ROS	Reactive oxygen species
RPMI	Roswell park memorial institute
RT	Room temperature
SEM	Scanning electron microscopy
ST	Shallow trap
STM	Scanning tunnelling microscopy
TCD	Trinity College Dublin
TEM	Transmission electron miscoscopy
TGA	Thioglycolic acid
THP-1	Macrophage cells
TLC	Thin layer chromatography
TOPO	tri-*n*-octylphosphine oxide
UV-vis	Ultraviolet-visible
VB	Valence band
XPS	X-ray photoelectron spectroscopy

Summary

The main goal of this research is to develop new CdTe QD based nanomaterials and demonstrate their potential for biological applications, in particular their use as fluorescent bioimaging tools. This work involves the synthesis and characterisation of CdTe QDs using various thiol capping agents, modification of QDs to improve their luminescence efficiencies, stability and biocompatibility, conjugation of QDs to drug molecules and investigations into their photophysical behaviour, distribution and toxicity in live cells.

In Chapter 2, the preparation and characterisation of thiol capped CdTe QDs is explored. A statistical study to optimise the reactions conditions for the production of highly luminescent QDs is implemented and experiments to improve the luminescence QYs are undertaken. Photoetching experiments were performed on TGA QDs resulting in substantial emission enhancements. Raman investigations prove the existence of a mixed Cd-S-Te phase on the QD surface as a result of irradiation, giving rise to the luminescence improvements seen. Tests with macrophage THP-1 cells show the TGA QDs being internalised by the cells and sequestered to the cytoplasm within a 10 minute co-incubation time. Irradiated and non-irradiated QDs show similar distributions but etched QDs show far higher imaging capacities for the various cellular organelles.

Chapter 3 is focused on the development of QDs as bioimaging probes and the factors that influence their uptake. Various thiol ligands are used to cap the QDs but charge and surface functionality play crucial roles in their behaviour with the cells. Those QDs possessing an amino rich (positively charged) surface remain bound to the outer membrane of the THP-1s even after vigorous washings; however, no penetration of the membrane is witnessed. A mixed functionality of amine and carboxylic acid does not enable the QDs to pass into the cytoplasm and a protection of the amine group is required to allow the QDs to enter the cell. Carboxylic acid capped QDs how the most promising results illustrating how charge plays a vital role in outer membrane penetration, while nuclear accumulation is found to depend on size. Small (~ 2 nm) green QDs are found to enter and accumulate within the nucleolus, while larger (~ 4 nm) red QDs are retained primarily in the cytoplasm and at the nuclear gates.

Investigations into the reduction of QD toxicity is presented in Chapter 4. Gelatin was utilised as a co-capping agent during the synthesis of the QDs. It was found that the addition of gelatin influenced not only on QD growth but also their emission properties. These gelatin nanocomposites show far higher luminescence efficiencies that their non-gelatinated counterparts. In tests with THP-1 cells, the gelatinated QDs show up to 80% less toxicity upon analysis of the lysosomal pH and cell membrane permeability. These gelatin – QDs also show different uptake distributions within the cells indicating an interaction with the various protein species present.

Chapter 5 describes the development of new QD conjugates, where the non-steroidal anti-inflammatory drugs (NSAIDs) ibuprofen and naproxen are successfully bound to the surface of the QDs. These new conjugates are investigated spectroscopically and their stability in an enzymatic environment is analysed. Naproxen conjugates prove more stable than their ibuprofen counterparts and demonstrate a weak release of the drug moiety form the surface upon addition of the enzyme. This verifies the presence of the drug on the QD surface and illustrates how further modification of the bond between QD and NSAID may lead to an easier and more controlled release. The biological testing of these nanocomposites reveals a similar uptake and distribution when compared to non-conjugated QDs indicating that they are indeed stable and biocompatible with THP-1 cells.

Chapter 6 presents the conclusions of this work, some preliminary studies and future work. Preliminary studies include research into the development of new capping agents, the interaction of QDs with selected polyelectrolytes, investigations of their behaviour with neuron cells and examinations of luminescence enhancements in Au nanoparticles / QD thin films prepared layer by layer deposition. All of these areas are planned to be explored and developed in the future.

Finally Chapter 7 describes all experimental details and instrumental techniques used in this research.

Overall, we believe that in this work will contribute to the better understanding and future development of new QD systems and to their utilisation in biological imaging and medical diagnostics.

Acknowledgements

Firstly, I would like to sincerely thank my supervisor Prof. Yurii Gun'ko, for giving me the opportunity to work in such a novel and exciting field of materials chemistry. The last four years have been thoroughly enjoyable and your support and guidance has been invaluable.

It has been my privilege to work with a great group of people. Many thanks to all members of Yurii's group, both past and present – Serena, Bertrand, Áine, Amro, Anna, Arunas, Gemma, Ian, Joe, Matt, Michele, Mick, Maciej, Renata, Rowan and Sivakumar. Our time at work and more importantly in the pub has been truly fantastic. I must also thank all of my students that I have had the privilege to look after throughout my studies. Without their help, I may have been here for even longer!!! – Alex, Ciara, Claire, Jerome, Pascal, Phillip, Russell, Tanya and Tim.

Thank you to Prof. Corish for the use of the facilities within the School of Chemistry, and to all the staff, especially Patsy and Martin for putting up with us for longer than expected!!!

During my time in Trinity I have also been very fortunate to meet and establish collaborations with other researchers not only in chemistry but across other disciplines. Thank you to Dr. Yuri Volkov for enabling us to expand our knowledge in the field of cell biology and in particular Dr. Siobhan Mitchell, Yvonne Williams and Jennifer Conroy for all your cell culture work and the many hours spent in front of the confocal. Other cellular studies were also carried out at the NCBES, NUI Galway under the supervision of Dr Yury Rochev. Many thanks for your kind hospitality and I look forward to seeing the results.

Thanks also to Dr. Yury Rakovich for all the time spent running fluorescence lifetime measurements and also for all the help with the Raman studies. A big thanks to Dr. Paul Evans (formerly TCD, now UCD) for all the help with the synthetic work and for giving me an organic chemists view on nanochemistry!!

I would like to thank my family for all their support throughout my time in college. To Dad, I miss you lots, Mam and Caroline, without you all I would not be the person that I am today. Thank you for all your love and encouragement.

To all my friends, in particular Dave and Serena, you guys have been invaluable to me and I can't say enough to thank you for all your help and support.

Finally I'd like to thank Pam, for all that you have given me. I'm so lucky to have someone like you, my best friend; I love you so much and couldn't have done it without you.

Table of Contents

		Page
Chapter 1: Introduction		**1**
1.1	A brief look at the land down under 100 nm!	1
1.2	Optical properties of semiconducting nanocrystals	3
1.3	Synthesis and growth	7
1.3.1	Organometallic syntheses	8
1.3.2	Aqueous syntheses	13
1.3.2.1	CdSe	13
1.3.2.2	CdTe	15
1.3.3	Comparison of organic versus aqueous syntheses	16
1.4	The nanocrystal surface and luminescence improvement	16
1.4.1	Ligand stability	21
1.5	Uses of semiconducting nanocrystals	24
1.5.1	Biological imaging	26
1.5.2	Bio-conjugation	29
1.6	Nano-toxicity	32
1.7	Aims and objectives of this work	36
References		38
Chapter 2:	**Optimisation of the synthesis and modification of CdTe quantum dot (QD) luminescence for live cell imaging**	**48**
2.1	Introduction	48
2.2	Synthesis and characterisation of CdTe QDs	50
2.2.1	Synthesis of CdTe QDs	50
2.2.2	Characterisation of QDs by UV-vis absorption and luminescence emission spectroscopy	52
2.2.3	Electron Microscopy	54
2.2.4	Infrared spectroscopy	55

2.3 Statistical analysis and optimisation of the synthesis of CdTe QDs 55
2.4 Experiments on enhancement of quantum efficiencies 60
2.4.1 Ageing 60
2.4.2 Photoetching 62
2.4.2.1 Fluorescence lifetime decay analysis 68
2.4.2.2 Raman spectroscopy 71
2.5 *In vitro* biological studies of TGA capped QDs 74
2.6 Conclusions 76
References 78

Chapter 3: Synthesis of CdTe QDs and investigations into their biolabelling capabilities 83
3.1 Introduction 83
3.2 Investigations into TGA capped QDs with THP-1 cells 84
3.2.1 Size targeting of TGA capped CdTe QDs 86
3.3 Synthesis and characterisation of CdTe QDs capped with commercially available thiol stabilisers 93
3.3.1 FTIR spectroscopy of QDs produced using commercially available thiols 95
3.4 Bioimaging investigations of CdTe QDs stabilised by commercially available thiols 96
3.4.1 3-Mercapto-1,2-propanediol – QDs 96
3.4.2 Glutathione – QDs 98
3.4.3 Cysteamine – QDs 99
3.4.4 *L*-cysteine – QDs 102
3.4.5 N-acetyl-*L*-cysteine – QDs 103
3.4.6 MPA – QDs 105
3.5 Conclusions 107
References 110

Chapter 4: "Jelly dots" Synthesis and cytotoxicity studies of CdTe QD - gelatin nanocomposites **112**

4.1 Introduction 112

4.2 Preparation and characterisation of TGA – gelatin nanocomposites 116

4.2.1 Addition of gelatin to TGA capped QDs 116

4.2.2 Addition of gelatin to MPA capped QDs 118

4.2.3 Preparation and characterisation of gel-TGA-QDs at 1.75:1 TGA : Cd ratio 119

4.2.4 Fluorescence lifetime decay analysis 122

4.2.5 Preparation and characterisation of gel-TGA-QDs at 1.4:1 TGA : CD ratio 124

4.3 Preparation and characterisation of gelatin-MPA nanocomposites 128

4.3.1 Preparation and characterisation of gel-MPA-QDs at 1.4:1 MPA : Cd ratio 128

4.4 Preparation and characterisation of gelatin-cysteamine nanocomposites 130

4.4.1 Preparation and characterisation of gel-cys-QDs at 1.4:1 cys : Cd ratio 131

4.5 Size exclusion of gelatin QD nanocomposites 134

4.6 Toxicity of CdTe QDs and their gelatin counterparts 136

4.6.1 Introduction 136

4.6.2 Investigation into the uptake and distribution of TGA and gel-TGA-QDs in THP-1 cells 137

4.6.3 Toxicity of QDs coincubation with THP-1 cells 139

4.7 Conclusions 144

References 146

Chapter 5: Non-steroidal anti-inflammatory drug (NSAID) – QD conjugates **150**

5.1 Introduction 150

5.1.1 Initial reaction sequence to be employed 151
5.2 Synthesis of new thiol containing drug conjugates 153
5.2.1 Synthesis and characterisation of N-(2-Mercaptoethyl)benzamide 153
5.2.2 Synthesis and characterisation of N-(2-Mercaptoethyl)benzamide capped QDs 154
5.3 Synthesis and characterisation of water soluble NSAIDs 157
5.3.1 Introduction 157
5.3.2 Spectroscopic characterisation of ibuprofen and naproxen 159
5.3.3 Synthesis of water soluble NSAIDs 159
5.4 Preparation of NSAID CdTe QD conjugates 161
5.4.1 UV-vis absorption and luminescence emission spectra of the NSAID – QD conjugates 162
5.4.2 Fluorescence lifetime decay analysis 165
5.4.3 TEM analysis of the NSAID – QD conjugates 168
5.4.4 UV-vis absorption and luminescence emission analysis of the conjugation reaction 168
5.4.5 Stability of the NSAID conjugates in an enzymatic environment 171
5.5 Investigation of the NSAID conjugates in THP-1 cells 174
5.6 Conclusions 176
References 178

Chapter 6: Conclusions, preliminary studies and future work 181
6.1 Conclusions 181
6.2 Preliminary studies and future work 183
6.2.1 Development of novel stabilisers for CdTe QDs 183
6.2.2 Investigation of CdTe QDs in neuron cells 185
6.2.3 Luminescence enhancement in Au / QD layer by layer systems 187
References 190

Chapter 7: Experimental **191**

7.1 General Procedures 191

7.1.1 Instrumental techniques used 191

7.1.2 Measurement of the fluorescence Quantum Yield (QY) 192

7.1.3 Cell biolabelling experiments 193

7.2 Experimental Details for Chapter 2 193

7.2.1 Preparation of CdTe QDs using Al_2Te_3 193

7.2.2 Preparation of CdTe QDs using Na_2Te 194

7.2.3 Statistical analysis 194

7.2.4 Photoetching 195

7.2.5 Ageing 195

7.3 Experimental Details for Chapter 3 195

7.3.1 Synthesis and characterisation of CdTe QDs using commercially available thiol stabilisers 195

7.3.2 Electrophoresis 196

7.3.3 Live cell experiments 196

7.4 Experimental Details for Chapter 4 196

7.4.1 Preparation of TGA and gel-TGA-QDs 196

7.4.1.1 Preparation of gel-TGA-QDs at 1.75 : 1 TGA :Cd ratio 196

7.4.2 Biological cytotoxicity testing 197

7.4.2.1 Cell culture 197

7.4.2.2 Toxicity assay 197

7.5 Experimental Details for Chapter 5 199

7.5.1 Synthesis of N-(2-Mercaptoethyl)benzamide (Figure 5.4 B) 199

7.5.2 Synthesis of boc-amino-PEG: **compound 1** 200

7.5.3 Synthesis of npx-boc-amino-PEG: **compound 2** 200

7.5.4 Synthesis of npx-amino-PEG-NH_2: **compound 2a** 201

7.5.5 Synthesis of ibu-boc-amino-PEG-NH_2: **compound 3** 202

7.5.6 Synthesis of ibu-amino-PEG-NH_2: **compound 3a** 202

7.5.7 Synthesis of NSAID – QD conjugates 203

7.6 Description of experimental techniques 203
7.6.1 Fluorescence / Luminescence spectroscopy 203
7.6.2 UV-vis absorption spectroscopy 204
7.6.3 Infrared (IR) spectroscopy 205
7.6.4 Raman spectroscopy 205
7.6.5 Confocal microscopy 208
7.6.6 Photon correlation spectroscopy (PCS) / Dynamic light scattering (DLS) 209
7.6.7 Nuclear magnetic resonance (NMR) 210
7.6.8 Transmission electron microscopy (TEM) 212
References 213

Chapter 8: Appendices **214**
Appendix 2a: HRTEM sizing data for CdTe QDs correlated to UV-vis absorption maxima 214
Appendix 3a: Table of IR data taken for the QDs capped by the thiols described in Table 3.1 215
Appendix 3b: IR spectra of mercaptopropionic acid (MPA) – QDs 216
Appendix 3c: IR spectra of 3-mercapto-1,2-propandiol – QDs 216
Appendix 3d: IR spectra of glutathione – QDs 216
Appendix 3e: IR spectra of cysteamine – QDs 217
Appendix 3f: IR spectra of N-acetyl-*L*-cysteine – QDs 217
Appendix 3g: IR spectra of *L*-cysteine – QDs 217
Appendix 5a: ^{1}H spectrum of N-(2-Mercaptoethyl)benzamide (Figure 5.4 B) 218
Appendix 5b: ^{1}H and ^{13}C spectra of boc-amino-PEG: **compound 1** 219
Appendix 5c: ^{1}H spectrum of npx-amino-PEG-NH_2: **compound 2a** 220
Appendix 5c: ^{13}C spectrum of npx-amino-PEG-NH_2: **compound 2a** 221
Appendix 5d: ^{1}H spectrum of ibu-amino-PEG-NH_2: **compound 3a** 222
Appendix 5d: ^{13}C spectrum of ibu-amino-PEG-NH_2: **compound 3a** 223

List of publications **224**

List of Figures, Schemes and Tables

Chapter 1 Introduction

Figure 1.1 Schematic representation of the band gap (E_g) structure of a semiconducting material and the change in that structure on going from the bulk to the nanoscale. The absorption and subsequent emission pathways upon excitation by a photon are also shown.

Figure 1.2 Typical UV-vis absorption (blue line) and luminescence emission (red line) profiles (λ_{ex} 450 nm) of a solution of CdTe nanocrystals in water. The Stokes shift (~ 40 nm) is the shift in the emission peak with respect to the lowest absorption peak.

Figure 1.3 Quantum confinement effects on (**a**) the UV-vis absorption and (**b**) luminescence emission spectra of CdTe nanocrystals. As the size of the crystallite increases (2 - 5.5 nm), the spectral profiles shift to higher wavelengths.

Figure 1.4 HRTEM image of monodisperse, highly crystalline CdSe nanocrystals, without any post-preparative treatment.

Figure 1.5 **a)** Luminescence emission spectra showing the QY evolution for each fraction of CdSe nanocrystals precipitated from a crude parent solution. **b)** Luminescence emission spectra (λ_{ex} 450 nm) of CdTe nanocrystals [synthesised in our group] showing a similar evolution of the QY for each fraction precipitated.

Figure 1.6 Graphical representation of a nanocrystal produced by the Quantum Dot Corporation.

Figure 1.7 **a)** Illustration of a ZnS-capped CdSe QD that is covalently coupled to a protein by mercaptoacetic acid (TGA). **b)** Schematic, illustrating the transfer of ZnS capped CdSe nanocrystals to water *via* the use of mercaptopropionic acid (MPA). A thiol containing oligonucleotide was then immobilised and subsequently bound to a complementary strand.

Figure 1.8 Graphical illustration of the mixed occupancy on the surface of a CdTe nanocrystal. Note, when surface Te sites dominate, this results in a high quantity of surface dangling bonds and lower luminescence efficiencies. The occupation of these 3 fold coordinate sites with a thiol molecule results in increased stabilisation and the removal of surface dangling bonds (passivation). This also leads to the formation of a core-shell like structure of Cd and S, which acts like a

potential well giving a better confinement of the excitons and increased QYs for the nanocrystals.

Figure 1.9 Illustration of the location of the anion (Te) site and the cation (Cd) defect sites within the band gap (Eg).

Figure 1.10 Illustration of the trapping of the charged carriers in "rough" states where photooxidation eliminates the atomic scale imperfections. This reduces the size of the crystallite and enhances the QY.

Figure 1.11 **a)** Graphical illustration of the secondary (5 or 6 coordinate) stabilisation of TGA capped CdTe nanocrystals due to interactions of the carbonyl oxygen of the thiol capping group at the primary or secondary thiol containing cadmium. **b)** Graphical illustration of the surface structure of CdTe nanocrystals modified with MPA and PAA [poly(acrylic acid)]. The coil represents the PAA alkyl chain and R represents a carboxylic acid group. The coordination between the carbonyl oxygen and cadmium on the particle surface is represented as dot line. The naked sulfur species in the particle resulted from the decomposition of thiols which occurs in the acidic pH region.

Figure 1.12 Mouse 3T3 fibroblast cells labelled with silica coated CdSe nanocrystals. Red emitting nanocrystals label the F-actin while green stain the nucleus.

Figure 1.13 Fluorescent micrographs illustrating the effects of mercury lamp exposure on QDs (green, left panels) and Mitotracker (red, right panels). The QDs can be clearly seen to retain their fluorescence after 8 minutes while the dye is completely bleached after only 30 seconds.

Figure 1.14 Graph illustrating the number of published manuscripts between 1996 and 2004 that report the use of nanomaterials (specifically, metallic and semiconductor nanocrystals) in biological applications. These data were compiled using the Medline database.

Figure 1.15 Near IR window available for *in vivo* imaging illustrating the minimal light absorbed by haemoglobin and water in this region.

Figure 1.16 Mechanism of cell death due to nanocrystal induced toxicity as proposed by Lovrić and co-workers.

Figure 1.17 Autofluorescence image (left) and fluorescence image (right) of nanocrystal conjugates illustrating that nanocrystals accumulated in a prostate tumour growing in a live mouse.

Scheme 1.1 Photocorrosion of CdSe to give free Cd^{2+} and SeO_2.

Scheme 1.2 Mechanism of the oxidation of sulfur by photogenerated holes as proposed by Henglein.

Scheme 1.3 Mechanism proposed by Fischer and Henglein which describes the photocatalytic removal of the surface capping thiol molecules from CdS nanocrystals. **1:** light absorption generates an exciton (e^-/h^+ pair), **2:** exciton can recombine radiatively or nonradiatively (main reaction) or **3:** oxidation of thiolate anion to form a thiyl radical which is released from the nanocrystal. **4:** thiyl radical can dimerise to form the disulfide. **5:** electron can pick up another one to form CdS and free thiol.

Chapter 2 Optimisation of the synthesis and modification of CdTe quantum dot (QD) luminescence for live cell imaging

Figure 2.1 Graph illustrating the distribution of the various cadmium complexes in solution and the QY of the QDs after 20 hours of synthesis depending on the TGA/Cd ratio used.

Figure 2.2 **a**) UV-vis absorption and **b**) normalised luminescence emission spectra (λ_{ex} 400 nm) taken sequentially (20, 40, 60, 80, 100, 120, 180 and 250 minutes) during the reflux of TGA capped CdTe QDs.

Figure 2.3 Solutions of individual fractions of TGA capped QDs exposed under a UV light illustrating quantum confinement and the change in emission wavelength (from 510 nm to 600 nm) with increasing size (left to right).

Figure 2.4 Characteristic absorption (dotted line) and luminescence emission spectra (solid line, λ_{ex} 450 nm) of green (~ 2 nm) and red (~ 4 nm) TGA capped CdTe QDs.

Figure 2.5 **a**) TEM image and **b**) a HRTEM image of TGA capped CdTe QDs. Insert **b** - a magnified image of an isolated 4 nm QD.

Figure 2.6 IR spectrum (KBr) of TGA (blue) and TGA capped QDs (red).

Figure 2.7 Graphical representation of the 2^2 statistical factorial design. Each point represents a metal to metal and metal to stabiliser ratio. Numbers in bold represent the Cd : Te ratios while those in italics represent the thiol : Cd ratio.

Figure 2.8 Room temperature absorption spectra of TGA capped CdTe QDs taken 24 hours after synthesis.

Figure 2.9 Normalised room temperature emission spectra (λ_{ex} 450nm) of TGA capped CdTe QDs taken 24 hours after synthesis.

Figure 2.10 Statistical 3-D surface response (response measured was the QY) curve for TGA capped CdTe QDs with variations in the metal to metal and stabiliser to metal ratios as shown in Table 2.1.

Figure 2.11 UV-vis absorption and normalised luminescence emission spectra (λ_{ex} 450 nm) of TGA capped QDs aged over 22 days. Insert graph: evolution of the emission intensity as a function of ageing time.

Figure 2.12 **a)** Illustration of patterned monochromatic irradiation of a SiO_2/CdSe (film). **(b)** Photographs of photoetched SiO_2/CdSe (film) placed under i) ambient (ii), ultraviolet (350 nm) and iii) both lights.

Figure 2.13 UV-vis absorption and normalised room temperature luminescence emission spectra (λ_{ex} 425 nm) (filter present) of TGA capped CdTe QDs subject to irradiation.

Figure 2.14 **a**) UV-vis absorption and **b**) normalised room temperature luminescence emission spectra (λ_{ex} 425 nm) of TGA capped CdTe QDs subject to irradiation (no filter present) over 30 minutes.

Figure 2.15 Four luminescence decay curves for TGA capped QDs recorded during the photoetching process. Insert: radiative and nonradiative rate constants calculated by Equations (3) and (4) respectively. Dashed lines are simply guides to the eye.

Figure 2.16 Raman spectra of aqueous TGA capped CdTe QDs, **a**) before photoetching and **b**) after photoetching. The solid lines are fitted curves obtained using Lorentzian functions.

Figure 2.17 Phase contrast **(a)** and fluorescent image **(b)** of TGA QDs adhering rapidly to the macrophage cell surface following a short (5 minute) coincubation treatment.

Figure 2.18 **a-b)** Fluorescent microscope images of TGA QDs penetrating the membrane of THP-1 cells and illuminating the cytoplasm. **c-e)** Fluorescent images of photoetched TGA QDs displaying the same cytoplasmic localisation but illuminating the organelles with a far greater intensity enabling a more detailed analysis of the region. Co-incubation time for both samples of QDs was 15-30 minutes.

Table 2.1 Reagent ratios for reaction with resultant QYs and full width at half maximum (FWHM) values for the crude, unpurified TGA QD solutions.

Scheme 2.1 Schematic illustration of the setup used to produce water soluble CdTe QDs. Al_2Te_3 is decomposed by the dropwise addition of H_2SO_4 and argon carries the evolved H_2Te gas through a solution of $Cd(ClO_4)_2 \cdot {}_6H_2O$ and the desired thiol. This solution is then heated under reflux.

Chapter 3 **Synthesis of CdTe QDs using a variety of different capping agents and their investigation as probes for biological imaging**

Figure 3.1 Live cell fluorescent images of TGA QDs in live THP-1 cells. Blue colour is due to Hoechst nuclear staining. **Panel a**: QDs viewed under red (λ_{ex} 568 nm) filter, **panel b**: QDs viewed under yellow (λ_{ex} 488 nm) filter and **panel c**: composite (both channels) view of the QDs.

Figure 3.2 UV-vis absorption and normalised luminescence emission spectra (λ_{ex} 450 nm) of the different sized TGA QDs [green: 2 nm, red 4 nm] investigated in the THP-1 cells.

Figure 3.3 HRTEM images showing isolated 2 nm (left) and 4 nm (right) TGA capped QDs, taken from each differently sized sample. Lattice spacings are in agreement with that expected for the (111) plane of cubic zinc blend CdTe.

Figure 3.4 PCS measurements (by volume) of the two TGA QD samples used. Red and blue lines are the measured curves based on 2 nm and 4 nm QDs respectively.

Figure 3.5 **(a)** Accumulation of the 2 nm green TGA QDs in THP-1s after 10 minutes. The arrows highlight an early compact perinuclear localisation. **(b)** Cytoplasmic compartmentalisation of 4 nm red QDs in the THP-1 cells after a 30 minute coincubation time. **(c)** Addition of green and red QDs after 30 minutes of coincubation with the THP-1 cells. Arrows indicate the translocation of smaller green QDs to the nucleus while the red QDs are retained in the cytoplasm. (**d**, **e**) Analysis of the green QDs intracellular distribution dynamics in individual THP-1 cells after 10 (**d**) and 30 (**e**) minute coincubation times respectively. The coloured images reflect the integrated fluorescence intensity levels. ['*c*' and '*n*' represent the cytoplasm and nucleus respectively. The calibration bar indicates relative fluorescence intensities and images are representative of several experiments].

Figure 3.6 Quantitative assessment of the uptake of green CdTe QDs into the nucleus of THP-1 cells. Relative fluorescence units (RFU) convey the shift in the

fluorescence of the green QDs from the cytoplasm 'C' to the nucleus 'N' over time. Mean values and standard errors were calculated from 30 cells randomly selected from the microscopic fields.

Figure 3.7 Slices taken from a confocal movie as the excitation laser was moved through a cell from top to bottom. Each slice enables the analysis of a layer of the cell and visualisation of the individual components highlighted by the QDs.

Figure 3.8 Confocal optical cross section at the level of the ER demonstrating green and red QD localisation in THP-1s. Green QDs are localised to the nucleus while red QDs display a diffuse cytoplasmic fluorescence. Both types of QDs co-localise at the perinuclear ER (yellow colour) indicated by arrows.

Figure 3.9 Live fluorescent images (**a** and **c**) and phase contract **(b)** of green TGA QDs staining the nucleolus within the nucleus of the THP-1 cells.

Figure 3.10 **(a)** Green QDs exhibit an early (10 minute) accumulation around the perinuclear membrane. **(b)** Green QDs penetrate the nucleus and accumulation within the nucleolus is highlighted by intense fluorescence and a circular distribution (arrows). **(c)** Thapsigargin treatment blocks the entry of the QDs to the nucleus and results in only a diffuse cytoplasmic localisation.

Figure 3.11 Photographic image (under UV lamp) of an electrophoresis experiment containing the CdTe QDs stabilised by the thiols outlined in Table 3.1. **Note:** The cysteamine sample (lane 2) ran slightly towards the negative electrode but decomposed during the process, thus not illuminating under UV excitation.

Figure 3.12 Phase contrast **(a)** and fluorescent image **(b)** of 3-mercapto-1,2-propanediol stabilised QDs attached only to the outer membrane the macrophages.

Figure 3.13 Phase contrast **(a)** and fluorescent images (**b** and **c**) of 3-mercapto-1,2-propanediol stabilised QDs entering dead macrophage cells.

Figure 3.14 Phase contrast **(a)** and fluorescent image **(b)** of glutathione stabilised QDs excluded from live cells and present only inside a dead macrophage cell.

Figure 3.15 Phase contrast (**a** and **c**) and corresponding fluorescent images (**b** and **d**) of cysteamine stabilised QDs adhering only to the outer membrane of the macrophages.

Figure 3.16 Fluorescent image of a dead THP-1 cell, which is now highly permeable showing the uptake of the previously excluded cysteamine QDs.

Figure 3.17 Phase contrast **(a)** and fluorescent image of green *L*-cysteine **(b)** and also red *L*-cysteine **(c)** stabilised QDs adhering to the outer membrane of the macrophages.

Figure 3.18 Structure of N-acetyl-*L*-cysteine (NAC).

Figure 3.19 (**a**) Phase contrast and (**b**) fluorescent image of green N-acetyl-*L*-cysteine QDs penetrating the outer membrane of THP-1 cells.

Figure 3.20 (**a**) Phase contrast and (**b**, **c**) fluorescent images of green N-acetyl-*L*-cysteine QDs penetrating the nucleus of THP-1 cells.

Figure 3.21 Phase contrast (**a**) and subsequent fluorescent images (**b**-**c**) of MPA QDs in THP-1 cells. Image (**b**) illustrates (following a short incubation time) the plan view of the cell showing both an intra and outer nuclear accumulation of the QDs while image (**c**) (longer incubation) illustrates the accumulation of QDs in the nucleolus (arrow).

Figure 3.22 Fluorescent images [**a**) green filter, **b**) red filter] of a THP-1 cell incubated with an MPA QD sample containing a mixture of sizes. Small, green QDs are seen to predominantly accumulate within the nucleoli (arrows) while larger, red QDs remain predominantly outside the nuclear periphery (arrow).

Table 3.1 Commercial thiols used for QD stabilisation, the pH of reaction and the resultant QYs of the QDs obtained.

Chapter 4 **"Jelly dots" Synthesis and cytotoxicity studies of CdTe QD - gelatin nanocomposites**

Figure 4.1 Fragment from the structure of gelatin illustrating the various functional groups and charged atoms present along the backbone.

Figure 4.2 Graphical illustration of the secondary interactions occurring on the surface of TGA [both 5 and 6 membered ring interactions possible] and MPA [6 membered ring interactions] stabilised CdTe QDs.

Figure 4.3 **a**) UV-vis absorption and **b**) normalised luminescence emission spectra (λ_{ex} 450 nm) for the addition of 0, 50, 100, 150, 200 and 250 µl of a 1 g / 20 ml solution of gelatin in water to a purified TGA capped QD solution.

Figure 4.4 **a**) UV-vis absorption and **b**) normalised luminescence emission spectra (λ_{ex} 450 nm) for the addition of 0, 10, 30, 50, 70 and 90 µl of a 0.1 g / 20 ml solution of gelatin in water to a purified CdTe QD solution in tris-HCl buffer (pH 11).

Figure 4.5 Luminescence emission spectra (λ_{ex} 450 nm) for the addition of gelatin (0.1 g / 20 ml buffer) to three different sizes of MPA QDs [a – λ_{em} 555 nm, b – λ_{em} 590 nm, c – λ_{em} 630 nm].

Figure 4.6 **a**) UV-vis absorption and **b**) normalised luminescence emission spectra (λ_{ex} 425 nm) of TGA capped and gel-TGA-QDs prepared under the same conditions. Sample aliquots were taken at 15, 30, 40, 55, 70, 85, 100, 130 and 160 minutes after the start of reflux.

Figure 4.7 Graph of normalised luminescence intensity versus wavelength for each aliquot taken during the reflux period. Insert: graph of emission wavelength versus sample taken, showing an 8 nm difference in emission wavelength between the TGA and gel-TGA-QD produced under the same conditions.

Figure 4.8 HRTEM image of gel-TGA-QDs.

Figure 4.9 Plot of sample taken against lifetime values of the short (τ_1) and long (τ_2) lifetime components of the luminescence decays estimated from a biexponential fitting of the experimental curves of TGA (black) and gel-TGA-QDs (red).

Figure 4.10 Normalised luminescence emission spectra (λ_{ex} 450 nm) for a control (no gelatin present) and repeat experiments containing varying amounts of gelatin (0.1 g, 0.25 g, 0.5 g and 1 g).

Figure 4.11 Graph of normalised luminescence intensity versus each sample analysed for a control experiment of QDs without gelatin (light blue) and also samples containing 0.1 g (orange), 0.25 g (green), 0.5 g (red) and 1 g (blue) of gelatin.

Figure 4.12 **a**) UV-vis absorption and **b**) normalised luminescence emission (λ_{ex} 450 nm) spectra of MPA and gel-MPA-QDs taken 30, 40, 50, 60, 75, 90, 105 and 120 minutes after the start of heating.

Figure 4.13 Graph of **a**) luminescence intensity versus wavelength and **b**) wavelength versus sample taken for MPA and gel-MPA-QDs taken 30, 40, 50, 60, 75, 90, 105 and 120 minutes after the start of heating.

Figure 4.14 HRTEM images [**a**) lower magnification, **b**) higher magnification] of gel-MPA-QDs. Lattice spacing is 2.95 Å, consistent with the (200) plane of cubic zinc blend CdTe.

Figure 4.15 **a**) UV-vis absorption spectra and **b**) normalised luminescence emission spectra (λ_{ex} 450 nm) recorded for gelatin-cysteamine [gel-cys-QDs] (top) and cys-QDs (bottom) taken after 30, 40, 50, 60, 75, 90, 105 and 120 minutes from the start of heating.

Figure 4.16 Plot of luminescence intensity of cys- (blue line) and gel-cys-QDs (red line) against the samples taken after 30, 40, 50, 60, 75, 90, 105 and 120 minutes from the start of heating.

Figure 4.17 Fluorescent microscope images (**a** - green channel, **b** - red and yellow channels) of THP-1 cells incubated with gel-TGA-QDs indicating that size exclusion is still present for gelatin coated QDs.

Figure 4.18 Enhanced fluorescence images of gel-MPA-QDs in live THP-1 cells. Panel **a** shows the accumulation of green emitting QDs in the nucleus, while panel **b** shows the accumulation of the larger red emitting QDs in the cytoplasm.

Figure 4.19 Live cell fluorescent images of cys-gel-QDs and THP-1s after a 1 hour incubation time.

Figure 4.20 Live cell Cellomic® images of TGA QDs cultured with THP-1 cells and analysed over coincubation times of three and six hours.

Figure 4.21 Live cell Cellomic® images of gel-TGA-QDs cultured with THP-1 cells and analysed over coincubation times of three and six hours.

Figure 4.22 Live cell Cellomic® images of the dye staining, taken using the Cellomics KineticScan®. The Hoescht nuclear staining (blue), changes in cell permeability (green) and lysosomal pH (red) were recorded for unmodified cells and cells with added TGA QDs, gel-TGA-QDs, cadmium, gelatin and TGA in solution. Cell permeability and pH changes are measured by intensity. For cell permeability, an increase in intensity is indicative of an increased permeability, while for pH, a decreased intensity indicates a more basic pH.

Figure 4.23 Histogram indicating changes in nuclear size measured in pixels with increasing incubation time for all QD and control samples tested.

Figure 4.24 **a)** Histogram illustrating the changes in lysosomal pH with incubation time. Decreases in intensity are indicative of a more basic lysosomal pH while increases are due to acidic pH values. **b)** Histogram illustrating the changes in cell permeability with incubation time. Increases in intensity are indicative of increased cellular permeability.

Table 4.1 Lifetime data recorded for samples taken 30, 40, 55, 70, 85, 100, 130 and 160 minutes after reflux for both TGA and gel-TGA-QDs. The shorter lifetime (τ_1) can be attributed to the intrinsic recombination of populated core states, while the longer lifetime (τ_2) can be associated with the involvement of surface states in the carrier recombination processes. Comparison of the α values gives us an indication of the relative contribution that each part of the radiative lifetime contributes to the average total (τ_{av}).

Table 4.2 Nuclear size, cell permeability and lysosomal pH data collected upon analysis of the TGA and gel-TGA-QDs *via* high content screening using a Cellomics KineticScan®. Nuclear size is measured in pixels, while cell permeability and lysosomal pH is measured by dye intensity. Increases in pixel intensity indicate increased cell permeability and a decreased lysosomal pH respectively.

Chapter 5 **Non-steroidal anti-inflammatory drug (NSAID) – QD conjugates**

Figure 5.1 **a)** Structure of the ibuprofen hybrid [2-(4-Isobutyl-phenyl)-N-(3-mercapto-propyl)-propionamide] and **b)** structure of the naproxen hybrid [N-(3-Mercapto-propyl)-2-(6-methoxy-naphthalen-2-yl)-propionamide].

Figure 5.2 Structure of 2,2'-dithiobis(ethylamine) dihydrochloride (cystamine dihydrochloride).

Figure 5.3 **a**) Structure of benzoyl chloride and **b)** N-(2-mercaptoethyl)benzamide.

Figure 5.4 UV-vis absorption spectrum of N-(2-mercaptoethyl)benzamide in DMF. Insert: expanded region between 250 & 400 nm.

Figure 5.5 Luminescence emission spectra of N-(2-mercaptoethyl)benzamide (λ_{ex} 290, 300 and 330 nm) in DMF.

Figure 5.6 Luminescence emission spectra of the purified N-(2-mercaptoethyl)benzamide nanocomposite excited at a variety of wavelengths. Insert: Luminescence spectrum of the unpurified sample.

Figure 5.7 Structure of 2,2′-(ethylenedioxy)diethylamine [amino-PEG].

Figure 5.8 **a)** UV-vis absorption (blue) and luminescence emission spectrum (λ_{ex} 220 nm / λ_{em} 287 nm) (red) of ibuprofen. **b)** UV-vis absorption (blue) and luminescence emission spectrum (λ_{ex} 233 nm / λ_{em} 353 nm) (red) of naproxen. (Spectra taken in water).

Figure 5.9 UV-vis absorption and luminescence emission spectra (λ_{ex} 450 nm) taken before, during and after the conjugation of npx-amino-PEG-NH_2 to the QDs. [Red line: original QDs, blue line: conjugation reaction after 1 hour, pink line: QDs following storage overnight, green line: QDs following sephadex purification].

Figure 5.10 UV-vis absorption and luminescence emission spectra (λ_{ex} 450 nm) taken during and after the conjugation of ibu-amino-PEG-NH_2 to the QDs. [Red line: original QDs, blue line: conjugation reaction after 1 hour, pink line: QDs following storage overnight, green line: QDs following purification].

Figure 5.11 Time-dependent luminescence intensity decays for solutions of original TGA-QDs (green line) and the ibuprofen (red line) and naproxen (blue line) QD conjugates. Results of a two-exponential analysis of the decay curves are shown by thick black lines.

Figure 5.12 Fluorescence lifetime images illustrating the lifetime distribution and uniformity of the NSAID QD samples. **(a)** original CdTe QD solution, **(b)** npx-amino-PEG-NH_2 conjugated QDs, **(c)** ibu-amino-PEG-NH_2 conjugated QDs, **(d)** naproxen QD conjugate solution left in ambient conditions over 48 hours.

Figure 5.13 TEM images of **a**) original and **b**) NSAID conjugated QDs illustrating that upon conjugation no discernable changes in morphology of the QDs can be seen. (Scale bar = 100 nm for both images).

Figure 5.14 Luminescence emission spectra (λ_{ex} 267 nm) of the npx-amino-PEG-NH_2 derivative (red line), the original TGA-QDs (blue line) and the purified npx-amino-PEG-NH_2 QD conjugate (black line).

Figure 5.15 Luminescence emission spectra (λ_{ex} 220 nm) of the ibu-amino-PEG-NH_2 derivative (red line), the original TGA-QDs (blue line) and the ibu-amino-PEG-NH_2 QD conjugate (black line).

Figure 5.16 Luminescence emission spectra showing the washings from the sephadex columns following conjugation of **a**) ibu-amino-PEG-NH_2 and **b**) npx-amino-PEG-NH_2 to the QDs.

Figure 5.17 Luminescence emission spectrum (λ_{ex} 220 nm) taken after 15, 60 and 180 minutes of mixing the ibu-amino-PEG-NH_2 QD conjugate with trypsin.

Figure 5.18 Luminescence emission spectra (λ_{ex} 267 nm) of the purified npx-amino-PEG-NH_2 QD conjugate before (red line), 15 min. (green line), 1 hour (blue line) and 3 hours (pink line) after mixing with trypsin (5 mg/mL). [Note, no discernable change in QD emission after the initial increase from 15 minutes of mixing]. Insert: blown up section (λ_{em} 356 nm) showing a small increase of the naproxen emission after 15 min of mixing time.

Figure 5.19 Luminescence emission spectra (λ_{ex} 450 nm) of TGA QDs and the trypsin enzyme taken after 0, 10, 30 and 120 minutes.

Figure 5.20 Live cell fluorescent images showing the localisation of **a)** naproxen conjugated (λ_{em} 566 nm) QDs onto the outer cellular membrane of THP-1. **b)** More intensely luminescent intra and extra cellular distributions are noted for the original non-conjugated QDs.

Table 5.1 Two exponential fit parameters to the observed luminescence decays (in solution) of original TGA QDs and the npx-amino-PEG-NH_2 and ibu-amino-PEG-NH_2 QD conjugates. The shorter lifetime (τ_1) can be attributed to the intrinsic recombination of populated core states, while the longer lifetime (τ_2) can be associated with the involvement of surface states in the carrier recombination processes. Comparison of the α values gives us an indication of the relative contribution that each part of the radiative lifetime contributes to the average total (τ_{av}).

Scheme 5.1 Reaction sequence for the chlorination of the carboxylic acid function of a molecule, its reaction with cystamine and the subsequent reduction of the disulfide via triphenyl phosphine (PPh_3) to give the free thiol.

Scheme 5.2. Structure of aspirin and the reaction of a nucleophile (Nu^-) illustrating the lability of the *O*-acetyl group.

Scheme 5.3 Reaction sequence for conjugation of the amino-PEG with diTGA. $SOCl_2$ is used to generate the acid chloride of the carboxylic acid, Boc_2O (di-tert-butyl dicarbonate)is used as a typical protection group for amines. TFA (trifluoracetic acid) is then used to remove the Boc protecting group while the disulfide bond is reduced with PPh_3 to give the free thiol.

Scheme 5.4 Synthetic pathway for the Boc protection of 2,2′-(ethylenedioxy)diethylamine (**compound 1**), its reaction with naproxen / ibuprofen chloride and subsequent deprotection to give the TFA salt of the free amine (**compounds 2a** and **3a**).

Scheme 5.5 Schematic representation of the conjugation reaction between the water soluble NSAIDs and CdTe QDs (not to scale).

Chapter 6 Conclusions and Future Work

Figure 6.1 Structure of α-mercapto-ω – PEG400.

Figure 6.2 Photographs of the fractions (left panel – normal light, right panel – UV light) obtained during the synthesis of TGA QDs in the presence of PEI.

Figure 6.3 Luminescence emission spectra (λ_{ex} 450 nm) taken for each fraction of TGA-PEI QDs analysed.

Figure 6.4 Cellomics (HCS) images depicting the changes in neurite outgrowth, due to coincubation of the QD with NG108-15 cells. Cell were incubated with TGA

QDs and gel-TGA-QDs at various concentrations for 6 h and induced to differentiate for 4 additional days in low-serum medium. Cells were stained for β-tubulin III (green) and nuclei (blue).

Figure 6.5 (A) Neurite outgrowth was assessed in terms of total neurite length per field. The result is an average of 3 independent experiments and final figures are expressed as percentages relative to the total neurite length per field of the untreated control sample. (B) Coloured composite fluorescent image [blue – nucleus, green - neurites] of neurite outgrowth is shown here.

Figure 6.6 Luminescence emission of QDs as a monolayer and embedded in 10 (dots), 14 (dash dots) and 18 (dash) polyelectrolyte multilayers.

Figure 6.7 UV-vis absorption spectrum of the gold nanoparticles (pink - plasmon band at 565 nm) and the luminescence emission spectra of the donor (green – λ_{em} 525 nm) and acceptor (red – λ_{em} 600 nm) QDs.

Figure 6.8 Graph of the increases in luminescence emission intensity when QDs are layered on gold nanoparticles.

Chapter 7 Experimental

Figure 7.1 Jablonski diagram for an excited molecule showing the possible processes involved in returning to the ground state.

Figure 7.2 Diagram illustrating the possible light scattering events in Raman spectroscopy.

Figure 7.3 Diagram illustrating the Raman shifts due to photon scattering.

Figure 7.4 Graphical illustration of a confocal microscope setup.

Figure 7.5 Diagram of the pinhole setup in a confocal microscope.

Figure 7.6 Correlation graphs illustrating the difference between small and large particles.

Figure 7.7 Size distribution (by intensity) for a standard sample.

Figure 7.8 Illustration of the rotating planes and the net magnetisation induced upon application of a magnetic field upon a spin ½ nucleus.

Figure 7.9 Diagram illustrating resonance, the condition where the applied radiofrequency equals the Larmour frequency and the net magnetisation changes plane.

Chapter 8 Appendices

Appendix 2a Empirical sizing data for CdTe QDs. Data taken from HRTEM measurements and correlated to UV-vis absorption maxima.

Appendix 3a Table of IR data taken for the QDs capped by the thiols described in Table 3.1

Appendix 3b IR spectra of mercaptopropionic acid (MPA) – QD

Appendix 3c IR spectra of 3-mercapto-1,2-propandiol – QDs

Appendix 3d IR spectra of glutathione – QDs

Appendix 3e IR spectra of cysteamine – QDs

Appendix 3f IR spectra of N-acetyl-L-cysteine – QDs

Appendix 3g IR spectra of *L*-cysteine – QDs

Appendix 5a: ^{1}H spectrum of N-(2-Mercaptoethyl)benzamide (Figure 5.4 B)

Appendix 5b: ^{1}H and ^{13}C spectrum of 2-[2-(2-amino-ethoxy)-ethoxy}-ethyl}-carbamic acid tert butyl ester] (boc-amino-PEG): **compound 1**

Appendix 5c: ^{1}H and ^{13}C spectrum of N- 2-(2-(2aminoethoxy)ethoxy)ethyl)-2-(6-methoxynaphthalen-2-yl)propanamide:(npx-amino-PEG-NH_2): **compound 2a**.

Appendix 5d: ^{1}H and ^{13}C spectrum of N-(2-{2-[2-aminoethoxy]ethoxy}ethyl)-2-(4-isobutylphenyl propanamide: ibu-amino-PEG-NH_2: **compound 3a**

Every year Ireland hosts the Young Scientist competition at the Royal Dublin Society (RDS) where up and coming school students demonstrate their skills in the hope of making a significant discovery, or perhaps just go for the day off school. I have had the privilege of demonstrating on behalf of Trinity College for a number of years and with the aid of colleagues from both chemical and physical backgrounds we set about giving the kids a glimpse into our everyday world, which we sometimes take for granted. We set up experiments with solutions oscillating in colour and real euro notes were burned before their eyes before being handed back in one piece. I once took along a sample of magnetite on a stirring plate and explained (with the aid of a transmission electron microscope (TEM) image) that these particles were one millionth the size of a human hair, while a colleague demonstrated the use of a portable scanning tunnelling microscope (STM) in visualising a silicon surface. Some stood with eyes wide open, some asked a few tentative questions but, try as we might, their introduction to the nanoscale was nothing short of boring compared to the freezing and breaking of "stuff" after a shout from the gallery to show them the liquid nitrogen!!!!

Chapter 1: Introduction

1.1 A brief look at the land down under 100 nm!

There has been a fluorishing in the world-wide "nanoscience" research initiative over the past number of decades. Nanotechnology and nanoscience (the term "nano" comes from the Greek word νᾶνος, meaning *dwarf*) is an ever growing field, encompassing a variety of areas including chemistry, biology, physics, engineering and materials science. [1] It is the study of phenomena less than 100 nm and involves the manipulation of these materials on the atomic scale. These materials can differ greatly from their bulk composition and can give rise to new and exciting phenomena by controlling their size, shape and composition.

"The world of neglected dimensions", a phrase first coined by Wolfgang Ostwald in 1927, quickly became synonymous with modern colloid chemistry. It is quite ironic that an area of research that was so seemingly "neglected" would become one of the most

hotly contested, highly funded and exciting some 80 years later. Nanocrystal research was initially motivated by an effort to understand the evolution of bulk structural and electronic properties on going to the molecular scale. [2] New fields and novel disciplines have emerged resulting in seemingly countless numbers of publications, bringing us into what may previously have been thought of as the realm of science fiction.

The public imagination has been captured by illustrations of "nanobots" and "nanocomputers" which can further our technical advancement by elucidating previously unheralded regions of our world and possibly increase our collective knowledge. From the original 1950's work by Isaac Asimov to the recent onscreen adaptation, I-Robot highlighted the possibility that our most mundane of tasks may be entrusted to robots in the future and when things don't go according to plan, the "nanobites" are called upon to rescue the day.

These wondrous fascinations perhaps act as a goal for us scientists also, as we strive towards the discovery of a nano system that may help to cure disease *via* a targeted drug delivery system, generate electricity or energy using energy transfer reactions in solar cells or light emitting diodes (LED's) or enable enhanced visualisation of anatomical systems by magnetic resonance imaging (MRI). The push towards the nanoscale has been aided greatly by the advent of machines capable of probing this tiny world. Techniques such as atomic force microscopy (AFM), scanning electron microscopy (SEM), transition electron microscopy (TEM) and confocal microscopy to name but a few have enabled us to view and explain phenomena at a scale of one thousand millionth of a metre. In this region, materials that were previously inactive in the bulk may become reactive, while new optical, strength and electrical properties may be enhanced. As such, control over a materials size and consequently its properties is highly desirable and semiconductor nanocrystals, due to their unique size dependant and tuneable qualities certainly fit this brief. [3-5]

1.2 Optical properties of semiconducting nanocrystals

Nanotechnology and its study is no longer a field in its infancy and is most certainly no longer "neglected". Over the past two decades, not only has it been one of the fastest growing research topics, it has also become one of the most important and dynamic interdisciplinary fields of modern science. This extensive research effort which was pioneered by Brus, [6-9] Henglein, [10, 11] and others [5, 12, 13] has led to a greater understanding of these smaller physical size regimes along with their structural and spectroscopic properties.

One of the attractive aspects of nanoscale materials is the possibility of controlling characteristic properties by limiting the particle size. By maintaining control over size, it is possible to monitor potential interactions with many organic and inorganic materials ranging from relatively simple compounds to proteins which may constitute many thousands of atoms. There is also a whole host of potential nanoscale materials chemists can play with, from metal systems (gold and silver) [14, 15] to magnetic particles (magnetite and maghemite) [16, 17] to II-VI [CdTe, CdSe, CdS] and III –VII [GaAs, [18, 19] InAs/InP, [20, 21] CdHgTe [22] and HgTe [23]] semiconductor nanocrystals.

Ever since primary investigations into their properties began in the 1980's, semiconducting nanocrystals [often referred to as quantum dots / QDs] have provided scientists with a material that has a rich variety of properties, characteristics and potential applications. Microscale and larger semiconducting crystals have electronic and optical properties that depend on their bulk band structures. When these crystals are reduced to the nanoscale, they essentially become "molecule like" and this gives rise to unique properties which result in the nanocrystals differing greatly from their bulk counterparts. [4, 5, 24] They enter a new regime where certain properties are no longer influenced by their band structure but by size and shape. [25, 26] For example in the case of CdS, the band gap can be tuned between 4.5 (275 nm) and 2.5 eV (450 nm) as the size is varied from the macro to the molecular scale. The energy above the band gap required to add excess charge also decreases by 0.5 eV [27] and the melting temperature increases from 400 to 1600° C. [28] This enormous range in the fundamental properties of a material opens up further possibilities to trace the evolution of electronic and optical properties of the matter from the bulk material to the atomic cluster. [3, 24, 29]

Depending on their size, nanocrystals can have between 10 and 50% of their total number of atoms residing on the particle surface. [30-33] As a consequence, these particles possess an extremely large surface to volume ratio; hence, surface coverage and interactions with the surrounding media play vital roles in determining the stability of these materials. Cadmium chalcogens are one type of nanocrystal which have been widely investigated, in particular CdSe [34-37] and CdS [38-40] while there has been a growing interest in the area of CdTe. [41-44] Unlike their bulk counterparts, nanocrystals possess discrete energy levels [delocalised molecular orbitals (MOs)] and a band gap that increases as the size of the material decreases. [45, 46]

In bulk semiconductors, the valence band (VB) and conduction band (CB) are separated by the band gap (E_g), which corresponds to the energy difference between the highest occupied molecular orbital (HOMO) of the VB and the lowest unoccupied molecular orbital (LUMO) of the conduction band. [47] Electrons (e^-) may travel from the VB to the CB, leaving behind a hole (h^+), if energy (in the form of an absorbed photon) greater than E_g is supplied. This creates an electron / hole pair (e^-/h^+), also known as the Wannier exciton and if the e^- and h^+ subsequently recombine, a photon is emitted (Figure 1.1). Traditionally, the absorption of one high-energy photon was thought to generate one exciton, but recently it has been shown by Ellingson *et al.* [48] that for PbSe and PbS nanocrystals, multiple excitons can be generated from a single photon. Extremely large quantum yields (QYs) (up to 300%) were recorded making them very attractive for use in solar cells.

Within the nano-region, the crystallite can be smaller than the natural radius of the e^-/h^+ pair, which possesses a characteristic dimension known as the exciton Bohr radius. If the crystallite size is greater than this dimension, the exciton wavefunction can extend out beyond its natural limit; however, when the nanocrystal size is less than that of its characteristic Bohr radius (1.56 eV / 790 nm for CdTe, 1.7 eV / 730 nm for CdSe and 2.4 eV / 516 nm for CdS), [2, 49, 50] the carriers are independently confined. Between electron and hole states, interband transitions accompanied by optical absorption or emission may occur, giving rise to a discrete series of optical lines. Thus, the smaller the nanocrystal, the greater the confinement energy and the higher the energy of light it absorbs. There is a simple relationship between crystal size and emission colour; the smaller the size the

shorter (higher energy) the emission wavelength, enabling the spectral properties to be tuned *via* manipulation of the crystallite size. Tuning of the properties can also be further achieved by controlling the shape in 1-D (quantum well), [51] 2-D (quantum wires) [52, 53] and 3-D (nanocrystals). [41]

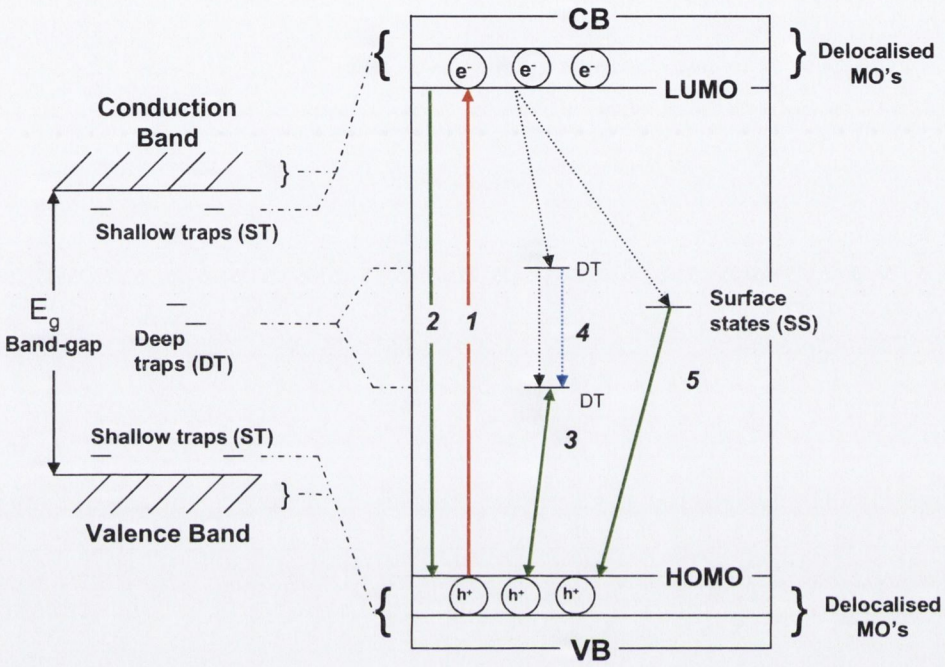


Figure 1.1 Schematic representation of the band gap (E_g) structure of a semiconducting material and the change in that structure on going from the bulk to the nanoscale. The absorption and subsequent emission pathways upon excitation by a photon are also shown. Adapted from literature. [54, 55]

On going from the bulk to the nanoscale, carrier confinement leads to the removal of continuous energy levels and the creation of discrete energy levels in the CB and VB (Figure 1.1). Due to the presence of these discrete energy levels, one would expect to see a well defined structure and distinctive absorption and emission bands, [5] as shown in Figure 1.2.

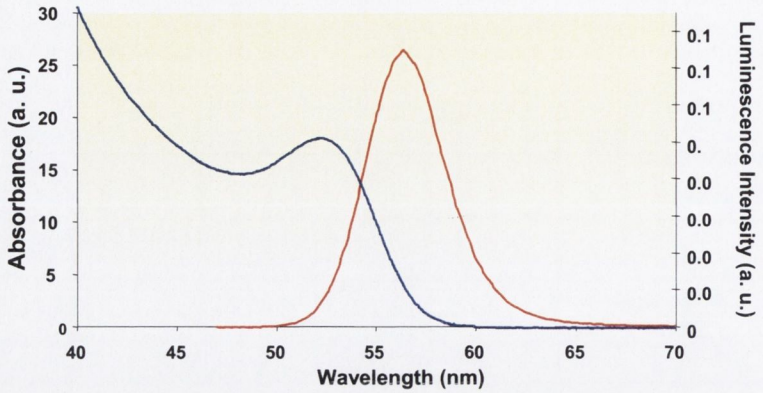


Figure 1.2. Typical UV-vis absorption (blue line) and luminescence emission (red line) profiles (λ_{ex} 450 nm) of a solution of CdTe nanocrystals in water. The Stokes shift (~ 40 nm) is the shift in the emission peak with respect to the lowest absorption peak.

Figure 1.2 illustrates the spectral features characteristic of CdTe semiconductor nanocrystals. The absorption peak corresponds to the 1s-1s electronic transition, while the emission results from radiative recombination of the photoexcited carriers. The resolution of the absorption maximum and the narrowness of the emission peak, measured at the full width half maximum [FWHM] value, give an indication of the homogeneity throughout the sample. An inhomogeneous or broad size distribution gives rise to a less defined absorption spectrum and an increase in the FWHM of the emission. A small Stokes shift from the absorption maximum indicates intrinsic emission while emission at far higher energies (red shifted) is indicative of a more defect related emission. This type of emission profile with large FWHM values and Stokes shifts [38, 56] generally occurs for CdS nanocrystals; [10, 54] however, the presence of defects (i.e. recombination of carriers from these trap states) in both CdTe and CdSe nanocrystals manifest themselves at slightly higher wavenumbers than the intrinsic recombination. [54] These defect states reduce the symmetry of the emission profile and can only be further resolved at lower (liquid nitrogen) temperatures, where an independent peak can be seen elucidated alongside the band gap emission. [43] One of the most dramatic properties of semiconductor nanocrystals is the size dependence of their spectral features as illustrated in Figure 1.3.

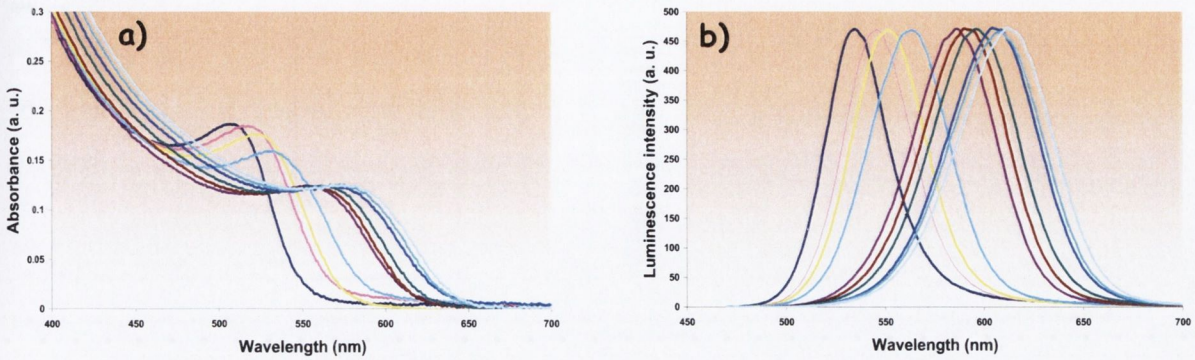


Figure 1.3. Quantum confinement effects on (**a**) the UV-vis absorption and (**b**) luminescence emission spectra of CdTe nanocrystals. As the size of the crystallite increases (2 - 5.5 nm), the spectral profiles shift to higher wavelengths.

Figure 1.3 illustrates the shifting in the absorption and emission profiles of CdTe nanocrystals with size that occurs during their production. From the UV-vis absorption (Figure 1.3, **a**) a red shift, accompanied by an inhomogeneous broadening of the nanocrystal ensemble can be seen. This is manifested by a reduction in the sharpness of the initially well resolved absorption peaks due to Ostwald ripening [process by which larger crystals grow at the expense of smaller ones], with the final bands appearing more shoulder-like. This inhomogeneity is further reinforced from the FWHM values taken from the emission spectra (Figure 1.3, **b**). Values increase from 40 nm initially to 58 nm as the nanocrystals grow under reflux.

As the size of the crystallite is reduced, the electronic excitations shift to lower wavenumbers (ie: higher energy). [24, 57] This illustrates the effect that quantum confinement has on the energy structures within the nanocrystals. The importance of particle size in determining the optical properties of QDs has led to an intense effort to obtain efficient synthetic methods for the preparation of QDs with controlled characteristics. These methods will be discussed in the following section.

1.3 Synthesis and growth

The intensity of investigations into the synthesis and behaviour of nanocrystal systems has been remarkable over the past few decades. Initial contributions on the synthesis of CdS and ZnS were made by Brus and co-workers during the 1980's. [6-8]

Moving on, other groups also continued with the production of CdS nanocrystals and comprehensively deciphered and analysed their unique properties. [7, 10, 57] Nozik *et al.* [5] investigated size quantisation in CdS and PbS nanocrystals, while Henglein and co-workers injected H_2S into a solution of cadmium perchlorate and sodium hexametaphosphate to give CdS nanocrystals with narrow size distributions. [10] The properties could be varied with pH and this led to the formation of a layer of $Cd(OH)_2$, which acted as an additional passivant for the removal of surface defect states. This shell was also attributed as the cause of dramatic luminescence increases without altering size when excess cadmium ions were added to a basic solution of CdS.

The emission from these CdS colloids is predominantly defect related and since then the best developed semiconductor nanocrystal syntheses have been for CdSe and CdTe. Here we will consider the synthetic approaches for both.

1.3.1 Organometallic syntheses

The synthetic methods employed have focused on obtaining highly crystalline, monodisperse and highly luminescent nanocrystals with desirable surface functionalities. Originally Murray *et al.* [58] were among the first to prepare CdE (E = S, Se, Te) nanocrystals, with a major emphasis on CdSe, *via* the use of dimethyl cadmium [$(CH_3)_2Cd$] and tri-*n*-octylphosphine selenide [TOPSe], which was then injected into a heated (180° C – 300° C) solution of the coordinating solvent tri-*n*-octylphosphine oxide [TOPO]. Slow growth and annealing in the coordinating solvent resulted in uniform surface derivatisation and regularity in the core structure, yielding CdSe nanocrystals with broad size ranges (1.2 – 11.5 nm). The ligands were exchanged using pyridine, precipitated with the addition of hexane, centrifuged and finally dispersed in a variety of organic solvents. This procedure enables the variability within the ensembles to be reduced down to < 5%.

A second approach, developed by Alivisatos *et al.* [33] was adapted slightly from the work of Murray. The principal difference between the preparations was the injection temperature, which affects the time evolution of the nanocrystal growth as well as their crystallinity and shape. Differences in temperature of less than 1° C changed both the average size and the quality of the size distribution. Unlike those produced by Murray,

the nanocrystals were crystalline, nearly monodisperse without the need for a size-selective precipitation procedure and spherical. Also, the TOPO was heated to 350° C under argon before injection (it was noted that this temperature was well above the flash point for TOPO and all manipulations were undertaken with extreme care) and after injection, the temperature was reduced to yield monodisperse ensembles. This change in temperature was utilised to distinctly separate both the nucleation and growth phases and resulted in high quality nanocrystals.

This work has been followed by other groups to produce high quality CdSe nanocrystals [59] but has been tweaked somewhat by Talapin *et al.* [37] in an effort to further reduce the amount of "defocusing" [60] or Ostwald ripening occurring during the growth period (Figure 1.4). They prepared CdSe using a three-component hexadecylamine-trioctylphosphine oxide-trioctylphosphine (HDA-TOPO-TOP) mixture which provided much better control over the growth dynamics.

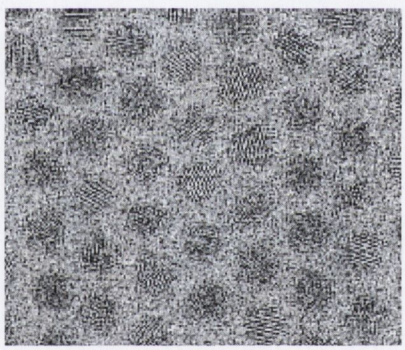


Figure 1.4. HRTEM image of monodisperse, highly crystalline CdSe nanocrystals, without any post-preparative treatment. Adapted from literature. [37]

This procedure, unlike previous reports, [33, 58, 61] allows for the production of monodisperse CdSe nanocrystals without the need for any post-preparative treatment to narrow the broad size distributions. In contrast to the growth of CdSe nanocrystals in TOPO-TOP, [34, 62, 63] a very fast "focusing" of the size distribution was observed with the HDA-TOPO-TOP system which continued throughout the entire growth process, while no "defocusing" (Ostwald ripening) was witnessed. This phenomenon was attributed to the large difference between the rate of nanocrystal growth in the "focusing" regime,

which occurs due to the initial excess of the monomer (cadmium species) in solution, and the rate of the Ostwald ripening process.

A somewhat "greener" approach was also been undertaken by Mekis *et al.* [59] They undertook a comparative study of the synthesis of CdSe QDs using the traditional but highly volatile $Cd(Me)_2$ and $Cd(Ac)_2$, a more "green" cadmium source and found differences in their reactivity. They found the $Cd(Me)_2$ to promote QDs growth *via* Ostwald ripening, while $Cd(Ac)_2$ promoted a more focussed growth.

This separation of nucleation and growth has led to various in-depth investigations into the mechanisms involved during the synthesis of nanocrystals. [60, 61, 64] Peng *et al.* [61] investigated the factors that influenced the growth of II-VI (CdSe) and III-V (InAs) nanocrystals. They began their investigations based on two important facts, **1)** diffusion-controlled growth leads to a narrowing of the size distributions with time [65] and **2)** a variation in surface energy with size, provided the crystallites are small enough that Gibbs-Thompson effects come into play, will directly influence the growth kinetics. [61, 64] They define the two distinct regimes within the growth cycle. Initially the size distribution is "focussed" during the first few minutes and then "defocused" as the nanocrystals grow more slowly. They explain that the size distribution can be influenced by the Gibbs-Thompson effect on Ostwald Ripening. At fixed monomer concentrations, the growth rate can be obtained by applying the Gibbs-Thompson equation:

$$S_r = S_b \exp (2\sigma V_m / rRT)$$

S_r / S_b = solubility of the nanocrystal and corresponding bulk
σ = specific surface energy
r = radius of the nanocrystal
V_m = molar volume of the material
R = Gas constant
T = temperature

If $2\sigma V_m / rRT \ll 1$, the diffusion controlled growth of a nanocrystal of size r is

$$dr/dt = K(1/r + 1/\delta)(1/r^* - 1/r)$$

K = a constant proportional to the diffusion constant of the monomer
σ = thickness of diffusion layer
r* = critical radius for which the solubility of the nanocrystals is equal to the monomer concentration in solution (zero growth rate)

They state that, according to this model, at any given monomer concentration there exists a critical size (r*) that is in equilibrium with the precursor concentration in solution. During focussing, the nanocrystals present are all larger than r* and the monomer concentration drops while particle concentration remains constant. Under these conditions smaller nanocrystals will grow at faster rates than the large ones.

During defocussing (Ostwald ripening), when the monomer concentration is depleted due to growth, r* becomes larger than the average size present. Thus, the distribution broadens while smaller nanocrystals disappear or dissolute and larger ones continue to grow. During Ostwald ripening, different nanocrystals grow at different rates within the ensemble leading to a distinct broadening of the size distribution.

Precursor concentration also plays a role. At higher concentrations, more nuclei are initially formed and these quickly expend the remaining monomers (cadmium containing species) as they grow. Thus, any remaining cadmium monomers induce an ineffective surface passivation of nanocrystal defects leading to a reduction in luminescence intensity. However, at low precursor concentrations, there is a reduction in the initial number of nuclei formed and cadmium monomers supplied to the surface effectively take part in ordering and reconstruction, leading to significant luminescence increases. [66]

Talapin *et al.* [64, 67] followed on from this work and applied a theoretical model to explain the evolution of sizes within a nanocrystal ensemble. Their model took the size dependence of the activation energies of the growth and dissolution processes into account and they applied Monte Carlo simulations to establish conditions leading to either focussing or defocussing. The same group undertook additional experiments to determine the influence that the distribution of growth rates within the nanocrystal ensemble would have on the luminescence properties. They attributed a loss in QY to a variation in the nanocrystal surface within the ensemble. Furthermore, they proposed that

after a size selective precipitation, the nanocrystal fraction with the highest quality or smoothest, defect-free surface corresponded to the crystal size with the smallest net growth rate during synthesis, (ie: r*, or zero growth rate as referred to previously) (Figure 1.5).

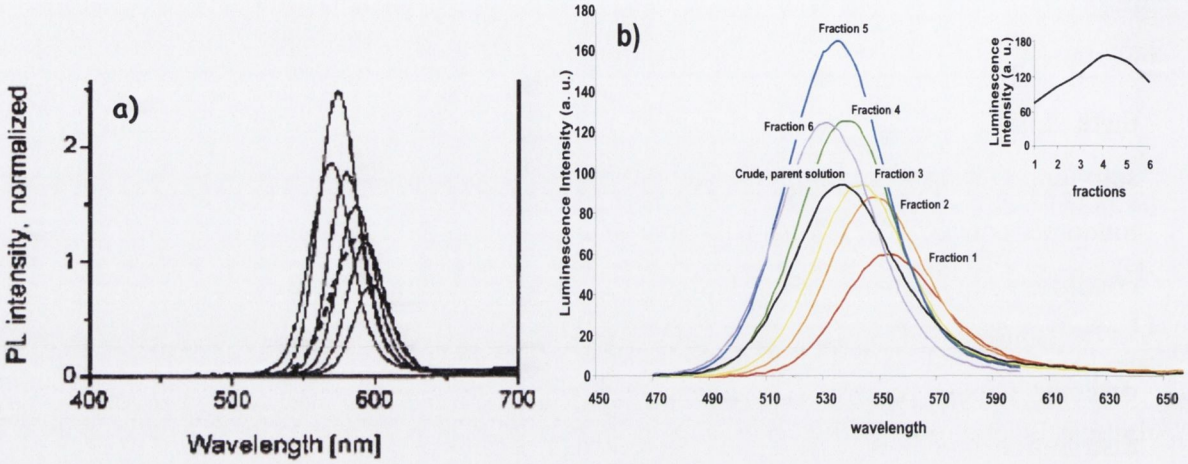


Figure 1.5. a) Luminescence emission spectra showing the QY evolution for each fraction of CdSe nanocrystals precipitated from a crude parent solution. [67] b) Luminescence emission spectra (λ_{ex} 450 nm) of CdTe nanocrystals [synthesised in our group] showing a similar evolution of the QY for each fraction precipitated.

This maximum emission intensity has further been investigated by Qu *et al.* [34] They found that during the growth of CdSe nanocrystals, the QY increases to a certain maximum value and then decreases gradually. They denote the maximum as a luminescence "bright point" and attribute this point to being the optimum surface structure during nanocrystal growth. The maximum is highly dependant on the initial Cd:Se ratio and a large Se excess was required to achieve the most substantial results with narrowest size distribution.

Qu *et al.* [36] have further demonstrated that contrary to the belief that the synthesis of high quality CdSe nanocrystals was a delicate affair; a variety of different systems can be used. They used a one-pot approach and different solvents (fatty acids, amines, phosphine oxides and phosphonic acids) to produce high quality CdSe nanocrystals.

1.3.2 Aqueous syntheses

1.3.2.1 CdSe

Unfortunately, even though these organometallically prepared nanocrystals possess high crystallinity, narrow size distributions and high fluorescence QYs, their further use in bioconjugation or imaging is hampered by their lack of solubility in aqueous solutions. To combat this problem, phase transferring from organic to aqueous has been utilised to produce water based colloidal solutions. This process takes advantage of the fact that the coordinating molecules such as TOPO are not covalently bound and can be easily replaced by thiol ligands. Due to the success of organometallically synthesised CdSe, explorations into their production under aqueous conditions have been sparse [68-70] and frequently yield polydisperse nanocrystals exhibiting trap emission which overlaps with the intrinsic luminescence. Rogach *et al.* [68] have demonstrated, as an expansion of the wet-chemical route for the production of II-VI semiconductor nanocrystals, that CdSe can be synthesised using mercaptothiols [2-mercaptoethanol and 1-thioglycerol] and mercapto acids [thioglycolic acid and thiolactic acid] as stabilisers. They found that smaller nanocrystals (1.2 – 2.2 nm in diameter) could be produced with the thiols while larger nanocrystals (2.1 – 3.2 nm) were produced using thioacids. The same group have also demonstrated the production of HgTe [23] using $Hg(ClO_2)_4$ and bubbling H_2Te through at basic pH values in the presence of 1- thioglycerol.

Due to their poorer aqueous properties, several strategies have been pursued to solubilise high quality hydrophobic CdSe nanocrystals in aqueous solvents. Initial developments in this area were conducted by the Quantum Dot Corporation (now Invitrogen). They developed and patented [19 issued patents, pioneering patent - U.S. Patent No. 5,990,479] aqueous CdSe nanocrystals for bioimaging by their encapsulation in a silica shell and their conjugation to various biomolecules (Figure 1.6). Bruchez *et al.* [71] have also grown a silica shell around CdSe nanocrystals which provided them with a suitable coating for further modifications to provide new labels for imaging mouse 3T3 fibroblast cells.

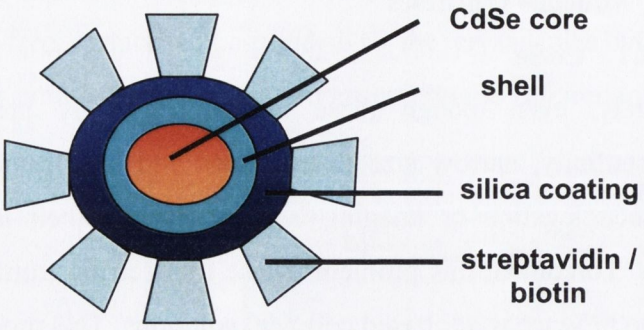


Figure 1.6. Graphical representation of a nanocrystal produced by the Quantum Dot Corporation.

Reiss and co-workers [72] reported the use of mercaptoundecanoic acid (MUA) for transferring CdSe nanocrystals into water. They found that uncapped CdSe cores exhibited a dramatic decrease in their luminescent properties upon transferring to water; however, those that were capped with a shell of ZnS displayed no adverse effects. Chan and Nie [73] utilised thioglycolic acid (TGA) to transfer the CdSe nanocrystals into water with the goal of attaching a protein to the nanocrystal surface. They were then incubated with HeLa cells and the experiments performed demonstrated the nanocrystals aggregated with antibody recognition of immunoglobulin G. Mitchell *et al.* [74] used 3-mercaptopropionic acid (MPA) to initially passivate the nanocrystal surface and act as a pH trigger for controlling the water solubility. Alkylthiol-capped oligonucleotides were subsequently immobilised on the surface and hybridised to a complementary strand (Figure 1.7).

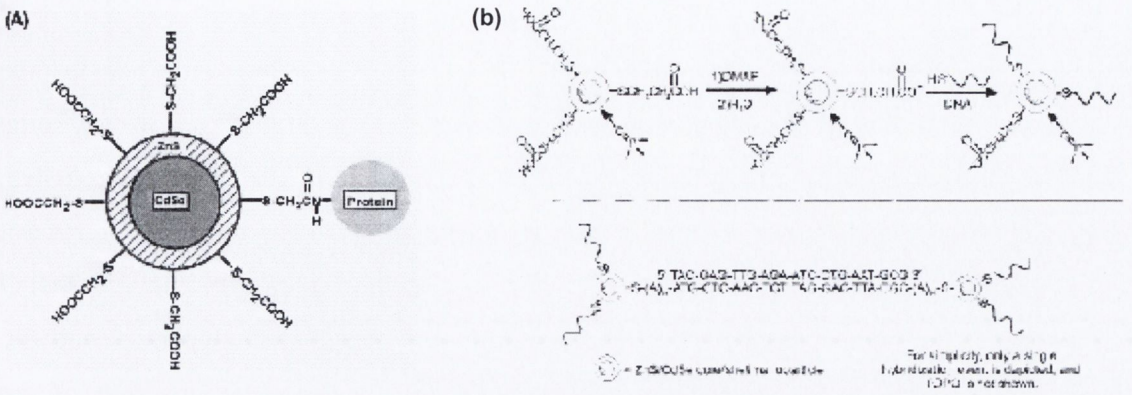


Figure 1.7. a) Illustration of a ZnS-capped CdSe QD that is covalently coupled to a protein by mercaptoacetic acid (TGA). [73] **b)** Schematic, illustrating the transfer of ZnS capped CdSe nanocrystals to water *via* the use of mercaptopropionic acid (MPA). A thiol containing oligonucleotide was then immobilised and subsequently bound to a complementary strand. [74]

1.3.2.2 CdTe

In contrast, the production of non-aqueous CdTe nanocrystals has had a relatively limited development [75-78] while its aqueous synthesis has expanded rapidly over the last few years. Precursors such as NaHTe [43, 66, 79, 80] and H_2Te [41, 81-84] are most commonly used but variations such as $(NH_4)_2Te$ [85] and Na_2TeO_3 [86] have been investigated recently. Highly luminescent CdTe nanocrystals have also been synthesised using microwave irradiation. [80]

The aqueous based preparation of mercaptoethanol and thioglycerol capped CdTe nanocrystals, was first investigated by Rogach and co-workers. [87] The same group also investigated the production if HgTe [23] and CdHgTe core-shell [22] nanocrystals soluble in an aqueous environment. Kapitonov *et al.* [43] were among the first to elucidate the trap states at lower temperatures and carried out lifetime studies for CdTe nanocrystals in water. Gaponik *et al.* [41] were among the first to use H_2Te (however, this is a very toxic gas [85, 88]) as a tellurium source and carried out thorough investigations into the properties, stability and photoetching of these nanocrystals. They found that thiols acted as efficient passivants due to their incorporation into a mixed CdTe(S) phase on the surface. This phase was further investigated by our group using Raman spectroscopy. [82]

1.3.3 Comparison of organic versus aqueous syntheses

The production of CdSe nanocrystals *via* an organometallic route has led the synthesis of high quality semiconductor nanocrystals for about 10 years. However, some key chemicals used in this traditional route are extremely toxic, pyrophoric, explosive, and can be very expensive. Also, until recently, the synthesis was hard to control and not very reproducible. Generally CdSe nanocrystals are synthesised in a mixture of TOPO and TOP; however, the problem of irreproducibility of the growth dynamics and the shape of the CdSe nanocrystals was mediated by the uncertain composition of the coordinating solvent. Technical grade TOPO (90%, Aldrich), for instance, provides better conditions for the growth of CdSe nanocrystals than distilled TOPO. [37] The solvent itself must be heated to extreme temperatures (300° C), which is well above its flash point giving rise to the risk of explosion or fire. Typically $(CH_3)_2Cd$ is used and this is a highly dangerous and toxic compound. It is extremely air and moisture sensitive and must be handled with great care and respect. In an effort to overcome this problem variations such as CdO, [89, 90] $Cd(Ac)_2$ [59] and cadmium myristate [91] have been used.

Recently alternative routes with safer and less expensive cadmium precursors and ligands have been reported [34, 90, 92] and have promoted the synthesis of CdSe nanocrystals to an easily adoptable level. Reiss *et al.* [72] and Li *et al.* [92] have employed CdO for the synthesis of high-quality CdSe/ZnSe core/shell nanocrystals without the use of the traditional pyrophoric organometallic precursors. Qu *et al.* [34] have explored further and used CdO for the production of not only CdSe but also of CdS and CdTe.

The cost of production is a further factor and traditionally aqueous prepared nanocrystals are cheaper, safer and somewhat easier to make and manipulate than their organometallic counterparts.

1.4 The nanocrystal surface and luminescence improvement

As noted earlier, one very important characteristic of nanocrystals is the abundance of atoms that reside on their surface. [33, 93, 94] Nanocrystals possess an extremely high surface-to-volume ratio, and as such, the nature of the surface becomes critical and its passivation or coordination can lead to the formation of surface trap states that can strongly influence the recombination of the charged carriers. Semiconductor

nanocrystals typically contain quite a high density of defect states and since a large majority of the atoms reside on the surface, so do many of the defect sites (Figure 1.8). It is important that we understand the processes occurring at these interfaces as the synthetic procedures employed for the production of nanocrystals and the capping agents used directly influence the nature of these defects.

Upon optical excitation, an electron is promoted to the CB and radiation occurs upon its recombination with the hole left behind in the VB (also termed radiative recombination). Recombination may occur between the bands, surface states or crystal defect sites which reside at energy levels within the band gap (Figure 1.1). Energy loss occurs *via* the creation of phonons in the lattices which enable the free carriers to be trapped at these recombination centres, which may be radiative or non-radiative. [95]

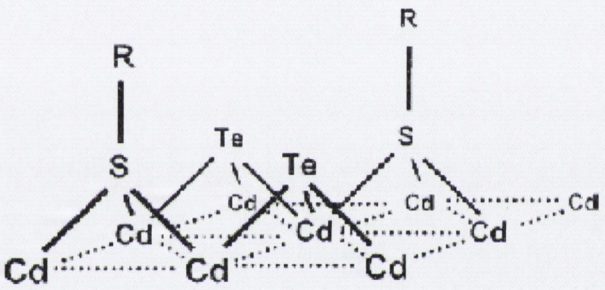


Figure 1.8. Graphical illustration of the mixed occupancy on the surface of a CdTe nanocrystal. Note: when surface Te sites dominate, this results in a high quantity of surface dangling bonds and lower luminescence efficiencies. The occupation of these 3-fold coordinate sites with a thiol molecule results in increased stabilisation and the removal of surface dangling bonds (passivation). This also leads to the formation of a core-shell like structure of Cd and S, which acts like a potential well giving a better confinement of the excitons and increased QYs for the nanocrystals. Adapted from literature. [83]

In general, a high luminescence QY results from predominantly intrinsic recombination, while a low QY is considered a result of the defect states located within the band gap acting as traps for the photogenerated carriers. These defect states provide alternate routes for the rapid (< 1 ns) recombination of the exciton, resulting in radiationless transitions. [30] Borchert *et al.* [83] have found there were less Te atoms on the surface of highly luminescent CdTe nanocrystals with respect to those with low

luminescence. Removal of the anion (Te) site passivation leads to the formation of a dangling bond (DB) state just above the valence band, which acts as a trap for photogenerated holes. Conversely, removal of the cation (Cd) site passivation leads to an e^- trap just below the CB (Figure 1.9.). [93]

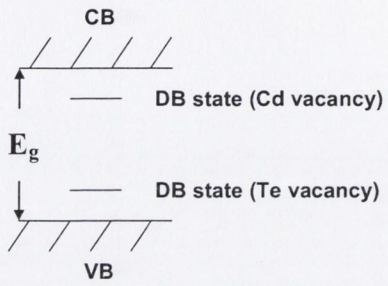


Figure 1.9 Illustration of the location of the anion (Te) site and the cation (Cd) defect sites within the band gap (E_g). Adapted from literature. [93]

As such, the nanocrystal surface can be viewed as an ensemble of dangling and terminal bonds [20, 34, 96, 97] as well as vacancies, dislocations, screw and other defects which are all in various forms of coordination with the surrounding solvent and any associated ionic or adsorbed entities. [94, 98]

To ensure a reduction in the number of surface dangling bonds, a larger ratio of cadmium to tellurium can be added to the reaction mixture. This encourages a greater surface coverage by the binding ligands and helps reduce the number of non-radiative centres. Theoretical treatments indicate that the efficiency of the passivation provided by the surface ligands depends strongly on the surface structure and the nature of the surface states of the nanocrystals themselves. [20]

The ligand dynamics depend highly on the reaction temperature and the ligand-ligand interactions greatly affect the surface quality. [20, 99] If the surface ligands can provide a good electronic passivation for the surface states of the nanocrystals, a high QY should be expected. By comparing the QY of the nanocrystals coated by various ligands, it can be concluded that passivation and steric effects play a vital role in the resulting luminescence efficiencies of the nanocrystals.

The capping of the nanocrystals by a wider band gap material (such as CdS, ZnS) also provides another route to increased luminescence intensity and QY. This generally

occurs for nanocrystals synthesised in organic solvents and numerous reports have indicated that an epitaxial layer of an inorganic passivant significantly reduces the number of non-radiative centres by efficiently capping the unsaturated surface atoms. [2, 3, 100, 101]

Occupation of the vacant surface sites by, in this case, sulfur atoms with an additional bond to the organic stabiliser gives a more favourable passivation (Figure 1.8). When the Te vacancies are occupied by sulfur, the dangling bonds are removed and a core-shell like structure is formed which acts as a potential well, enabling better confinement of the photogenerated carriers. This shell of material can be grown around the core inorganically in an organic medium but can also, in the case of thiol stabilised, water soluble nanocrystals, be generated by the decomposition of the thiol capping reagent [82] and the incorporation of sulfur into the surface structure. In fact, Zhang *et al.* [102] and Gaponik *et al.* [41] have found that effective surface passivation by the formation of Cd-thiol complexes [66] was the origin of high luminescence QYs.

Photoetching of the nanocrystal solutions has also been widely investigated as another method for the improvement in QYs. [41, 103-105] This process is quite an important route towards the production of highly luminescent nanocrystals and opens up possibilities for their use in photolithographic processes. [106] The illumination procedure is dependant on a number of conditions; excitation wavelength, lamp power, nitrogen or oxygen environment, duration of irradiation and several theories have been proposed to explain the observed phenomena. We ourselves have conducted several photoetching experiments, the details of which can be found in Chapter Two. The presence of oxygen has been found to play an intricate role in the luminescence improvement. Wang *et al.* [107] found that an approximate 10% increase was noted for CdSe nanocrystals when irradiation was conducted in the presence of oxygen as opposed to 1.5% without. They suggest that a reconstruction or annealing of the surface takes place to remove defects and this is further confirmed as photoactivation was often accompanied by photocorrosion, as given by Scheme 1.1 and shown in Figure 1.10.

$$CdSe + O_2 \xrightarrow{hv} Cd^{2+} + SeO_2$$

Scheme 1.1. Photocorrosion of CdSe to give free Cd^{2+} and SeO_2.

They conclude that the blue shift in the emission spectra that accompanies illumination is due to the removal of mid-gap states and structural features from the surface. [108] The gradual erosion of the topological features arises from the trapping of the charged carriers in surface states. Here the excitons activate reactions towards the oxidation of O_2 to O_2^- and Se to SeO_2, resulting in the removal of atomic moieties from the surface and giving rise to a shift in the emission spectrum to lower wavenumbers. This surface curing results in the reconstruction of the stabiliser shell and annealing of the surface defects (Figure 1.9). [67]

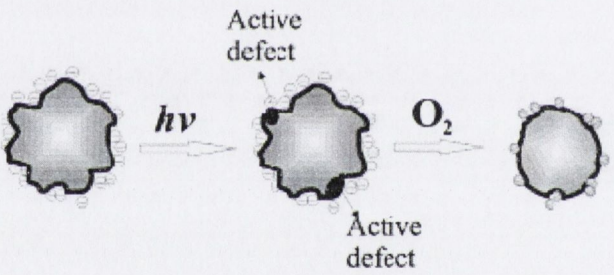


Figure 1.10. Illustration of the trapping of the charged carriers in "rough" states where photooxidation eliminates the atomic scale imperfections. This reduces the size of the crystallite and enhances the QY. Adapted from literature. [107]

For different types of nanocrystals, different shell compounds are created. Bol *et al.* [109] have shown that irradiation and subsequent oxidation of $ZnS:Mn_2^+$ crystallites results in the production of $ZnSO_4$ and $Zn(OH)_2$, which serve as a passivation layer. Dunstan *et al.* [95] have shown that for ZnS nanocrystals the decomposition products are SO_4^{2-}, S, Zn and SO_3^{2-} and these species act as individual recombination centres at the surface. While these processes result in the formation of new layers at the nanocrystal surface, it has also been postulated that the decomposition of thiol capping molecules results in increased QY values. [41, 82, 110] Zhang *et al.* [110] used XPS (X-ray photoelectron

spectroscopy) to experimentally observe that Cd–thiol complexes on the crystal surface provide the crucial chemical passivation responsible for high luminescence efficiency. Also, the high stability and QY corresponded to the nanocrystals with the greatest Cd-thiol surface coverage, as S was found to occupy Te sites in the lattice. Holes have also been shown to oxidize sulphide anions [11] (Scheme 1.2), creating elemental sulphur which can add to and cap the nanocrystal surface.

$$H^+ + S^{2-} \longrightarrow S^{\cdot -}$$

$$S^{\cdot -} + O_2 \longrightarrow S + O_2^{\cdot}$$

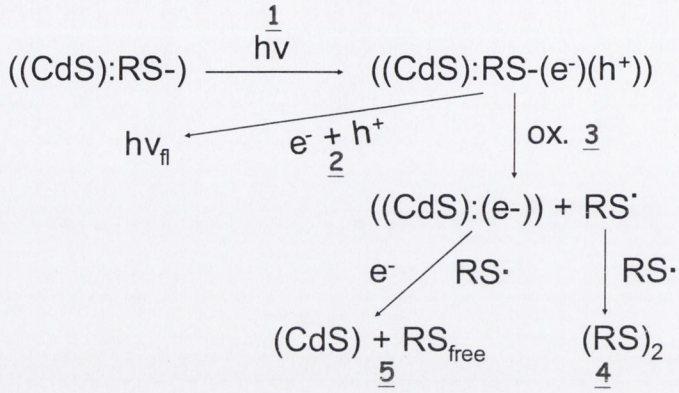
Scheme 1.2. Mechanism of the oxidation of sulfur by photogenerated holes as proposed by Henglein. Adapted from literature. [11]

1.4.1 Ligand stability

Coupled to this oxidation of the nanocrystal, the stability of the capping agents must also play a crucial role in the luminescent properties and solubility of the nanocrystals in solution. This is further emphasised by the fact that, before purification from the crude parent solution, the nanocrystals can be stable for years. However, after size selective precipitation, the surface coverage can be compromised due to the removal of thiols by the addition of a non-solvent. On a positive note, this instability can be utilised to generate new nanostructures such as tetrapods or wires. [52, 111-113] Nanocrystal instability can manifest itself in three distinct processes: [104] the photocatalytic oxidation of the stabilising ligands (generating disulfides), the photooxidation of the nanocrystal itself (as shown previously) and finally precipitation.

Due to their large surface to volume ratios and the quantity of atoms present on the nanocrystal surface, the capping ligands act to both sterically prevent each individual particle from aggregating and to neutralise surface dangling bonds due to unpassivated atoms. [94, 96] Activation and subsequent decomposition of these capping agents gives one explanation as to why irradiation times can vary from sample to sample and why decomposition of the nanocrystals and their subsequent aggregation and precipitation from the solution arises. It has been shown by Fischer and Henglein, [114] that thiolate

(SR^-) stabilised CdS nanocrystals photodissolve in the presence of oxygen; however, they are also sensitive to irradiation in its absence. They proposed the following mechanism, which illustrates the various processes initiated by the absorption of light (Scheme 1.3).



Scheme 1.3. Mechanism proposed by Fischer and Henglein [114] which describes the photocatalytic removal of the surface capping thiol molecules from CdS nanocrystals. **1:** light absorption generates an exciton (e^-/h^+ pair), **2:** exciton can recombine radiatively (fluorescence, fl) or nonradiatively [main reaction], **3:** oxidation of thiolate anion to form a thiyl radical which is released from the nanocrystal. **4:** thiyl radical can dimerise to form the disulfide. **5:** electron can pick up another one to form CdS and free thiol.

Scheme 1.3 shows the mechanism proposed to explain the removal of the thiol capping group from the surface of CdS nanocrystals. The thiol ligands can be gradually photoxidised to disulphides, with a net result of a loss in the number of stabilising groups. However, at a certain threshold of illumination time the nanocrystals will lose a critical amount of their capping groups and due to this thiol loss, their stabilisation is compromised and they are no longer able to remain in solution.

Another contributing factor is pH, which also affect greatly the nanocrystal and ligand stability and consequently the QY. It has been shown that, while the nanocrystals are synthesised at basic (~ 11) pH values for carboxylic acid capping agents, a reduction in pH to approximately 4.5 can generate an improvement in the QY. Any further lowering of the pH results in decomposition. [44]

Gao *et al.* [44] determined that the luminescence efficiency depends greatly on the pH of the solution. They witnessed a dramatic five fold increase in QY upon decreasing

the pH. They attribute this behavior to structural reorganisation of the nanocrystal surface, due to the formation of a Cd-TGA complex shell in acidic ranges. This complex, formed from the hydrolysis of the stabiliser, essentially acts as an additional capping reagent and has been explored by various other groups. [41, 67, 102] Aldana *et al.* [115] have also analysed pH alterations and found that the dissociation of ligands from the surface of the nanocrystals was the main cause for their precipitation in relatively acidic solutions. However, they also state that the equilibrium pH values for this dissociation process were highly dependent on the size of the nanocrystals.

The interaction due to the different functionalities of the various capping groups also plays a role in nanocrystal stabilisation and luminescence QY. By analysing the crystal structure of $Cd(SCH_2COOCH_2CH_3)_2$, Dance *et al.* [116] proved the existence of secondary coordination behaviour between the carbonyl oxygen from ($SCH_2COOCH_2CH_3$) and the primary thiol combining cadmium. This interaction, depending on the chain length of the thiol molecule, gives rise to a stable 5 or 6-membered ring formation (Figure 1.11, **a**) An enhancement of the QY was also observed by Zhang *et al.* [102] for 3-mercaptopropionic acid-stabilised CdTe upon reduction of the pH to 6. They attributed the dependent luminescence behaviors of the thiol stabilised nanocrystals to the protonation of carboxylate groups from particle surface binding thiols. They also investigated, with the use of carboxylic acid rich polymers, the effects that may occur when the interference from surface binding thiols was removed (Figure 1.11 **b**).

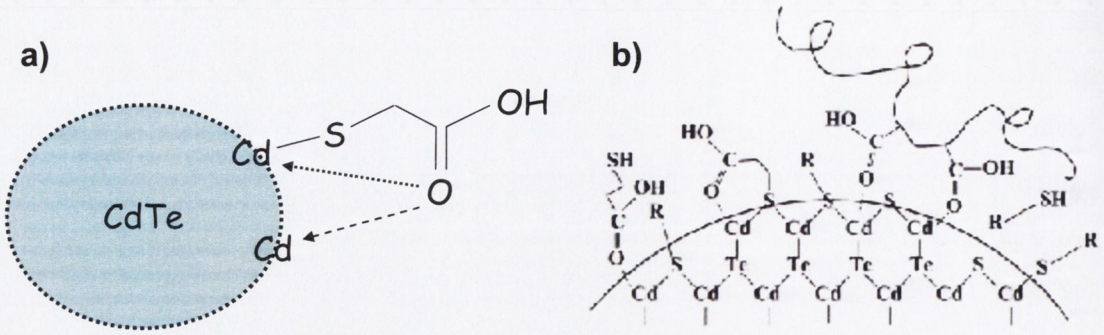


Figure 1.11. a) Graphical illustration of the secondary (5 and 6 coordinate) stabilisation of TGA capped CdTe nanocrystals due to interactions of the carbonyl oxygen of the thiol capping group at the primary or secondary thiol containing cadmium. **b)** Graphical illustration of the surface structure of CdTe nanocrystals modified with MPA and PAA (poly(acrylic acid). The coil represents the PAA alkyl chain and R represents a carboxylic acid group. The coordination between the carbonyl oxygen and cadmium on the particle surface is represented as a dotted line. The naked sulfur species in the particle results from the decomposition of thiols which occurs in the acidic pH region. Adapted from literature. [102]

QY increases were demonstrated indicating that carboxylic acid moieties can indeed provide an additional stabilisation for the nanocrystal surface. This reinforces the theory that secondary interactions from external or internal (thiol capping group) can in fact lead to luminescence increases. The application of QDs is highly dependant on their QY and other properties that will be discussed in the next section.

1.5 Uses of semiconducting nanocrystals

The unique properties displayed by some materials upon their reduction to the nanoscale have led to their use in many potential applications. Nanomaterials are beginning to have a significant impact on the world around us and are being incorporated into some of our everyday items. Currently, nanosized TiO_2 and ZnO are being incorporated in some sunscreens, as they absorb and reflect ultraviolet (UV) rays and yet are transparent to visible light. Nanoparticle or nanotube composites, due to their advantageous mechanical and electrical properties are finding uses in anti-static packaging or sports equipment such as tennis racquets or golf clubs. Cutting tools made

of nanocrystalline materials, such as tungsten carbide, tantalum carbide and titanium carbide, are more wear and erosion-resistant than their predecessors and are finding applications in the drill bit industry.

Because of their unique size dependent and highly luminescent characteristics, semiconducting nanocrystals have been investigated as potential LEDs [117-120] and lasers. [121, 122] Other possible uses that have been proposed are in biosensor applications. In this case fluorescence resonance energy transfer (FRET) can play a crucial role. [123-126] Clapp *et al.* [125] immobilised Cy3-labeled proteins onto CdSe-ZnS nanocrystals and found that FRET was the dominant mechanism involved, as the nanocrystals acted as efficient energy donors. Zhang *et al.* [127] have also shown the use of a CdSe QD-FRET nanosensor for DNA detection with ultrahigh sensitivity, while Bakalova *et al.* [128] have investigated the potential of nanocrystals to act as photosensitisers for photodynamic therapy and diagnostics.

Experiments based of the quenching of nanocrystal luminescence have been conducted to evaluate their potentials as detection agents for metal ions in solution. Bovine serum albumin (BSA) conjugated CdSe/ZnS nanocrystals were utilised for copper determination, [129] while TGA – BSA CdSe [130] and *L*-cysteine [131] capped CdS nanocrystals have been used for silver ion detection. Water-soluble CdSe nanocrystals whose surface was modified either with 2-mercaptoethane sulphonic acid or with 2-mercaptoacetic acid, [132] and with mercaptopropionic acid [133] were investigated for the detection of copper(II) ions in aqueous solutions. Li *et al.* [134] have utilised water soluble CdTe nanocrystals and nanorods to investigate the effect on their luminescence responses when exposed to divalent metal ions, such as zinc, calcium, magnesium, manganese, nickel, and cobalt.

The use of nanocrystals for these applications also runs in parallel with the ease of detection of these materials in biological systems. This is a rapidly developing area that has come under much focus recently. Here, we will focus on some of the biological aspects of nanocrystal imaging that are relevant to this project.

1.5.1 Biological imaging

With the advent of improved synthetic procedures, efficient capping and labelling with biocompatible moieties, semiconducting nanocrystals are becoming widely used in biotechnology and possible imaging applications. [135-139]

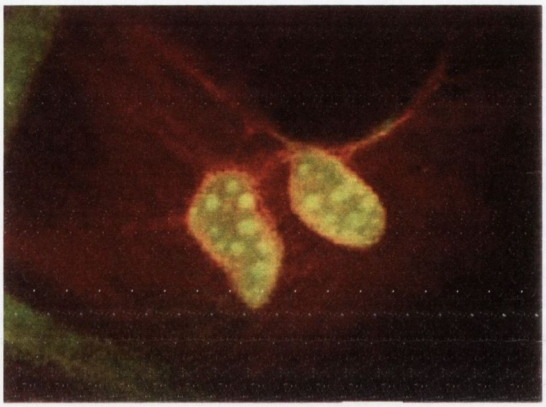


Figure 1.12. Mouse 3T3 fibroblast cells labelled with silica coated CdSe nanocrystals. Red emitting nanocrystals label the F-actin while green stain the nucleus. Adapted from literature. [71]

Nanocrystals possesses optical properties that are ideal for imaging of biological systems (Figure 1.12). The use of nanocrystals *in vivo* has been explored [140-143] but further research may well be hampered by their toxic core materials. As such, many studies have focussed on the *in vitro* labelling of cellular components [144-147] and the use of nanocrystals as replacements for traditionally organic dyes has become a possibility.

Organic fluorophores are hampered by narrow excitation bands and broad emission spectra which limit the amount of dye that can be deployed in unison [multiplexing]. [148] They also possess a low resistance to photo and chemical degradation which limit their detection effectiveness over longer experimental time periods. [149, 150] In contrast, nanocrystals possess excellent fluorescent properties with molar extinction coefficients up to 100 times that of organic dyes, [100, 141, 150] good chemical stability and high photobleaching thresholds to help overcome current imaging limitations (Figure 1.13).

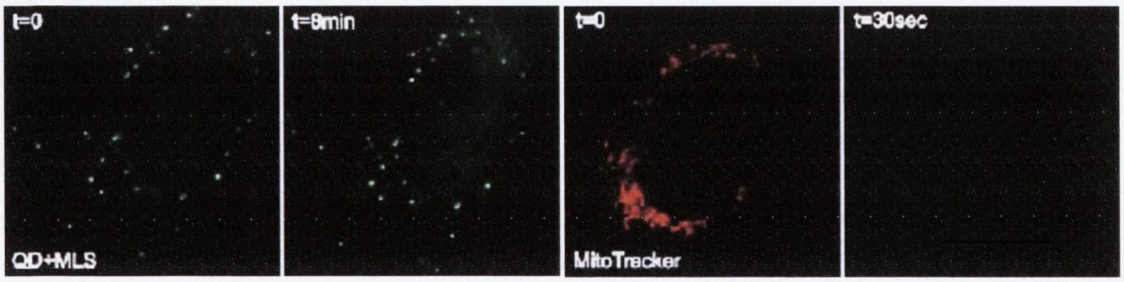


Figure 1.13. Fluorescent micrographs illustrating the effects of mercury lamp exposure on QDs (green, left panels) and Mitotracker (red, right panels). The QDs can be clearly seen to retain their fluorescence after 8 minutes while the dye is completely bleached after only 30 seconds. Adapted from literature. [151]

They also exhibit long fluorescence lifetimes making them easy to distinguish from background autofluorescence. However, most significantly they have tuneable sizes, narrow emission wavelengths with FWHM of between 30-40 nm and broad excitation ranges. [71, 73, 137] Thus, nanocrystals can be tuned across a wide spectral range by altering the composition, from UV-blue [ZnS], [152, 153] to the visible [CdS/CdTe/CdSe] [24, 41, 75, 154] to the near-IR [PbS, CdS/HgS/CdS, HgTe]. [22, 155-157]

QD bioimaging is a topic that was first explored a number of years ago [71, 73] and since then has become the focus of a great amount of research. As illustrated by Klostranec and Chan, [1] the number of publications for both metal and semiconducting particles, focussed on their potential biomedical applications over the past 10 years has increased dramatically (Figure 1.14).

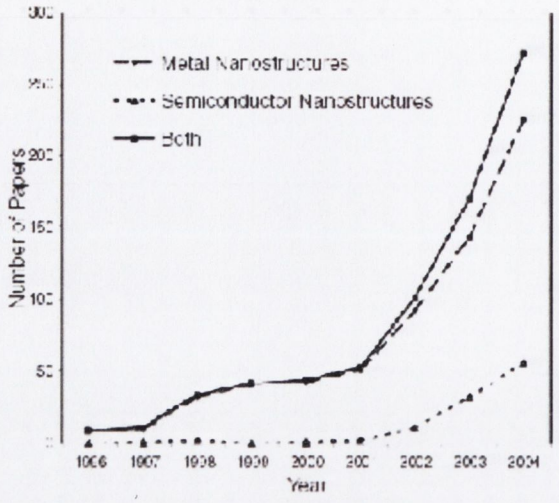


Figure 1.14. Graph illustrating the number of published manuscripts between 1996 and 2004 which report the use of nanomaterials (specifically, metallic and semiconductor nanocrystals) in biological applications. These data were compiled using the Medline database. Adapted from literature. [1]

There are also some drawbacks for the utilisation of QDs in biomedicine. Depending on the surface functionalisation and capping they may aggregate easily once exposed to a cellular environment and are particularly susceptibly to changes in pH, most notably in the acidic (pH <5) range. [151, 158] Long term stability is also an issue and studies have indicated that di-thiol capped nanocrystals have longer shelf-lives than their mono-thiol capped counterparts. [159] Thus, the possibility of replacing traditional fluorophores cannot be fully realised just yet. Another hindering feature is the intermittent blinking [160-162] of nanocrystals when excited by high intensity light which arises due to the inefficient confinement of the charge carriers and multiple charge nonradiative scattering. [163] The non-specific binding of nanocrystals also varies with surface coating and similar batches can stain different regions leading to false signals. This can be overcome to some degree by employing poly(ethylene glycol) [PEG] as a capping agent. [140, 151]

Bio- and chemical conjugation allows for the improved stability and biocompatibility of nanocrystals enabling them to be used for specific biological targeting. We will consider this area in more detail below.

1.5.2 Bio-conjugation

Conjugation of nanocrystals to biomolecules has been shown to reduce aggregation and improve stability within cellular regions [73, 164-166] Conjugation strategies follow three major routes, (i) 1-ethyl-3-(3-dimethylaminopropyl) carbodiimide (EDC) coupling enables cross conjugation between carboxylic acids and the primary amino functionalities of the biomolecule. [127, 164] However, this can lead to problems of crosslinking due to the variety of functionalities present within the protein or oligonucleotide which allow for non-specific and indiscriminate binding. (ii) The biomolecules can possess binding moieties themselves and can be directly attached to the surface, generally through thiol containing cysteine [62, 140] linkages or *via* the metal-affinity coordination of histidines. [167] (iii) Non-covalent binding involving the use of electrostatic self-assembly to conjugate nanocrystals to proteins, antibodies or intermediate molecules. [139, 168, 169]

The labelling of cells can be distinctly separated into two categories, targeted *via* bio-conjugation and non-specific labelling. A key issue for the use of nanocrystals in cell tracking is their delivery to the cytoplasm or organelles such as the nucleus or mitochondria. While there are various dyes available which can penetrate cell membranes easily (although they can adversely affect the cells) and label these cellular features (DAPI, Mitotracker, Hoescht), nanocrystal properties such as size and functionality may prevent crossing of the lipid bi-layer. As such, Derfus *et al.* [151] have explored several strategies for enhanced delivery of nanocrystals into live cells. They found that nanocrystals were sequestered by endocytosis into the endolysosomal compartments which renders them unavailable for further assays but microinjection delivered the nanocrystals as monodisperse entities. However, this requires specific and individual manipulation of the cells and is extremely time consuming.

Different types of functionalisation [primary antibodies, [170] DNA, [127] serotonin, [136] biotin-avidin, [62] avidin, [139] chitosan [171] and peptides [140]] have been utilised to explore how nanocrystals target specific cell proteins or receptors. Other moieties such as antibody (eg. immunoglobulin G and streptavidin) linked nanocrystals were shown to label the Her2 breast cancer marker on the surface of cancer cells, stain actin and microtubule markers and detect antigens in the nucleus. [137] Also, nanocrystals linked to

DNA probes were reported as new nanosensors for the detection of low concentrations of DNA by FRET. [127]

Clarke *et al.* [126] have investigated the conjugation of dopamine (an electron donating molecule) to nanocrystals in an effort to increase specific binding and recognition by cells that bear dopamine receptors. The conjugates display a redox sensitive patterning, and oxidation or reduction results in particular localisation of the nanocrystal. Antioxidants were also shown to reduce the level of toxicity from any singlet oxygen produced upon irradiation.

Winter *et al.* [172] have attached CdS nanocrystals to live neurons utilising both antibody and peptide recognition molecules, while CdSe/ZnS nanocrystals labelled with the protein transferrin underwent receptor-mediated endocytosis when cultured with HeLa cells. Those nanocrystals labeled with immunomolecules were shown to recognize specific antibodies or antigens. [73] Neurons have further been illuminated by Dahan *et al.* [173] who showed that nanocrystal size controls penetration into neural synapses where glycine receptor tracking was possible over extended time durations when compared to organic molecules (20 minutes in this case).

Pathak *et al.* [174] have also conjugated 5' aminated oligonucleotides to produce stable water soluble CdSe/ZnS nanocrystals. They found that these nanocrystals could be used for specific binding to cells containing Y chromosomes in an *in situ* hybridisation assay.

Autofluorescence from tissues due to the presence of low amounts of fluorophores (eg. nicotinamide, flavins or collagen) or overlap of the nanocrystal emission with that of the fluorophore can often impair the resolution of the fluorescence imaging. [175] As we have discovered ourselves, this overlap of emission wavelengths can result in a masking of the nanocrystal fluorescence. This problem can be somewhat circumvented by using near infra-red (IR) excitation [window from 650 - 900 nm], which has been shown to penetrate deep into tissues, 10 cm of breast tissue and 4 cm of skull tissue [176]. As demonstrated by Weissleder and co-workers, [176] near IR light is appealing due to the low overlap with biological systems such as haemoglobin and water, which have their lowest absorption coefficients in this region (Figure 1.15).

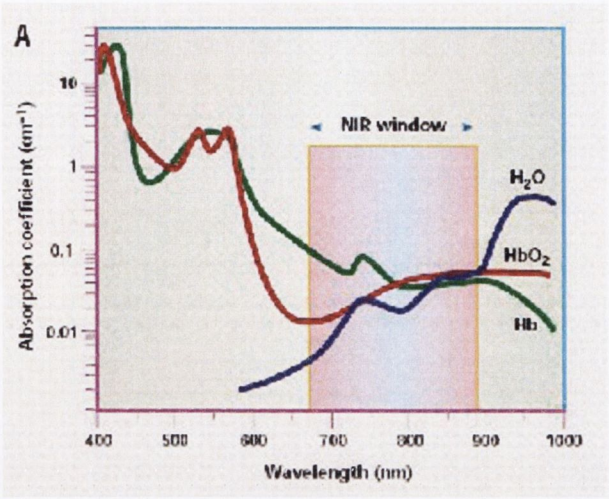


Figure 1.15. Near IR window available for *in vivo* imaging illustrating the minimal light absorbed by haemoglobin and water in this region. Adapted from literature. [176]

Typically, imaging in this area is conducted using cyanine dyes [1, 176] and has been investigated by Becker *et al.* [177] who imaged tumours displaying somatostatin receptors by using a cyanine fluorophore coupled to an analogue of somatostatin. Since nanocrystals can have their emission tuned to a desired wavelength it has been possible to prepare near IR emitting nanocrystals with imaging in mind. Such nanocrystals have been synthesised and characterised but not biotested (although they can be transferred into an aqueous medium) by Harrison *et al.* [CdHgTe], [22] Bailey *et al.* [CdSeTe], [156] and Bakueva *et al.* [PbS]. [157]

However, only a few reports into *in vivo* models have been demonstrated. Kim and co-workers have made use of CdSe, CdTe [155] and alloyed nanocrystals such as $InAs_xP_{1-x}$ core / InP intermediate and CdSe shells [21] that emit in the near-IR (840 - 860 nm) for mapping sentinel lymph-nodes in cancer surgery. Only 400 pmol of nanocrystals were required and enabled the researchers to visualise 1 cm deep into the tissue. Levene *et al.* [143] have utilised near-IR emitting nanocrystals for *in vivo* multiphoton microscopy of deep brain tissue in mice to depths of hundreds of micrometers, while capillaries have also been visualized by Larson *et al.* [178] and Akerman *et al.* [140] who conjugated peptides and targeted tumours in mice.

1.6 Nano-toxicity

Due to the ever increasing production and our subsequent exposure to various types of nanomaterials, the debate on nano-toxicity has been gathering significant momentum. [179, 180] Recently, scientists in Australia have found that office printers pose a potential risk for workers. They have shown that printers emit large amounts of particulate matter, which may have a serious impact on the respiratory system. [181] These materials are so small that they are readily distributed throughout the environment, are easily absorbed by biological entities and may disrupt or hinder particular vital biological functions. Thus, the production, composition and stability of nano-sized materials are of paramount importance for their use in bioimaging. [182]

A key issue in evaluating the possible uses of these materials is to assess their potential toxicity as a result of their inherent chemical composition (e.g. heavy metals) or as a consequence of their nanoscale properties (e.g., inhalation of particulate carbon nanotubes). [183] Research has shown that cell death can be directly linked to heavy metals binding to metallothioneins proteins, which can be sequestered to various tissues an induce apoptosis. [179, 184] In particular, due to the inherently toxic elements present in the core of semiconductor nanocrystals (cadmium, selenium, mercury etc.) toxicity is a subject of major concern currently, as they have been touted as possible replacements for traditional fluorophores in biolabelling. Several groups have investigated toxic effects due to cadmium poisoning [185, 186] and have found that low and high cadmium concentrations induced apoptosis and necrosis respectively.

Over the past number of years quite a few publications have highlighted toxicity related issues upon incorporation of these nanocrystals into biological systems. [179, 187, 188] Initially, *in vitro* studies did not demonstrate any observable toxicity; however, the experiments were of a short time scale and test analysis of heavy metal leakage was not conducted. [137, 170] Subsequently, this has proved not to be the case. Almost simultaneously, Hoshino [144] and Derfus [145] published articles probing the physiochemical properties and cytotoxicity of nanocrystals; however, they come to different conclusions as to the origin of the toxic phenomena.

Derfus *et al.* [145] reported that external influences and environmental parameters dramatically contributed to the cell cytotoxicity. Cytotoxicity was evaluated by

measuring mitochondrial activity and morphologically using bright field microscopy. They found that CdSe nanocrystals were not toxic until externally agitated (induced oxidation by bubbling air and illumination) at which point oxidation leads to a perturbed surface and the release of free Cd^{2+} ions or CdSe complexes. [10] Thus, this prolonged exposure to an oxidative environment leads to desorption of species, which induced toxicity *via* heavy metal poisoning. They found that coating with ZnS and BSA reduced the cytotoxicity by rendering the surface less susceptible to oxidation by acting as a diffusion barrier between the surface and the O_2 molecules in the medium. Consequently, the coated nanocrystals were useful for long term live cell labelling of hepatic tissue without deleterious effects on viability, migration or differentiation.

In contrast, work undertaken by Hoshino *et al.* [144] came to a different conclusion. Previously, they had imaged a cell line of mouse lymphocytes exposed to CdSe/ZnS nanocrystals and concluded that they did not affect either cell activation or cell function. [189] They claim that it is the interaction of the surface of the nanocrystals with the cells, not the cadmium content that determines toxicity. For their new experiments, they investigated novel surface-modified nanocrystals in lymphoma cells. They varied the surface using carboxylic acids, polyalcohols, and amines and evaluated their physicochemical character testing their behaviour in various biological buffers. Cytotoxicity studies were carried out using three different assays: comet assay (detects DNA damage by electrophoresis by assessing the DNA fragments), flow cytometry, and an MTT (colorimetric assay) assay. Crucially, they report that once again the cytotoxicity was caused by the surface covering molecules and not the core itself.

The cytotoxicity of MPA coated CdSe and CdSe/ZnS nanocrystals were further investigated by Kirchner and co-workers. [190] They determined that the concentration of cadmium atoms on the surface and also the nanocrystal precipitation on the cells can directly contribute to toxicity. In agreement with previous studies, [145] they found that for uncapped CdSe, approximately 75% of the cadmium atoms on the surface are released while a ZnS shell reduces this to around 8% and attributed this to the lack of stability of the MPA shell. No toxic effects were witnessed for selenium or zinc ions and they also discovered that a shell of silica drastically reduces the toxic phenomenon. They

concluded that the nature of the surface chemistry contributes significantly to the leaking of toxic molecules and ultimately cell death.

Another possible cause of cell death is the generation of reactive oxygen species [ROS] by the nanocrystals. [187] As aggregation of the nanocrystals occurs in solution upon removal of the surface ligands, [104] these processes may also be occurring in biological environments. In an effort to understand some of the processes occurring in a cellular environment once nanocrystals are introduced, Lovrić *et al.* [187] investigated the possible transfer of energy to oxygen molecules with the generation of ROS. They conclude that cell death was indeed induced by non-classical apoptosis initiated by these species (Figure 1.16).

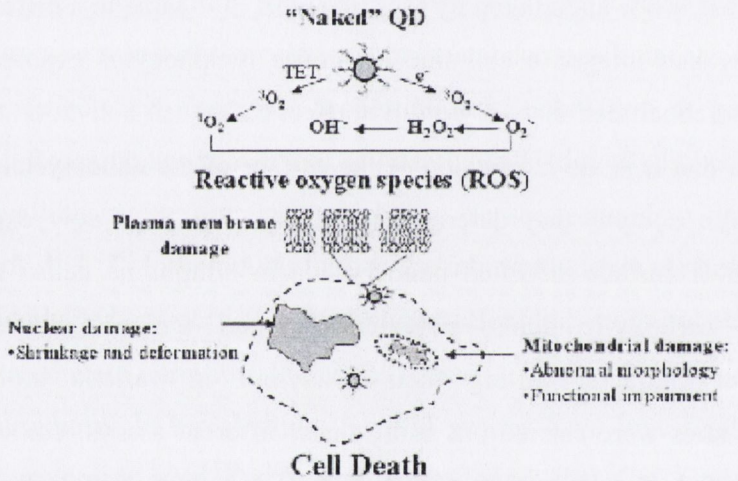


Figure 1.16. Mechanism of cell death due to nanocrystal induced toxicity as proposed by Lovrić and co-workers. Adapted from literature. [187]

They hypothesise that this sequence of events could be reduced by binding proteins or biocompatible polymers to the nanocrystals. The same group have also investigated the effect of nanocrystal size and tested for pharmacological means of reducing cell toxicity. [191] They found a striking difference in uptake, with red emitting nanocrystals only present in the cytoplasm while green emitting nanocrystals were localised in the nucleus. They found that cytotoxicity was in part dependent on nanocrystal size and is characterised by chromatin condensation and membrane blebbing (irregular bulging in the cell membrane). In addition, cytotoxicity was significantly

reduced by treatment of cells with the antioxidant N-acetyl-*L*-cysteine (NAC) and covalently linked BSA conjugates were significantly less toxic than free nanocrystals, supporting previous observations with CdSe QDs. [145]

A slightly different approach was taken by Chang *et al.* [192] in an effort to further characterise the various factors governing nanocrystal cytotoxicity. They examined surface-coated CdSe/CdS nanocrystals and evaluated toxicity based on both extracellular and intracellular exposure levels in cells. They concluded that the surface does indeed play a significant role but also that the biocompatibility arises due to a decreased uptake by endocytosis. Thus, the cytotoxicity correlates directly to the levels of nanocrystals taken up by the cells and their breakdown by cellular mechanisms.

Surface degradation by metallothioneins (small cysteine-rich proteins that accumulate and transport intracellular soft metal ions such as Zn^{2+}, Cd^{2+}, Cu^{+}) has also been explored, [184] while assemblies of CdTe nanocrystals (formed by layer by layer techniques) have been used to show that the release of Cd^{2+} ions is directly proportional to cell viability and may be significantly reduced by proper collagen coating. [193]

While most work has focussed on *in vitro* analysis and uptake of nanocrystals, several *in vivo* studies have provided the first insights into their live tissue distributions. Akerman *et al.* [140] were among the first to conduct investigations in this area and found that CdSe/ZnS nanocrystals with lung targeting peptides accumulated within the lungs of mice. They also found that non-specific binding could be reduced by adding polyethylene glycol. Ballou *et al.* [194] tested four different surface coatings on CdSe/ZnS nanocrystals for *in vivo* imaging. They found that surface coatings determined the *in vivo* localisation and nanocrystals were found to be stable for up to 4 months.

The use of biocompatible polymers to reduce the toxicity of the II-VI semiconductor nanocrystals might also be of great importance. Long chain biopolymer molecules can wrap the nanocrystals, interacting with the capping groups or defects and metal atoms on the surface. This may reduce the impact of the toxic Cd- and Te-containing core. Some recent publications have highlighted the use of gelatin nanoparticles [147, 195] as new biopolymer-based nanocomposites in an effort to generate a biocompatible nano-probing system.

Dubertret *et al.* [138] have encapsulated individual nanocrystals in phospholipid block–copolymer micelles and microinjected them into Xenopus embryos. When conjugated to DNA, the nanocrystal-micelles acted as *in vitro* fluorescent probes and are hybridised to specific complementary sequences. They were found to be stable and non-toxic up until the tadpole stage.

Gao *et al.* [141] developed multifunctional (co-block polymer encapsulated and bio-functionalised) nanocrystals for cancer targeting and imaging in live animals (Figure 1.17). They showed the nanocrystals accumulated in the prostate cancer region by enhanced permeability, tumour retention and antibody binding to cancer specific surfaces.

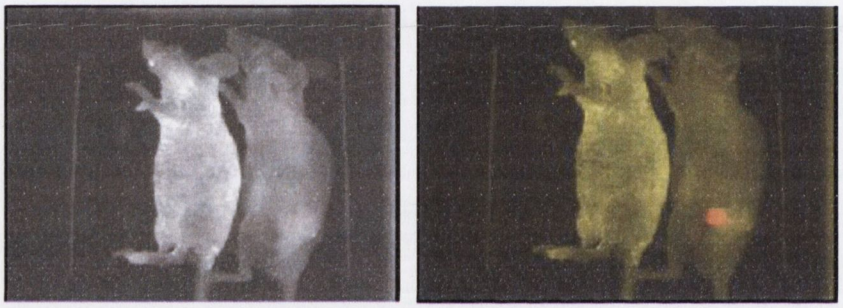


Figure 1.17. Autofluorescence image (left) and fluorescence image (right) of nanocrystal conjugates illustrating that nanocrystals accumulated in a prostate tumour growing in a live mouse. Adapted from literature. [141]

1.7 Aims and objectives of this work

From analysis of the literature above, it is clear that semiconductor nanocrystals have an enormous potential for biological and medical applications. However, there are a number of questions to be answered and problems to be addressed. In this project we are going to develop and study new CdTe based nanocomposite materials and demonstrate some of their prospective biological uses. The main aim of this work is to produce CdTe QDs and modify them towards the development of new nanocomposite materials with possible applications in the *in vitro* imaging of live cells. The major technical objectives of our work are as follows:

- Synthesise CdTe nanocrystals using a range of commercially available stabilisers and investigate their photophysical properties using UV-vis absorption, photoluminescence and Raman spectroscopy and fluorescence lifetime studies.
- Development of approaches to improve QD luminescence efficiencies, stability and biocompatibility. We expect that photocatalytic etching should greatly enhance the QY of the CdTe nanocrystals through the elimination of defect states, most notably unsaturated surface tellurium atoms. This is achieved through the substitution of traps states with atoms from stabiliser molecules or *via* the photo-creation a stable shell of CdS which acts as a wide band-gap material for defect capping.
- Studies of QD biocompatibility and behaviour in live THP-1 cells. This will be undertaken to elucidate the labelling properties of the nanocrystals with respect to conventional dyes. In particular, our research will focus on an investigation into the influence of the nanocrystal size and charge on their uptake and intracellular distribution.
- Investigation into nanocrystal biocompatibility, cytotoxicity and related phenomena upon culturing the nanocrystals with the cells.
- Conjugation of nonsteroidal anti-inflammatory drugs (NSAIDs) to the surface of the nanocrystals and investigation of their behaviour with cells of the immune system. Biological activation and terminal group manipulation are major goals in nanocrystal chemistry and as a result, their surface modification is of paramount importance. In this project we plan to prepare new stabilisers containing a thiol functionality and linkers to the different drug molecules such as aspirin, ibuprofen, naproxen. The stabilisers will be used to prepare novel water soluble CdTe nanocrystal – drug conjugates for biological testing.

We expect this research will contribute to further development within the area of CdTe nanocrystals and their biological applications.

References

[1] J. M. Klostranec, W. C. W. Chan, *Adv. Mater.* **2006**, *18*, 1953.

[2] M. Nirmal, L. Brus, *Acc. Chem. Res.* **1999**, *32*, 407.

[3] A. Eychmüller, *J. Phys. Chem. B* **2000**, *104*, 6514.

[4] A. P. Alivisatos, *J. Phys. Chem.* **1996**, *100*, 13226.

[5] A. J. Nozik, F. Williams, M. T. Nenadovic, T. Rajh, O. I. Micic, *J. Phys. Chem.* **1985**, *89*, 397.

[6] R. Rossetti, R. Hull, J. M. Gibson, L. E. Brus, *J. Chem. Phys.* **1985**, *82*, 552.

[7] R. Rossetti, J. L. Ellison, J. M. Gibson, L. E. Brus, *J. Chem. Phys.* **1984**, *80*, 4464.

[8] L. E. Brus, *J. Chem. Phys.* **1984**, *80*, 4403.

[9] R. Rossetti, Brus, L., *J. Phys. Chem.* **1982**, *86*, 4470.

[10] L. Spanhel, M. Haase, H. Weller, A. Henglein, *J. Am. Chem. Soc.* **1987**, *109*, 5649.

[11] A. Henglein, *J. Phys. Chem.* **1982**, *86*, 2291.

[12] S. Schmitt-Rink, D. A. B. Miller, D. S. Chemla, *Phys. Rev. B* **1987**, *35*, 8113.

[13] S. V. Nair, S. Sinha, K. C. Rustagi, *Phys. Rev. B* **1987**, *35*, 4098.

[14] B. L. Cushing, V. L. Kolesnichenko, C. J. O'Connor, *Chem. Rev.* **2004**, *104*, 3893.

[15] M. C. Daniel, D. Astruc, *Chem. Rev.* **2004**, *104*, 293.

[16] S. A. Corr, Y. K. Gun'ko, A. P. Douvalis, M. Venkatesan, R. D. Gunning, *J. Mat. Chem.* **2004**, *14*, 944.

[17] S. J. Byrne, S. A. Corr, Y. K. Gun'ko, J. M. Kelly, D. F. Brougham, S. Ghosh, *Chem. Comm.* **2004**, 2560.

[18] N. Skold, J. B. Wagner, G. Karlsson, T. Hernan, W. Seifert, M. E. Pistol, L. Samuelson, *Nano Lett.* **2006**, *6*, 2743.

[19] E. Marx, D. S. Ginger, K. Walzer, K. Stokbro, N. C. Greenham, *Nano Lett.* **2002**, *2*, 911.

[20] H. Fu, A. Zunger, *Phys. Rev. B* **1997**, *56*, 1496.

[21] S. W. Kim, J. P. Zimmer, S. Ohnishi, J. B. Tracy, J. V. Frangioni, M. G. Bawendi, *J. Am. Chem. Soc.* **2005**, *127*, 10526.

[22] M. T. Harrison, S. V. Kershaw, M. G. Burt, A. Eychmüller, H. Weller, A. L. Rogach, *Mater. Sci. and Eng. B* **2000**, *69-70*, 355.

[23] A. Rogach, S. V. Kershaw, M. Burt, M. Harrison, A. Kornowski, A. Eychmüller, H. Weller, *Adv. Mater.* **1999**, *11*, 552.

[24] A. P. Alivisatos, *Science* **1996**, *271*, 933.

[25] D. Ramadurai, D. Geerpuram, D. Alexson, M. Dutta, N. A. Kotov, Z. Tang, M. A. Stroscio, *Superlattices Microstruct.* **2006**, *40*, 38.

[26] L. Brus, *J. Phys. Chem. Solids* **1998**, *59*, 459.

[27] V. L. Colvin, A. P. Alivisatos, J. G. Tobin, *Phys. Rev. Lett.* **1991**, *66*, 2786.

[28] A. N. Goldstein, C. M. Echer, A. P. Alivisatos, *Science* **1992**, *256*, 1425.

[29] T. Trindade, P. O'Brien, N. L. Pickett, *Chem. Mater.* **2001**, *13*, 3843.

[30] S. A. Majetich, A. C. Carter, *J. Phys. Chem.* **1993**, *97*, 8727.

[31] M. Nirmal, C. B. Murray, M. G. Bawendi, *Phys. Rev. B* **1994**, *50*, 2293.

[32] Y. Wang, N. Herron, *J. Am. Chem. Soc.* **1991**, *95*, 525.

[33] J. E. Bowen Katari, V. L. Colvin, A. P. Alivisatos, *J. Phys. Chem.* **1994**, *98*, 4109.

[34] L. Qu, X. Peng, *J. Am. Chem. Soc.* **2002**, *124*, 2049.

[35] Z. A. Peng, X. Peng, *J. Am. Chem. Soc.* **2001**, *123*, 1389.

[36] L. Qu, Z. A. Peng, X. Peng, *Nano Lett.* **2001**, *1*, 333.

[37] D. V. Talapin, A. L. Rogach, A. Kornowski, M. Haase, H. Weller, *Nano Lett.* **2001**, *1*, 207.

[38] Z. Yu, J. Li, D. B. O'Connor, L. W. Wang, P. F. Barbara, *J. Phys. Chem. B* **2003**, *107*, 5670.

[39] S. Santra, H. S. Yang, P. H. Holloway, J. T. Stanley, R. A. Mericle, *J. Am. Chem. Soc.* **2005**, *127*, 1656.

[40] Z. H. Zhang, W. S. Chin, J. J. Vittal, *J. Phys. Chem. B* **2004**, *108*, 18569.

[41] N. Gaponik, D. V. Talapin, A. L. Rogach, K. Hoppe, E. V. Shevchenko, A. Kornowski, A. Eychmüller, H. Weller, *J. Phys. Chem. B* **2002**, *106*, 7177.

[42] S. F. Wuister, F. van Driel, A. Meijerink, *J. Lumin.* **2003**, *102-103*, 327.

[43] A. M. Kapitonov, A. P. Stupak, S. V. Gaponenko, E. P. Petrov, A. L. Rogach, A. Eychmüller, *J. Phys. Chem. B* **1999**, *103*, 10109.

[44] M. Gao, S. Kirstein, H. Möhwald, A. Rogach, A. Kornowski, A. Eychmüller, H. Weller, *J. Phys. Chem. B* **1998**, *102*, 8360.

[45] L. Brus, *J. Phys. Chem.* **1986**, *90*, 2555.

[46] A. L. Efros, A. L. Efros, *Sov. Phys. Semicond.* **1982**, *16*, 772.

[47] S. V. Gaponenko, *Cambridge University Press, Cambridge* **1998**.

[48] R. J. Ellingson, M. C. Beard, J. C. Johnson, P. Yu, O. I. Micic, A. J. Nozik, A. Shabaev, A. L. Efros, *Nano Lett.* **2005**, *5*, 865.

[49] J. P. Ge, S. Xu, J. Zhuang, X. Wang, Q. Peng, Y. D. Li, *Inorg. Chem.* **2006**, *45*, 4922.

[50] R. H. A. R. Kortan, R. L. Opila, M. G. Bawendi, M. L. Steigerwald, P. J. Carroll, and Louis E. Brus, *J. Am. Chem. Soc.* **1990**, *112*, 1327.

[51] M. D. Frogley, J. F. Dynes, M. Beck, J. Faist, C. C. Phillips, *Nat. Mater.* **2006**, *5*, 175.

[52] Z. Tang, N. A. Kotov, M. Giersig, *Science* **2002**, *297*, 237.

[53] Y. Volkov, S. Mitchell, N. Gaponik, Y. P. Rakovich, J. F. Donegan, D. Kelleher, A. L. Rogach, *ChemPhysChem* **2004**, *5*, 1600.

[54] N. Chestnoy, T. D. Harris, R. Hull, L. E. Brus, *J. Phys. Chem.* **1986**, *90*, 3393.

[55] L. Brus, *IEEE J. Quant. Elec.* **1986**, *22*, 1909.

[56] M. Okamura, K. Ebina, S. Akimoto, I. Yamazaki, K. Uosaki, *J. Photochem. Photobiol. A: Chem.* **2006**, *178*, 156.

[57] T. Vossmeyer, L. Katsikas, M. Giersig, I. G. Popovic, K. Diesner, A. Chemseddine, A. Eychmüller, H. Weller, *J. Phys. Chem.* **1994**, *98*, 7665.

[58] C. B. Murray, D. J. Norris, M. G. Bawendi, *J. Am. Chem. Soc.* **1993**, *115*, 8706.

[59] I. Mekis, D. V. Talapin, A. Kornowski, M. Haase, H. Weller, *J. Phys. Chem. B* **2003**, *107*, 7454.

[60] Z. A. Peng, X. Peng, *J. Am. Chem. Soc.* **2002**, *124*, 3343.

[61] X. Peng, J. Wickham, A. P. Alivisatos, *J. Am. Chem. Soc.* **1998**, *120*, 5343.

[62] F. Pinaud, D. King, H. P. Moore, S. Weiss, *J. Am. Chem. Soc.* **2004**, *126*, 6115.

[63] Y. Ebenstein, T. Mokari, U. Banin, *Appl. Phys. Lett.* **2002**, *80*, 4033.

[64] D. V. Talapin, A. L. Rogach, M. Haase, H. Weller, *J. Phys. Chem. B* **2001**, *105*, 12278.

[65] H. Reiss, *J. Chem. Phys.* **1951**, *19*, 482.

[66] L. Li, H. Qian, N. Fang, J. Ren, *J. Lumin.* **2006**, *116*, 59.

[67] D. V. Talapin, A. L. Rogach, E. V. Shevchenko, A. Kornowski, M. Haase, H. Weller, *J. Am. Chem. Soc.* **2002**, *124*, 5782.

[68] A. L. Rogach, A. Kornowski, M. Gao, A. Eychmüller, H. Weller, *J. Phys. Chem. B* **1999**, *103*, 3065.

[69] A. E. Raevskaya, A. L. Stroyuk, S. Y. Kuchmiy, Y. M. Azhniuk, V. M. Dzhagan, V. O. Yukhymchuk, M. Y. Valakh, *Coll. Surf. A: Physicochem. Eng. Asp.* **2006**, *290*, 304.

[70] H.-y. Han, Z.-h. Sheng, J.-g. Liang, *Mater. Lett.* **2006**, *60*, 3782.

[71] M. Bruchez, Jr., M. Moronne, P. Gin, S. Weiss, A. P. Alivisatos, *Science* **1998**, *281*, 2013.

[72] P. Reiss, J. Bleuse, A. Pron, *Nano Lett.* **2002**, *2*, 781.

[73] W. C. Chan, S. Nie, *Science* **1998**, *281*, 2016.

[74] G. P. Mitchell, C. A. Mirkin, R. L. Letsinger, *J. Am. Chem. Soc.* **1999**, *121*, 8122.

[75] S. F. Wuister, I. Swart, F. van Driel, S. G. Hickey, C. de MelloDonega, *Nano Lett.* **2003**, *3*, 503.

[76] K. Akamatsu, T. Tsuruoka, H. Nawafune, *J. Am. Chem. Soc.* **2005**, *127*, 1634.

[77] S. F. Wuister, C. D. Donega, A. Meijerink, *J. Phys. Chem. B* **2004**, *108*, 17393.

[78] S. F. Wuister, F. van Driel, A. Meijerink, *Phys. Chem. Chem. Phys.* **2003**, *5*, 1253.

[79] T. Rajh, O. I. Micic, A. J. Nozik, *J. Phys. Chem.* **1993**, *97*, 11999.

[80] L. Li, H. Qian, J. Ren, *Chem. Comm.* **2005**, 528.

[81] C. L. Li, N. Murase, *Chem. Lett.* **2005**, *34*, 92.

[82] S. J. Byrne, S. A. Corr, T. Y. Rakovich, Y. K. Gun'ko, Y. P. Rakovich, J. F. Donegan, S. Mitchell, Y. Volkov, *J. Mat. Chem.* **2006**, *16*, 2896.

[83] H. Borchert, D. V. Talapin, N. Gaponik, C. McGinley, S. Adam, A. Lobo, T. Möller, H. Weller, *J. Phys. Chem. B* **2003**, *107*, 9662.

[84] A. Shavel, N. Gaponik, A. Eychmüller, *J. Phys. Chem. B* **2006**, *110*, 19280.

[85] M. Green, H. Harwood, C. Barrowman, P. Rahman, A. Eggeman, F. Festry, P. Dobson, T. Ng, *J. Mat. Chem.* **2007**, *17*, 1989–1994.

[86] H. Bao, E. Wang, S. Dong., *Small* **2006**, *2*, 476.

[87] A. L. Rogach, L. Katsikas, A. Kornowski, D. Su, A. Eychmüller, H. Weller, *Ber. Bunsen-Ges* **1996**, *100*, 1772.

[88] Y. Gong, M. Gao, D. Wang, H. Möhwald, *Chem. Mater.* **2005**, *17*, 2648.

[89] M. T. Fernández-Argüelles, W. J. Jin, J. M. Costa-Fernández, R. Pereiro, A. Sanz-Medel, *Anal. Chimica Acta* **2005**, *549*, 20.

[90] C.-Y. Chen, C.-T. Cheng, C.-W. Lai, Y.-H. Hu, P.-T. Chou, Y.-H. Chou, H.-T. Chiu., *Small* **2005**, *1*, 1215.

[91] Y. A. Yang, H. Wu, K. R. Williams, Y. C. Cao., *Angew. Chem. Int. Ed.* **2005**, *44*, 6712.

[92] J. J. Li, Y. A. Wang, W. Z. Guo, J. C. Keay, T. D. Mishima, M. B. Johnson, X. G. Peng, *J. Am. Chem. Soc.* **2003**, *125*, 12567.

[93] D. F. Underwood, T. Kippeny, S. J. Rosenthal, *J. Phys. Chem. B* **2001**, *105*, 436.

[94] M. O'Neil, J. Marohn, G. McLendon, *J. Phys. Chem.* **1990**, *94*, 4356.

[95] D. E. Dunstan, A. Hagfeldt, M. Almgren, H. O. G. Siegbahn, E. Mukhtar, *J. Phys. Chem.* **1990**, *94*, 6797.

[96] A. C. Carter, C. E. Bouldin, K. M. Kemner, M. I. Bell, J. C. Woicik, S. A. Majetich, *Phys. Rev. B* **1997**, *55*, 13822.

[97] M. G. Bawendi, P. J. Carroll, W. L. Wilson, L. E. Brus, *J. Chem. Phys.* **1992**, *96*, 946.

[98] H. Yang, C. Huang, X. Li, R. Shi, K. Zhang, *Mater. Chem. Phys.* **2005**, *90*, 155.

[99] N. Pradhan, D. Reifsnyder, R. Xie, J. Aldana, X. Peng, *J. Am. Chem. Soc.* **2007**, *129*, 9500.

[100] B. O. Dabbousi, J. Rodriguez-Viejo, F. V. Mikulec, J. R. Heine, H. Mattoussi, R. Ober, K. F. Jensen, M. G. Bawendi, *J. Phys. Chem. B* **1997**, *101*, 9463.

[101] M. A. Malik, P. O'Brien, N. Revaprasadu, *Chem. Mater.* **2002**, *14*, 2004.

[102] H. Zhang, Z. Zhou, B. Yang, M. Y. Gao, *J. Phys. Chem. B* **2003**, *107*, 8.

[103] H. B. Bao, Y. J. Gong, Z. Li, M. Y. Gao, *Chem. Mater.* **2004**, *16*, 3853.

[104] J. Aldana, Y. A. Wang, X. Peng, *J. Am. Chem. Soc.* **2001**, *123*, 8844.

[105] M. Jones, J. Nedeljkovic, R. J. Ellingson, A. J. Nozik, G. Rumbles, *J. Phys. Chem. B* **2003**, *107*, 11346.

[106] Y. Wang, Z. Tang, M. A. Correa-Duarte, L. M. Liz-Marzan, N. A. Kotov, *J. Am. Chem. Soc.* **2003**, *125*, 2830.

[107] Y. Wang, Z. Tang, M. A. Correa-Duarte, I. Pastoriza-Santos, M. Giersig, N. A. Kotov, L. M. Liz-Marzan, *J. Phys. Chem. B* **2004**, *108*, 15461.

[108] X. Wang, L. Qu, J. Zhang, X. Peng, M. Xiao, *Nano Lett.* **2003**, *3*, 1103.

[109] A. A. Bol, A. Meijerink, *J. Phys. Chem. B* **2001**, *105*, 10203.

[110] H. Zhang, B. Yang, *Thin Solid Films* **2002**, *418*, 169.

[111] H. Zhang, D. Wang, H. Möhwald, *Angew. Chem. Int. Ed.* **2006**, *45*, 748.

[112] Q. Pang, L. J. Zhao, Y. Cai, D. P. Nguyen, N. Regnault, N. Wang, S. H. Yang, W. K. Ge, R. Ferreira, G. Bastard, J. N. Wang, *Chem. Mater.* **2005**, *17*, 5263.

[113] T. Mokari, E. Rothenberg, I. Popov, R. Costi, U. Banin, *Science* **2004**, *304*, 1787.

[114] C. H. Fischer, A. Henglein, *J. Phys. Chem.* **1989**, *93*, 5578.

[115] J. Aldana, N. Lavelle, Y. Wang, X. Peng, *J. Am. Chem. Soc.* **2005**, *127*, 2496.

[116] I. G. Dance, M. L. Scudder, R. Secomb, *Inorg. Chem.* **1983**, *22*, 1794.

[117] M. C. Schlamp, X. G. Peng, A. P. Alivisatos, *J. Appl. Phys.* **1997**, *82*, 5837.

[118] V. L. Colvin, M. C. Schlamp, A. P. Alivisatos, *Nature* **1994**, *370*, 354.

[119] J. Lee, V. C. Sundar, J. R. Heine, M. G. Bawendi., K. F. Jensen, *Adv. Mater.* **2000**, *12*, 1102.

[120] N. Tessler, V. Medvedev, M. Kazes, S. Kan, U. Banin, *Science* **2002**, *295*, 1506.

[121] V. I. Klimov, A. A. Mikhailovsky, S. Xu, A. Malko, J. A. Hollingsworth, C. A. Leatherdale, H. J. Eisler, M. G. Bawendi, *Science* **2000**, *290*, 314.

[122] E. V. Lutsenko, A. L. Gurskii, V. N. Pavlovskii, V. Z. Zubialevich, G. P. Yablonskii, I. V. Sedova, S. V. Sorokin, A. A. Toropov, S. V. Ivanov, P. S. Kop'ev, *Phys. Stat. Sol. (c)* **2006**, *3*, 1233.

[123] A. R. Clapp, I. L. Medintz, B. R. Fisher, G. P. Anderson, H. Mattoussi, *J. Am. Chem. Soc.* **2005**, *127*, 1242.

[124] I. L. Medintz, A. R. Clapp, H. Mattoussi, E. R. Goldman, B. Fisher, J. M. Mauro, *Nat. Mater.* **2003**, *2*, 630.

[125] A. R. Clapp, I. L. Medintz, J. M. Mauro, B. R. Fisher, M. G. Bawendi, H. Mattoussi, *J. Am. Chem. Soc.* **2004**, *126*, 301.

[126] S. J. Clarke, C. A. Hollmann, Z. Zhang, D. Suffern, S. E. Bradforth, N. M. Dimitrijevic, W. G. Minarik, J. L. Nadeau, *Nat. Mater.* **2006**, *5*, 409.

[127] C. Y. Zhang, H. C. Yeh, M. T. Kuroki, T. H. Wang, *Nat. Mater.* **2005**, *4*, 826.

[128] R. Bakalova, H. Ohba, Z. Zhelev, T. Nagase, R. Jose, M. Ishikawa, Y. Baba, *Nano Lett.* **2004**, *4*, 1567.

[129] H. Y. Xie, J. G. Liang, Z. L. Zhang, Y. Liu, Z. K. He, D. W. Pang, *Spectrochim. Acta (A): Mol. Biomol. Spec.* **2004**, *60*, 2527.

[130] J. G. Liang, X. P. Ai, Z. K. He, D. W. Pang, *Analyst* **2004**, *129*, 619.

[131] J. L. Chen, C. Q. Zhu, *Anal. Chimica. Acta* **2005**, *546*, 147.

[132] C. Kirchner, A. M. Javier, A. S. Susha, A. L. Rogach, O. Kreft, G. B. Sukhorukov, W. J. Parak, *Talanta* **2005**, *67*, 486.

[133] C. Bo, Z. Ping, *Anal. Bioanal. Chem.* **2005**, *381*, 986.

[134] J. Li, D. Bao, X. Hong, D. Li, J. Li, Y. Bai, T. Li, *Colloids Surf. A: Physicochem. Eng. Aspects* **2005**, *257-258*, 267.

[135] J. K. Jaiswal, E. R. Goldman, H. Mattoussi, S. M. Simon, *Nat. Methods* **2004**, *1*, 73.

[136] S. J. Rosenthal, I. Tomlinson, E. M. Adkins, S. Schroeter, S. Adams, L. Swafford, J. McBride, Y. Wang, L. J. DeFelice, R. D. Blakely, *J. Am. Chem. Soc.* **2002**, *124*, 4586.

[137] X. Wu, H. Liu, J. Liu, K. N. Haley, J. A. Treadway, J. P. Larson, N. Ge, F. Peale, M. P. Bruchez, *Nat. Biotech.* **2003**, *21*, 41.

[138] B. Dubertret, P. Skourides, D. J. Norris, V. Noireaux, A. H. Brivanlou, A. Libchaber, *Science* **2002**, *298*, 1759.

[139] E. R. Goldman, E. D. Balighian, H. Mattoussi, M. K. Kuno, J. M. Mauro, P. T. Tran, G. P. Anderson, *J. Am. Chem. Soc.* **2002**, *124*, 6378.

[140] M. E. Akerman, W. C. W. Chan, P. Laakkonen, S. N. Bhatia, E. Ruoslahti, *PNAS* **2002**, *99*, 12617.

[141] X. Gao, Y. Cui, R. M. Levenson, L. W. K. Chung, S. Nie, *Nat. Biotech.* **2004**, *22*, 969.

[142] X. Gao, L. Yang, J. A. Petros, F. F. Marshall, J. W. Simons, S. Nie, *Curr. Op. Biotech.* **2005**, *16*, 63.

[143] M. J. Levene, D. A. Dombeck, K. A. Kasischke, R. P. Molloy, W. W. Webb, *J. Neurophysiol.* **2004**, *91*, 1908.

[144] A. Hoshino, K. Fujioka, T. Oku, M. Suga, Y. F. Sasaki, T. Ohta, M. Yasuhara, K. Suzuki, K. Yamamoto, *Nano Lett.* **2004**, *4*, 2163.

[145] A. M. Derfus, W. C. W. Chan, S. N. Bhatia, *Nano Lett.* **2004**, *4*, 11.

[146] J. Li, C. Wu, F. Gao, R. Zhang, G. Lv, D. Fu, B. Chen, X. Wang, *Bioorg. Med. Chem. Lett.* **2006**, *16*, 4808.

[147] C. Coester, P. Nayyar, J. Samuel, *Eur. J. Pharm. Biopharm.* **2006**, *62*, 306.

[148] A. Miyawaki, *Dev. Cell* **2003**, *4*, 295.

[149] T. Sugimoto, G. E. Dirige, A. Muramatsu, *J. Colloid Interface Sci.* **1996**, *182*, 444.

[150] W. C. W. Chan, D. J. Maxwell, X. Gao, R. E. Bailey, M. Han, S. Nie, *Curr. Op. Biotech.* **2002**, *13*, 40.

[151] A. M. Derfus, W. C. W. Chan, S. N. Bhatia, *Adv. Mater.* **2004**, *16*, 961.

[152] Y. Zhao, Y. Zhang, H. Zhu, G. C. Hadjipanayis, J. Q. Xiao, *J. Am. Chem. Soc.* **2004**, *126*, 6874.

[153] L. S. Li, N. Pradhan, Y. Wang, X. Peng, *Nano Lett.* **2004**, *4*, 2261.

[154] A. Eychmüller, A. L. Rogach, *Pure and Appl. Chem.* **2000**, *72*, 179.

[155] S. Kim, Y. T. Lim, E. G. Soltesz, A. M. De Grand, J. Lee, A. Nakayama, J. A. Parker, T. Mihaljevic, R. G. Laurence, D. M. Dor, L. H. Cohn, M. G. Bawendi, J. V. Frangioni, *Nat. Biotech.* **2004**, *22*, 93.

[156] R. E. Bailey, S. Nie, *J. Am. Chem. Soc.* **2003**, *125*, 7100.

[157] L. Bakueva, Gorelikov, I., Musikhin, S., Zhao, X. S., Sargent, E. H., Kumacheva E., *Adv. Mater.* **2004**, *16*, 926.

[158] I. L. Medintz, H. T. Uyeda, E. R. Goldman, H. Mattoussi, *Nat. Mater.* **2005**, *4*, 435.

[159] H. T. Uyeda, I. L. Medintz, J. K. Jaiswal, S. M. Simon, H. Mattoussi, *J. Am. Chem. Soc.* **2005**, *127*, 3870.

[160] W. G. J. H. van Sark, P. L. T. M. Frederix, A. A. Bol, H. C. Gerritsen, A. Meijerink, *Chemphyschem* **2002**, *3*, 871.

[161] M. Nirmal, B. O. Dabbousi, M. G. Bawendi, J. J. Macklin, J. K. Trautman, T. D. Harris, L. E. Brus, *Nature* **1996**, *383*, 802.

[162] M. Kuno, D. P. Fromm, H. F. Hamann, A. Gallagher, D. J. Nesbitt, *J. Chem. Phys.* **2000**, *112*, 3117.

[163] A. P. Alivisatos, *Nat. Biotech.* **2004**, *22*, 47.

[164] S. Wang, N. Mamedova, N. A. Kotov, W. Chen, J. Studer, *Nano Lett.* **2002**, *2*, 817.

[165] D. Gerion, F. Pinaud, S. C. Williams, W. J. Parak, D. Zanchet, S. Weiss, A. P. Alivisatos, *J. Phys. Chem. B* **2001**, *105*, 8861.

[166] W. J. Parak, D. Gerion, D. Zanchet, A. S. Woerz, T. Pellegrino, C. Micheel, S. C. Williams, M. Seitz, R. E. Bruehl, Z. Bryant, C. Bustamante, C. R. Bertozzi, A. P. Alivisatos, *Chem. Mater.* **2002**, *14*, 2113.

[167] J. M. Slocik, J. T. Moore, D. W. Wright, *Nano Lett.* **2002**, *2*, 169.

[168] H. Mattoussi, J. M. Mauro, E. R. Goldman, G. P. Anderson, V. C. Sundar, F. V. Mikulec, M. G. Bawendi, *J. Am. Chem. Soc.* **2000**, *122*, 12142.

[169] H. Mattoussi, J. M. Mauro, E. R. Goldman, T. M. Green, G. P. Anderson, V. C. Sundar, M. G. Bawendi, *Phys. Stat. Sol. B* **2001**, *224*, 277.

[170] J. K. Jaiswal, H. Mattoussi, J. M. Mauro, S. M. Simon, *Nat. Biotech.* **2003**, *21*, 47.

[171] M. Xie, H. H. Liu, P. Chen, Z. L. Zhang, X. H. Wang, Z. X. Xie, Y. M. Du, B. Q. Pan, D. W. Pang, *Chem. Comm.* **2005**, 5518.

[172] J. O. Winter, T. Y. Liu, B. A. Korgel, C. E. Schmidt, *Adv. Mater.* **2001**, *13*, 1673.

[173] M. Dahan, S. Levi, C. Luccardini, P. Rostaing, B. Riveau, A. Triller, *Science* **2003**, *302*, 442.

[174] S. Pathak, S. K. Choi, N. Arnheim, M. E. Thompson, *J. Am. Chem. Soc.* **2001**, *123*, 4103.

[175] P. Sharma, S. Brown, G. Walter, S. Santra, B. Moudgil, *Adv. Colloid Interface Sci.* **2006**, *123-126*, 471.

[176] R. Weissleder, *Nat. Biotech.* **2001**, *19*, 316.

[177] A. Becker, C. Hessenius, K. Licha, B. Ebert, U. Sukowski, W. Semmler, B. Wiedenmann, C. Grötzinger, *Nat. Biotech.* **2001**, *19*, 327.

[178] D. R. Larson, W. R. Zipfel, R. M. Williams, S. W. Clark, M. P. Bruchez, F. W. Wise, W. W. Webb, *Science* **2003**, *300*, 1434.

[179] V. L. Colvin, *Nat. Biotech.* **2003**, *21*, 1166.

[180] A. Nel, T. Xia, L. Madler, N. Li, *Science* **2006**, *311*, 622.

[181] C. He, L. Morawska, L. Taplin, *Environ. Sci. Technol.* **2007**.

[182] K. Boldt, O. T. Bruns, N. Gaponik, A. Eychmüller, *J. Phys. Chem. B* **2006**, *110*, 1959.

[183] D. B. Warheit, B. R. Laurence, K. L. Reed, D. H. Roach, G. A. M. Reynolds, T. R. Webb, *Toxicol. Sci.* **2004**, *77*, 117.

[184] B. P. Aryal, K. P. Neupane, M. G. Sandros, D. E. Benson., *Small* **2006**, *2*, 1159.

[185] M. Kondoh, S. Araragi, K. Sato, M. Higashimoto, M. Takiguchi, M. Sato, *Toxicol.* **2002**, *170*, 111.

[186] E. Lopez, S. Figueroa, M. J. Oset-Gasque, M. P. Gonzalez, *Br. J. Pharmacol.* **2003**, *138*, 901.

[187] J. Lovrić, S. J. Cho, F. M. Winnik, D. Maysinger, *Chem. Biol.* **2005**, *12*, 1227.

[188] C. Seydel, *Science* **2003**, *300*, 80.

[189] A. Hoshino, K.-i. Hanaki, K. Suzuki, K. Yamamoto, *Biochem. Biophys. Res. Comm.* **2004**, *314*, 46.

[190] C. Kirchner, T. Liedl, S. Kudera, T. Pellegrino, A. MunozJavier, H. E. Gaub, S. Stolzle, N. Fertig, W. J. Parak, *Nano Lett.* **2005**, *5*, 331.

[191] J. Lovrić, H. S. Bazzi, Y. Cuie, G. R. A. Fortin, F. M. Winnik, D. Maysinger, *J. Mol. Med.* **2005**, *83*, 377.

[192] E. Chang, N. Thekkek , W. W. Yu, V. L. Colvin, R. Drezek, *Small* **2006**, *2*, 1412.

[193] V. A. Sinani, D. S. Koktysh, B. G. Yun, R. L. Matts, T. C. Pappas, M. Motamedi, S. N. Thomas, N. A. Kotov, *Nano Lett.* **2003**, *3*, 1177.

[194] B. Ballou, B. C. Lagerholm, L. A. Ernst, M. P. Bruchez, A. S. Waggoner, *Biocon. Chem.* **2004**, *15*, 79.

[195] S. Balthasar, K. Michaelis, N. Dinauer, H. von Briesen, J. Kreuter, K. Langer, *Biomater.* **2005**, *26*, 2723.

Chapter 2: Optimisation of the synthesis and modification of CdTe quantum dot (QD) luminescence for live cell imaging

2.1. Introduction

Semiconducting nanocrystals or quantum dots (QDs) can be synthesised *via* a number of different methods, encompassing both organometallic [1-3] and aqueous precursors. [4-7] Recently, much work has been undertaken with regard to CdSe QDs and the improvement of their characteristic properties by controlling the synthetic conditions, most notably precursor concentration and injection temperature. [8-10] Generally, production of CdSe QDs is conducted in organic solvents, while CdTe QDs are primarily synthesised in water. Some investigations for CdTe have been carried out, using tri-octylphosphine and dodecylamine. [11-14] For aqueous syntheses, various conditions utilising microwave irradiation [15] or hydrothermal [16, 17] routes have also been recently explored. Traditionally, sodium borohydride has been used to reduce tellurium powder to produce NaHTe and this was then added to a mixture of the stabiliser molecules and cadmium salt in water. [18-20] However, the use of Al_2Te_3 to generate H_2Te gas by reaction with H_2SO_4 has improved the ease of experimentation and reduced synthetic procedure times. [4, 21, 22]

Several investigations have been undertaken recently to explore the impact of altering the reaction conditions on the properties of CdTe QDs. Further improvements in the QYs of the QDs were demonstrated by Li *et al.*, [21] Guo *et al.* [23] and Shavel *et al.* [22] who have all investigated the lowering of the stoichiometric precursor (cadmium: stabiliser) ratios. While high quantum yield (QY) values have been achieved, there are problems with this reduction in quantitative precursor amounts, primarily due to the formation of a variety of cadmium complexes in solution. The main cadmium complexes that play the significant role in determining the QY in solution are CdL_2^{2-}, CdL_3^{4-} and CdL (L = thiol stabiliser). [22, 23] Each complex dominates depending on the ratio of cadmium to thiol used (Figure 2.1).

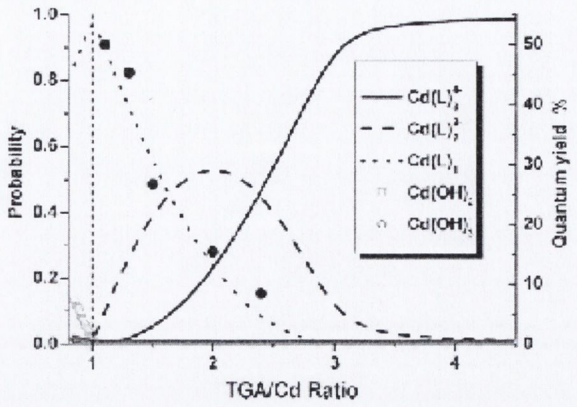


Figure 2.1. Graph illustrating the distribution of the various cadmium complexes in solution and the QY of the QDs after 20 hours of synthesis depending on the TGA/Cd ratio used. Adapted from literature. [22]

At higher ligand to metal ratios (> 2.5 :1), $Cd(L)_3^{4-}$ dominates while at ratios of (2 : 1) CdL_2^{2-} dominates. These complexes are completely soluble due to the carboxylic acid stabilising groups present and these solutions remain completely transparent throughout the entire reflux duration. However, this is not the case for lower ligand ratios, where the complex CdL now dominates. This complex, due to the presence of only one thiol stabiliser, is not as soluble as those previously highlighted and gives rise to a distinct turbidity during reflux with the formation of a white precipitate. The precipitate may also be due to the production of cadmium hydroxide [$Cd(OH)_2$]. This is formed as a white, insoluble powder when sodium or potassium hydroxide is added to a solution of a cadmium salt. [24]

$$Cd^{2+} + 2\,OH^- \longrightarrow Cd(OH)_2 \downarrow$$

The overall impact, is that this precipitate must be filtered from the reaction mixture before further purification is undertaken. This results in a decrease of the overall cadmium and thiol concentrations in solution, giving rise to lower reaction yields and QD solutions which are less concentrated than those synthesised at higher ratios.

The CdL monomer can also release excess Cd in solution during the growth process, which acts to increase the amount of $Cd(OH)_2$. Nevertheless, for the production of large quantities of CdTe QDs, this reduced ratio process is not really feasible as a large

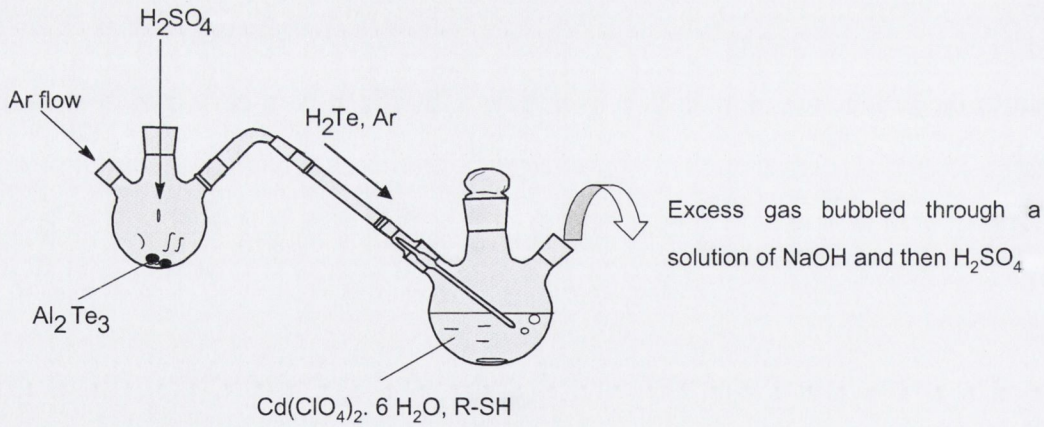
amounts of cadmium must be added to compensate for the precipitate formed, leading to a more costly procedure.

The aim of this work was to utilise thioglycolic acid (TGA), one of the most widely used thiol stabilisers for the production of highly luminescent, aqueous CdTe QDs. [4, 25, 26] We wished to systematically investigate further changes to the reaction procedure to optimise the reaction conditions under which the QDs are synthesised. We also intended to improve the resulting luminescent properties of the QD solutions produced, while also obtaining significant quantities for further analysis. The QDs were spectroscopically characterised *via* UV-vis absorption, luminescence emission, FTIR and Raman spectroscopy, TEM, HRTEM and confocal microscopy. Finally, a significant objective was to investigate the behaviour of the TGA capped QDs in live THP-1 macrophage cells.

2.2. Synthesis and characterisation of CdTe QDs

2.2.1. Synthesis of CdTe QDs

The standard water based synthesis of CdTe QDs initially developed by Gaponik *et al.* [4] was utilised as our main synthetic route (Scheme 2.1 for the experimental setup).



Scheme 2.1. Schematic illustration of the setup used to produce water soluble CdTe QDs. Al_2Te_3 is decomposed by the dropwise addition of H_2SO_4 and argon carries the evolved H_2Te gas through a solution of $Cd(ClO_4)_2 \cdot 6H_2O$ and the desired thiol. This solution is then heated under reflux.

Briefly, $Cd(ClO_4)_2 \cdot 6H_2O$ and TGA stabiliser were dissolved in degassed Millipore water and the pH was adjusted to 11 by the addition of a 2M NaOH solution. H_2Te gas, generated from the reaction of 0.5M H_2SO_4 with Al_2Te_3, was bubbled through the solution under a slow argon flow for approximately 10 minutes. The resultant, non luminescent solution was then heated under reflux and the growth of the QDs was monitored spectroscopically (Figure 2.2).

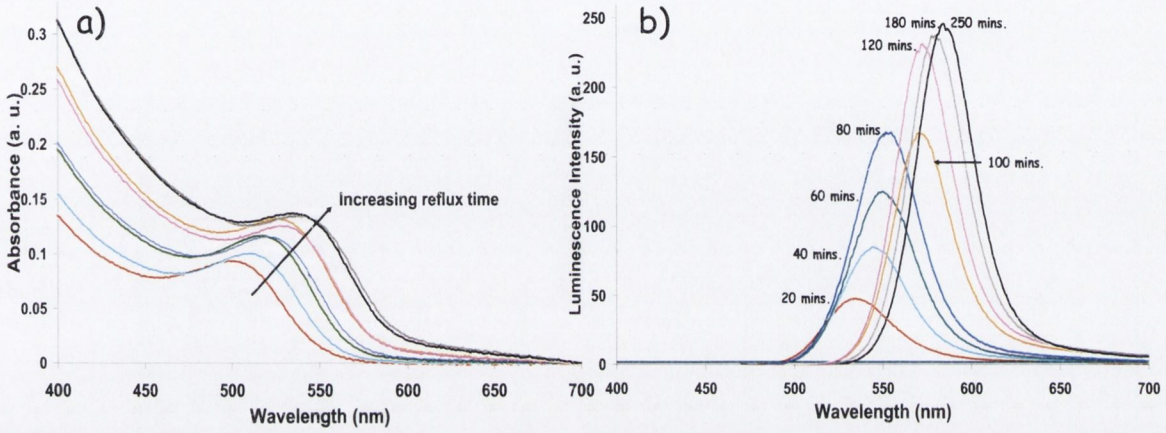


Figure 2.2. a) UV-vis absorption and **b**) normalised luminescence emission spectra (λ_{ex} 400 nm) taken sequentially (20, 40, 60, 80, 100, 120, 180 and 250 minutes) during the reflux of TGA capped CdTe QDs.

Figure 2.2 shows the typical absorption and emission profiles indicative of CdTe QDs. Most notably, a red shift in both absorption and emission spectra is seen with increasing reflux time due to QD growth and the emission intensity increases with heating time and QD size. Each luminescence spectrum illustrates the spectral properties of an ensemble of QDs of varying sizes. Following heating under reflux, the crude solution was then concentrated by rotary evaporation to approximately one fifth of its original volume. The QDs were then size selectively precipitated *via* the addition of isopropanol, which acts as a non-solvent, followed by centrifugation (3000 rpm / 10 minutes). Each individual fraction was re-dissolved in Millipore water, purified on a sephadex (G25) column, to remove any unreacted molecules or starting material and stored at 4° C for further characterisation and use. It must be noted that the addition of an alcohol to induce precipitation results in partial removal of the capping ligand.

Occasionally, QD fractions became discoloured and aggregated or decomposed due to this ligand removal.

CdTe QDs were also prepared starting from sodium telluride (Na_2Te), which was produced by the reaction of tellurium metal powder with a solution of sodium borohydride in aqueous NaOH. Both synthetic approaches resulted in the formation of purified fractions of QDs (Figure 2.3), dispersed in water, varying in size and easily distinguishable by colour. However, as the Al_2Te_3 route is far quicker and easier, it was subsequently used for all experiments.

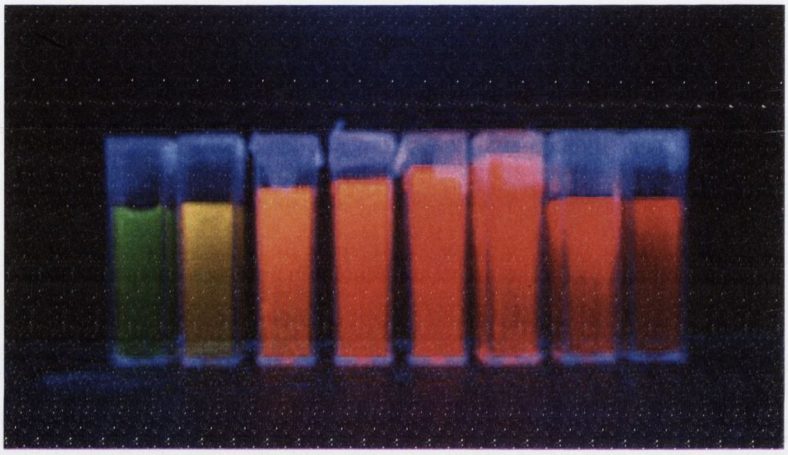


Figure 2.3. Solutions of individual fractions of TGA capped QDs exposed under a UV light illustrating quantum confinement and the change in emission wavelength (from 510 nm to 600 nm) with increasing size (left to right).

2.2.2. Characterisation of QDs by UV-vis absorption and luminescence emission spectroscopy

UV-vis absorption and luminescence spectroscopy are two of the main characterisation techniques for analysis of aqueous solutions of CdTe QDs. The band edges are tuneable by size selective precipitation and a wide variety of fractions can be separated from a single crude parent solution. The different sizes can be inferred from HRTEM and are easily distinguishable by their spectral characteristics and colour. Typically, for CdTe QDs, sizes can range from the smallest ~ 2 nm (green / λ_{em} ~ 510 nm) to those which are ~ 6 nm in size (red / λ_{em} > 650 nm).

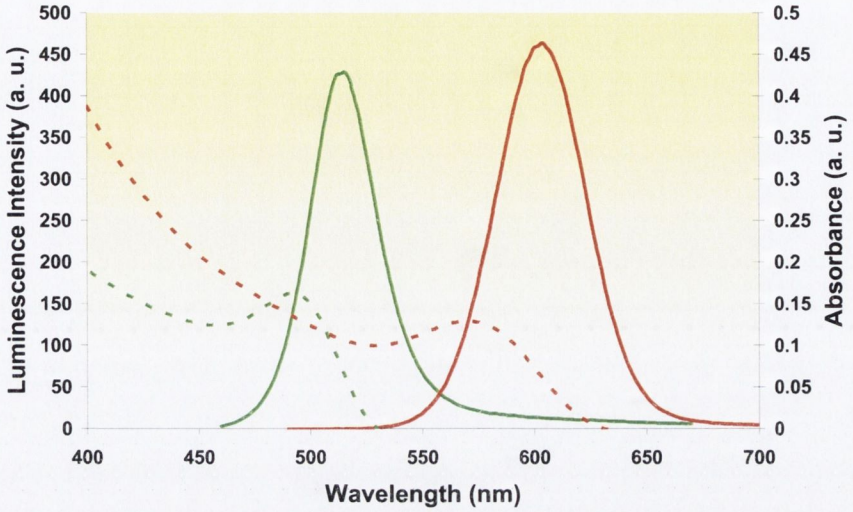


Figure 2.4. Characteristic absorption (dotted line) and luminescence emission spectra (solid line, λ_{ex} 450 nm) of green (~ 2 nm) and red (~ 4 nm) TGA capped CdTe QDs.

The UV-vis absorption and emission profiles for green and red CdTe QDs are shown in Figure 2.4. The dotted lines show the absorption spectra of the (1s-1s) electronic transition from the lowest excited state which is often referred to as the first excitonic peak. [18, 27] The peak for the small QDs is sharp and well defined indicating a relatively narrow size distribution and good crystallinity within the sample. For CdSe QDs, more transitions and narrower peaks widths have been reported at lower temperatures (10 K). [28] If the size distribution of the sample had been greater, the absorption peak would be broader and more shoulder-like due to a series of unresolved electronic transitions of different energy. This phenomenon is common for the larger QDs (red dotted line) due to their growth *via* Ostwald Ripening, which results in the sacrifice of the smaller QDs, their dissolution and addition to the larger QDs. [4, 9, 29]

This broader size distribution effect can be further seen in the emission spectra (solid lines). Here, the FWHM of the emission peaks for the green and red QDs, 37 and 45 nm respectively, show that the spectra broaden with increasing size. For a highly defective ensemble, a dramatic broadening of the emission can indicate the presence of two components, a dominant band-edge emission and a wider band which resides at lower energy (higher wavelength). This adds cumulatively to the dominant emission peak. This peak, due to defect recombination, is masked and only appears to alter the

symmetrical nature of the emission peak at room temperature. It may however, be elucidated at low temperatures. [18]

Thus, the FWHM value and symmetrical nature of the peak are indicative of a high quality, homogeneous sample with a narrow size distribution.

2.2.3. Electron microscopy

Transmission electron microscopy (TEM) analysis (Figure 2.5, **a**) of the aqueous TGA capped QDs shows the formation of string like structures which are due to dipole-dipole interaction and solvent evaporation effects. In contrast, QDs prepared in organic solvents typically show a more distinct crystalline structure (Chapter 1, Figure 1.4). [1, 6] Using only high resolution TEM, is it possible to resolve the highly crystalline nature of the QDs (Figure 2.5, **b**).

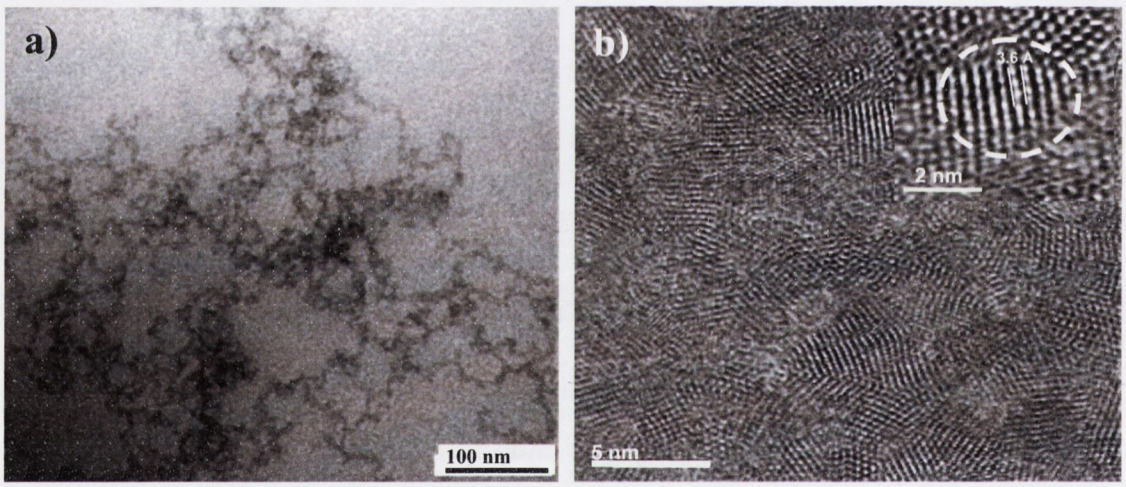


Figure 2.5. a) TEM image and **b**) a HRTEM image of TGA capped CdTe QDs. Insert **b** - a magnified image of an isolated 4 nm QD.

The HRTEM image (**b**) shows that the CdTe QDs were highly crystalline and the magnified images shows a 4 nm QD with an inter plane distance of approximately 3.6 Å, which is consistent with the 3.7 Å separation of the (111) plane in cubic zinc blend CdTe. [30]

2.2.4. Infrared spectroscopy

Figure 2.6 shows the IR spectrum [KBr, 4000 – 400 cm^{-1}] of TGA (blue line) and TGA capped QDs (red line) following purification.

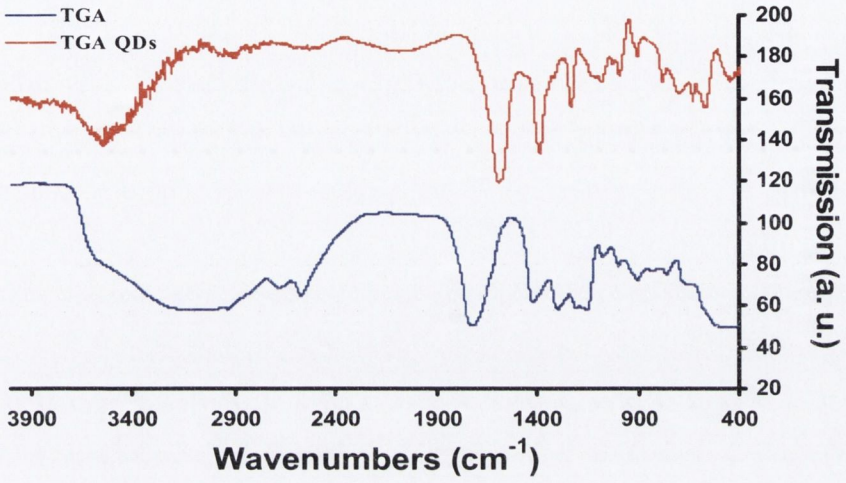


Figure 2.6. IR spectrum (KBr) of TGA (blue) and TGA capped QDs (red).

The IR spectra for TGA alone (blue line) and TGA QDs (red line) (Figure 2.6) clearly illustrate the changes in the stretching frequencies of the TGA once bound to the QD surface. The main IR bands for TGA occur as a broad peak at ~ 3000 cm^{-1} (O-H, str., symmetrical and unsymmetrical modes), 2555 cm^{-1} (S-H str.), 1705 cm^{-1} (COO^- str.), 1414 (O-H bend) and 1286 / 1193 cm^{-1} (C-O str.). The C-H str. bands that usually occur at around 2950 cm^{-1} are masked by the large water absorption. It is worth noting that this COO^- peak is red shifted to lower wavenumbers when bound to the QD surface, but most notable is the absence of any peak at 2555 cm^{-1} indicating the binding of the free thiol of the TGA to the cadmium rich surface of the QDs. [31]

2.3 Statistical analysis and optimisation of the synthesis of CdTe QDs

One of the major goals of this work was the utilisation of QDs for fluorescent biological imaging in live THP-1 cells. As such, the QY is a very important property as autofluorescence from the surrounding medium can often interfere with the cellular visualisation. Consequently, highly luminescent QDs can provide for higher imaging

capabilities for compartmental analysis of the cell components. [32-34] In order to fine tune the resultant QYs, a statistical analysis was carried out on the reaction conditions and reagents used for the preparation of the TGA capped QDs. This was undertaken in order to determine, develop and optimise the synthetic routine for the production of high quality, aqueous QDs with high QYs and narrow size distributions.

We wished to investigate subtle changes in the precursor ratios at higher values, in an effort to generate highly luminescent QDs with high reaction yields. This gave us larger quantities of QDs, which allowed us to investigate the photoetching processes and any effects on the spectroscopic and Raman properties. The improvement of QYs could lead to QDs being incorporated into various optoelectronic devices [35] or as more efficient fluorescent labelling materials for intercellular visualisation. [36]

The study was implemented using a 2^2 factorial design (Figure 2.7), where the main factors involved were the metal-to-metal and the stabiliser-to-metal ratios present in the reaction.

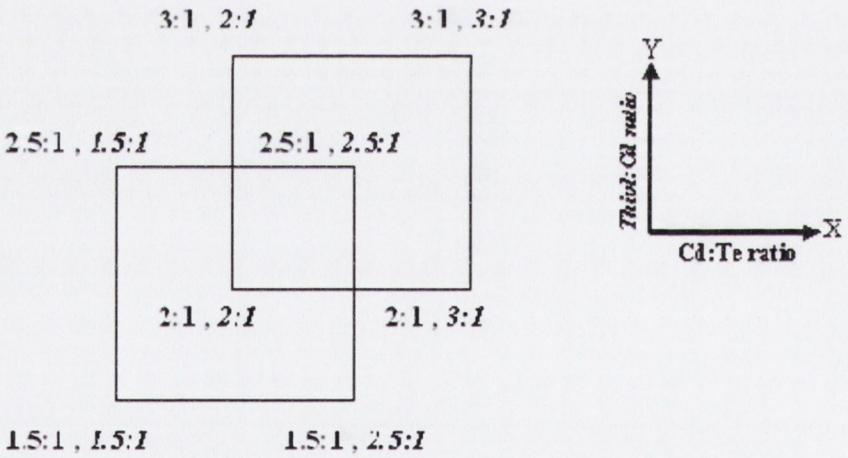


Figure 2.7. Graphical representation of the 2^2 statistical factorial design. Each point represents a metal-to-metal and metal-to-stabiliser ratio. Numbers in bold represent the Cd : Te ratios while those in italics represent the thiol : Cd ratio.

This type of statistical experimental design enables us to vary the reaction conditions systematically over a series of eight experiments, allowing us to determine both the effect of these main factors involved and any interaction between them. The

QDs were prepared as indicated at the beginning of the chapter (see also Chapter 7) and the crude solutions were left overnight in the dark to allow them to equilibrate. The spectra were recorded 24 hours after the QDs were synthesised to maintain the same conditions throughout all eight experiments. The experimental data are summarised in Table 2.1.

Table 2.1. Reagent ratios for reaction with resultant QYs and full width at half maximum (FWHM) values for the crude, unpurified TGA QD solutions.

	Cd : Te ratio	**Cd : TGA ratio**	**QY after 100 minute reflux**	**FWHM (nm)**
A	1.5	1.5	10%	52
B	1.5	2.5	7%	50
C	***2.5***	***1.5***	***15%***	***44***
D	***2***	***2***	***16%***	***44***
E	2	3	8%	51
F	***3***	***2***	***13%***	***46***
G	2.5	2.5	9%	49
H	3	3	8%	50

The values shown in Table 2.1 were recorded for all eight samples prepared. Samples with the largest QY and lowest FWHM values are highlighted in bold. The table indicates that sample **d** (2:1, 2:1 reagent ratios) results in the highest QY and that samples **c** and **f** give the next best set of results. This outcome also manifests itself in the spectroscopic data. Figure 2.8 shows the room temperature UV-vis absorption spectra taken for the various QD solutions.

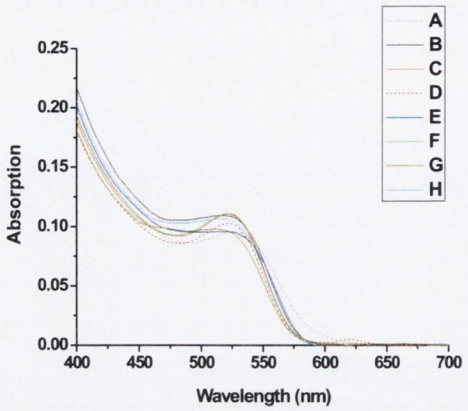


Figure 2.8. Room temperature absorption spectra of TGA capped CdTe QDs taken 24 hours after synthesis.

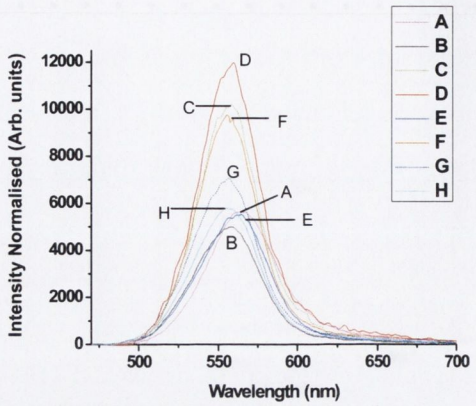


Figure 2.9. Normalised room temperature emission spectra (λ_{ex} = 450 nm) of TGA capped CdTe QDs taken 24 hours after synthesis.

As shown in Figure 2.8, certain reaction conditions are congruent with a clearly resolved first electronic transition in the absorption spectrum (**c, d, f**), thus indicating a relatively high crystallinity and a sufficiently narrow size distribution within the crude parent sample. Others show a less structured spectrum indicative of a more inhomogeneous sample (**a, b, e, h, g**). This broad size distribution within the sample is further emphasised by the FWHM values taken from the luminescence emission spectra, given in Table 2.1 and highlighted in bold. These data show that those samples which give well resolved absorption peaks also possess the narrowest luminescence emission spectra. As such, the excess concentration of the cadmium complexes and also their charge play a vital role in both the initial nucleation events and the subsequent Ostwald Ripening, which gives rise to size variations within the ensemble. [9]

It is interesting to note, that even for a crude unpurified solution, the FWHM values are relatively small. In the case of samples **c** and **d**, FWHM values were 44 nm, but these can approach 35 – 40 nm for purified fractions. These relatively small FWHM values are indicative of a more uniform crystal growth for those particular reagent ratios. It is evident that the conditions which produce QDs with greater QYs have narrower size distributions and also fewer defects, as seen *via* the symmetrical nature of the excitonic emission (Figure 2.9) and absorption maxima (Figure 2.8). A small red shift at the emission maxima can also be identified in samples **a** and **e**, demonstrating that over the

same reflux period, the varying reaction conditions can promote different QD growth rates.

For this study, the initial conditions (metal and stabiliser ratios) were chosen and then varied as a function of one another throughout eight experiments. The response measured was the resultant QY and consequently the FWHM was determined from the emission spectra. The design was carried out according to Table 2.1 and the values obtained were used to construct a 3-D surface response plot incorporating the QY, metal-to-metal and stabiliser-to-metal ratios (Figure 2.10). From this plot the optimal ratio levels can be easily identified from the colour map surface.

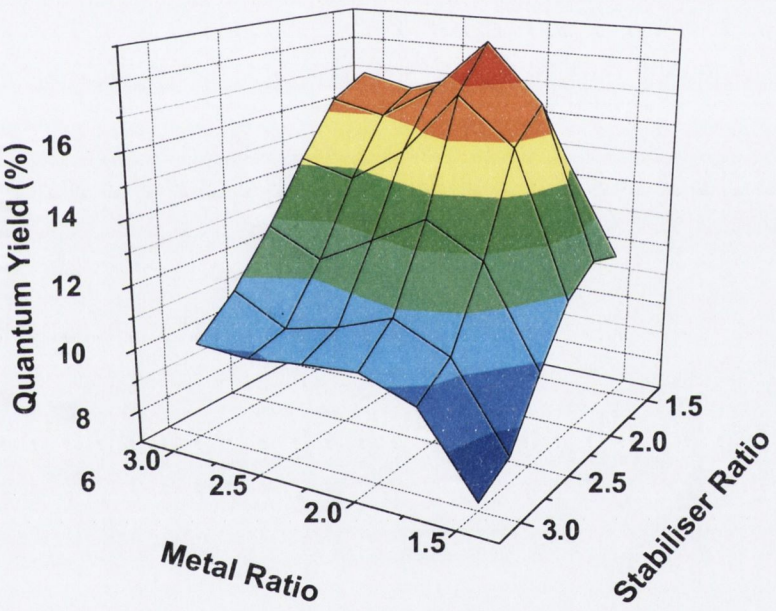


Figure 2.10. Statistical 3-D surface response (response measured was the QY) curve for TGA capped CdTe QDs with variations in the metal to metal and stabiliser to metal ratios as shown in Table 2.1.

According to this plot, the highest QYs can be achieved at a Cd : Te ratio of 2:1 and a Cd : TGA ratio of 1.75:1. This ratio allows the CdL_2^{2-} monomer to dominate but an overall reduction in the concentration of TGA results in less competition between the ligand molecules for vacant surface sites. At these ratios, excess cadmium atoms reside

on the surface of the QDs and these must then be sufficiently passivated by the TGA capping groups. This cadmium excess maximises band-gap emission and reduces the number of defects which may be present should excess Te atoms, possessing non-saturated dangling bonds, fill the vacant surface sites. [37] Thus, the quantum efficiencies and FWHM of TGA capped CdTe QDs are directly proportional to both the stabiliser and metal ratios and the highest quality of QDs can be controlled by the incorporation of the required stoichiometric amounts of the precursors.

2.4 Experiments on enhancement of quantum efficiencies

2.4.1 Ageing

Re-evaluation of the synthetic conditions has enabled us to generate crude QD solutions possessing QYs of approximately 20% and this was now our starting point from which we sought to improve the efficiencies further. To monitor the effect of time and the presence of excess reagents on the optical properties of the TGA capped QDs, the samples synthesised above were kept in darkness, under ambient conditions and were monitored spectroscopically (Figure 2.11) over a period of 3 weeks.

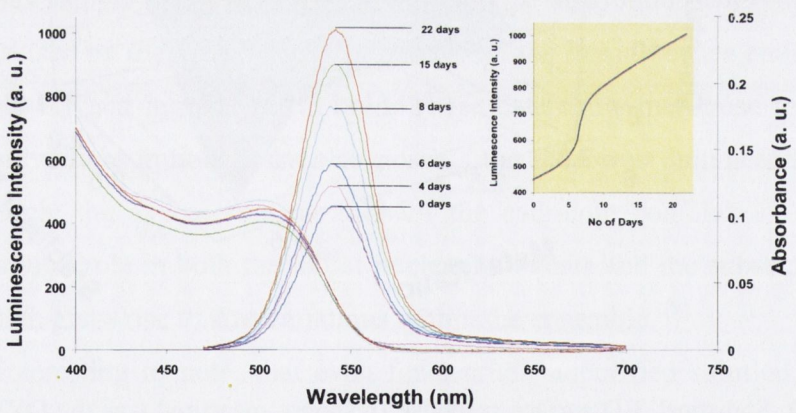


Figure 2.11. UV-vis absorption and normalised luminescence emission spectra (λ_{ex} 450 nm) of TGA capped QDs aged over 22 days. Insert graph: evolution of the emission intensity as a function of ageing time.

Figure 2.11 shows the well established absorption and emission profiles of a crude TGA QD solution aged over 22 days. As can be seen, the luminescence increased

quite substantially over the period of ageing and this is further emphasised by the inserted graph. Solutions contained all excess reagents used in the reaction including unreacted cadmium containing species and stabiliser molecules.

No change in absorption values or the wavelength of emission reinforces the premise that the intensity increase is due to the structural reorganisation of the surface framework. [4, 25, 38] Thus, as more ions and molecules are present in the crude solution, it can be concluded that with time we see an increase in surface passivation and stabiliser packing [39] due to further reaction of the excess reagents with the QD surface. In addition, it must also be noted that the solutions were left at a pH of 11. As mentioned before, cadmium hydroxide can be formed from free cadmium ions in solution under these conditions. Notably, the lack of any precipitate shows that all cadmium atoms are either incorporated into the QDs or as soluble complexes (CdL_x).

Increased surface coverage can be accompanied by the formation of a Cd-thiol complex, similar in effect to capping of the QDs by a material which posseses a wider band-gap such as CdS or ZnS. [4] This complexation on the surface will increase the luminescence by reducing the number of nonradiative pathways available for exciton recombination. Similar cases of improvements up to 50% QY have been shown for CdSe QDs. Mekis *et al.* [2] synthesised CdSe QDs from $Cd(Ac)_2$ and after 3 weeks of storage significant improvements in emission intensities were noted. They ruled out oxidation, as comparisons of solutions stored in air and under nitrogen proved similar and attributed the increases to a reconstruction of the surface resulting in a better passivation of defects.

For our samples, the final QYs of the solutions were in the range of 30%. There seems to be a threshold for the incorporation of these excess moieties into the QD surface and only those initially poorer QDs seem able to be "improved", with subsequent increases noted in their emissive properties. Indeed, at a later date, similar experiments but using higher quality QDs with QYs in the region of 35% were undertaken. However, these proved unsuccessful and the emission intensity remained quite stable throughout the ageing period.

Ageing proved most successful when TGA was employed, possibly due to the fact it was the smallest stabiliser used. Other stabilisers [see Table 3.1] were also investigated, but no significant changes were noted in their spectra with time. As such, it

can be concluded that reagent sizes, charge and steric effects directly influence the enhancement of the surface passivation. [39]

Zhang *et. al.* [25] have also shown that the carboxylic acid groups of the bound and excess stabiliser molecules present play a crucial role in luminescent enhancement. These carboxylic acid groups can interact with the excess Cd^{+} ions on the surface *via* a secondary coordination, resulting in an increased stabilisation. This has also been shown for carboxylic rich polymers and poly(ethylene glycol) mediated CdS nanoclusters. [40]

As mentioned, the starting QY for the solution is crucial and higher quality QDs (larger QYs) do not undergo the same improvements under ageing conditions. Thus, a large resident defect population must still exist on the QD surface as the QY does not exceed 50%. This is due to the presence of free metal atoms, vacant sites and surface dangling bonds on the surface. Structural reorganisation must also be hindered thereby preventing the capping of these defects by any free stabiliser molecules. Adsorbed species can also play a crucial role. Before production, all solutions are degassed to reduce the amount of free oxygen present at the initial stages but they are stored under ambient conditions. For organically prepared QDs, large coordinating molecules are used to reduce the amount of reactive species. Therefore, for aqueous QDs, oxygen and water molecules adsorbed onto the surface may provide additional routes towards nonradiative recombination of the excited charge carriers (e^{-} / h^{+}).

2.4.2 Photoetching

In terms of quantum efficiencies, non-aqueous syntheses produce nanocrystals with superior luminescence properties than that of their water based counterparts. However, transfer of these dots to an aqueous phase results in a reduction in the overall luminescence efficiency of the QDs. [41, 42] As QDs possess the potential to be used in photovoltaic, opto-electronic or sensing devices, [35, 43] increases in their fluorescence intensity is very much desirable (Figure 2.12).

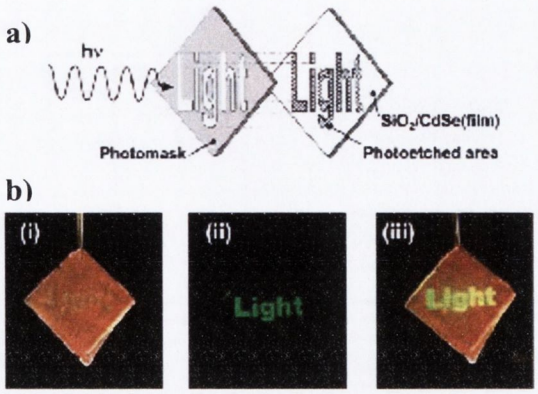


Figure 2.12. **a)** Illustration of patterned monochromatic irradiation of a SiO_2/CdSe (film). **(b)** Photographs of photoetched SiO_2/CdSe (film) placed under i) ambient (ii), ultraviolet (350 nm) and iii) both lights. Adapted from literature. [44]

It is important to understand the intricacies and photochemical properties on the surface of the crystallite, leading to increased QYs with higher photostabilities and photobleaching thresholds. It has been shown that thiol capped CdSe QDs are relatively unstable to photochemical oxidation, [45, 46] while some thiol capped CdTe QDs can exhibit quite remarkable behaviour under exposure to light. [47-49] Investigations have shown that the luminescence efficiency seems to depend more on the surface environment and its reconstruction and suffers less due to imperfections within the crystal lattice framework itself. [4, 39]

The strong quantum confinement-controlled size dependence of the QDs makes them ideal candidates for studying their photochemical properties, which could possibly lead to new optoelectronic devices or improved probes for biological detection. This has particular implications for *in vitro* studies utilising QDs in cellular environments, as they will be subjected to a harsh medium and must compete with phenomena such as autofluorescence which can mask the QD emission should it not be strong or stable enough. In an effort to improve the QY of TGA stabilised QDs, we have employed the statistical analysis shown previously and analysed the effects of illumination on the resultant QY.

Photoetching as an alternate process of improving the emission properties of QDs has been explored by various groups yielding positive results and substantial increases in

luminescence. Using a low pressure Hg lamp, Bao *et al.* [47] witnessed a substantial increase in QY up to 85% over a 20 day illumination period at room temperature. However, their emission spectra experienced a red shift with illumination, indicating particle growth or aggregation with time. This may be caused by an increase in temperature of the solution with exposure time or the decomposition and subsequent incorporation of excess reagents into the Cd-Te-SH shell around the QDs. Post-preparative size-selective precipitation and selective photochemical etching have also been proposed as methods for increasing the QY of the QDs up to 40%, when TGA stabilised QDs were irradiated for 5 days. [4]

As our aim was to investigate CdTe QDs in living cells, we required the smallest possible particle sizes. Also, we wanted to achieve an increase in the luminescence intensity through sacrifice of the smaller and poorer quality dots and possibly even reduce the sizes of the dots throughout the ensemble. Thus, unlike the photoetching experiments carried out by and Bao *et al.* [47] where illumination times stretched from hundreds of hours to days of illumination, our experiments were undertaken in accordance with previously reported procedures [4] aimed at quickly obtaining samples for both Raman and intracellular studies.

The QD solutions were irradiated with a 500 W high pressure Hg lamp, with a range > 450 nm with a filter (Figure 2.13) and > 350 nm without a filter (Figure 2.14) present. The resultant absorption and luminescence spectra were monitored as a function of exposure time. Various different stabilisers (Table 3.1) and QD sizes were analysed; however, once again TGA gave the most significant and positive results as luminescence increases were not as substantial and quenching, followed by coagulation of the colloid was far quicker for other thiols tested.

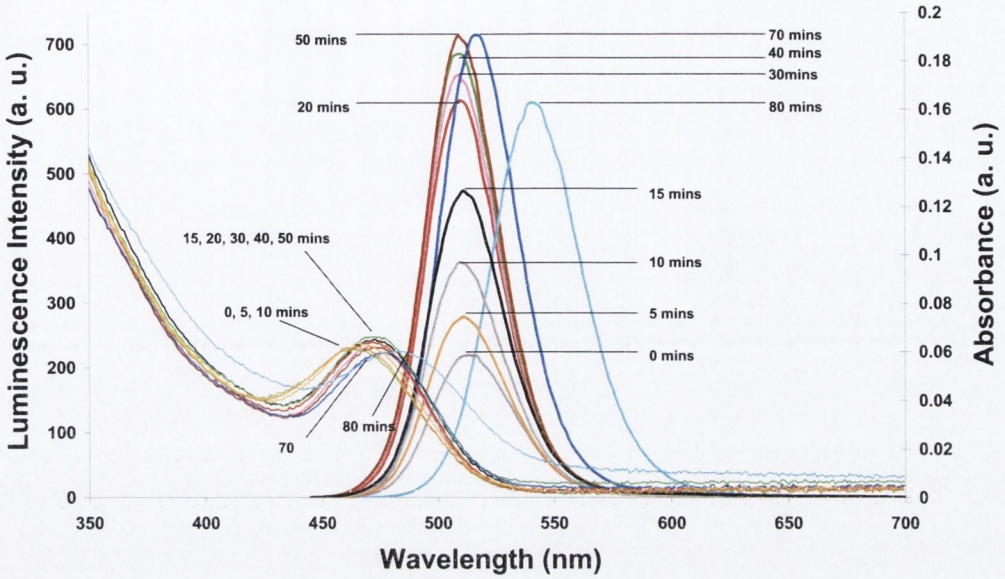


Figure 2.13. UV-vis absorption and normalised room temperature luminescence emission spectra (λ_{ex} 425 nm) (filter present) of TGA capped CdTe QDs subject to irradiation.

Figure 2.13 shows the UV-vis absorption and luminescence emission spectra for a sample of TGA QDs that was irradiated for 80 minutes in the presence of a filter. This resulted only in radiation greater than 450 nm / 2.75 eV illuminating the samples and interestingly both spectra are seen to charge markedly with time. An initial red shift in the UV-vis spectrum is noted, but no fluctuations are witnessed in the absorption values indicating that there are no changes to the QD concentration. These alterations may arise due to QD dissolution or decomposition and are only seen to manifest themselves at the very end of the irradiation period. At this point a distinct red shift, a decrease in absorption value and a broadening of the peak was seen. This change results from the degradation and initial aggregation of the sample and was quickly followed by precipitation.

This decomposition is further conveyed in the emission spectrum but significantly, as the absorption peak remained stable during the irradiation, the emission intensity increased substantially. A 3-fold intensity increase is seen over the photoetching period and the start of decomposition is clearly illustrated by a red shift after 70 minutes of illumination. This is possibly due to an additional sulfuration reaction at the surface of the QDs from decomposing thiols, [25] or the dissolution of smaller QDs and their

subsequent incorporation into the capping shell. Previously, this has been shown for ZnS QDs. [50] With prolonged irradiation, the sample then began to change colour, its luminescence dropped and precipitation soon followed.

To investigate if altering the range of irradiation would change the degree of etching, the filter was removed and the experiment repeated (Figure 2.14).

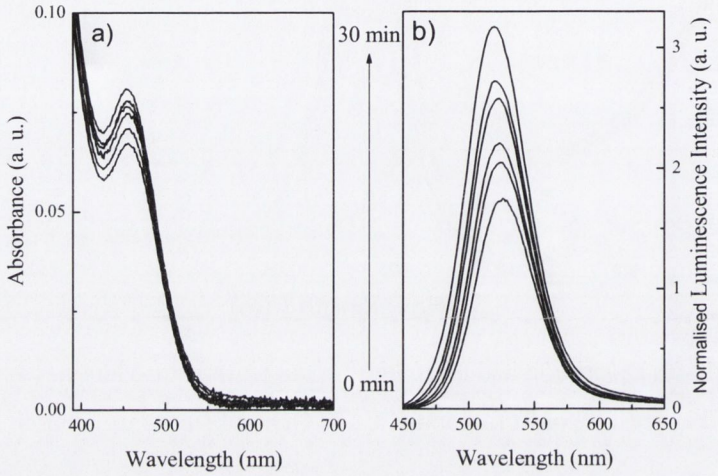


Figure 2.14. a) UV-vis absorption and **b**) normalised room temperature luminescence emission spectra (λ_{ex} 425 nm) of TGA capped CdTe QDs subject to irradiation (no filter present) over 30 minutes.

Figure 2.14 **a**) shows the UV-vis absorption and **b**) luminescence emission spectrum for TGA QDs irradiated without the presence of a filter. Unlike the previous experiment where no initial change seen in the absorption spectrum, a decrease in the absorbance values is seen here. This change in the optical densities has been recorded previously and can be accredited to the dissolution of poorer QDs and a reconstruction of the surface to accommodate these moieties. [44, 51, 52]

Previously, no shift in emission wavelength was noted until the decomposition point was reached (Figure 2.13), however a slight blue shift to lower wavelength is evident for this experiment (Figure 2.14, **b**). This is an indication of a reduction in overall crystallite size. [47, 51] Thus, the irradiation between 350 – 450 nm and the increased power without the filter present for only 30 minutes caused a decrease in crystallite size, accompanied by an increase in band-gap energy.

Increasing the luminescence *via* photoactivation can be accredited to a number of processes. Annealing and reconstruction of the nanocrystal surface results in the removal of the dangling bonds associated with unsaturated Te atoms present on the surface, which act as hole traps. [53, 54] Annealing of these impurities should be higher for those QDs possessing a large quantity of defects. [51, 54] These and other defect states are broader, less pronounced and appear as an independent feature which is red shifted compared to that of the band-gap emission. [55] At low temperature, these states can be clearly resolved and identified. [18] However, at room temperature, they appear to cumulatively add to the intrinsic emission resulting in spectral broadening, increased FWHM values and a decreased symmetry of the emission spectrum.

Most commonly, an increase in luminescence is achieved by capping the surface with a material possessing a larger band-gap such as CdS or ZnS. [1, 2, 56] but this is accompanied by an increase in size. This layer effectively caps the defects present on the surface, thus reducing the number of nonradiative channels and increasing the overall quantum efficiency. For this to be occurring in our case, it must also be accompanied by a restructuring of the QD surface as no increase in size is witnessed. In fact, a decrease is seen under certain conditions indicating a photocorrosive process, as a result of irradiation. A topological reconstruction accompanies this photocorrosion, which manifests itself as a blue shift in the emission spectrum due to shrinkage of the crystallite.

Another theory involves the initiation of corrosion by the photoinduced carriers which initiate the formation of the elemental components from the QDs. [52] These photocorrosion products may cumulatively add onto the surface and the formation of an oxide layer can result in increased passivation. [44, 50, 57] The composition of the QDs themselves may also contribute to any effects witnessed. It has been shown that different QDs are capable of producing free radicals in solution [CdS – hydroxyl & superoxide, CdSe – hydroxyl, CdSe/ZnS – no radicals]. [46] As such, efficient passivation of the surface successfully reduces the number of adsorbed oxygen-containing species available for radical formation. However, the presence of oxygen has been shown to play a vital role during the irradiation process. Increases have been recorded of up to 10% in the presence of oxygen while only 1.5% was witnessed in a nitrogen atmosphere. [51] Bol *et. al.* [50] postulate that oxygen is photochemically absorbed upon irradiation and efficiently

reduces nonradiative recombination. This oxidation or hydrolysis of the available thiol groups can result in the formation of holes within the QD monolayer and accelerate the photooxidation process.

Another possibility for the increase in QY upon irradiation is the activation of so called "dark" dots that are dormant in solution. [49, 58] Research by Ebenstein *et al.* [58] using single particle fluorescence, proved that within an ensemble of QDs a significant proportion do not undergo radiative recombination, thus reducing the overall resultant fluorescence QY. Possibly, these QDs are quenched due to the presence of adsorbed oxygen, which can be removed upon irradiation. Jones *et al.* [49] also postulate that one reason for the QY enhancement is the inducement of these "dark dots" to fluoresce while they also speculate that the "intermittent blinking" [59-61] of single QDs within the ensemble can, by having an increased "off" time, contribute to the reduction of the overall QY. They attribute the luminescence enhancement to chemical changes caused by the irradiation that results in higher efficiencies for the nanocrystals experiencing an "on" time period.

It must also be noted that even with TGA capped QDs not all of the samples produced the desired improved results. Those high quality samples tested, with QYs greater than 25% had little or no change in their absorption or emission spectra, except for those subjected to long irradiation times which led to their decomposition. This leads to the conclusion, that only the poorer quality QDs such as those with large surface anomalies, are in fact improved or dissoluted by the irradiation.

2.4.2.1 Fluorescence lifetime decay analysis

One direct way to understand the role of surface defect states in the photoinduced fluorescent enhancement of the QDs is to monitor the QY of photoetched samples along with the emission decay dynamics, as these provide additional and important information on the recombination of the photoinduced carriers in CdTe QDs. One important concern for optoelectronic devices is the radiative lifetime, which directly determines the average interval time between two consecutive emitting photons from a single source, thus impacting the speed of the device. [48]

Unlike CdSe QDs, whose time-resolved dynamic properties affected by photoetching have been thoroughly examined, [48] CdTe QDs are much less studied. Figure 2.15 shows the luminescence decay curves measured at the respective emission peak wavelengths for photoetched CdTe QDs. The decay curves for each sample can be successfully simulated using a biexponential function with a shorter lifetime on the scale of a few nanoseconds, and a longer one in the order of nanoseconds. This multiexponential behaviour is almost universal in the decay dynamics of colloidal II-VI QDs. [62-64] Previously, reports into the luminescence decay dynamics of CdTe QDs have shown that decay behaviours for QDs possessing high defect populations (QY ~ 3%) are distinctly non-exponential and lifetimes can range from a few hundred picoseconds to a few hundred nanosecond. [18] The luminescence decay curve has a biexponential form of

$$A_1 \exp(\tau/\tau_1) + A_2 \exp(\tau/\tau_2)$$

A_1 Amplitude of the lifetime
τ Measured time
τ_1 short lifetime component
τ_2 long lifetime component

For a biexponential system, the shorter lifetime (τ_1 ~ 2-5 ns) can be attributed to the radiative recombination from band edge states, [65, 66] while the longer lifetime (τ_2 ~ 15 - 25 ns) can be accredited to the recombination of the charge carriers at surface states. [48, 67]

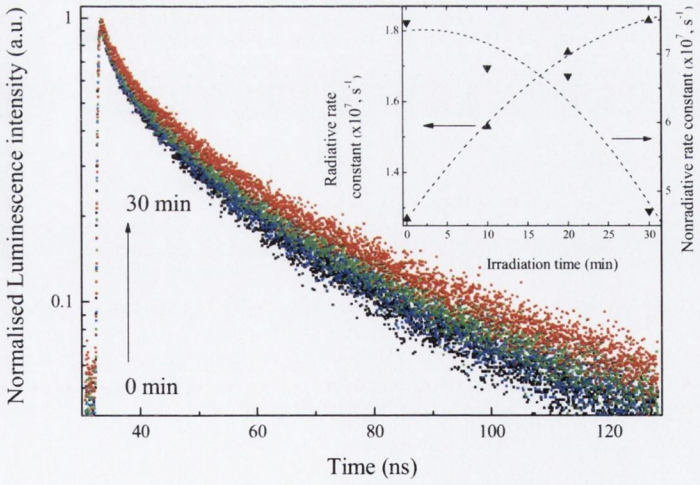


Figure 2.15. Four luminescence decay curves for TGA capped QDs recorded during the photoetching process. Insert: radiative and nonradiative rate constants calculated by Equations (3) and (4) respectively. Dashed lines are simply guides to the eye.

The shorter lifetime observed in our experiments correlate with theoretically obtained values of ~ 3 ns, taking into account the screening of electromagnetic fields inside the QDs. [68] With regard to the longer-lifetime component, the poor overlap of the carrier wavefunctions results in their trapping by the surface states and accounts for lifetimes longer than 10 ns. [67] It has been shown that the transfer of the carriers to surface quenching defects usually happens on a time scale of tens of picoseconds, [65] so it should not contribute to the measured lifetime components.

In our case, longer lifetime values were found to systematically increase with irradiation time in conjunction with luminescence efficiency, indicating the involvement of surface states in carrier recombination. However, observed biexponential luminescent decays give no way of deducing quantitative information on the character of the recombination parameters in QDs. Therefore, to gain a good understanding of luminescence modification dynamics during photoetching, an estimate for the average lifetime was obtained from the time in which emission intensity drops to 1/e of the initial value, τ. [12, 62] This allowed us to obtain a single decay parameter, which can be considered as an effective average lifetime. Deducing τ from luminescence decay curves and taking into account the QY (Φ) values of the photoetched samples, we can calculate nonradiative (n_{nr}) and radiative (k_r) constants using the following equations:

$$\frac{1}{\tau} = k_r + k_{nr} \quad (1) \qquad \Phi = \frac{k_r}{k_r + k_{nr}} \quad (2) \qquad k_r = \frac{\Phi}{\tau} \quad (3) \qquad k_{nr} = \frac{1}{\tau} - k_r \quad (4)$$

The insert in Figure 2.16 shows the estimated effective nonradiative coefficients in comparison with radiative rate constants. There is a clear correlation between the efficiency of luminescence (Figure 2.14), the increased radiative rate constants and substantial suppressing of nonradiative transitions.

As it has been suggested, [4] all these phenomena can be accredited to the photodegradation of excess and surface reacted TGA molecules and their subsequent incorporation into a CdS shell around the QDs. This epitaxial shell caps the defect

surface states, reducing the number of nonradiative pathways and increases the QY, but also results in a decrease in the size of the QD core as indicated by a blue shift in the emission spectra. Thus, incorporation into the shell must be due to a structural reorganisation of the surface features as a red shift would generally be expected if QDs were coated by an epitaxial shell. Although very plausible, this suggestion has not yet been put to the experimental test.

2.4.2.2 Raman spectroscopy

In order to gain a deeper insight into the mechanism of surface modification during photoetching we have performed Raman spectroscopy experiments. The high sensitivity of the resulting Raman spectra to the reconstruction of the QD surface was demonstrated recently for CdSe QDs capped with an organic ligand, [69] an inorganic capping shell, [70] as well as QDs embedded in glass or polymer matrices. [71, 72] It was also shown that a strong dependence on the frequency of longitudinal optical (LO) phonons on the thickness of the QD shell can be used as a tool to control the shell thickness to an accuracy of half a monolayer. [70]

In our Raman experiments, CdTe QDs were deposited and dried from solution on to a Si wafer (Figure 2.16). Because of the high quantum efficiency of the QDs, resonant Raman spectra were superimposed on a broad luminescence background. This background has been subtracted in all spectra in order to show the Raman signal more clearly.

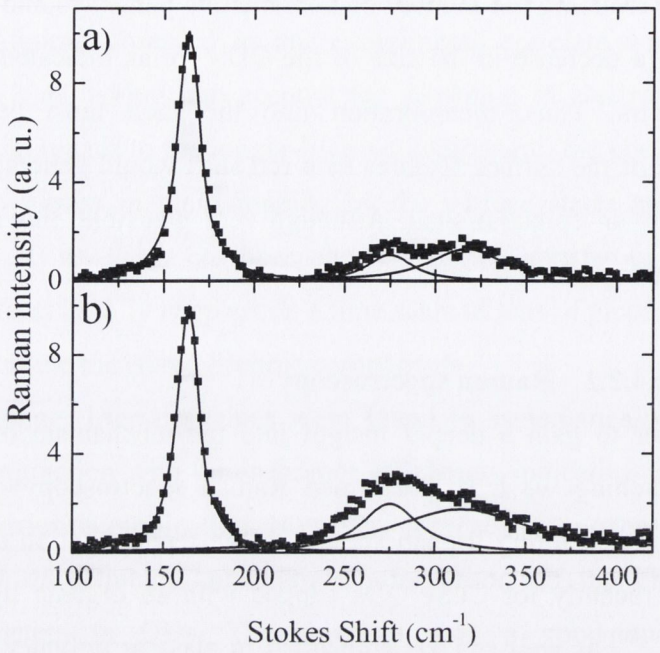


Figure 2.16. Raman spectra of aqueous TGA capped CdTe QDs, **a**) before photoetching and **b**) after photoetching. The solid lines are fitted curves obtained using Lorentzian functions.

The group of lines shown in Figure 2.16 can be well fitted by three Lorentzians with variable amplitudes, peak positions, and FWHM. The more pronounced peak in both spectra can be assigned to the fundamental LO phonon mode of CdTe. [73] The Stokes shift of this peak, Ω_{LO} of 164 cm^{-1}, is smaller than the corresponding bulk value of 168 cm^{-1}. [74] The shift originates from a contribution of two sources: a red shift due to confinement of the optical phonons, [75] and a blue shift caused by lattice contraction. [69] The 15 cm^{-1} width of the LO phonon line for CdTe QDs in our experiment reflects the size distribution of the QDs (about 12% as estimated from the spectral width of the absorption peak). The Raman spectra also show a signal in the region of the first overtone at 320 cm^{-1} belonging to the CdTe, which partly overlaps the peak centred at 275 cm^{-1}. This last peak shows an increased intensity after photoetching of the QDs, indicating the contribution of a crystallographic phase which cannot be assigned, either to the CdTe core or the TGA capping layer. Considering the presence of excess surface TGA molecules in our samples and an increase in intensity of the peak at 275 cm^{-1} after

photoetching, we can assume that this peak is caused mainly by the formation of a ternary Cd-S-Te interlayer between the CdTe core and thiol stabilising TGA group.

The observed changes in the Raman spectra after photoetching can originate from the elimination of defect states, which are most probably unsaturated surface tellurium atoms [29] and the formation of a Cd-S-Te crystallographic structure which is associated with an increase in intensity of the corresponding LO phonon peak. It has been previously reported that depending on the contribution of the CdTe or CdS crystallographic phases, phonon modes of a ternary compound can span the spectral region between 250 and 305 cm^{-1}. [76] A significant broadening of this peak, with a FWHM value of 27 cm^{-1} may suggest a strong strain effect at the interface, due to an approximate 7% lattice mismatch between CdTe and CdS. [77] In fact, the existence of a ternary phase on the surface of the CdTe core should cause the appearance of two additional peaks in Raman spectra: one belonging to the ternary compound, and another signal in the region of the fundamental CdS LO phonon frequency (305 cm^{-1}). Therefore it may be suggested that the band observed in both Raman spectra at 320 cm^{-1} consists, of two strongly overlapped peaks. The first one may be indeed assigned to the first CdTe overtone, as was suggested above, with a maximum at 328 cm^{-1}. The second peak may belong to the CdS LO phonon, although this peak can also be shifted from its expected position due to quantum confinement and strain. Strong broadening of the band observed at 320 cm^{-1} with a FWHM of 47 cm^{-1}, may justify this possibility.

The results of our Raman studies, along with observed strong increases in QY and radiative rates, (Figures 2.14 and 2.15 respectively) reinforce the theory that TGA capped QDs contain a mixed phase of CdTe and CdS on the surface and increases in the emission intensity are a result of light-induced incorporation of surface thiol molecules into this phase. This increase must result from a further amalgamation of Cd(S) on the surface and an efficient reduction in the nonradiative pathways. It is worth noting that obtained evidence of light-induced growth of a CdS shell and/or a Cd-S-Te phase on the surface of the QDs is of great importance for the application of these QDs as biological labels for intracellular imaging *in vitro*. It has long been known that one of the mechanisms employed by living organisms, such as bacteria and yeasts, to counter the toxic effects of

free cadmium ions involves complexation of the metal ion by peptides or proteins incorporating sulphide ions [78, 79] or even by peptide-assisted growth of CdS QDs. [80]

2.5 *In vitro* biological studies of TGA capped QDs

Accordingly, we assessed the ability of TGA stabilised QDs to act as suitable labels for the interaction and illumination of THP-1 cells. THP-1 cells were differentiated to macrophages as described in Chapter 7 and the QDs (10^{-5} M) [81] were added at a 1 in 100 dilution followed by incubation for the indicated times at 37° C. To remove any loosely bound QDs, washing with phosphate buffered saline (PBS) followed the incubation period. Live fluorescent microscope images were taken to characterise the relationship between the QD and cells.

Following a five minute coincubation time with the cells, the TGA QDs are seen to rapidly accumulate around the exterior of the cellular membrane, while no adverse effects to the cells were noted (Figure 2.17).

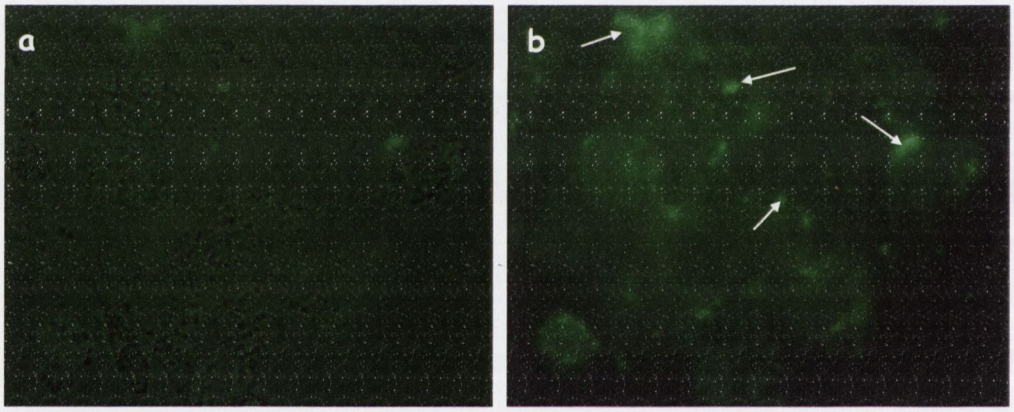


Figure 2.17 Phase contrast **(a)** and fluorescent image **(b)** of TGA QDs adhering rapidly to the macrophage cell surface following a short (5 minute) coincubation treatment.

Figure 2.17 shows intense binding of the QDs to the cell surface following a coincubation time of only five minutes and the highlighted cell borders visible in panel **(b)** are decorated by a patchy QD distribution. All cells within the analysed regions seem to attract the QDs and highlighted regions (arrows) indicate their accumulation on the membrane envelope.

Further experimentation shows that after extending the co-incubation time beyond ten minutes, the TGA QDs previously adhering to the cell membrane are internalised by the macrophages and sequestered to the cytoplasm (Figure 2.18 (**a, b**)). Interestingly, following the extended co-incubation time, these internalised QDs exhibit a diffuse cytoplasmic distribution and an enhanced nuclear membrane localisation.

We next evaluated the effects that photoetching of the TGA QDs would have on their behaviour and properties within the cellular environment (Figure 2.18). Luminescence increases have been shown spectroscopically (Figures 2.13, 2.14) and this is directly translated and confirmed upon visualisation of these photoetched QDs in the presence of THP-1 cells. These etched QDs possess far greater luminescent properties than their non etched counterparts and, while they display the same cellular compartmentalisation, they exhibit a far greater optical enhancement of the cell region making them ideal tools for a greater detailed examination of the cytoplasm and nuclear membrane (Figure 2.18 **c-e**). This apparent *in vitro* biocompatibility of TGA QDs led us on to further investigations into the behaviour of a variety of thiol capped QDs in these cellular systems (see Chapter 3).

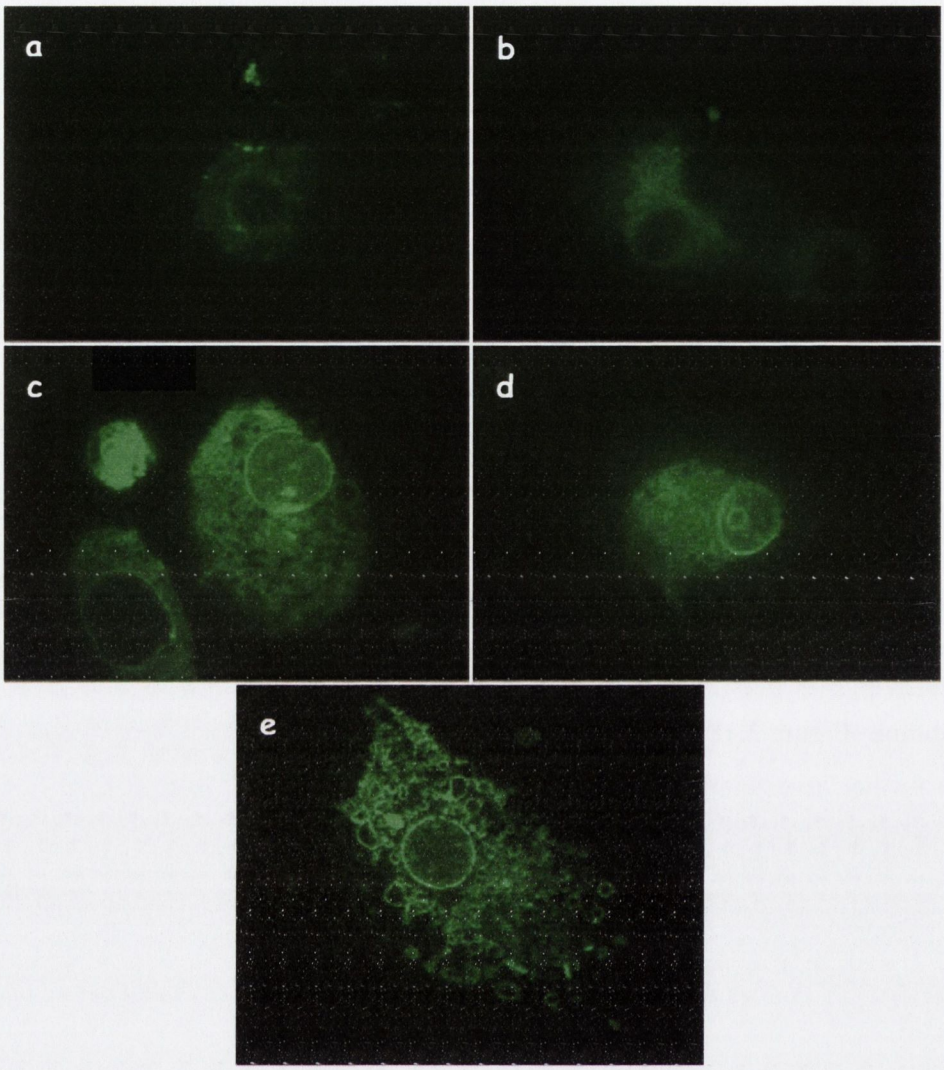


Figure 2.18. a-b) Fluorescent microscope images of TGA QDs penetrating the membrane of THP-1 cells and illuminating the cytoplasm. **c-e)** Fluorescent images of photoetched TGA QDs displaying the same cytoplasmic localisation but illuminating the organelles with a far greater intensity enabling a more detailed analysis of the region. Co-incubation time for both samples of QDs was 15-30 minutes.

2.6 Conclusions

TGA capped CdTe QDs have been successfully prepared and characterised. Investigations have been conducted into determining the optimum synthetic conditions for the production of highly luminescent QDs. A statistical analysis over eight experiments (Figure 2.7) showed that the optical properties of the QDs were highly dependant on the precursor ratios. Consequently a 2:1 metal-to-metal and ligand-to-metal

ratio was shown to produce QDs with the highest QY (16 %) and narrowest FWHM (44 nm) for these conditions. From these data, we were able to generate a 3-D surface response curve (Figure 2.10). This plot indicated that a ligand : metal ratio of 1.75 would lead to the highest quality QDs.

Ageing and photoetching experiments were carried out to further improve the QY of the samples. We allowed the QD solutions to age in the presence of unreacted molecules resulting in a two and a half fold increase in emission intensity. Photoetching of the samples on a smaller than previously reported time scale, [4, 47] in the range of tens of minutes, with and without a filter present also resulted in a significant (up to 3 fold) enhancement of the luminescence emission.

Employing time-resolved luminescence spectroscopy, in combination with Raman spectroscopy, we have addressed the issue of how the surface states influence the recombination efficiency of the charge carriers in photoetched CdTe QDs. Our results contribute to the fundamental understanding of the role of surface ligands and prove the existence of a mixed ternary phase of Cd-S-Te, which facilitates the increases witnessed in the emission intensities. Both of these factors are critical to the design of stable, highly luminescent CdTe QDs.

We have also investigated the potential use of TGA stabilised QDs and their highly luminescent photoetched counterparts as fluorescent bioimaging agents. We demonstrated that TGA capped QDs can serve as excellent live cell imaging agents as they exhibit strong luminescence and excellent photostability while maintaining cell viability over a number of extended incubation periods. In addition, the ability of the TGA QDs to traverse the cell membrane of macrophages is a formidable quality that may potentially be harnessed for imaging and therapeutics. Modulating the delivery of QDs to subcellular locations in living cells opens a myriad of exciting potential applications, ranging from targeted drug delivery to examination of intracellular processes.

References

[1] P. Reiss, J. Bleuse, A. Pron, *Nano Lett.* **2002**, *2*, 781.

[2] I. Mekis, D. V. Talapin, A. Kornowski, M. Haase, H. Weller, *J. Phys. Chem. B* **2003**, *107*, 7454.

[3] C. B. Murray, D. J. Norris, M. G. Bawendi, *J. Am. Chem. Soc.* **1993**, *115*, 8706.

[4] N. Gaponik, D. V. Talapin, A. L. Rogach, K. Hoppe, E. V. Shevchenko, A. Kornowski, A. Eychmüller, H. Weller, *J. Phys. Chem. B* **2002**, *106*, 7177.

[5] S. Zhang, J. Yu, X. Li, W. Tian, *Nanotech.* **2004**, *15*, 1108.

[6] J. J. Li, Y. A. Wang, W. Z. Guo, J. C. Keay, T. D. Mishima, M. B. Johnson, X. G. Peng, *J. Am. Chem. Soc.* **2003**, *125*, 12567.

[7] J. P. Ge, S. Xu, J. Zhuang, X. Wang, Q. Peng, Y. D. Li, *Inorg. Chem.* **2006**, *45*, 4922.

[8] C. R. Bullen, P. Mulvaney, *Nano Lett.* **2004**, *4*, 2303.

[9] X. Peng, J. Wickham, A. P. Alivisatos, *J. Am. Chem. Soc.* **1998**, *120*, 5343.

[10] Z. A. Peng, X. Peng, *J. Am. Chem. Soc.* **2002**, *124*, 3343.

[11] S. F. Wuister, I. Swart, F. van Driel, S. G. Hickey, C. de MelloDonega, *Nano Lett.* **2003**, *3*, 503.

[12] S. F. Wuister, F. van Driel, A. Meijerink, *J. Lumin.* **2003**, *102-103*, 327.

[13] S. F. Wuister, C. D. Donega, A. Meijerink, *J. Phys. Chem. B* **2004**, *108*, 17393.

[14] S. F. Wuister, F. van Driel, A. Meijerink, *Phys. Chem. Chem. Phys.* **2003**, *5*, 1253.

[15] L. Li, H. Qian, J. Ren, *Chem. Comm.* **2005**, 528.

[16] M. Li, Y. Ge, Q. Chen, S. Xu, N. Wang, X. Zhang, *Talanta* **2007**, *72*, 89.

[17] H. Zhang, L. Wang, H. Xiong, L. Hu, B. Yang, W. Li., *Adv. Mater.* **2003**, *15*, 1712.

[18] A. M. Kapitonov, A. P. Stupak, S. V. Gaponenko, E. P. Petrov, A. L. Rogach, A. Eychmüller, *J. Phys. Chem. B* **1999**, *103*, 10109.

[19] Y. Liu, W. Chen, A. G. Joly, Y. Wang, C. Pope, Y. Zhang, J. O. Bovin, P. Sherwood, *J. Phys. Chem. B* **2006**, *110*, 16992.

[20] M. Green, H. Harwood, C. Barrowman, P. Rahman, A. Eggeman, F. Festry, P. Dobson, T. Ng, *J. Mat. Chem.* **2007**, *17*, 1989–1994.

[21] C. L. Li, N. Murase, *Chem. Lett.* **2005**, *34*, 92.

[22] A. Shavel, N. Gaponik, A. Eychmüller, *J. Phys. Chem. B* **2006**, *110*, 19280.

[23] J. Guo, W. Yang, C. Wang, *J. Phys. Chem. B* **2005**, *109*, 17467.

[24] E. J. Holmyard, W. G. Palmer, *Inorganic Chemistry* **1952**, *Dent and Sons*.

[25] H. Zhang, Z. Zhou, B. Yang, M. Y. Gao, *J. Phys. Chem. B* **2003**, *107*, 8.

[26] A. A. Yaroslavov, V. A. Sinani, A. A. Efimova, E. G. Yaroslavova, A. A. Rakhnyanskaya, Y. A. Ermakov, N. A. Kotov, *J. Am. Chem. Soc.* **2005**, *127*, 7322.

[27] A. L. Rogach, A. Kornowski, M. Gao, A. Eychmüller, H. Weller, *J. Phys. Chem. B* **1999**, *103*, 3065.

[28] D. J. Norris, M. G. Bawendi, *Phys. Rev. B* **1996**, *53*, 16338.

[29] H. Borchert, D. V. Talapin, N. Gaponik, C. McGinley, S. Adam, A. Lobo, T. Möller, H. Weller, *J. Phys. Chem. B* **2003**, *107*, 9662.

[30] Z. Tang, B. Ozturk, Y. Wang, N. A. Kotov, *J. Phys. Chem. B* **2004**, *108*, 6927.

[31] K. Hoppe, Geidel, E., Weller, H., Eychmu¨ller A., *Phys. Chem. Chem. Phys.* **2002**, *4*, 1704–1706.

[32] A. P. Alivisatos, *Nat. Biotech.* **2004**, *22*, 47.

[33] J. K. Jaiswal, H. Mattoussi, J. M. Mauro, S. M. Simon, *Nat. Biotech.* **2003**, *21*, 47.

[34] X. Michalet, F. F. Pinaud, L. A. Bentolila, J. M. Tsay, S. Doose, J. J. Li, G. Sundaresan, A. M. Wu, S. S. Gambhir, S. Weiss, *Science* **2005**, *307*, 538.

[35] V. L. Colvin, M. C. Schlamp, A. P. Alivisatos, *Nature* **1994**, *370*, 354.

[36] J. K. Jaiswal, E. R. Goldman, H. Mattoussi, S. M. Simon, *Nat. Methods* **2004**, *1*, 73.

[37] H. Fu, A. Zunger, *Phys. Rev. B* **1997**, *56*, 1496.

[38] M. Gao, S. Kirstein, H. Mohwald, A. Rogach, A. Kornowski, A. Eychmüller, H. Weller, *J. Phys. Chem. B* **1998**, *102*, 8360.

[39] L. Qu, X. Peng, *J. Am. Chem. Soc.* **2002**, *124*, 2049.

[40] Y. A. Wang, J. J. Li, H. Y. Chen, X. G. Peng, *J. Am. Chem. Soc.* **2002**, *124*, 2293.

[41] A. R. Clapp, I. L. Medintz, B. R. Fisher, G. P. Anderson, H. Mattoussi, *J. Am. Chem. Soc.* **2005**, *127*, 1242.

[42] S. Jeong, M. Achermann, J. Nanda, S. Ivanov, V. I. Klimov, J. A. Hollingsworth, *J. Am. Chem. Soc.* **2005**, *127*, 10126.

[43] V. I. Klimov, A. A. Mikhailovsky, S. Xu, A. Malko, J. A. Hollingsworth, C. A. Leatherdale, H. J. Eisler, M. G. Bawendi, *Science* **2000**, *290*, 314.

[44] T. Torimoto, S. y. Murakami, M. Sakuraoka, K. Iwasaki, K. i. Okazaki, T. Shibayama, B. Ohtani, *J. Phys. Chem. B* **2006**, *110*, 13314.

[45] J. Aldana, Y. A. Wang, X. Peng, *J. Am. Chem. Soc.* **2001**, *123*, 8844.

[46] B. I. Ipe, M. Lehnig, C. M. Niemeyer., *Small* **2005**, *1*, 706.

[47] H. B. Bao, Y. J. Gong, Z. Li, M. Y. Gao, *Chem. Mater.* **2004**, *16*, 3853.

[48] X. Wang, L. Qu, J. Zhang, X. Peng, M. Xiao, *Nano Lett.* **2003**, *3*, 1103.

[49] M. Jones, J. Nedeljkovic, R. J. Ellingson, A. J. Nozik, G. Rumbles, *J. Phys. Chem. B* **2003**, *107*, 11346.

[50] A. A. Bol, A. Meijerink, *J. Phys. Chem. B* **2001**, *105*, 10203.

[51] Y. Wang, Z. Tang, M. A. Correa-Duarte, I. Pastoriza-Santos, M. Giersig, N. A. Kotov, L. M. Liz-Marzan, *J. Phys. Chem. B* **2004**, *108*, 15461.

[52] U. Resch, H. Weller, A. Henglein, *Langmuir* **1989**, *5*, 1015.

[53] L. Spanhel, M. Haase, H. Weller, A. Henglein, *J. Am. Chem. Soc.* **1987**, *109*, 5649.

[54] D. V. Talapin, A. L. Rogach, E. V. Shevchenko, A. Kornowski, M. Haase, H. Weller, *J. Am. Chem. Soc.* **2002**, *124*, 5782.

[55] S. F. Wuister, A. Meijerink, *J. Lumin.* **2003**, *105*, 35.

[56] D. V. Talapin, A. L. Rogach, A. Kornowski, M. Haase, H. Weller, *Nano Lett.* **2001**, *1*, 207.

[57] S. R. Cordero, P. J. Carson, R. A. Estabrook, G. F. Strouse, S. K. Buratto, *J. Phys. Chem. B* **2000**, *104*, 12137.

[58] Y. Ebenstein, T. Mokari, U. Banin, *Appl. Phys. Lett.* **2002**, *80*, 4033.

[59] M. Nirmal, B. O. Dabbousi, M. G. Bawendi, J. J. Macklin, J. K. Trautman, T. D. Harris, L. E. Brus, *Nature* **1996**, *383*, 802.

[60] U. Banin, M. Bruchez, A. P. Alivisatos, T. Ha, S. Weiss, D. S. Chemla, *J. Chem. Phys.* **1999**, *110*, 1195.

[61] M. Kuno, D. P. Fromm, H. F. Hamann, A. Gallagher, D. J. Nesbitt, *J. Chem. Phys.* **2000**, *112*, 3117.

[62] T. Franzl, D. S. Koktysh, T. A. Klar, A. L. Rogach, J. Feldmann, N. Gaponik, *Appl. Phys. Lett.* **2004**, *84*, 2904.

[63] E. P. Petrov, F. Cichos, E. Zenkevich, D. Starukhin, C. von Borczyskowski, *Chem. Phys. Lett.* **2005**, *402*, 233.

[64] M. Nirmal, C. B. Murray, M. G. Bawendi, *Phys. Rev. B* **1994**, *50*, 2293.

[65] V. I. Klimov, D. W. McBranch, C. A. Leatherdale, M. G. Bawendi, *Phys. Rev. B* **1999**, *60*, 13740.

[66] J. Y. Zhang, X. Y. Wang, M. Xiao, *Opt. Lett.* **2002**, *27*, 1253.

[67] M. G. Bawendi, P. J. Carroll, W. L. Wilson, L. E. Brus, *J. Chem. Phys.* **1992**, *96*, 946.

[68] B. L. Wehrenberg, C. Wang, P. Guyot-Sionnest, *J. Phys. Chem. B* **2002**, *106*, 10634.

[69] J.-Y. Zhang, X.-Y. Wang, M. Xiao, L. Qu, X. Peng, *Appl. Phys. Lett.* **2002**, *81*, 2076.

[70] A. V. Baranov, Y. P. Rakovich, J. F. Donegan, T. S. Perova, R. A. Moore, D. V. Talapin, A. L. Rogach, Y. Masumoto, I. Nabiev, *Phys. Rev. B* **2003**, *68*, 165306.

[71] J. J. Shiang, A. V. Kadavanich, R. K. Grubbs, A. P. Alivisatos, *J. Phys. Chem.* **1995**, *99*, 17417.

[72] Y.-N. Hwang, S. Shin, H. L. Park, S.-H. Park, U. Kim, H. S. Jeong, E.-j. Shin, D. Kim, *Phys. Rev. B* **1996**, *54*, 15120.

[73] S. Jimenez-Sandoval, S. Lopez-Lopez, B. S. Chao, M. Melendez-Lira, *Thin Solid Films* **1999**, *342*, 1.

[74] M. L. Scheepers, R. J. Meier, L. Markwort, J. M. Gelan, D. J. Vanderzande, B. J. Kip, *Vib. Spect.* **1995**, *9*, 139.

[75] M. A. Hines, P. Guyot-Sionnest, *J. Phys. Chem.* **1996**, *100*, 468.

[76] A. Fischer, L. Anthony, A. D. Compaan, *Appl. Phys. Lett.* **1998**, *72*, 2559.

[77] C. Jia-Yaw, W. Shiuann-Ren, Y. Cheng-Hsien, *Nanotech.* **2007**, *18*.

[78] R. N. Reese, D. R. Winge, *J. Biol. Chem.* **1988**, *263*, 12832.

[79] R. K. Mehra, Winge, D. R., *J. Cell. Biochem.* **1991**, *45*, 30.

[80] C. T. Dameron, R. N. Reese, R. K. Mehra, A. R. Kortan, P. J. Carroll, M. L. Steigerwald, L. E. Brus, D. R. Winge, *Nature* **1989**, *338*, 596.

[81] W. W. Yu, L. H. Qu, W. Z. Guo, X. G. Peng, *Chem. Mater.* **2003**, *15*, 2854.

Chapter 3: Synthesis of CdTe QDs and investigations into their biolabelling capabilities

3.1. Introduction

Ever since their the initial discovery and characterisation in cellular studies, [1, 2] QDs have been touted as exciting novel materials which may provide the building blocks for a new generation of nano-structured imaging materials. [3-5] The ability to fluorescently label and track subcellular structures in living cells is of great importance for molecular and cell biology. [6]

QDs have shown tremendous potential to rival if not replace traditional organic fluorophores. One problem is their heavy metal composition, which has given genuine cause for concern due to their potential cytotoxicity. [7-9] In an effort to combat this problem, much research has been conducted into the mechanisms that result in QDs acting as toxic agents once exposed to a cellular environment [10-14] and ways of reducing their toxicological impact. [15]

Advances in molecular medicine require the optimum detection of individual biomolecules, cell components and other biological entities. For analysis of this submicrometre range, optical microscopy has proven a valuable tool for investigations into biological systems. Traditional methods for detecting biological entities and compounds both *in vivo* and *in vitro* rely mostly on the use of radioactive markers or fluorescent dyes as tags, e.g. fluorescein, ethidium, methyl coumarin, rhodamine, mitotracker and Hoescht. [16] However, dyes have a number of chemical and physical limitations, which include the cost and complexity of methods utilising multiple fluorescent dyes and the deterioration of their fluorescence intensity upon prolonged exposure to excitation light, also called photobleaching. [6] QDs do not suffer from the same limitations. They can be readily tuned to emit at a variety of wavelengths by altering their size, making multi-detection possible over a broad range [17, 18] and they are highly photostable resulting in their use for experiments over longer time scales. [6, 19]

For our cellular studies we have utilised the THP-1 human monocyte cell line. Monocytes are white blood cells or leukocytes, which act as part of the bodies' immune

system to defend against infection, disease, inflammation and pathogens. Monocytes that have left the bloodstream are called macrophages but they can be stimulated or differentiated to become macrophages under laboratory conditions. These differentiated cells are called phagocytes and their defensive role is to remove foreign entities, particulates, dead cells, bacteria etc. by ingesting and subsequently digesting these unwanted moieties. Due to their propensity to ingest foreign bodies, these cells are ideal for use in QD studies and can also act as indicators to show how cells of the immune system respond to the presence of foreign nanoparticulate matter.

The aim of this part of our work was to prepare TGA capped CdTe QDs (TGA QDs) of different sizes and investigate their behaviour in THP-1 cells using optical fluorescence microscopy. We also wished to investigate if changing the stabiliser group altered the interaction and uptake of the QDs. This would enable us to analyse how functionality, size and charge influences the behaviour of the QDs upon incubation with this cell type.

3.2 Investigations into TGA capped QDs with THP-1 cells

Due to their highly luminescent properties and potential for cellular imaging (see Chapter 2), TGA capped QDs were further investigated to analyse how QD size affects their intracellular uptake and distribution. Imaging of the QDs in live cell cultures was performed using a fluorescent microscope and confocal analysis, which enables a 3-D image of the cell in question to be built up and was utilised to elucidate nuclear penetration. This work was undertaken in collaboration with the department of Clinical Medicine, TCD in St. James Hospital Dublin

Two filters (λ_{ex} 488 ± 10 nm; λ_{em} 525 ± 50 nm [green image] and λ_{ex} 568 ± 10 nm; λ_{em} 600 ± 45 nm [red image]) were available for imaging of the QD luminescence once present in or around the cells. Unfortunately, due to the ranges covered by the filters, the QD sizes cannot be inferred from the fluorescent images and can only be verified spectroscopically using UV-vis absorption and luminescence emission spectroscopy (Figure 3.2). Accordingly small QDs (2 - 3 nm) will only appear under the green fluorescent filter, while larger QDs (3 - 4 nm) will appear in the red region with some overlap occurring. Indeed, even purified batches of QDs with relatively narrow size

distributions (FWHM ~ 40 nm) can result in fluorescence that is detectable (yellow colour) in both the green and red channels (Figure 3.1 **c**). This indicates that even for a sample within a relatively uniform size distribution, there exists luminescent ranges that cannot be individually distinguished (Figure 3.1).

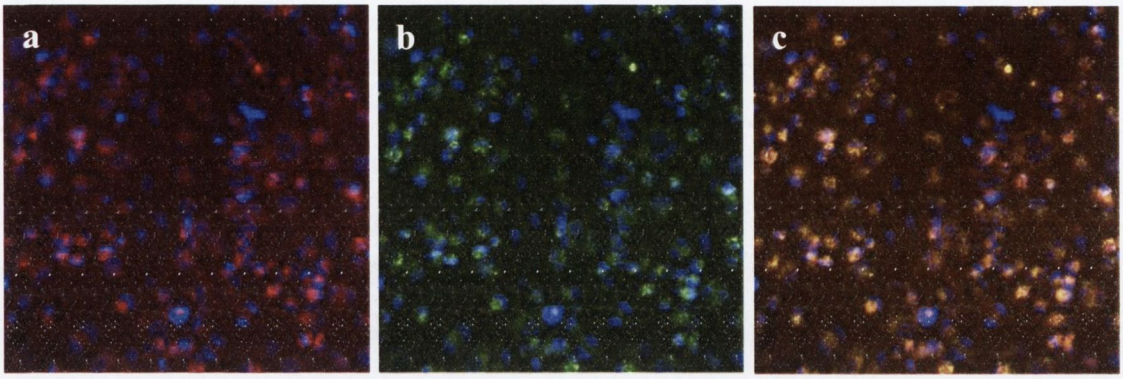


Figure 3.1. Live cell fluorescent images of TGA QDs in live THP-1 cells. Blue colour is due to Hoechst nuclear staining. **Panel a**: QDs viewed under red (λ_{ex} 568 nm) filter, **panel b**: QDs viewed under yellow (λ_{ex} 488 nm) filter and **panel c**: composite (both channels) view of the QDs.

Figure 3.1 illustrates the fluorescent images of TGA QDs viewed under the different filters available and also a composite overlay view of the sample. Clearly, the error in filter range substantially affects the imaging analysis and similar QDs display seemingly different emission wavelengths. As a result we aimed to investigate if the QDs have the potential to not only label the individual organelles within the cells, but also to penetrate the nuclear membrane, thereby enabling us to visualise any sub–nuclear compartments.

TGA QDs were synthesised as described in Chapter 2. However, only certain fractions that displayed distinct and differing spectral characteristics [small, green (2 nm) and larger, red (3.5 - 4 nm) QDs], were isolated, purified and used in our cellular studies (Figure 3.2). Our objective was to evaluate if the size of the QDs plays any role in their uptake and intracellular compartmentalisation.

3.2.1 Size targeting of TGA QDs

UV-vis absorption and fluorescence emission spectra of the two QD samples reveal characteristic peaks at 487 and 515 nm for the smaller and 588 and 615 nm for the larger QDs respectively.

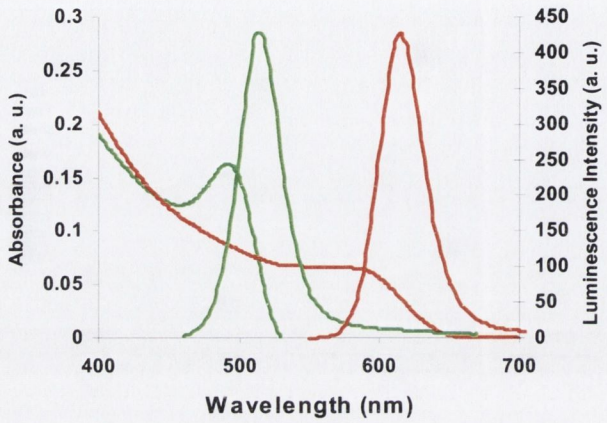


Figure 3.2. UV-vis absorption and normalised luminescence emission spectra (λ_{ex} 450 nm) of the different sized TGA QDs [green: 2 nm, red 4 nm] investigated in the THP-1 cells.

The size of CdTe QDs was estimated from high resolution transmission electron microscopy (HRTEM) images. For HRTEM based sizing curves see Appendix 2a. In this case, the sizes were approximately 2 nm for green emitting QDs and 4 nm for the larger red emitting QDs (Figure 3.3).

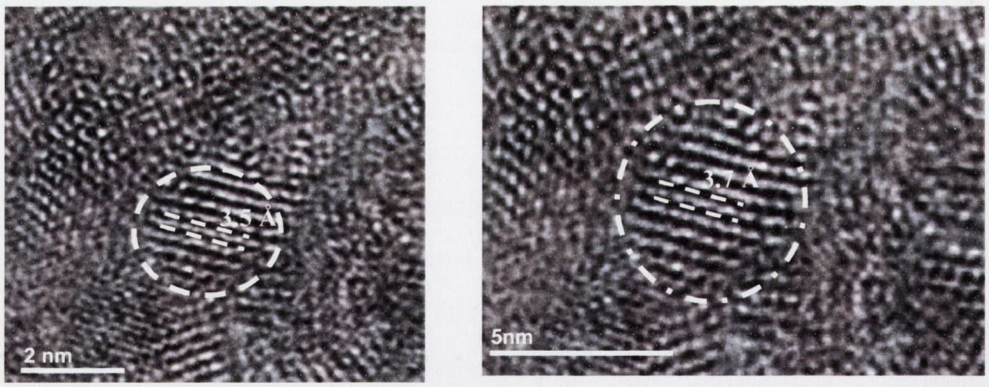


Figure 3.3. HRTEM images showing isolated 2 nm (left) and 4 nm (right) TGA capped QDs, taken from each differently sized sample. Lattice spacings are in agreement with that expected for the (111) plane of cubic zinc blend CdTe. [20]

The actual size of the QDs is larger than the observed HRTEM size because of the surface shell formed by the covalently attached TGA molecules which contribute up to 1 nm to the total particle diameter. [20] This larger dimension for the QDs in solution is further evident from sizing measurements by photon correlation spectroscopy (PCS) (Figure 3.4).

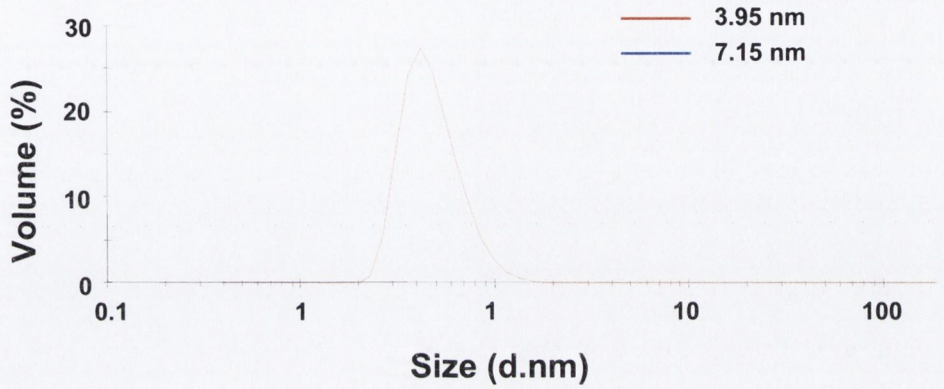


Figure 3.4. PCS measurements by volume of the two TGA QD samples used. Red and blue lines are the measured curves based on 2 nm and 4 nm QDs respectively.

From Figure 3.4, the difference in sizes between the QDs is obvious as is the effect of the TGA capping molecules on the size measured by PCS. The red line is indicative of a 2 nm while the blue line is for the 4 nm QD sample.

PCS measures the Brownian motion of the particles in solution and also takes into account their hydrodynamic radii. Also, intermolecular forces such as hydrogen bonding can lead to a larger observed particle size. Indeed, this can be seen for our QDs, with the 2 and 4 nm QDs giving peaks at 3.95 and 7.45 nm respectively.

As shown previously in Chapter 2, TGA QDs act as intensely luminescent and biocompatible markers. For these experiments the luminescence efficiency of the QDs was sufficient to allow for a 1 in 100 dilution [1 mg/ml] upon addition to the cell cultures. Fluorescent imaging revealed an accumulation of the green QDs into the cytoplasm within ten minutes and an initial enhancement of the luminescence intensity around the nucleus. This is indicated by the arrows in Figure 3.5 **(a)**.

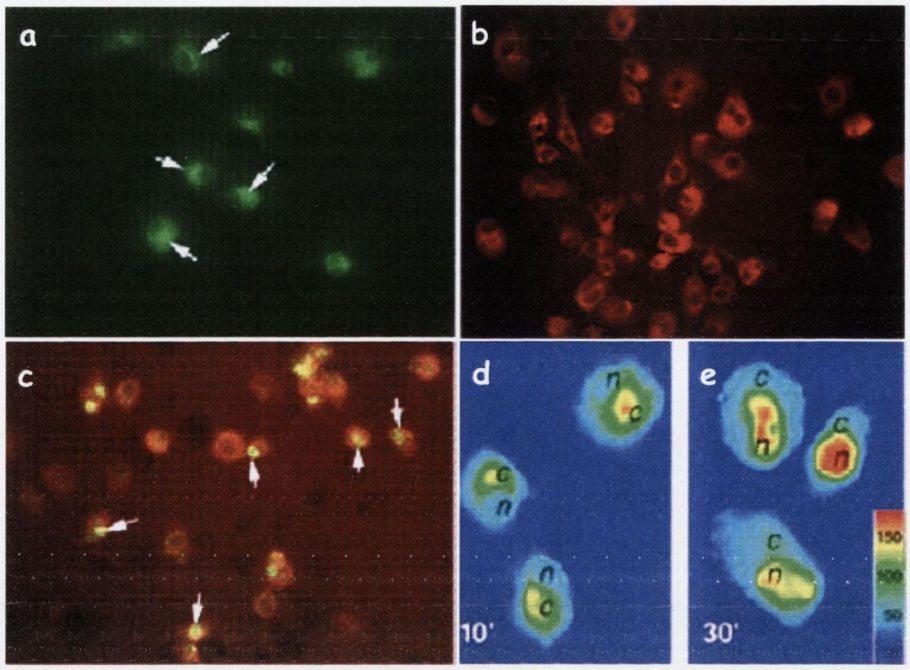


Figure 3.5. (a) Accumulation of the 2 nm green TGA QDs in THP-1s after 10 minutes. The arrows highlight an early compact perinuclear localisation. **(b)** Cytoplasmic compartmentalisation of 4 nm red QDs in the THP-1 cells after a 30 minute coincubation time. **(c)** Addition of green and red QDs after 30 minutes of coincubation with the THP-1 cells. Arrows indicate the translocation of smaller green QDs to the nucleus while the red QDs are retained in the cytoplasm. (**d**, **e**) Analysis of the green QDs intracellular distribution dynamics in individual THP-1 cells after 10 (**d**) and 30 (**e**) minute coincubation times respectively. The coloured images reflect the integrated fluorescence intensity levels. ['*c*' and '*n*' represent the cytoplasm and nucleus respectively. The calibration bar indicates relative fluorescence intensities and images are representative of several experiments].

Following further coincubation of 30 minutes, a rapid and specific nuclear accumulation of the green QDs is seen within the phagocytic cells (Figure 3.5 **c**, **d** and **e**), while the red QDs display only a cytoplasmic compartmentalisation (Figure 3.5 **b** and **c**). Simultaneous addition of both the red and green QDs resulted in a distinct cellular differentiation due to their size, with a nuclear localisation visible for the green QDs, as denoted by arrows, while the red QDs were once again retained only in the cytoplasm (Figure 3.5 **c**).

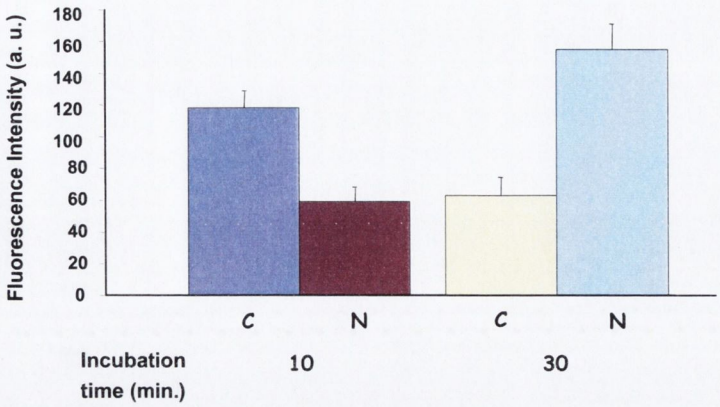


Figure 3.6. Quantitative assessment of the uptake of green CdTe QDs into the nucleus of THP-1 cells. Relative fluorescence units (RFU) convey the shift in the fluorescence of the green QDs from the cytoplasm 'C' to the nucleus 'N' over time. Mean values and standard errors were calculated from 30 cells randomly selected from the microscopic fields.

A quantitative assessment (Figure 3.6) of the intracellular fluorescence levels in individual cells revealed a rapid shift in the prevalence of cytoplasmic (10 minute) versus nuclear localisation (30 minute) of green QDs over the incubation period. The evolution of the QD distribution over time can be seen and this rapid accumulation was not associated with any severe adverse effects on cell viability, as determined by an extended culture over 24 hours.

To prove that the QDs were present within and not just residing on top of the cellular compartments, confocal microscopy was used. Confocal microscopy allows for the 3-D imaging of cells by analysis at varying levels as one slices through the cell from top to bottom. It enables the user to selectively analyse particular levels and regions within the cell (Figure 3.7).

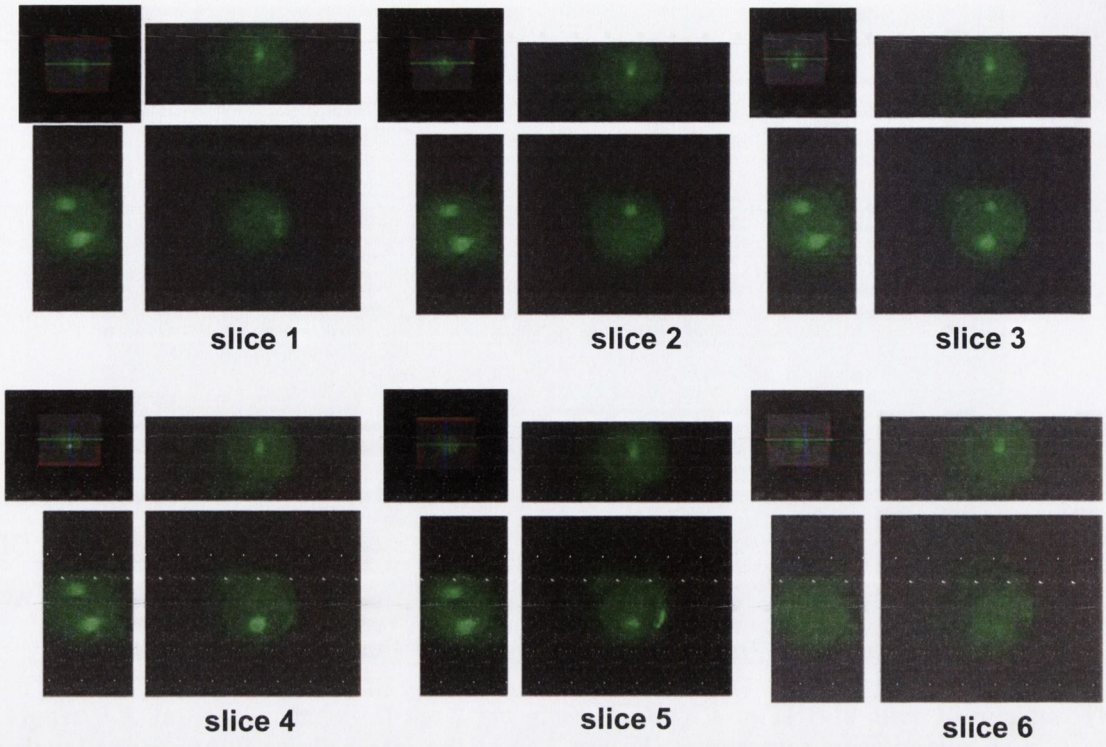


Figure 3.7. Slices taken from a confocal movie as the excitation laser was moved through a cell from top to bottom. Each slice enables the analysis of a layer of the cell and visualisation of the individual components highlighted by the QDs.

Figure 3.7 illustrates the power of confocal imaging to elucidate the individual layers of a cell under analysis. A video and 3-D schematic of the cell can be generated, depicting the regions of the cytoplasm and nucleus illuminated by TGA QDs. It enables the user to assign conclusively the compartments highlighted by the QDs and removes any ambiguity that may arise if the QDs were seen to only lie on top, but not penetrate the nucleus. From these images, we can clearly see as we cycle through the cell, the appearance and disappearance of the stained nuclear compartments indicating QD uptake.

High resolution live confocal imaging of cells dual-labelled with green and red QDs focused at the level of the endoplasmic reticulum (ER) uncovered that the red particles were predominantly retained in the cells internal fluid or cytosol. The cytosol and the cellular organelles make up the cytoplasm, which consists of water, salts, various organic molecules and many enzymes and proteins. These red QDs were also co-

localised with some of the green QDs at characteristic structures corresponding to the perinuclear ER, shown as the yellow regions in Figure 3.8.

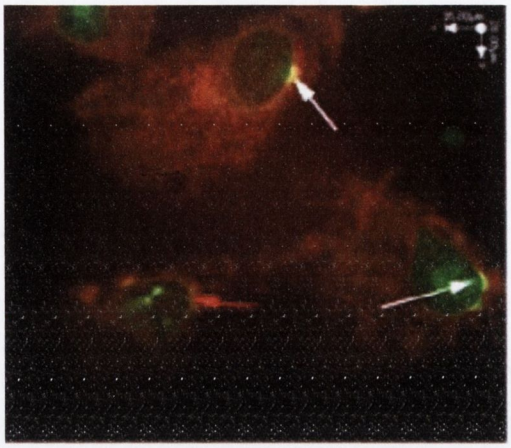


Figure 3.8. Confocal optical cross section at the level of the ER demonstrating green and red QD localisation in THP-1s. Green QDs are localised to the nucleus while red QDs display a diffuse cytoplasmic fluorescence. Both types of QDs co-localise at the perinuclear ER (yellow colour) indicated by arrows.

Significantly, only the smallest green QDs were able to penetrate further into the nucleus displaying confined areas of compact concentration highlighting the nucleoli (green agglomerates, Figure 3.8 and 3.9).

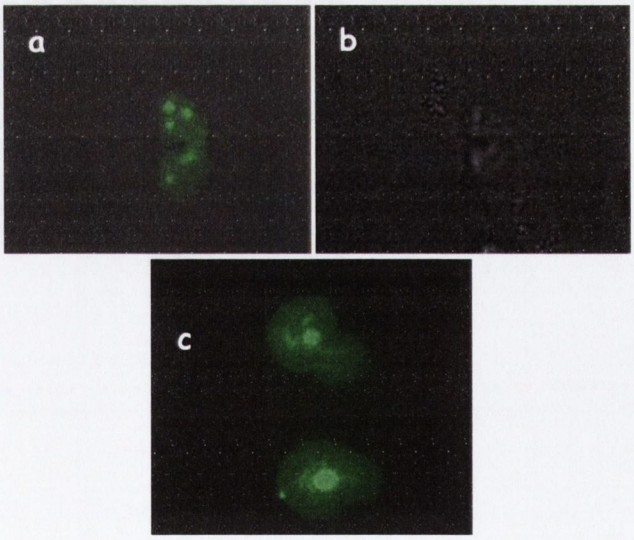


Figure 3.9. Live fluorescent images (**a** and **c**) and phase contract **(b)** of green TGA QDs staining the nucleolus within the nucleus of the THP-1 cells.

The nucleus protects its pool of RNA and ribosomes within the nucleolus. This power-house within the nucleus assembles ribosomal subunits that must make their way through the nuclear pores to the rough ER, to aid protein synthesis in the cytosol. This raises the intriguing possibility that very small green QDs may exploit similar or identical intracellular transport routes that are naturally operating between the nucleolus and the ribosome-rich perinuclear ER.

The factors which may contribute to the uptake, intracellular transport and selective nuclear accumulation of the smaller green CdTe QDs in the macrophages were investigated further. Given the rapid movement of the green QDs within 30 minutes to a nuclear position, the sensitivity of this response was examined in the presence of the nuclear import inhibitor Thapsigargin (Figure 3.10).

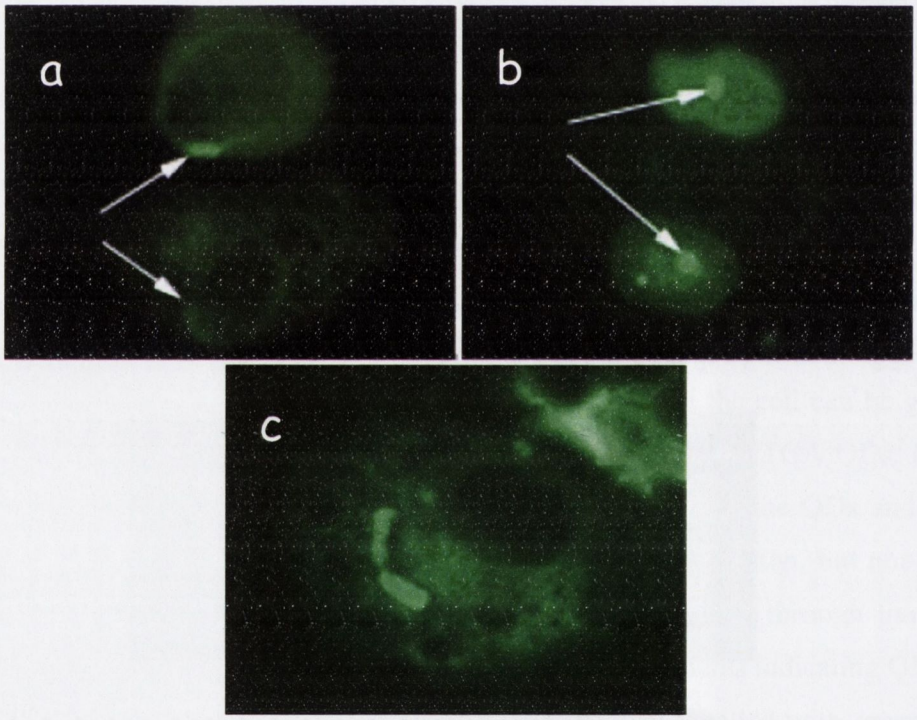


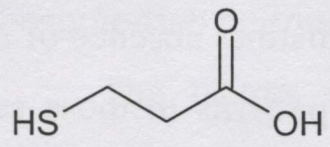
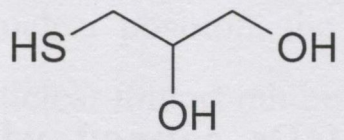
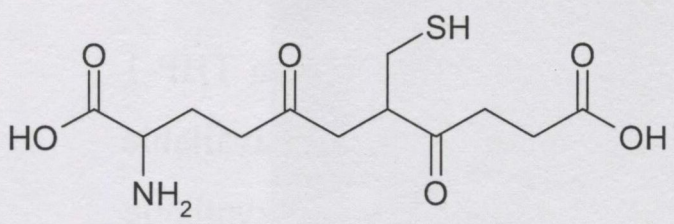
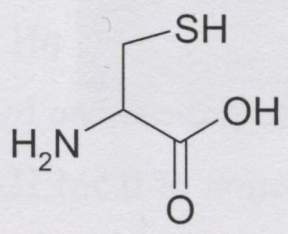
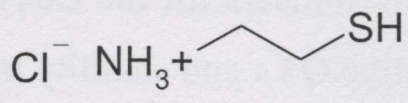
Figure 3.10. (a) Green QDs exhibit an early (10 minute) accumulation around the perinuclear membrane. **(b)** Green QDs penetrate the nucleus and accumulation within the nucleolus is highlighted by intense fluorescence and a circular distribution (arrows). **(c)** Thapsigargin treatment blocks the entry of the QDs to the nucleus and results in only a diffuse cytoplasmic localisation.

Figure 3.10 **a)** demonstrates the rapid accumulation of the green QDs around the perinuclear membrane (highlighted with arrows) after 10 minutes, prior to their accumulation within the nuclei and nucleoli after 30 minutes (Figure 3.10 **b**). To inhibit this nuclear penetration, the cells were then treated before addition of the QDs with thapsigargin which actively blocks the ability of the cell to pump calcium into the endoplasmic reticulum. Treatment with thapsigargin resulted in a distinct absence of any nuclear penetration or localisation by the QDs and gave similar patterns to those seen previously for TGA QDs (Figure 2.19, Chapter 2). The smaller green QDs were now only retained in the sub cellular compartments and the surrounding cytosol.

3.3 Synthesis and characterisation of CdTe QDs capped with commercially available thiol stabilisers

Following on from the exciting results demonstrated by the TGA QDs in THP-1 cells, we synthesised CdTe QDs employing a variety of different commercially available thiol stabilisers with a view to analysing their biocompatibility. Similar synthetic procedures described previously [21] were employed but with some alterations. Briefly, $Cd(ClO_4)_2 \cdot 6H_2O$ and thiol stabiliser were dissolved in millipore water and the pH was adjusted to 11 for a negatively charged but to 6 for a positively charged surface by the addition of a 2M NaOH solution. H_2Te gas, generated from the reaction of 0.5M H_2SO_4 on Al_2Te_3, was then bubbled through the solution. All synthetic procedures, except for cysteamine, where a change in pH was used to induce precipitation, were the same as previously described. Information on commercial thiols used as stabilisers for the CdTe QDs are summarised below in Table 3.1, along with their respective QYs and stability in solution over a period of months when stored at 4° C.

Table 3.1. Commercial thiols used for QD stabilisation, the pH of reaction and the resultant QYs of the QDs obtained.

Thiol Stabilisers used	pH and QY	Stability* after purification & additional comments
3-mercaptopropionic acid (MPA) 	11 and 16%	Stable. Used for or the synthesis of PVC-stabilisers and as chain transfer and cross-linking agents in polymerisation reactions. Can also be used as a reducing agent for organic reactions.
3-mercapto-1,2-propanediol 	11 and 12%	Moderate stablity Has been used for the fabrication of LEDs and as a matrix for mass spectrometry.
glutathione 	11 and 25%	Relatively unstable. Electron-donating capacity linked to its sulfhydryl (-SH) group. Important antioxidant and essential cofactor for antioxidant enzymes. It also provides protection for mitochondria against oxygen radicals.
L-cysteine 	11 and 23% **and** 6 and 10%	Stable. Cysteine is important biologically as an antioxidant, a glutathione precursor, and a natural source of sulfur for metabolism.
2-aminoethanethiol hydrochloride 'Cysteamine' 	6 and 5%	Unstable when purified Antioxidant protecting agent, displays chelating properties, masking heavy metal ions in solution.

*'Stable' means that the colloidal solution remained stable for months when stored under darkness and in air at 4°C. 'Moderate' means that the colloidal solution coagulated occasionally during storage. 'Unstable' means that the colloidal solution coagulated shortly within days or weeks after storage.

To investigate the surface charge of the respective QDs produced according to Table 3.1 (TGA also analysed), an electrophoresis experiment was conducted and the photographic image of the gel taken under exposure to a UV lamp is shown in Figure 3.11.

1. **propanediol**
2. **cysteamine**
3. **mercaptopropionic acid**
4. **thioglycolic acid**
5. **N-acetyl-*L*-cysteine**
6. ***L*-cysteine**
7. **glutathione**

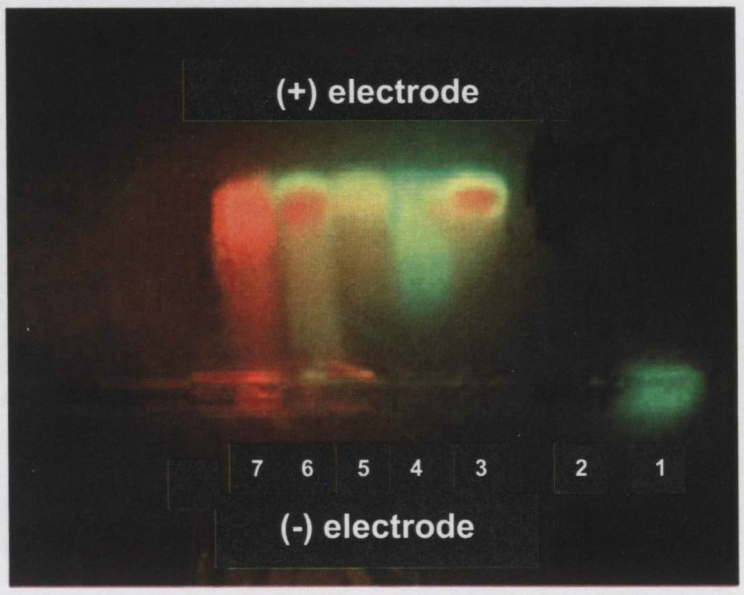


Figure 3.11. Photographic image (under UV lamp) of an electrophoresis experiment containing the CdTe QDs stabilised by the thiols outlined in Table 3.1. **Note:** The cysteamine sample (lane 2) ran slightly towards the negative electrode but decomposed during the process, thus not illuminating under UV excitation.

This experiment confirmed the presence of a negative surface charge for all stabilisers used, except for the positively charged cysteamine and the neutral 3-mercapto-1,2-propanediol. The propanediol QDs in lane 1 show no movement indicating a predominantly neutral surface charge, while the cysteamine QDs in lane 2 decomposed but had previously moved more towards the negative electrode, indicating a positive surface charge.

3.3.1 FTIR spectroscopy of QDs produced using commercially available thiols

IR spectra of the varying stabilisers are directly comparable to their nanocomposite counterparts (Appendix 3 **a-g**). For those stabilisers containing a carboxylic acid group, the main band associated with carbonyl stretch at typically found at approximately 1700 cm^{-1} is distinctly shifted to lower wavenumbers when bound to the crystallite surface; however, no significant shifts are seen for the other functional groups.

Most notably, the characteristic SH stretch found typically at 2550 cm^{-1}, which is clearly visible in the spectrum of the free thiol, disappears in the corresponding nanocomposite spectrum indicating the incorporation of the thiol group onto the surface of the QDs.

3.4 Bioimaging investigations of CdTe QDs stabilised by commercially available thiols

The objective of this work was to evaluate the biological behaviour of a series of thiol capped CdTe QDs in live THP-1 cell studies. A variety of CdTe QDs capped with different thiol ligands (Table 3.1) have been tested to investigate how functional group alteration would impact on the cellular uptake and biocompatibility of the QDs. The CdTe QDs were synthesised directly in water so that no post-preparative treatment, which would result in their size enlargement was required.

We have used the THP-1 monocytic cell line as the basis of our investigations in order to evaluate the potential of the various capped CdTe QDs as imaging agents. THP-1 cells were differentiated to macrophages as described in materials and methods (Chapter 7) and the QDs (particle concentartion 10^{-5} M) [22] were added at a 1 in 100 dilution followed by incubation for the indicated times at 37° C. Vigorous washing with PBS followed the incubation period to detach any loosely bound QDs that have not penetrated or adhered to the cells. Imaging of the QDs in live cell cultures was accomplished *via* a fluorescent microscope. Phase contrasting, where applicable, was used to assess and confirm cell viability and to give a "before and after" overview to help highlight the regions illuminated by the QDs under biological conditions.

3.4.1 3-Mercapto-1,2-propanediol - QDs

Figure 3.11 shows 3-mercapto-1,2-propanediol (diol) stabilised QDs coincubated with the macrophages for 30 minutes at 37° C. These QDs possessed a weak fluorescence with a QY of 10% (Table 3.1), which results in a distinct lack of luminescence intensity when viewed under the microscope. As can be seen from Figure 3.12, the background fluorescence almost masks the QD emission and from what can be detected there is only a minimal particle binding to the cell surface. There was no change following a longer

incubation period and samples frequently photobleached, as a strong laser excitation energy was required to visualise the QDs due to their poor luminescence properties.

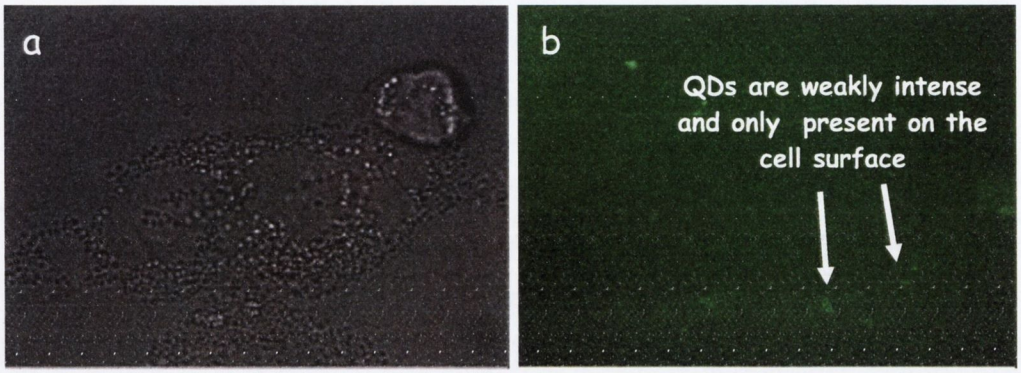


Figure 3.12. Phase contrast (**a**) and fluorescent image (**b**) of 3-mercapto-1,2-propanediol stabilised QDs attached only to the outer membrane the macrophages.

No cell membrane penetration was observed for these diol capped QDs and illumination of the cell structure was only seen for dead or dying cells (Figure 3.13). As a cell dies, its membrane becomes permeable and begins to break down. Consequently, its porosity increases and entities that were previously unable to penetrate can freely pass into the various cytoplasmic compartments.

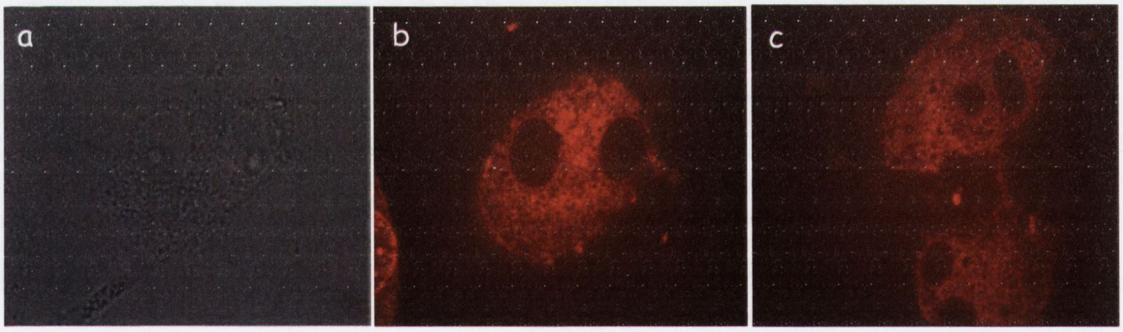


Figure 3.13. Phase contrast (**a**) and fluorescent images (**b** and **c**) of 3-mercapto-1,2-propanediol stabilised QDs entering dead macrophage cells.

Even though these QDs are synthesised at pH 11, following purification they are not as charged those QDs capped by a carboxylic acid. Consequently, they may be described as having a neutral charge (Figure 3.11) and they also do not possess the same high luminescence efficiencies. Indeed, it has been shown the carboxylic acid stabilised

QDs generate increased fluorescence intensities and stabilisation *via* secondary interactions between the carbonyl oxygen with the cadmium atoms on the surface. [23, 24]

Thus, the nature of the stabilising group is crucial not only for luminescence efficiency but also for their biocompatibility. These QDs are practically neutral and are unable to penetrate the cell membrane of the THP-1 cells indicating that charge is a crucial factor in determining the uptake of the QDs.

3.4.2 Glutathione - QDs

Next we investigated glutathione, which possesses a range of amino and carboxylic acid functionalities, as a QD stabiliser (Figure 3.14). These QDs possessed quite high QYs and were clearly visible under the microscope. Interestingly, the glutathione QDs did not display the same long term stability compared to the other stabilisers and readily decomposed after only two weeks. This can be attributed to the size and broad range of functionalities which inhibit efficient stabilisation and promote aggregation of the QDs.

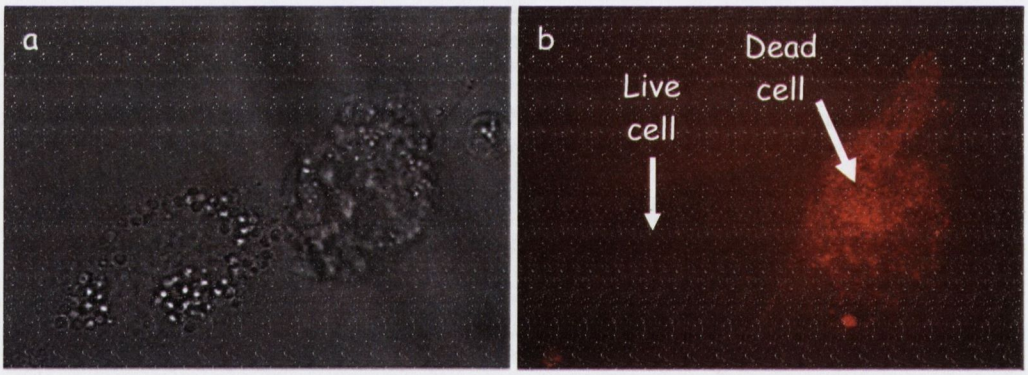


Figure 3.14. Phase contrast (**a**) and fluorescent image (**b**) of glutathione stabilised QDs excluded from live cells and present only inside a dead macrophage cell.

The QDs showed no affinity for the live cells and only displayed an intracellular localisation in dead or compromised cells. Repeated experiments proved unsuccessful and the lack of cell uptake could be due to the instability of the QDs which may be accelerated upon interaction with the growth medium, particularly once irradiated with the laser. This may cause a destabilisation and an aggregation of the QDs, thus preventing

them penetrating the cell membrane; however, recent work has shown that glutathione has potential for QD stabilisation and cell membrane penetration. [25, 26]

3.4.3 Cysteamine - QDs

The next QD sample investigated with the THP-1 cells were cysteamine stabilised (Figure 3.15). These QDs possess a predominantly positive surface charge and are soluble due to the presence of a protonated amine group. Unfortunately, this stabiliser proved to be the most problematic in terms of purification. Addition of the non-solvent isopropanol did not result in any turbidity and the QDs were extremely stable to centrifugation. It was noted that at higher pH values of 6 - 6.5 where the amine is no longer protonated, the QDs crashed out of solution. Thus, addition of a small amount of NaOH resulted in the precipitation of all of the QDs, which were then isolated from the precursor solution by centrifugation and could be redissolved once the pH was returned to between 5.5 and 6. Thus, no-size selective precipitation was possible as the QDs all crashed out together. This gave broader size distributions, with FWHM of 44 - 46 nm for the cysteamine QDs, when compared to those samples with values of 38 – 40 nm when purified by size selective precipitation. However, following this procedure, the QDs frequently decomposed as changing the pH invariably alters the stability of their ligand shell and increased inter particle interactions leading to agglomeration and decomposition.

As can be seen in Figure 3.15, upon addition and coincubation of the cysteamine capped QDs with the cells, only a binding to the outside of the cell membrane was observed, even after several washings. While the QDs displayed good luminescent properties, no membrane penetration or detectable cytoplasmic localisation was observed even after longer incubation periods. Cell viability was also not affected as assessed by cell shape and fragmentation; however, this can be attributed to the lack of membrane penetration.

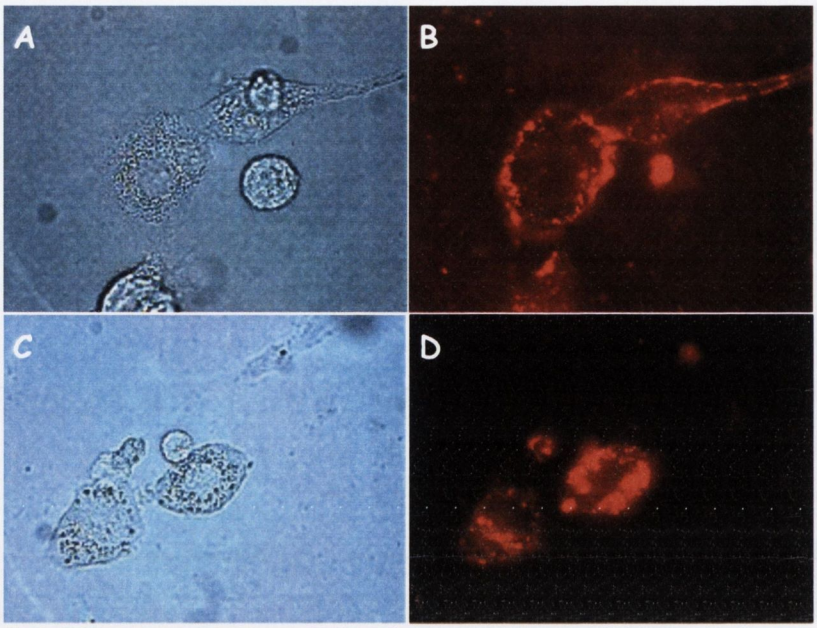


Figure 3.15. Phase contrast (**a** and **c**) and corresponding fluorescent images (**b** and **d**) of cysteamine stabilised QDs adhering only to the outer membrane of the macrophages.

Cell death, judged by cell morphology, membrane blebbing or irregular patterning on the cell surface and loss of cell attachment to the substrate, is associated with a significant increase in cell permeability. As this does not happen, it can be concluded that binding to the outside of the cells was not detrimental to the health of the cells. As seen in Figure 3.15 (**a** and **b**), the cell looks more elongated when compared to the cells in image (**c** and **d**) which are more rounded. While the cells in Figure (**c** and **d**) are live, the elongated shape seen in Figure (**a** and **b**) is due to cell migration and gives a clear indication that cell behaviour is not adversely affected upon coincubation with the QDs.

The penetration of QD and cationic liposome complexes has been investigated by Derfus *et al.* [6] Although QD uptake was detected, they rapidly agglomerated making subsequent trafficing impossible. This was circumvented somewhat *via* microinjection, but this technique is not feasible for a large quantity of cells as it requires an individual cell injection and is extremely tedious and time consuming.

The THP-1 cells, do subsequently, become permeable to the cysteamine capped QDs after fixing (using 3% formaldehyde followed by 1% TritonX100) as shown in Figure 3.16.

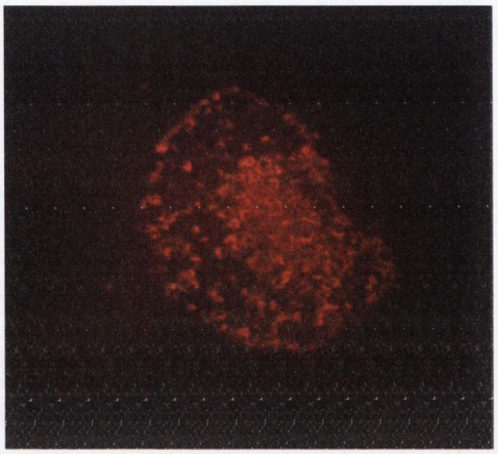


Figure 3.16. Fluorescent image of a dead THP-1 cell, which is now highly permeable showing the uptake of the previously excluded cysteamine QDs.

For fixed cells, analogous to those that are dead or dying, the membrane envelope becomes increasingly porous towards the surrounding medium and the accumulation of these positively charged QDs which previously displayed no cellular compartmentalisation, can now be seen (Figure 3.16).

As shown, in comparison to TGA QDs (Chapter 2), positively charged QDs do not display any membrane penetration of healthy living cells. Thus, it seems plausible to investigate if QDs possessing a mixed functionality on their surface, such as amine and carboxylic acids would exhibit any cell penetration and if this dual functionality has any specific influence on the probability of the QDs being taken up by the cells.

3.4.4 *L*-cysteine - QDs

Accordingly, *L*-cysteine stabilised QDs were synthesised and coincubated with the THP-1 cells as shown previously (Figure 3.17).

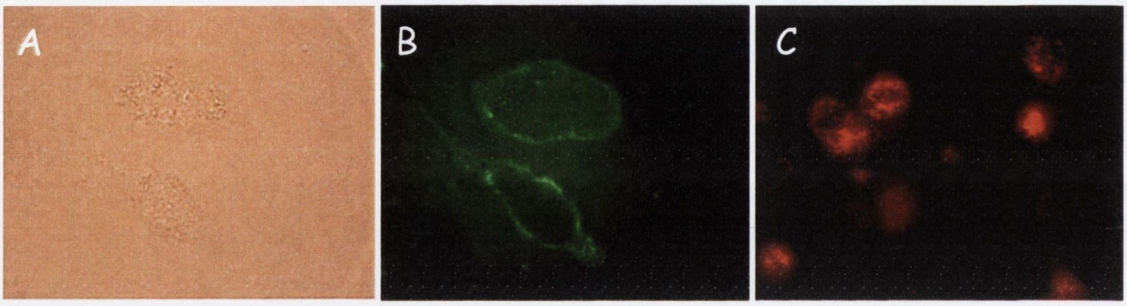


Figure 3.17. Phase contrast (**a**) and fluorescent image of green *L*-cysteine (**b**) and also red *L*-cysteine (**c**) stabilised QDs adhering to the outer membrane of the macrophages.

Figure 3.17 shows the phase contrast (**a**) and fluorescent images (**b**, **c**) of green and red *L*-cysteine stabilised QDs respectively after 30 minutes of incubation with the cells. As can be seen from images (**b** and **c**), enhanced clustering of the QDs was observed, in particular around the outer membrane of the cells. This is more localised for the smaller QDs, while the larger red QDs show a diffuse binding all around the cells outer membrane. Confocal 3-D imaging revealed that no localisation within the cytoplasm was observed.

These QDs are synthesised at pH 11 to promote a negative surface charge, those synthesised at pH 6 also showed no cell penetration. However, no visible sub-membrane emission was witnessed indicating that the mixed functionality of the *L*-cysteine stops any trans-membrane penetration or localisation within the cytoplasm. Size also does not play any significant role, as both small (green) and larger (red) QDs show similar extra-cellular patterning.

Thus, the presence of the free amine group (as has also been witnessed for cysteamine capped QDs, Figure 3.15) must in effect counteract the mechanisms leading to bi-lipid membrane penetration. One possibility is that this group, even at basic pH values, may cause clustering of the QDs rendering them unable to penetrate due to agglomerate size. The action of the amino group itself with the various surface receptors also remains a strong possibility.

As has become apparent over time, the penetration of cellular membranes only seems to occur for wholly negatively charged QDs and for those possessing an appropriate functionality. Positively charged amino containing QDs do not enter the cells even when gelatin has been used as a co-capping agent. For further analysis of this observation see Chapter 4.

It is also quite interesting to analyse the fact that at different pH values, substantial differences are observed for the QYs of *L*-cysteine QDs. *L*-cysteine QDs synthesised at pH 6 to promote a positively charged surface only show QYs in the region of 10%, quite low when compared to 23% for those produced at pH 11. This also ties in with the fact that cysteamine capped QDs never reach the same values as their carboxylic acid capped counterparts. There may be a number of reasons for this.

As shown previously, the carbonyl oxygen plays a significant role in the additional stabilisation and capping of the QD surface [23] (Figure 1.11). This process must be somewhat hindered due to the mixed functionality present, resulting in a poorer passivation of the surface. This may lead to QD clustering in solution and a significant drop in their fluorescence intensities. There may also be an electrostatic or H-bonding attraction between the mixed functionalities of different QDs in the same ensemble, resulting in their aggregation and possible quenching of their luminescence.

3.4.5 N-acetyl-*L*-cysteine - QDs

In an attempt to remove the impact of the amino group, N-acetyl-*L*-cysteine (acetyl derivative of *L*-cysteine) (NAC, Figure 3.18) has been employed as the stabiliser under the same reaction conditions as before.

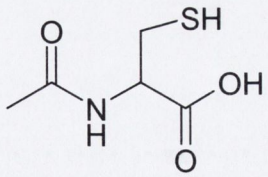


Figure 3.18. Structure of N-acetyl-*L*-cysteine (NAC).

NAC is a powerful antioxidant and acts to support the immune system by helping to neutralise free radicals. It can be taken orally as a dietary supplement and helps increase glutathione synthesis, which is the most abundant and effective cellular

antioxidant. It has been shown recently by Lovrić *et al.* [12, 27] that NAC can also aid in the reduction of the detrimental effects of QDs on cells. These authors have investigated the generation of reactive oxygen species (ROS), which are known to contribute to cell death by QDs in living tissues. They found that NAC reduced the concentration of ROS, induced the synthesis of glutathione and increased QD surface passivation. The production of ROS by CdSe QDs has also been shown by Green and Howman [28] and they attribute both surface and light generated radicals as the cause of DNA nicking.

Consequently, if NAC could be bound to the surface of the QDs, it would be interesting to see if it maintained its positive effect on the system. These NAC capped QDs were produced at a pH of 11 and 6 but the possible lability of the acetyl bond remains problematic and it may be broken at basic pH values under reflux conditions. Those QDs synthesised at pH 11, demonstrated similar behaviour to QDs capped with *L*-cysteine as shown before, but those produced at pH 6 demonstrated an enhanced capacity for cell labelling (Figure 3.19).

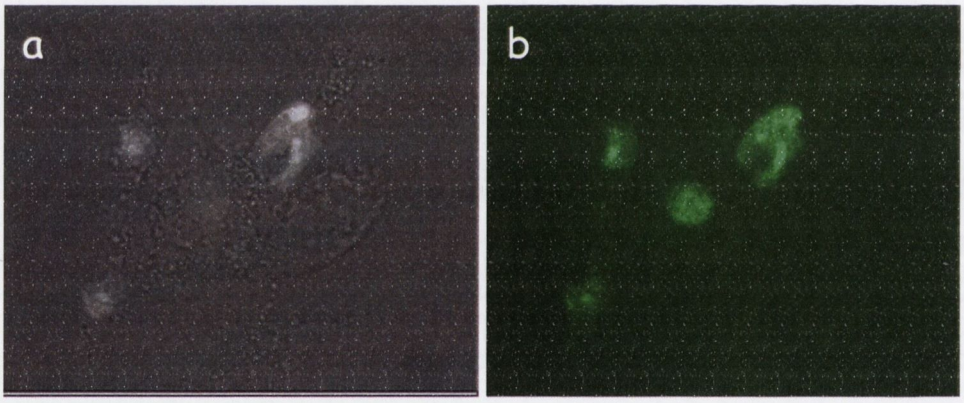


Figure 3.19. (**a**) Phase contrast and (**b**) fluorescent image of green N-acetyl-*L*-cysteine QDs penetrating the outer membrane of THP-1 cells.

Figure 3.19 shows the NAC stabilised QDs present in the cytoplasm of the THP-1 cells. These QDs appear green due to the filter used, but no nuclear localisation was observed. Thus, as they displayed promising labelling capacities, smaller QDs were also investigated. It must be stressed that these results were not fully reproducible and only certain fractions from the parent solution resulted in cell and nuclear penetration (Figure 3.20). This can possibly be attributed to the lability of the acetyl bond, not only to the

synthetic conditions, but also to the purification procedure. This will be further analysed in future investigations to confirm the stability and effectiveness of NAC when utilised in this system.

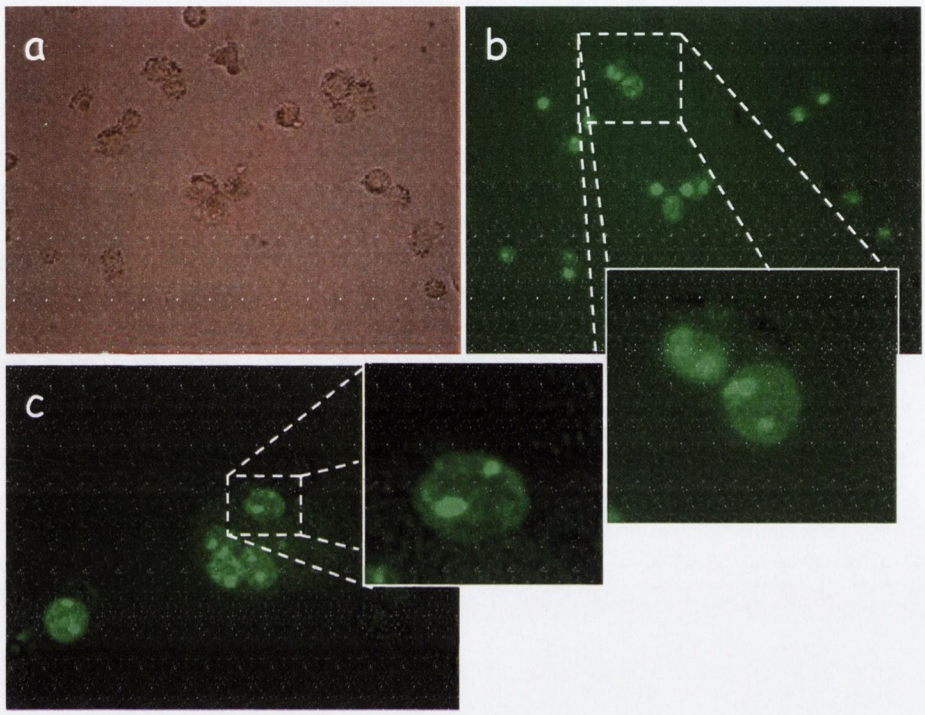


Figure 3.20. (**a**) Phase contrast and (**b**, **c**) fluorescent images of green N-acetyl-*L*-cysteine QDs penetrating the nucleus of THP-1 cells.

Figure 3.20 shows the nuclear and cytoplasmic localisation of small NAC QDs. This cytoplasmic distribution is due to a variety of sizes within the sample. Thus, protection of the amino group allows for the passage of the NAC QDs into the cells and also the nucleus. This observed penetration and accumulation of the QDs within the cells reinforces our previous findings that both charge and size do indeed play a crucial role in the uptake of QDs.

3.4.6 MPA - QDs

Mercaptopropionic acid (MPA) stabilised QDs have been tested similarly to those above. We expected that MPA stabilised QDs should act in an analogous manner to those with TGA, which has already been shown to exhibit excellent intracellular penetration. It

has an extra carbon (CH_2 group) in the chain, but still possesses the ability to coordinate in a secondary manner through a six membered ring to the thiol binding cadmium atom (Chapter 4, Figure 4.2) In an effort to reproduce the same nuclear localisation as their TGA counterparts, small, 2 – 2.5 nm MPA QDs were synthesised and coincubated with the THP-1 cells (Figure 3.21).

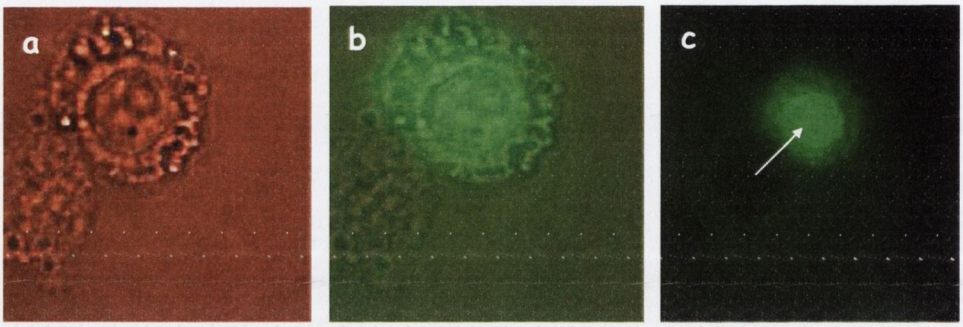


Figure 3.21. Phase contrast (**a**) and subsequent fluorescent images (**b-c**) of MPA QDs in THP-1 cells. Image (**b**) illustrates (following a short incubation time) the plan view of the cell showing both an intra and outer nuclear accumulation of the QDs while image (**c**) (longer incubation) illustrates the accumulation of QDs in the nucleolus (arrow).

Following only a short coincubation time of 10 minutes, the MPA QDs are seen to rapidly penetrate the cell membrane and accumulate within the cytoplasm. Longer incubation times also revealed a nuclear penetration (Figure 3.21, **c**) and show the accumulation of the QDs in the nucleolus, in a similar manner seen previously for TGA QDs (Figure 3.20). Thus, the extra carbon of MPA has no effect on the optical properties of the QDs and no change in their cellular activity with respect to TGA can be seen.

Previously, size variations in TGA QDs were shown to have a dramatic effect on their distribution within the THP-1 cells. This process of selective accumulation of the differently sized QDs in various cellular regions was also noted for MPA QDs. (Figure 3.22).

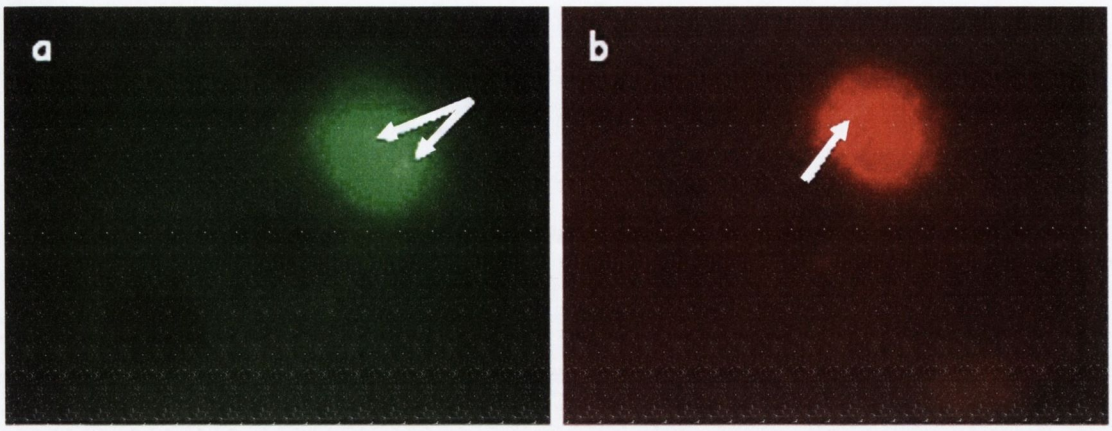


Figure 3.22. Fluorescent images [**a)** green filter, **b)** red filter] of a THP-1 cell incubated with an MPA QD sample containing a mixture of sizes. Small, green QDs are seen to predominantly accumulate within the nucleoli (arrows) while larger, red QDs remain predominantly outside the nuclear periphery (arrow).

From Figure 3.22 it is clear that the smaller green QDs can penetrate into the nucleus, while the larger red ones stay mainly around the nuclear membrane and in the cytoplasm. This certainly reinforces the fact that both TGA and MPA possess the right characteristics needed both for cell and nuclear membrane penetration. It also confirms that size does indeed play a crucial role in the uptake and distribution of these nanoparticulate materials within this cell line.

3.5 Conclusions

A range of CdTe QDs have been successfully synthesised using a variety of commercially available thiols (Table 3.1), in an effort to analyse and characterise the effect that altering the QD functionality has on their biocompatibility with THP-1 cells. While much work has been conducted into the synthesis and photophysical properties of QDs, little has been undertaken to evaluate the factors that enable cells to uptake QDs. We have shown that charge and functionality play crucial roles in QD uptake and sequestration within living cells, thus influencing their ability to be used as biological imaging contrast agents.

Fluorescent microscopy has proved an excellent tool for investigation and analysis of cell cultures coincubated in the presence of the various QD solutions. Tests

have shown that neutral QDs, capped with 3-mercapto-1,2-propanediol do not show any affinity for the cells until they were dead or dying at which point they become porous and allow the QDs to enter. A similar type of behaviour was recorded for glutathione QDs and they were unable to penetrate the cell membrane possibly due to size effects.

Following on from this, we have shown that there is a definitive link between QD charge and uptake. Positively charged cysteamine capped QDs do not enter healthy cells but readily form agglomerates and only stick to the outside of the cell membrane. This does not seem to adversely affect cell vitality or motility. To investigate if a mixed functionality would improve QD uptake, *L*-cysteine capped QDs were tested and displayed similar extracellular staining analogous to the cysteamine capped QDs. This suggests that not only charge but also surface functionality is crucial for successful uptake. Consequently, N-acetyl-*L*-cysteine capped QDs were synthesised with the amino functionality now protected and they demonstrated the ability to not only enter the cells but also to penetrate the nucleus, highlighting the nucleolus. Thus, the role of the amino group is crucial for QD – cell biocompatibility. This is a topic that will require much work in the future to determine the nature of the interactions.

The most promising and exciting results were obtained for TGA and MPA QDs. These both have carboxylic acid moieties on their surface and are negatively charged species. Following on from the previous results, we have shown that parallel to charge, the size of the QDs that are taken up by the cells also dictates their ability to accumulate within certain regions of the cells. Small, 2 nm QDs accumulated in the nuclei while larger 4 nm QDs stayed predominantly in the cytoplasm with some accumulation at the nuclear membrane.

As seen, dead or fixed cells, which are highly permeable also show the same behaviour and readily take up extra cellular moieties present in the surrounding medium due to membrane bleeding and increased pore size. This is not the case with live cells and clearly demonstrates that, contrary to the passive diffusion mechanisms that operate in dead or fixed cells, active selection processes must function at both the cell and nuclear membranes. This ability to deliver a specific sized particle to the nucleus has implications for the development of compounds that could potentially target DNA, its replication or even protein synthesis. It may also allow for the selective accumulation of cytotoxic

agents within the nuclear compartments for potential therapeutic use, eg. cancer therapy. However, this research area is just its initial stage and there is no clear understanding of all processes taking place at the molecular and cellular level. Therefore further detailed biological studies are necessary to understand the mechanisms of penetration and localisation of QDs in live cells.

This study demonstrated a selective uptake and accumulation of QDs into subcellular compartments of THP-1 cells. This may raise the possibility of using size selective targeting of labelled or conjugated QDs to intracellular structures in viable human cells. The ability of cells derived from a monocyte macrophage lineage to internalise the QDs raises the possibility that macrophages present in the respiratory system may also react in the same way. This research highlights the importance of strict environmental control of nanoparticulate material. The ability to deliver and target QDs to intracellular sites will further facilitate the application of these materials as potential site-specific bioimaging and drug delivery agents.

References

[1] M. Bruchez, Jr., M. Moronne, P. Gin, S. Weiss, A. P. Alivisatos, *Science* **1998**, *281*, 2013.

[2] W. C. Chan, S. Nie, *Science* **1998**, *281*, 2016.

[3] E. Klarreich, *Nature* **2001**, *413*, 450.

[4] A. P. Alivisatos, *Science* **1996**, *271*, 933.

[5] R. Weissleder, *Nat. Biotech.* **2001**, *19*, 316.

[6] A. M. Derfus, W. C. W. Chan, S. N. Bhatia, *Adv. Mater.* **2004**, *16*, 961.

[7] M. Kondoh, S. Araragi, K. Sato, M. Higashimoto, M. Takiguchi, M. Sato, *Toxicol.* **2002**, *170*, 111.

[8] L. E. Rikans, T. Yamano., *J. Biochem. Molec. Tox.* **2000**, *14*, 110.

[9] A. Nel, T. Xia, L. Madler, N. Li, *Science* **2006**, *311*, 622.

[10] A. Hoshino, K. Fujioka, T. Oku, M. Suga, Y. F. Sasaki, T. Ohta, M. Yasuhara, K. Suzuki, K. Yamamoto, *Nano Lett.* **2004**, *4*, 2163.

[11] A. M. Derfus, W. C. W. Chan, S. N. Bhatia, *Nano Lett.* **2004**, *4*, 11.

[12] J. Lovrić, H. S. Bazzi, Y. Cuie, G. R. A. Fortin, F. M. Winnik, D. Maysinger., *J. Mol. Med.* **2005**, *83*, 377.

[13] C. Kirchner, T. Liedl, S. Kudera, T. Pellegrino, A. MunozJavier, H. E. Gaub, S. Stolzle, N. Fertig, W. J. Parak, *Nano Lett.* **2005**, *5*, 331.

[14] E. Chang, N. Thekkek , W. W. Yu, V. L. Colvin, R. Drezek, *Small* **2006**, *2*, 1412.

[15] S. J. Byrne, Y. Williams, A. Davies, S. A. Corr, A. Rakovich, Y. K. Gun'ko, Y. P. Rakovich, J. F. Donegan, Y. Volkov, *Small* **2007**, *3*, 1152.

[16] J. Politz, C., *Trends in Cell Biol.* **1999**, *9*, 284.

[17] A. Miyawaki, *Dev. Cell* **2003**, *4*, 295.

[18] W. C. W. Chan, D. J. Maxwell, X. Gao, R. E. Bailey, M. Han, S. Nie, *Curr. Op. Biotech.* **2002**, *13*, 40.

[19] T. Sugimoto, G. E. Dirige, A. Muramatsu, *J. Colloid Interface Sci.* **1996**, *182*, 444.

[20] Z. Tang, B. Ozturk, Y. Wang, N. A. Kotov, *J. Phys. Chem. B* **2004**, *108*, 6927.

[21] N. Gaponik, D. V. Talapin, A. L. Rogach, K. Hoppe, E. V. Shevchenko, A. Kornowski, A. Eychmüller, H. Weller, *J. Phys. Chem. B* **2002**, *106*, 7177.

[22] W. W. Yu, L. H. Qu, W. Z. Guo, X. G. Peng, *Chem. Mater.* **2003**, *15*, 2854.

[23] H. Zhang, Z. Zhou, B. Yang, M. Y. Gao, *J. Phys. Chem. B* **2003**, *107*, 8.

[24] I. G. Dance, M. L. Scudder, R. Secomb, *Inorg. Chem.* **1983**, *22*, 1794.

[25] H. Qian, C. Dong, J. Weng, J. Ren, *Small* **2006**, *2*, 747.

[26] Y. Zheng, S. Gao, J. Y. Ying., *Adv. Mater.* **2007**, *19*, 376.

[27] J. Lovrić, S. J. Cho, F. M. Winnik, D. Maysinger, *Chem. Biol.* **2005**, *12*, 1227.

[28] M. Green, E. Howman, *Chem. Comm.* **2005**, 121.

Chapter 4: "Jelly dots" Synthesis and cytotoxicity studies of CdTe QD - gelatin nanocomposites

4.1. Introduction

The fabrication of novel nanomaterials using QDs as an intricate component has gathered momentum over the past number of years. [1-5] Extensive research has been conducted into the synthesis and characterisation of various forms of QDs, [6-8] with significant work focussing on their capping by a wider band gap material [9, 10] or various biomolecules. [11-15] These investigations have all looked to improve QD quantum efficiency and biocompatibility *via* encapsulation. Considering the potential of encapsulated QDs in various cell labelling and tracking applications, little work has been undertaken using biocompatible polymers as co-capping agents.

Matrices have been analysed recently, with explorations into the use of poly (methylmethacrylate) and polystyrene. [2] Stability, aggregation and quenching are some of the problems which can occur following transfer of the QDs from an aqueous to organic media and have recently been overcome by Zhang *et al.*, [16] who used octadecyl-p-vinyl benzydimethlammonium chloride (OVADC) as a transfer surfactant. Styrene monomers and radical polymerisation were then used to generate CdTe-polystyrene nanocomposites. Lorenz *et al.* [17] have also looked at how functionalisation of fluorescent-labelled polymeric particles in different cell lines, including stem cells, affect particle uptake.

The use of polyelectrolytes [18] during the production of QDs and also as components of layer by layer systems has been the subject of much interest. [19-21] A polyelectrolyte possessing a positive backbone, for example PDDA (Poly(diallyldimethylammonium chloride), has been shown to increases QY values by up to 30 times for MPA capped CdSe QDs, [18] while work in our group has also investigated differently charged CdTe QDs adsorbed onto polyelectrolyte multilayers and found enhancements of up to 31 times also. [22]

With a view to using QDs in biological systems, a more bio-friendly polymer in needed. As such, we have incorporated gelatin into the QD synthesis. The use of gelatin

has been explored for the production of CdS QDs by Sugimoto *et al.* [23] In this work, they comment on the striking effect that gelatin has as a protective agent against coagulation of the growing CdS nanoparticles, but do not refer to any influence it may have on the particle growth mechanisms. CdSe QDs have also been investigated. [24-26] Xu *et al.* [24] compared gelatin coated and sodium dioctyl sulfosuccinate (AOT) capped CdSe QDs but found the organic AOT QDs exhibited higher QYs than the gelatin QDs due to better passivation. Raevskaya *et al.* [25] used concentrated gelatin solutions of between 1 and 15% with sodium polyphosphate [26] and no additional capping agent. They found that the gelatin did influence the production and stability of the CdSe QDs and that reaction ratios and temperature were crucial.

However, no in-depth investigations into the use of gelatin as a capping moiety have been carried out for CdTe QDs. Furthermore, no investigations utilising gelatin to reduce any toxicity related phenomena arising from the incubation of QDs with live cells have been conducted.

Gelatin, also known as E441, is a tasteless and odourless substance that has become commonplace in everyday life and is used extensively in the food, pharmaceutical, photography and cosmetic manufacturing industries. It is a biocompatible, thermo responsive polymer and is prepared by the thermal denaturation of collagen, an abundant protein in the connective tissues of mammals, which can be obtained from animal skin and bones and fish skin. This process is undertaken in harsh acidic conditions. Consequently, when gelatin is dissolved in water, it actively reduces the pH of solution. Gelatin dissolves partially in cold water and completely once the water is heated to approximately 35° C, giving rise to a "gelling" effect if its concentration is high enough.

Gelatin is 98% protein, containing many single or multi-stranded polypeptides, predominantly the non-essential amino acids glycine ($HO_2CCH_2NH_2$) and proline ($HO_2CCH(NH[CH_2]_3)$), which provide a multitude of functional atoms available to interact with extraneous moieties. Its structure is shown in Figure 4.1.

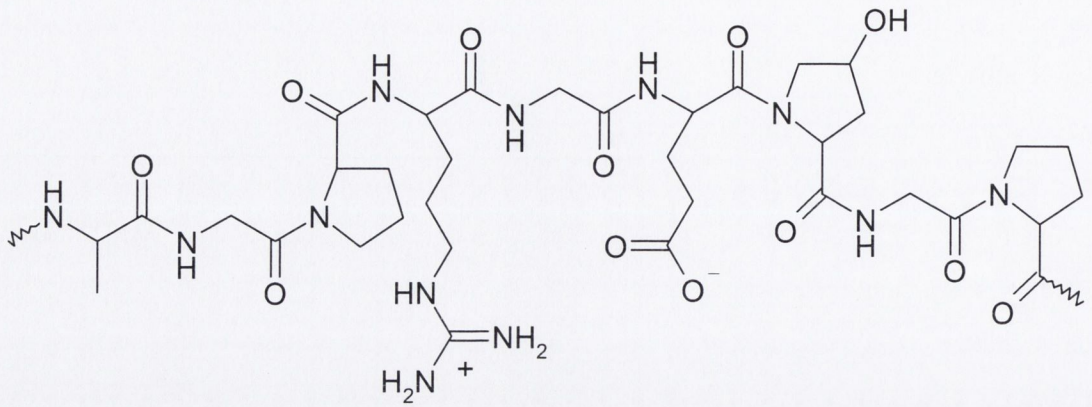


Figure 4.1. Fragment from the structure of gelatin illustrating the various functional groups and charged atoms present along the backbone.

As can be seen from its structure in Figure 4.1, gelatin possesses a wide variety of groups, including carbonyl, amine and alcohols, which are available to interact with the surface of the QDs. There are also different charges present along the polymer backbone, making it ideal for interacting with the charged thiol groups that are bound to the QD surface, any unsaturated atoms or surface dangling bonds. It has been shown by Zhang *et al.* [27] that the interaction of carboxylic acid polymers results in an increase in the luminescence properties of QDs by coordination with the surface cadmium atoms not already passivated with a thiol molecule. Gao *et al.* [28] and Dance *et al.* [29] have also previously investigated the secondary binding between the carbonyl oxygen of the stabiliser molecules and the surface cadmium atoms (Figure 4.2), while Zhang *et al.* [30] have postulated that the carbonyl oxygen may adsorb a free cadmium ion from solution and effectively place it in a tellurium site, thus reducing the number of unsaturated surface atoms.

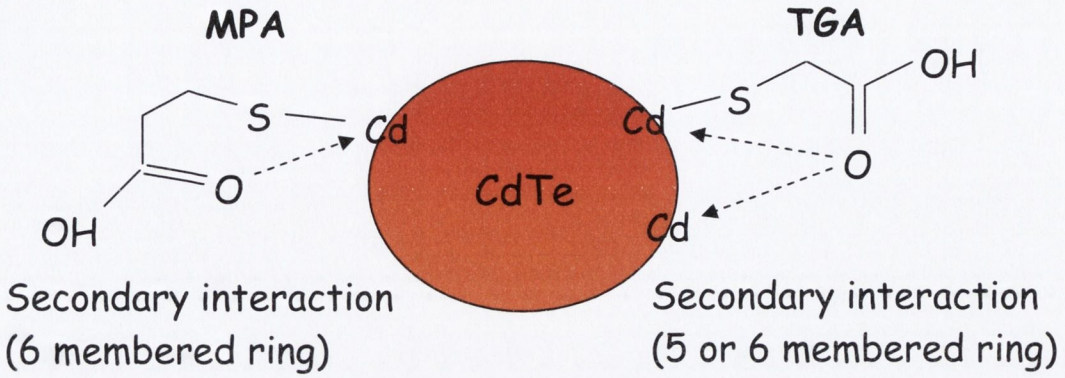


Figure 4.2. Graphical illustration of the secondary interactions occurring on the surface of TGA [both 5 and 6 membered ring interactions possible] and MPA [6 membered ring interactions] stabilised CdTe QDs.

Similarly for gelatin, these interactions may occur, but there is also the possibility of further binding due to the positively charged amino functionalities. These moieties may interact with the carboxylic acid groups of the capping molecules *via* both electrostatic and hydrogen bonding. This could provide further stabilisation, not only to improve the emissive response by reducing the number of non-radiative pathways available but also to enhance the stability of the QD surface by increasing the stability of the Cd-thiol interaction. The thiol capping shell is quite labile to external influences such as changes in the pH of solution or chemical interactions with other molecules, which often results in the aggregation and subsequent degradation of the QDs. On a positive note, this instability lends itself to the formation of new structures such as nanowires [31-33] or tetrapods. [34, 35] With all of these possible influences in mind, we decided to undertake a series of experiments to investigate and contrast the effect that gelatin would have on the stability, spectroscopic properties and biocompatibility of the QDs in solution.

4.2 Preparation and characterisation of TGA – gelatin nanocomposites

4.2.1 Addition of gelatin to TGA capped QDs

Initially, we spectroscopically analysed the effect of adding gelatin to a pre-prepared solution of TGA capped QDs. Thus, a solution (2 ml) of QDs of known concentration [36] was prepared and aliquots of gelatin (0 - 250 µl) taken from a 1 g / 20 ml solution were added (Figure 4.3).

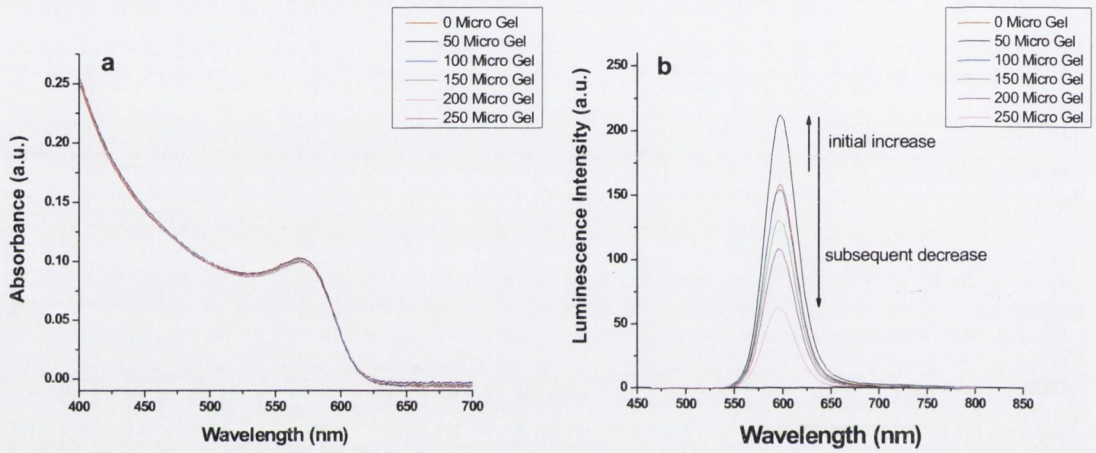


Figure 4.3. a) UV-vis absorption and **b**) normalised luminescence emission spectra (λ_{ex} 450 nm) for the addition of 0, 50, 100, 150, 200 and 250 µl of a 1 g / 20 ml solution of gelatin in water to a purified TGA capped QD solution.

Figure 4.3 shows **a)** the UV-vis absorption and **b)** the luminescence emission spectra (λ_{ex} 450 nm) for a solution of TGA capped CdTe QDs following the addition of 0, 50, 100, 150, 200 and 250 µl of a 1 g / 20 ml solution of gelatin in water. As can be seen from the absorption spectrum **(a)**, there is no structural change throughout the entire addition process indicating that no precipitation or detrimental effects have occurred to the QDs. Therefore, any changes must be occurring on the QD surface. The emission spectrum **(b)** shows an initial increase of 35% upon addition of 50 µl of the gelatin solution; however, subsequent additions resulted in a sequential decrease in intensity of 75% and a change of solution colour. This decrease in emission intensity results as a consequence of a gelatin mediated drop in pH.

Due to its preparation in an acidic environment, the addition of a large quantity of gelatin results in a drop in pH and this gives rise to a quenching of the QD luminescence and their eventual precipitation. [37] Consequently, the volume of gelatin solution added was reduced and the QDs were re-dissolved in a tris HCl buffer (pH 11) instead of water to help negate any effect of pH reduction. The same procedure as stated above with these slight modifications was implemented and the resultant spectra are shown in Figure 4.4.

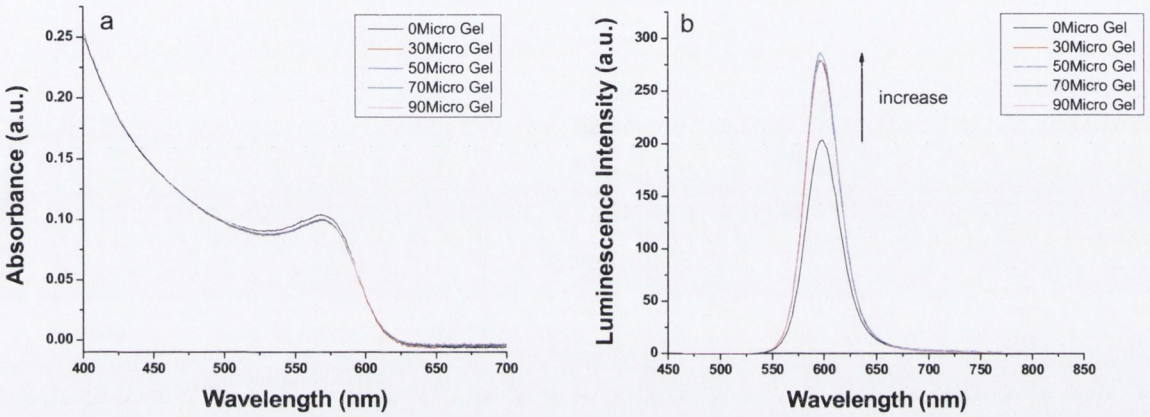


Figure 4.4. a) UV-vis absorption and **b**) normalised luminescence emission spectra (λ_{ex} 450 nm) for the addition of 0, 10, 30, 50, 70 and 90 µl of a 0.1 g / 20 ml solution of gelatin in water to a purified CdTe QD solution in tris-HCl buffer (pH 11).

Once again, no discernable changes are noted for the absorption maxima (Figure 4.4 **a**) indicating the integrity of the QDs remains unaltered; however, we do witness a significant change in the luminescence emission (Figure 4.4 **b**) Upon addition of the first 30 µl aliquot of gelatin solution, there is an approximate 35% increase in intensity and this does not change significantly upon subsequent additions. This indicates that the gelatin has acted as an additional co-capping agent for the increased passivation of the QDs, giving rise to a higher rate of radiative recombination. As there are no unfavourable decreases in intensity like those seen in the previous experiment, it can be deduced that the reduced gelatin concentration and use of buffer prevent any drop in pH of the solution, thus maintaining the integrity and high quantum efficiency of the sample. These experiments proved that the addition of gelatin results in significant increases in the luminescence efficiency of CdTe QDs.

4.2.2 Addition of gelatin to MPA capped QDs

In parallel experiments, gelatin was also added to pre-prepared MPA capped QDs under the same conditions and a range of samples with different sizes were analysed. As before, UV-vis absorption data remained unchanged (data not shown) but significant increases were noted for the emission spectra (Figure 4.5).

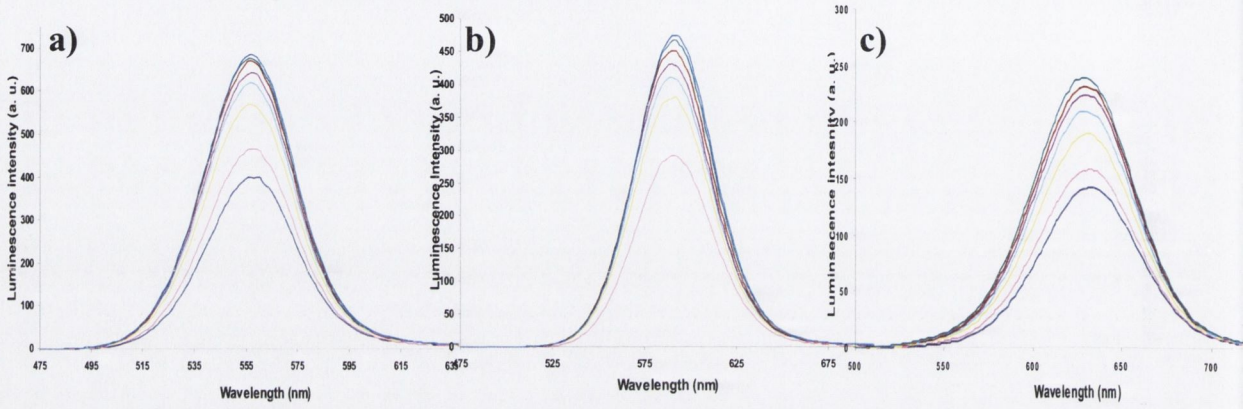


Figure 4.5. Luminescence emission spectra (λ_{ex} 450 nm) for the addition of gelatin (0.1 g / 20 ml buffer) to three different sizes of MPA QDs [**a** – λ_{em} 555 nm, **b** – λ_{em} 590 nm, **c** – λ_{em} 630 nm].

In a similar manner to those TGA QD experiments above, significant luminescence increases of between 60 and 70% were noted across the range of different sized MPA capped QDs (Figure 4.5). This shows that the behaviour of gelatin as a co-capping agent does not vary with respect to the size of the QDs.

These changes in the spectroscopic properties now raise the questions; 1) can gelatin be successfully incorporated *in situ* into the preparation of the QDs and 2) will it impart the same positive influences on the emission intensity that we have seen previously?

Nanocrystal synthesis proceeds *via* an initial nucleation which is then followed by a growth stage and the Ostwald ripening process. [8, 38-40] To investigate if the introduction of gelatin *in situ* could enhance theses processes, we carried out a series of experiments adding gelatin to the precursor reaction solution that has been used previously for the production of CdTe QDs. [41]

4.2.3 Preparation and characterisation of gel-TGA-QDs at 1.75:1 TGA : Cd ratio

Briefly, 0.5 g gelatin was added to a solution of $Cd(ClO_4)_2 \cdot 6H_2O$ and TGA stabiliser which was bubbled with argon for 1 hour. Following the addition of gelatin, the pH was subsequently adjusted to 11 with 2M NaOH. H_2Te gas generated from the reaction of H_2SO_4 and Al_2Te_3 was bubbled through the reaction mixture for 10 minutes and refluxed. Sample aliquots were taken at various time intervals, 15, 30, 40, 55, 70, 85, 100, 130 and 160 minutes, after the start of heating and were spectroscopically characterised. These data were then compared to a sample that did not contain any gelatin and was prepared under the same conditions. Comparative spectra are shown in Figure 4.6.

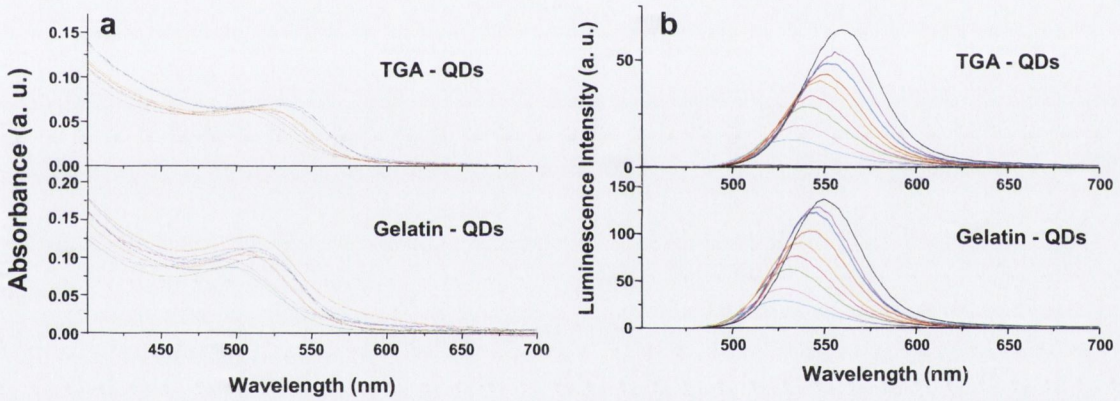


Figure 4.6. a) UV-vis absorption and **b**) normalised luminescence emission spectra (λ_{ex} 425 nm) of TGA capped and gel-TGA-QDs prepared under the same conditions. Sample aliquots were taken at 15, 30, 40, 55, 70, 85, 100, 130 and 160 minutes after the start of reflux.

Figure 4.6, **(a)** shows the UV-vis absorption spectra for the TGA and gel-TGA-QD samples and illustrates the changes in absorption that occur during heating. Both samples were diluted in water to optical ranges for characterisation. Clear evolution of the absorption band to higher wavenumbers is visible in the absorption spectra, Figure 4.5 **(a)**, while the peak-like structure of the band remains constant. Figure 4.5 **(b)** illustrates the corresponding normalised luminescence emission spectra (λ_{ex} 425 nm). While both sets of emission spectra are similar with FWHM values of 42 and 44 nm for

the gel-TGA and TGA QDs respectively, there are some important differences in their growth and photophysical properties.

Firstly, the initial emission for the aliquot taken after 15 minutes occurs at 526 nm for the gel-TGA-QD compared to 531 nm for the TGA QDs and this trend continues throughout the reflux period resulting in an 8 nm difference in emissive wavelengths for QDs produced after the same time periods (Figure 4.7).

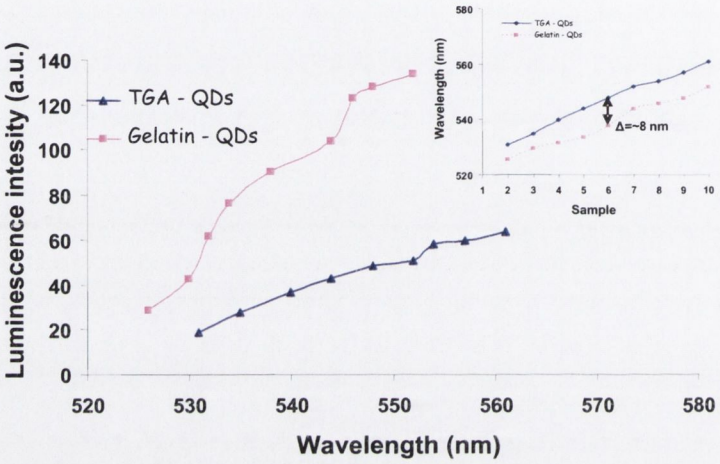


Figure 4.7. Graph of normalised luminescence intensity versus wavelength for each aliquot taken during the reflux period. Insert: graph of emission wavelength versus sample taken, showing an 8 nm difference in emission wavelength between the TGA and gel-TGA-QD produced under the same conditions.

The initial nucleation events during the formation of the QDs occur *via* a reaction of the stabiliser with excess cadmium [8] and then the growth of the QDs proceeds *via* Ostwald ripening. [8, 38-40] It is clear that the size and packing of the cadmium complexes [39] must play a vital role in the formation of the nanoclusters and their interaction with the functional groups of gelatin. In our system, the gelatin clearly demonstrates a very strong influence on the QD growth. It was clear that the gelatin did not adversely interfere with the formation of the initial cadmium complexes as the solution became turbid upon altering pH as expected, but became clear at pH 6 indicating a complete solubilisation of the precursor moieties. The QDs produced in the presence of gelatin were also highly crystalline, with lattice spacings of 3.9 Å, consistent with the (111) plane of cubic CdTe (Figure 4.8). [42]



Figure 4.8. HRTEM image of gel-TGA-QDs showing the crystalline nature of the QDs.

We believe that the gelatin acts in a two-fold manner upon the system. Firstly, due to the presence of a variety of functional groups, the gelatin can effectively interact and hold the Cd-TGA (CdL) precursor complex moieties (CdL, CdL_2^{2-}, CdL_3^{4-}) [43, 44] *via* electrostatic and hydrogen bonding interactions. Thus, the distance between these clusters is greater, enabling the initial nucleation events, upon introduction of the H_2Te gas, to occur on a more individual and separated basis. Secondly, once formed, the diffusion of these nanoclusters throughout the system during the growth stage is hindered due to the increased viscosity caused by the presence of gelatin. As a consequence of both of these factors, the Ostwald ripening process occurs at a slower rate since the individual nucleation centres take longer to interact. This enables the QDs to grow more discretely, giving rise to spectroscopic properties that are blue shifted when compared to non gelatin containing samples (Figure 4.6).

Secondly, the resultant luminescence intensities for the gel-TGA-QDs are far superior that of the TGA QDs alone (Figure 4.7). This results in QYs for the crude solution of up to 25% and, following purification, this gives fractions with QYs of between 30 and 35% compared to 20 - 25% for the TGA QDs alone. This increase must be due to the encapsulation of the QDs by the gelatin and its interaction with both the surface states and capping molecules. This encapsulation and protection of the surface [23]

from possible surrounding molecules results in greater surface passivation, analogous to capping with a wider band gap material and leads to a reduction in the number of non-radiative pathways available generating enhanced QYs.

4.2.4 Fluorescence lifetime decay analysis

To prove that the increase in QY of the QDs was due to the influence of the gelatin with surface states, comparative studies of the luminescence decay dynamics for both the TGA and gel-TGA-QDs were carried out. A drop of each sample on a glass slide in solution was analysed using a time-correlated single photon counter (Time-Harp, PicoQuant) and the data collected is shown in Table 4.1.

Table 4.1. Lifetime data recorded for samples taken 30, 40, 55, 70, 85, 100, 130 and 160 minutes after reflux for both TGA and gel-TGA-QDs. The shorter lifetime (τ_1) can be attributed to the intrinsic recombination of populated core states, while the longer lifetime (τ_2) can be associated with the involvement of surface states in the carrier recombination processes. [41] Comparison of the α values gives us an indication of the relative contribution that each part of the radiative lifetime contributes to the average total (τ_{av}).

Sample	τ_1 (ns)	α_1	τ_2 (ns)	α_2	τ_{av} (ns)
Gelatin - QDs	2.32	34.43	15.41	26.26	**13.25ns**
	2.88	44.46	19.61	38.79	**17.20ns**
	3.71	52.46	21.82	55.90	**19.33ns**
	4.71	47.01	22.81	61.74	**20.36ns**
	4.95	61.20	24.30	69.31	**21.35ns**
	3.43	56.27	22.25	79.96	**20.12ns**
	5.37	58.05	23.63	74.19	**20.87ns**
	3.79	23.66	20.11	38.85	**18.43ns**
TGA - QDs	2.20	27.59	15.12	16.89	**12.64ns**
	2.72	29.76	15.46	23.04	**13.10ns**
	3.02	25.82	15.97	26.11	**13.93ns**
	3.51	38.35	17.91	35.42	**15.39ns**
	3.91	51.27	19.33	46.70	**16.53ns**
	3.30	46.02	18.17	51.51	**16.10ns**
	3.75	61.15	19.02	63.33	**16.58ns**
	4.61	67.87	20.42	69.49	**17.56ns**

Table 4.1 shows the lifetimes recorded for both the TGA and gel-TGA-QD for each sample aliquot taken after 15, 30, 40, 55, 70, 85, 100, 130 and 160 minutes

following the start of reflux. All measured decay curves can be successfully simulated using a biexponential function with a shorter lifetime (τ_1 core recombination) equal to 2 – 5 ns, and a longer one (τ_2 surface recombination) in the range of 15 – 24 ns and these data are plotted in Figure 4.9). This multiexponential behaviour is almost universal in the emission dynamics of colloidal II–VI semiconductor QDs.

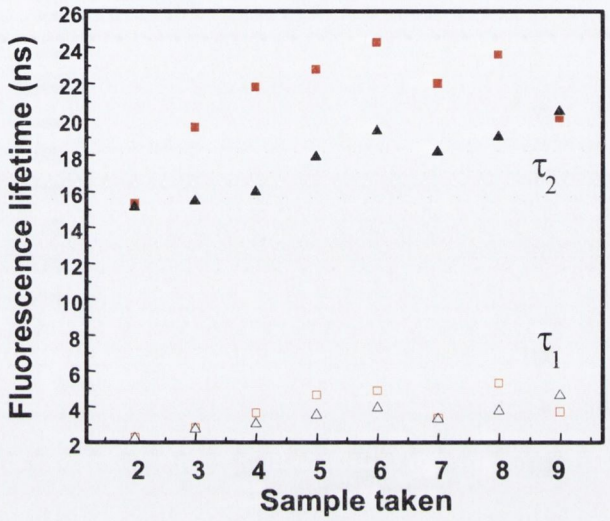


Figure 4.9. Plot of sample taken against lifetime values of the short (τ_1) and long (τ_2) lifetime components of the luminescence decays estimated from a biexponential fitting of the experimental curves of TGA (black) and gel-TGA-QDs (red).

Table 4.1 and Figure 4.9 clearly demonstrate a strong increase in the longer-lifetime (τ_2) component of gel-TGA-QD compared to those solely capped with TGA, whereas there is almost no difference in the short-lived (τ_1) components. Observed increases in the τ_2 values indicate an involvement of the surface states in the carrier recombination and substantial suppressing of their nonradiative transitions in gel-TGA-QD, while no change in τ_1 tells us that there are no alterations to the intrinsic emission when gelatin is used to encapsulate the QDs. This can further be reinforced by analysing the α values. For the gel-TGA-QD α_1 [short lifetime component] dominates initially but as heating proceeds α_2 [longer lifetime component] now dominates. Similarly, for the TGA QDs, α_1 initially dominates but unlike those with gelatin the α_1 and α_2 values remain approximately equal towards the end of experiment. This leads us to conclude that

with increasing reflux duration, we see an increased lifetime due to the contribution of the surface states that directly corroborate increases seen in the luminescence emission intensities.

4.2.5 Preparation and characterisation of gel-TGA-QDs at 1.4:1 TGA : Cd ratio

Several groups have investigated the influence that altering the concentrations of the precursor moieties has on the luminescence properties of the QDs. [7, 44-46] By lowering the stoichiometric quantity of stabiliser to cadmium (1.3 : 1), it has been shown that dramatic increases in QY could be generated due a more highly efficient packing of the thiol to the cadmium ions. [7, 43, 44, 46]

This luminescence increase is not seen for larger quantities of TGA added, as the molecules compete for the same binding sites and effectively block each others progress towards the surface. However, the production of more highly luminescent QDs using lower ratios comes with a sacrifice of reaction yields, as insoluble cadmium precipitates are formed during the reaction. [7, 43, 44] The concentration-dependent QY behavior may be attributed to the excess cadmium complexes existing in the initial stages of QDs growth. Gao *et al.* [44] have proposed that the formation of the appropriate thiol complexes may be responsible for the improvements observed and the importance of these complexes for a successful aqueous synthesis has been investigated by Winter *et al.* [47]

As gelatin altered the growth and influenced the luminescence properties to such a degree, we wished to investigate if the QY of the gel-TGA-QD could be improved further by altering the ratios of the Cd and TGA in the reaction solution. We also wanted to see how varying the amount of gelatin added would affect the growth and luminescent properties of the QDs at a different ratio of precursors.

Thus, we systematically carried out a series of experiments where the TGA : Cd ratio was fixed at 1.4 : 1 and the amount of gelatin was varied from 0 (control), 0.1, 0.25, 0.5 to 1 g. Following the aforementioned synthetic procedures, the reaction mixtures were all prepared with the same concentration of reagents in the same volume of water and were purged with argon, bubbled with H_2Te and refluxed for the same time periods so that the only variable present was the gelatin concentration. Once again, the sample

aliquots were spectroscopically characterised at the same time intervals (15, 30, 40, 55, 70, 85, 100, 130 and 160 after start of reflux) and the resultant luminescence data are shown in Figure 4.10. No discernable changed were witnessed in the UU-vis absorption spectra.

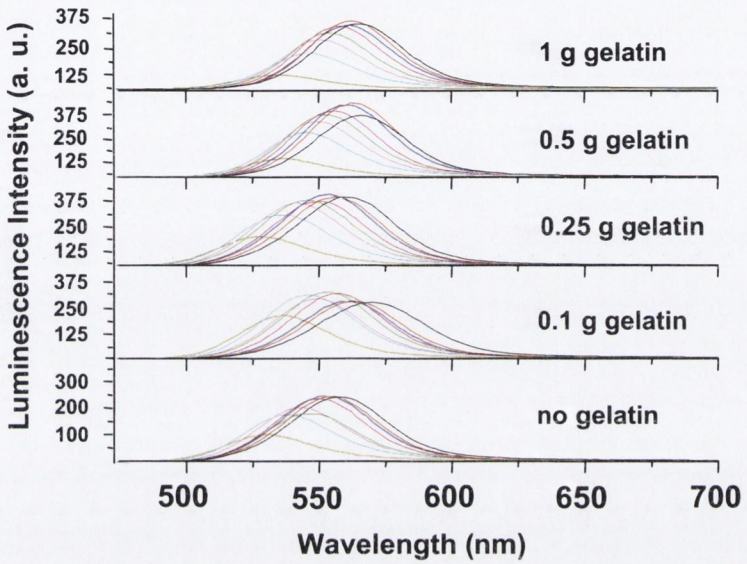


Figure 4.10. Normalised luminescence emission spectra (λ_{ex} 450 nm) for QDs with no gelatin and repeat experiments containing varying amounts of gelatin (0.1 g, 0.25 g, 0.5 g and 1 g).

Figure 4.10 shows the luminescence emission spectra taken during the reflux for the series of experiments containing varying amounts of gelatin and a control with no gelatin present. As we have seen previously, the growth of the QDs proceeds sequentially with an overall increase in luminescence efficiency (Figures 4.6 and 4.7). For these experiments, the final QYs for the crude gelatin containing parent solutions was 35 - 40%, which is significantly higher than those recorded previously for gel-TGA-QD produced at a ratio of 1.75 : 1, TGA : Cd (25 - 30%).

The synthesis of TGA QDs at this ratio was accompanied with the generation of a white precipitate. This precipitation can be attributed to the formation of cadmium hydroxide, which is insoluble in excess alkali [48] and could also be due to the insoluble nature of the cadmium species formed (CdL L= ligand) This cadmium species has been investigated by Vairavamurthy *et al.*, [49] who demonstrated that it is possible for cadmium to form complexes with MPA in both 1:1 and 1:2 ratios, resulting in the

presence of both a soluble and insoluble cadmium complexes within the reaction solution.

This precipitate is not seen at higher ratios [1.75:1], as the dithiol [CdL_2^{2-}] species dominates and is completely soluble. This precipitate must be filtered before analysis of any of the sample fractions can be taken and before any post-preparative treatments. This results in an overall reduction in the amount of both Cd and TGA available during the reflux and gives lower reactions yields and less concentrated solutions than the previously described experiments.

Once gelatin is incorporated into the reaction mixture, several significant changes were noted. i) Initially, upon addition of only 0.1 g of gelatin, a cloudy precipitate was formed upon heating. Interestingly, even with this small amount of gelatin, the initial increases in luminescence intensity in the blue region of the spectra are higher than for those QDs without gelatin present for the same time periods of heating. However, when the reflux was stopped and after filtration of the precipitated solution, the final QY of the crude solution remains quite similar to that of the TGA QDs alone (Figure 4.11, light blue and orange lines).

ii) As higher concentrations of gelatin were added, significant increases in the intensity of the emission were noted when compared to the TGA-QDs produced in the absence of gelatin. Measured QYs of 35 - 40% compared to 30% (Figure 4.11) were recorded. This increase can be attributed to the increased surface passivation and stabilisation due to gelatin adsorption onto the QD surface. Interestingly, no precipitate was generated. Therefore, the interaction and charge of the gelatin must lend itself to the efficient stabilisation of these previously insoluble species and a greater incorporation of them into the QDs. The lack of precipitate formed must also contribute to the luminescence increases witnessed. Also, no filtering was needed prior to characterisation of the sample aliquots, further increasing the concentration of the QD solutions.

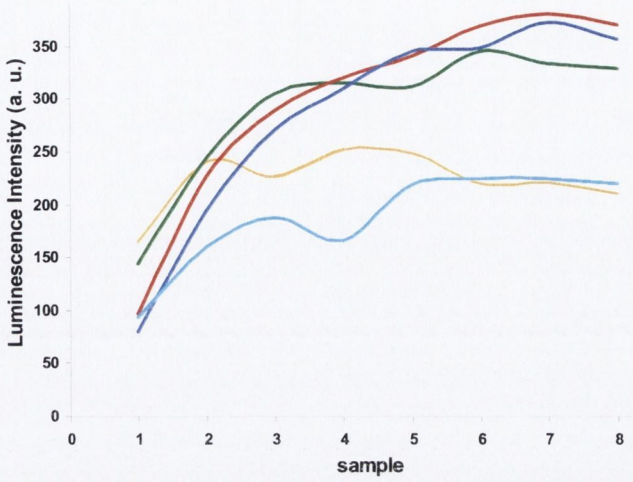


Figure 4.11. Graph of normalised luminescence intensity versus each sample analysed for a control experiment of QDs without gelatin (light blue) and also samples containing 0.1 g (orange), 0.25 g (green), 0.5 g (red) and 1 g (blue) of gelatin.

As can be seen from Figure 4.11, the luminescence efficiencies of the TGA QDs [control (light blue line)] and 0.1 g (orange line) gelatin containing solution are comparable, although initial increases are greater for the sample containing gelatin. However, an increase of up to one and a half times the luminescence emission intensity is clearly noted for the samples containing higher concentrations of gelatin. Each sample (0.25 g, 0.5 g and 1 g) gave emission intensities that follow similar paths and result in final QY values for the crude solutions of 35 - 40%. As all three showed results that seemed to plateau, it was decided not to increase the gelatin concentration further. Indeed, when very large excesses are added, the purification of the QDs *via* the addition of isopropanol becomes difficult as two distinctly coloured red and yellow layers are formed instead of the desired precipitate. Thus, the addition of gelatin *in situ* to a solution of TGA and cadmium results in significant increases in the QY throughout the evolution and growth of the QDs at this ratio.

4.3 Preparation and characterisation of gelatin-MPA nanocomposites

4.3.1 Preparation and characterisation of gel-MPA-QDs at 1.4:1 MPA :Cd ratio

It seems reasonable to assume that similar results should also be observed for MPA capped QDs. The same procedure, this time with a fixed (0.4 g) gelatin concentration was repeated and aliquot samples were once again taken at 15, 30, 40, 55, 70, 85, 100, 130 and 160 after start of reflux (Figure 4.12).

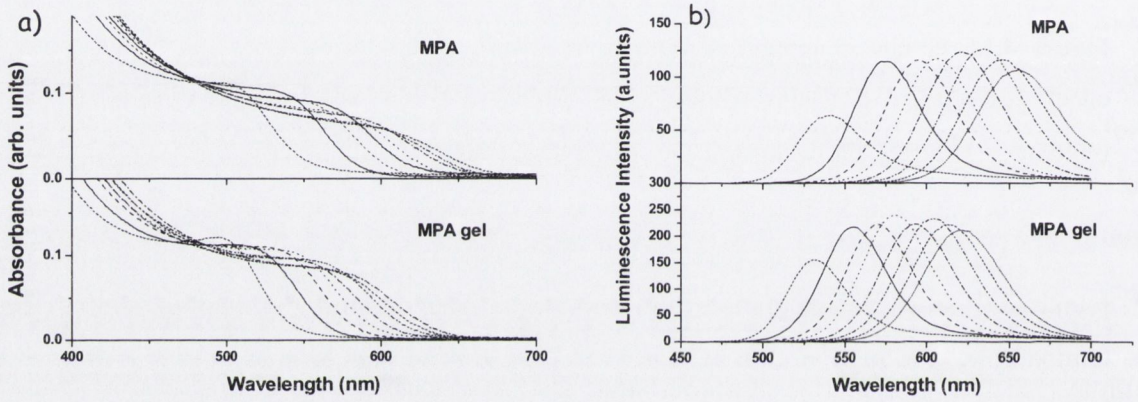


Figure 4.12. **a**) UV-vis absorption and **b**) normalised luminescence emission (λ_{ex} 450 nm) spectra of MPA and gel-MPA-QDs taken 30, 40, 50, 60, 75, 90, 105 and 120 minutes after the start of heating.

Figure 4.12 illustrates the changes in **a)** UV-vis absorption and **b)** luminescence emission spectra (λ_{ex} 450 nm) for the MPA and gelatin MPA QDs (gel-MPA-QDs). Interestingly, the absorption band for the gel-MPA-QDs is more peak-like indicating that initially, narrower size distributions are produced when gelatin is incorporated. As expected, with the advent of Ostwald ripening, this band becomes more shoulder-like as the size of the QDs increases throughout the ensemble. These QDs possess quite large QYs of 30 - 35%, but their absorption profiles are far less defined than those witnessed for the TGA capped samples. This infers that the packing and binding of the MPA throughout the growth process is not as efficient as that for the TGA QDs and gives rise to broader size distributions. It is worth noticing that even with these excess surface

defects and broad size distributions, the luminescence efficiency remains quite high confirming our previous observations that surface related anomalies contribute more significantly to the radiative processes than those within the lattice. The growth of the QDs is once again influenced by the addition of the gelatin (Figure 4.12 **b** and 4.13).

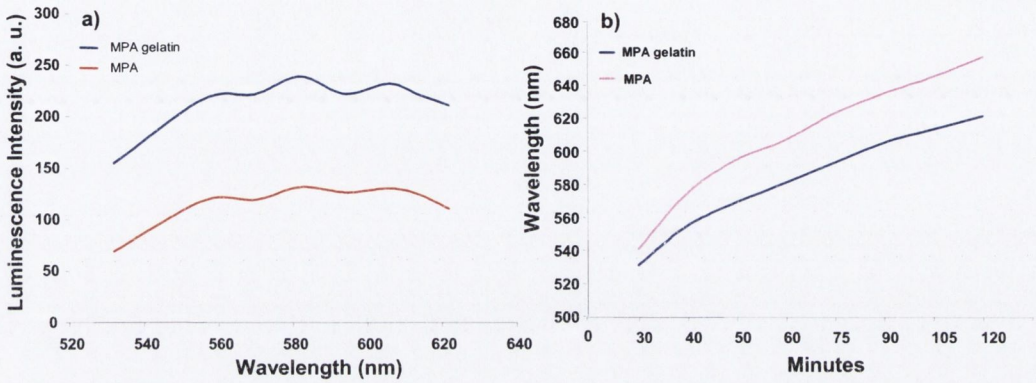


Figure 4.13. Graph of **a**) luminescence intensity versus wavelength and **b**) wavelength versus sample taken for MPA and gel-MPA-QDs taken 30, 40, 50, 60, 75, 90, 105 and 120 minutes after the start of heating.

Figure 4.13 above shows the effect gelatin has on the properties of the MPA and gel-MPA-QDs. With the incorporation of gelatin, luminescence efficiencies increased by 1.9 times giving final values for the QYs of 30 - 35%. The sizes of the respective QDs were also altered, as had been shown previously for TGA QDs. The emission of the gel-MPA-QDs appears at 10 nm lower than the MPA QDs and this continues to increase to 35 nm towards the end of the reflux duration. Interestingly, the overall size of the MPA QDs is far higher than those for the TGA QDs following the same reflux times.

It was possible to record HRTEM images of a purified fraction of the MPA QDs (Figure 4.14).

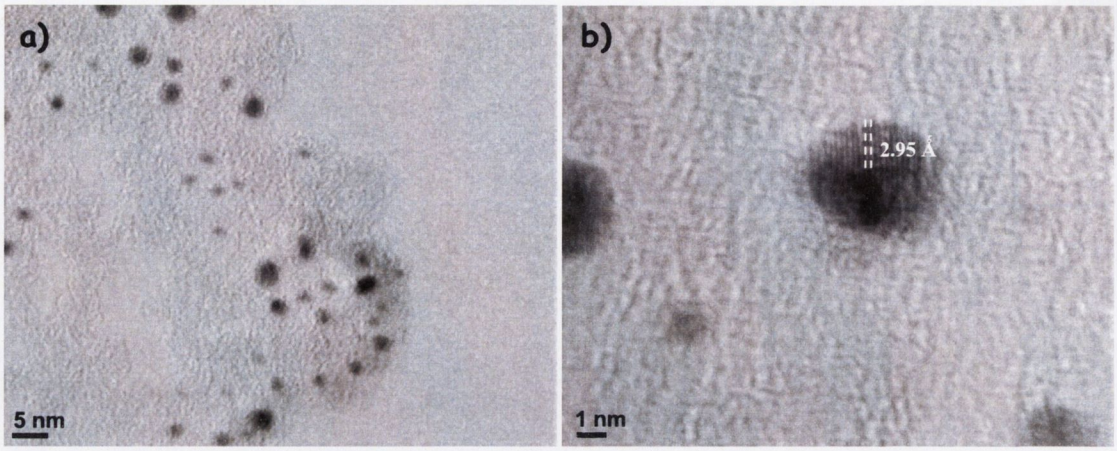


Figure 4.14. HRTEM images [**a**) lower magnification, **b**) higher magnification] of gel-MPA-QDs. Lattice spacing is 2.95 Å, consistent with the (200) plane of cubic zinc blend CdTe. [50, 51]

We have shown that for a capping agent that exists primarily as a deprotonated carboxylic acid on the surface of the QDs, the influence of gelatin is quite significant and the functional groups present along the polymer backbone play a major role in the surface interactions. As such, it was decided to change the surface stabiliser to investigate if gelatin could impart the same influences when we change the pH and also the surface charge at the time of synthesis. Thus, we investigated the growth and luminescent properties of cysteamine stabilised QDs [cys-QDs] synthesised under the same conditions as stated previously.

4.4 Preparation and characterisation of gelatin-cysteamine nanocomposites

The experimental procedures as stated above were repeated for cysteamine (cys) except the pH was changed to 6 to promote a positively charged surface. This was also to solubilise the cysteamine (cys) cadmium precursor complexes and as before, concentrations were kept the same, with 0.4 g gelatin added to the reaction mixture.

4.4.1 Preparation and characterisation of gel-cys-QDs at 1.4:1 cys : Cd ratio

The UV-vis absorption and luminescence emission spectra were recorded sequentially (30, 40, 50, 60, 75, 90, 105 and 120 minutes) during the reflux period and the data are shown in Figure 4.15. Of note, the pH of the synthesis was set at 6 however upon the generation of the QDs a slightly lower pH of 5.5 was required to keep the QDs stable in solution. At pH values above this, the solution appeared turbid and over time the QDs precipitated from solution. This phenomenon was utilised to aid the purification of the QDs.

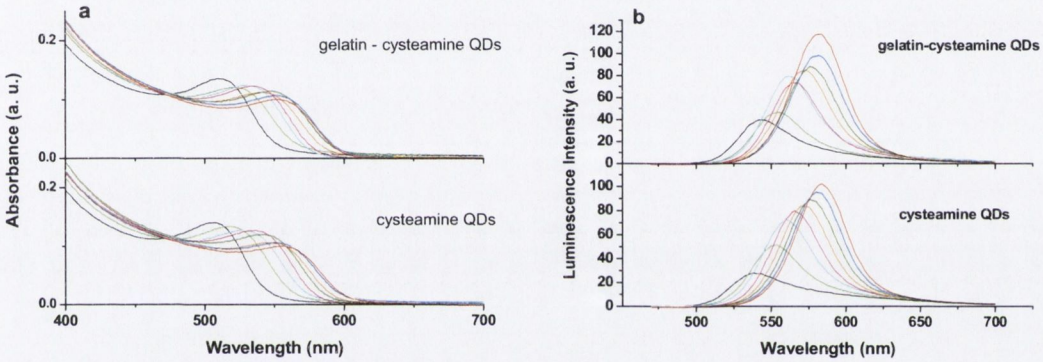


Figure 4.15. a) UV-vis absorption spectra and **b**) normalised luminescence emission spectra (λ_{ex} 450 nm) recorded for gelatin-cysteamine [gel-cys-QDs] (top) and cys-QDs (bottom) taken after 30, 40, 50, 60, 75, 90, 105 and 120 minutes from the start of heating.

The absorption spectra of both species (Figure 4.15 **a**) show well resolved first excitonic peaks that red shift with reflux time. This indicates a good crystallinity throughout the sample along with relatively narrow size distributions, which would otherwise generate shoulder-like features. The corresponding emission spectra are shown in Figure 4.15 **b**. Both spectra show similar growth patterns with no discernable variations in emission wavelength or FWHM of between 40 - 44 nm for both the gel-cys-QDs and cys-QDs respectively.

The cys-QDs possess an overall QY for the crude solution of 16%; however this is raised slightly to 18% for the gelatin QDs. Unlike their TGA or MPA capped counterparts, the cys- and gel-cys-QDs do not show the dramatic increases witnessed

previously but the final QY of those samples containing gelatin is slightly higher than those without (Figure 4.16). All through the heating process, the luminescence intensities of the two samples remain similar and consistent with only the final sample displaying some increase.

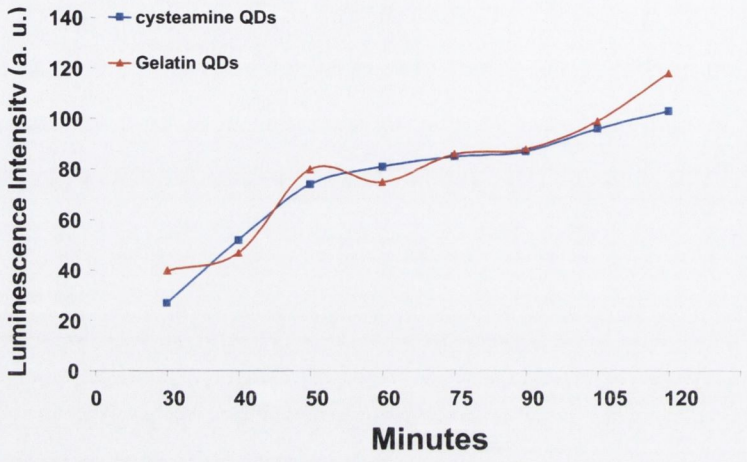


Figure 4.16. Plot of luminescence intensity of cys- (blue line) and gel-cys-QDs (red line) against the samples taken after 30, 40, 50, 60, 75, 90, 105 and 120 minutes from the start of heating.

These values coupled with the spectroscopic data once again reinforce the theory that surface states play the dominant role in exciton recombination. From the absorption data (Figure 4.15 **a**), well resolved peaks indicate a highly crystalline ensemble but QYs are not comparable to either the MPA or TGA QDs. As such, there may be a number of factors influencing the recombination processes. Firstly, packing of the thiol groups must be more efficient for the carboxylic species than the cysteamine and packing is a significant contributor to luminescence intensity. [39] This may be due to a stronger interaction of the nitrogen species with any unsaturated cadmium atoms. However, this is not as beneficial as those for the carboxylic acid species and can possibly lead to the increased blocking of other thiols binding to the surface and to the generation of aggregates that self-quench in solution.

This lack of a luminescence increase also demonstrates the fact that the influence of the gelatin is not as strong within this pH range compared to 11 for the TGA or MPA QDs. From the structure of gelatin (Figure 4.1), it can be seen that there are less groups

which could hold a positive charge compared to those alcohol and carboxylic functionalities which can maintain a negative charge. Unlike those interactions which have been shown previously for carboxylic acid stabilised QDs, [27] the gelatin cannot effectively coordinate to the QD surface. A 2:1 ratio of cadmium to tellurium is maintained throughout the synthesis which leads predominantly to a cadmium saturated surface. Should any of these atoms be left unpassivated, then they would be unable to become involved in secondary interactions with the gelatin due to the opposite charges present. There would be the possibility of hydrogen bonding between the protonated carboxylic moieties and the cadmium atoms and cysteamine molecules; however, this association must not be strong as only slight increases are witnessed in the emission properties. This proves that the gelatin must have an effective charge and corresponding groups must be present on the surface of the QDs in order for it to act as a durable, robust passivating agent.

Carrying on from these results we now wished to investigate the behaviour and toxicity of the QDs and their gelatin counterparts in live cellular systems.

4.5 Size exclusion of gelatin QD nanocomposites

Previously, in Chapter 3 the variation in size of TGA QDs was shown to have a dramatic effect on their distribution within the THP-1 cells. This result is not altered by the addition of gelatin and distinct patterns of uptake are clearly seen *via* imaging using a fluorescent microscope (Figure 4.17).

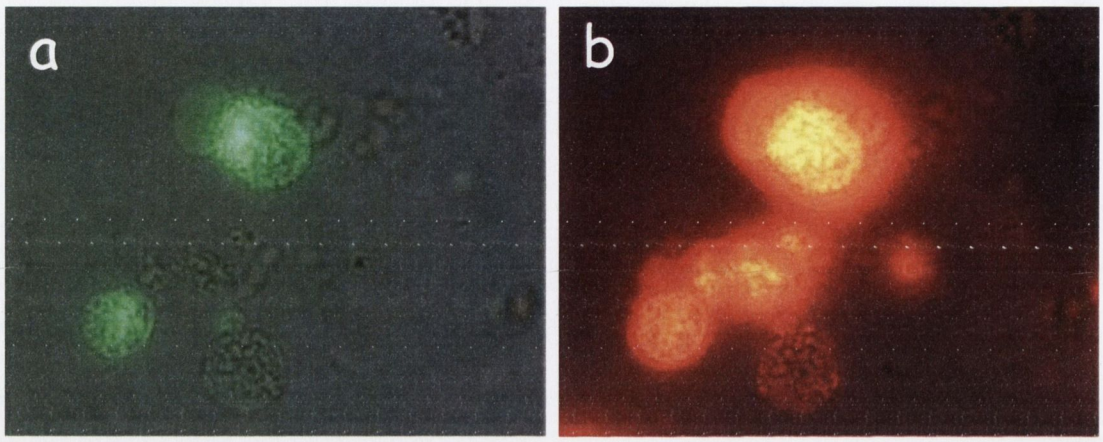


Figure 4.17. Fluorescent microscope images (**a** - green channel, **b** - red and yellow channels) of THP-1 cells incubated with gel-TGA-QDs indicating that size exclusion is still present for gelatin coated QDs.

From Figure 4.17, the difference in cellular distribution of the gel-TGA-QDs according to size can be clearly seen. Panel **a** was taken in the green channel and shows the QDs accumulating within the cells, predominantly in the nuclear region. This is confirmed by the brighter fluorescence intensity within the nuclear envelope. Panel **b** illustrates a composite image using both the red and green channels, to show that the larger QDs are present both around the cell and within the cytoplasm as indicated by the yellow fluorescence. This size separation within the cell is further illustrated for the MPA QDs (Figure 4.18).

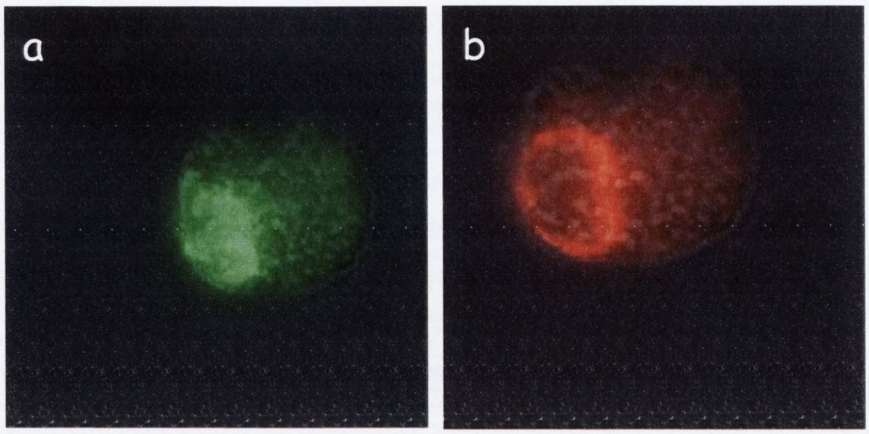


Figure 4.18. Enhanced fluorescence images of gel-MPA-QDs in live THP-1 cells. Panel **a** shows the accumulation of green emitting QDs in the nucleus, while panel **b** shows the accumulation of the larger red emitting QDs in the cytoplasm.

Figure 4.18 shows the size exclusion of small green QDs with respect to the larger red MPA capped QDs. The green QDs are predominantly found to accumulate within the nucleus (panel **a**) while the red QDs (panel **b**) accumulate outside the nuclear region, highlighting its borders with the cytoplasm quite clearly.

Cysteamine QDs were also analysed to investigate if altering the surface functionality altered QD toxicity (Figure 4.19). As has been shown previously, cysteamine QDs did not penetrate the cell membrane of the THP-1 cells (Figure 3.14, Chapter 3).

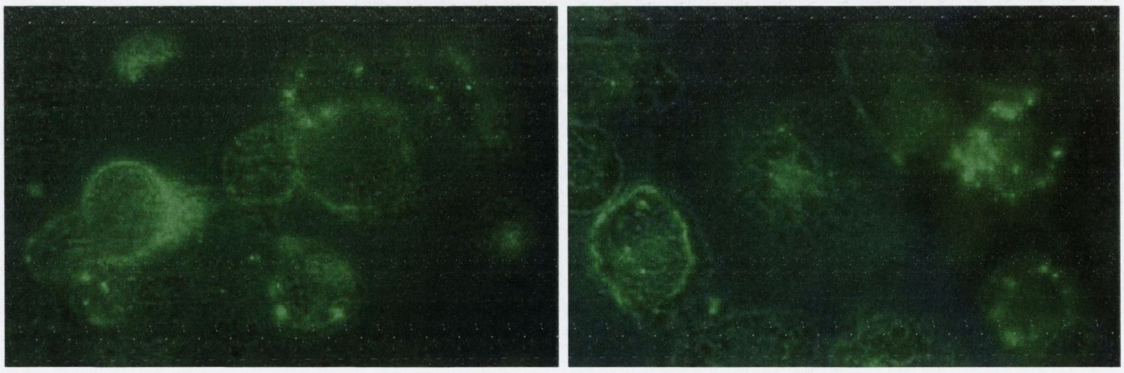


Figure 4.19. Live cell fluorescence images of cys-gel-QDs and THP-1 cells after a 1 hour incubation time.

Upon the addition of gelatin *in situ*, no discernable change can be realised in their uptake which illustrates the lack of trans-membrane penetration by the cys-gel-QDs (Figure 4.19). Only an exterior cell luminescence is visualised around the membrane and the QDs are highlighted in patchy agglomerates. This agglomeration is typical for positively charged QDs.

Due to the lack of cell penetration, this set of experiments proved inconclusive with regard to toxicity. No significant changes in cell behaviour were noted after extended incubation times, indicating that an exterior accumulation of QDs around the THP-1 cells does not seem to exhibit any deleterious effects upon their viability.

4.6 Toxicity of CdTe QDs and their gelatin counterparts

4.6.1 Introduction

Over the past number of years there has been an increased production of nanomaterials and consequently, on a never ending search for productive uses, there has been a dramatic increase in the levels of exposure to theses extremely small entities. Due to the tremendous focus on developing nanoparticles for imaging and therapeutic applications, there has been an increasing interest in evaluating the toxicity of nanomaterials, in particular, QDs. [52-54] As such, many *in vivo* and *in vitro* investigations have been conducted and the issue of safety for both the user and administrator due to an ever increasing exposure to these nanomaterials is a debate that has been gathering significant momentum. [55-59] Consequently, their composition and stability in biological media is of paramount importance [60] as they may easily be distributed throughout the environment and absorbed by biological entities.

Recently much work has focused on the determination of the cause of any toxicity related phenomena and various conclusions have been drawn as to the cause of cellular apoptosis. Leaching of toxic cadmium atoms, [53, 58] oxidative processes, [61] QD size, [56] concentration, [55] surface functionality, [52, 62] metallothionein interaction, [63] and the generation of reactive oxygen species (ROS) [64-66] have all been investigated. Deleterious effects have also been reduced by coating with ZnS, [52, 53, 58] silica, [67] or a protein such as BSA. [65]

4.6.2 Investigation into the uptake and distribution of TGA and gel-TGA-QDs in THP-1 cells

To investigate if the gelatin could act as a protective agent for the continued use of QDs in bioimaging, the gel-TGA-QD nanocomposites were tested alongside those capped solely by TGA in live THP-1 cell cultures. Firstly, the uptake and distribution of both samples of QDs was evaluated. Analysis of gelatin and non-gelatin QDs was conducted using a Cellomics® fluorescent imaging system in two channels, channel 1: λ_{ex} 475 ± 40 nm and channel 2: λ_{ex} 560 ± 45 nm. This high content screening approach allowed for investigations into and analysis of the emissive response and distributions of the QDs within the samples (Figures 4.20 and 4.21).

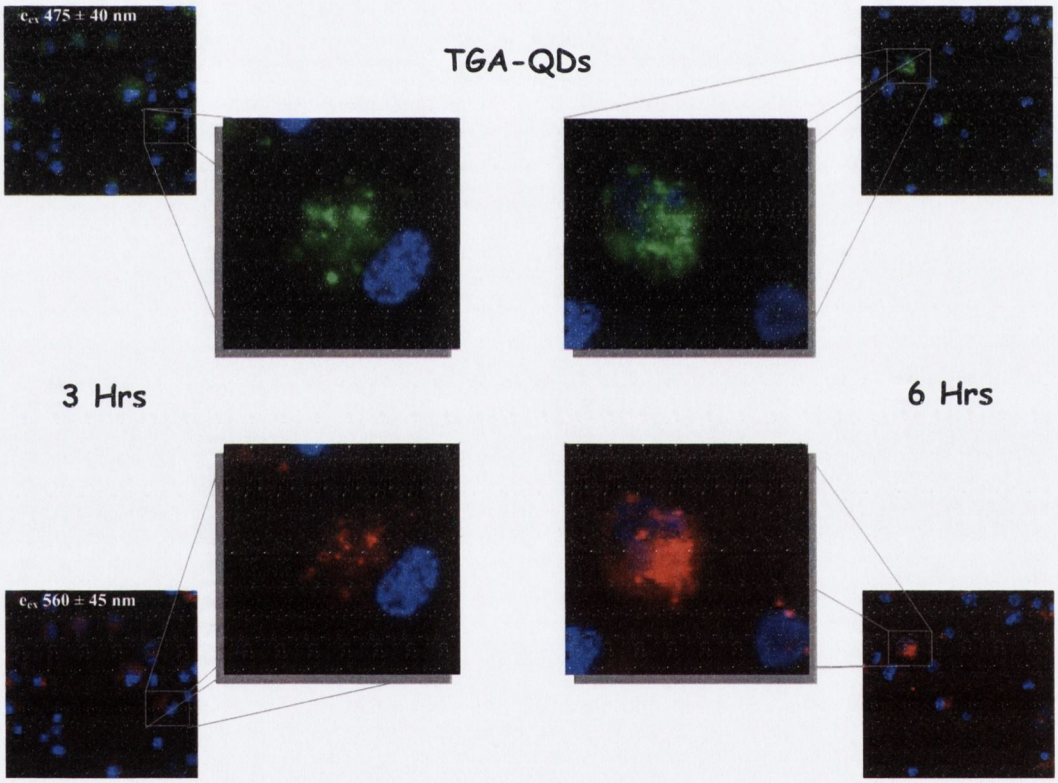


Figure 4.20. Live cell Cellomic® images of TGA QDs cultured with THP-1 cells and analysed over coincubation times of three and six hours.

From our previous studies we already knew that the QDs readily penetrated the cell membrane and depending on size would accumulate within the nucleus. From Figure

4.20, it can be clearly seen that the TGA QDs show emissive properties across both excitation ranges. Interestingly, they display a diffuse cytoplasmic localisation, which does not vary significantly with increasing coincubation time. Some regions are highlighted more intensely in one channel over the other, confirming the presence of a variety of sizes within the ensemble and illustrating the fact that different sized QDs do in fact localise in different areas. Upon analysis of the gel-TGA-QDs, a different distribution within the cells can be identified (Figure 4.21).

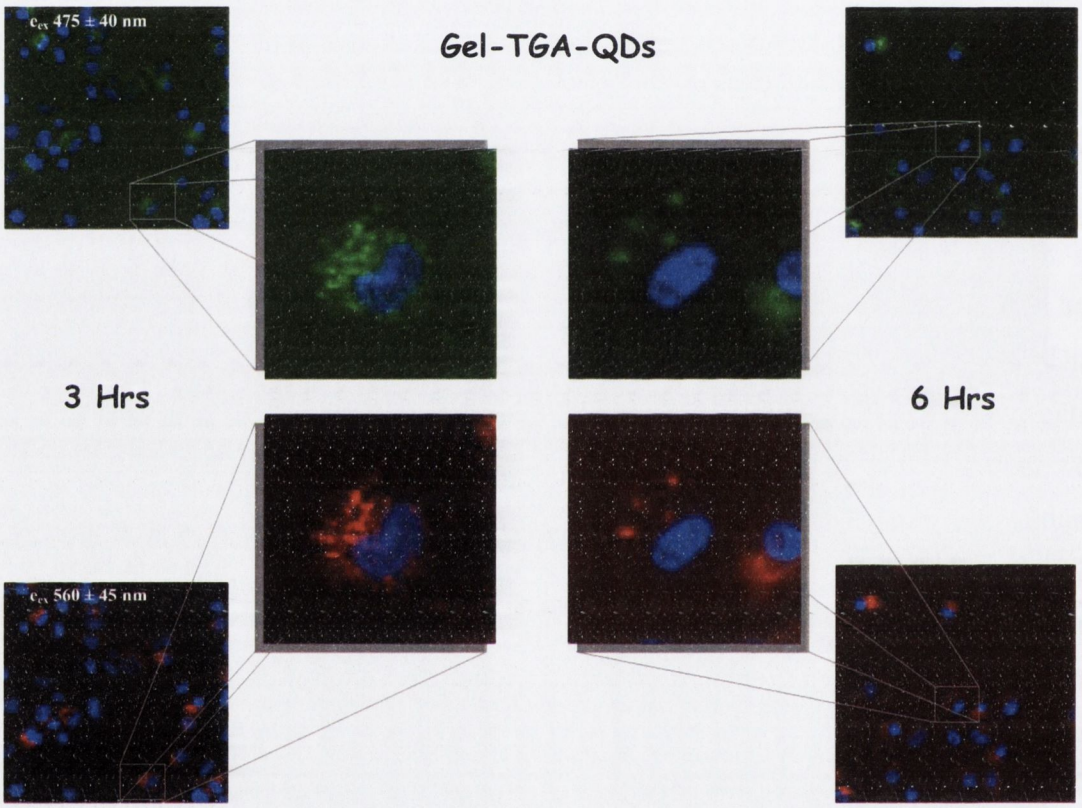


Figure 4.21. Live cell Cellomic® images of gel-TGA-QDs cultured with THP-1 cells and analysed over coincubation times of three and six hours.

From Figure 4.21, it can be seen once again that these gel-TGA-QDs do in fact display luminescence in both channels of excitation. Most notably, they exhibit different sub-cellular localisations when compared to the TGA QDs and this is further realised over the two coincubation periods. After 3 hours, the distribution is somewhat diffuse but

already sporadic accumulation can be seen. This is further emphasised after 6 hours, where the gel-TGA-QDs are seen to accumulate in easily detectible agglomerates. The accumulation of these nanocomposites can be attributed to interactions of the gelatin coating with the surrounding medium, which contains a variety of proteins and other biomolecules. So, the gel-TGA-QDs also readily penetrate the cellular membrane and accumulate in a patchier, more agglomerated fashion, but do they negatively influence the behaviour or viability of the cells?

4.6.3 Toxicity of QDs coincubation with THP-1 cells

The cells were cultured in 96 well microtitre plates and a commercial kit (multiparameter cytotoxicity 1 HitKit®, Cellomics, PA, USA) was used to monitor the toxic affects induced by the QDs on the cells. The images from the microtitre plates were acquired using the Cellomics KineticScan® (Figures 4.20 and 4.21 above). The cellular toxicity responses were measured using a multiparameter cytotoxicity HitKit® and dye luminescence intensities can be directly correlated to toxic phenomena. This kit contains a three-in-one fluorescent dye that stains for nuclei, cell permeability and lysosomal pH. The nuclear dye (Hoescht) with $\lambda_{ex/em}$ 350 (± 50) / 460 (± 20) nm stains a blue colour. For cell permeability, a green dye with $\lambda_{ex/em}$ 494 (± 40) / 517 (± 20) nm was used. Healthy cells are nearly impermeable to the dye, but become permeable after being compromised. Finally a red dye, $\lambda_{ex/em}$ 560 (± 15) / 590 (± 25) nm, was used to monitor the lysosomal pH since dye accumulation directly correlates to cytotoxicity and changes in pH are visualised by dye intensity. The images and data collected are presented in Figures 4.22 - 4.24 and Table 4.2.

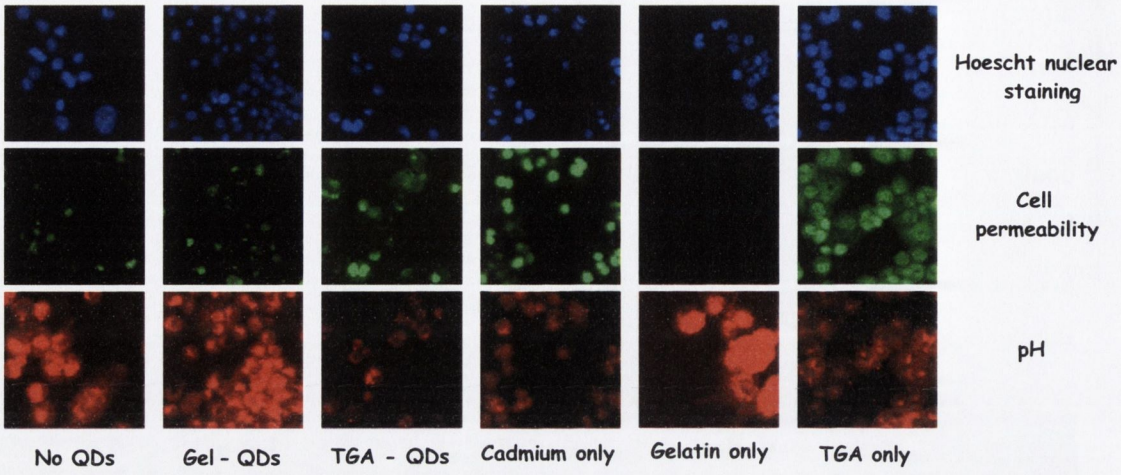


Figure 4.22. Live cell Cellomic® images of the dye staining, taken using the Cellomics KineticScan®. The Hoescht nuclear staining (blue), changes in cell permeability (green) and lysosomal pH (red) were recorded for unmodified cells and cells with added TGA QDs, gel-TGA-QDs, cadmium, gelatin and TGA in solution. Cell permeability and pH changes are measured by intensity. For cell permeability, an increase in intensity is indicative of an increased permeability, while for pH, a decreased intensity indicates a more basic pH.

Figure 4.22 illustrates, through the intensity of the staining dye, the resultant cell permeability and lysosomal pH responses demonstrated upon addition of the gelatin-QDs with respect to the TGA QDs and the control samples. Variations in permeability given by the green stain, measured as increases in luminescence intensity, indicate an enhancement of cell porosity and decreased cell viability. Alternatively, decreases in luminescence intensity with regard to pH, indicate a more basic cellular pH. This results in an increased rate of cellular apoptosis, as the specific internal pH ranges required for the cell to function properly are compromised.

The changes in luminescence intensity measured in response to the introduction of QDs to the cell cultures can be solely attributed to direct interactions of the staining dyes upon entering the cells. Energy transfer to the dyes can be ruled out for a number of reasons. Firstly, the dyes and QDs enter different regions of the cells and as such cannot interact directly on the scale required for FRET, an energy transfer between the dyes and the nanoparticles [68] or other energy transfer phenomena. Secondly, the dye emission is of the order of approximately 10^3 arbitrary units, while the QDs display about 10^2. Thus,

any energy transferred to the dye would be of an order of magnitude lower and would have a minimal effect on the emission intensity. Thirdly, the addition of free cadmium in solution with no QDs present as shown in Figure 4.22 column 4, results in responses that reinforce our previous observations. Indeed the changes for this system show emission intensity values that are higher for cell permeability and lower for pH than those witnessed for the QDs, indicating that the cadmium has the most severe detrimental effect upon the cells.

While Figure 4.22 illustrates the optical viewpoint for the analysis of the toxicity responses, the software can be used to quantitatively represent the data. The resultant responses are given in Table 4.2.

Table 4.2. Nuclear size, cell permeability and lysosomal pH data collected upon analysis of the TGA and gel-TGA-QDs *via* high content screening using a Cellomics KineticScan®. Nuclear size is measured in pixels, while cell permeability and lysosomal pH is measured by dye intensity. Increases in pixel intensity indicate increased cell permeability and a decreased lysosomal pH respectively.

time		No of Cells	Nuclear Size	Standard error	Cell permeability	Standard error	Lysosomal pH	Standard error
			Mean	SE	Mean	SE	Mean	SE
3 hours	No QDs	294	18.3	0.31	376	32	1989	47
	TGA-QDs	745	17	0.37	633	73	1838	55
	gelatin– QDs	826	16.9	0.31	460	48	2222	52
6 hours	No QDs	297	17.3	0.36	503	59	2173	52
	TGA-QDs	725	15.4	0.34	1067	107	1269	41
	gelatin– QDs	961	15.8	0.31	592	67	1631	46
Controls	gelatin	250	17.9	0.40	142	15	3304	80
	TGA	250	19.7	0.33	2104	67	1722	59
	cadmium	250	13.1	0.52	3336	145	329	8

Table 4.2 shows the data collected upon analysis of the cells using a multiparameter cytotoxicity HitKit. The controls chosen were gelatin, TGA, cadmium only and a blank well. Values for the size of the nucleus are in pixel numbers, while the

permeability and lysosomal pH are quantified as the average intensity of luminescent pixels within the area gated. Experiments were conducted over 3 and 6 hours and controls were used to compare any differences that may arise. All of the data shown in Table 4.2 is also represented in histogram form in Figures 4.23 and 4.24.

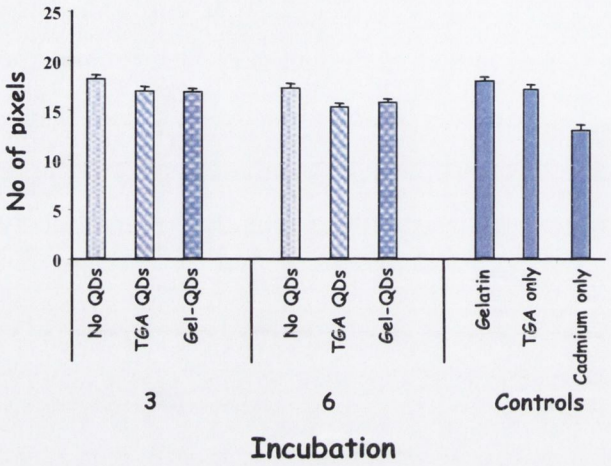


Figure 4.23. Histogram indicating changes in nuclear size measured in pixels with increasing incubation time for all QD and control samples tested.

Figure 4.23 illustrates the changes that occurred in nuclear size during the experiments. As was seen from Figures 4.20 and 4.21, no nuclear penetration was observed for either the TGA or gel-TGA-QDs. Thus, the impact of the QDs on the nucleus was minimal and as a consequence, no discernable changes to nuclear size were recorded. Free cadmium was the exception and this resulted in a decrease in nuclear size, indicating the initiation of cell death due to an external influence which conforms to previous observations into cell apoptosis. [69-72] Therefore, analysis of the nuclear changes was somewhat inconclusive, whereas changes in permeability and pH were far more informative (Figure 4.24).

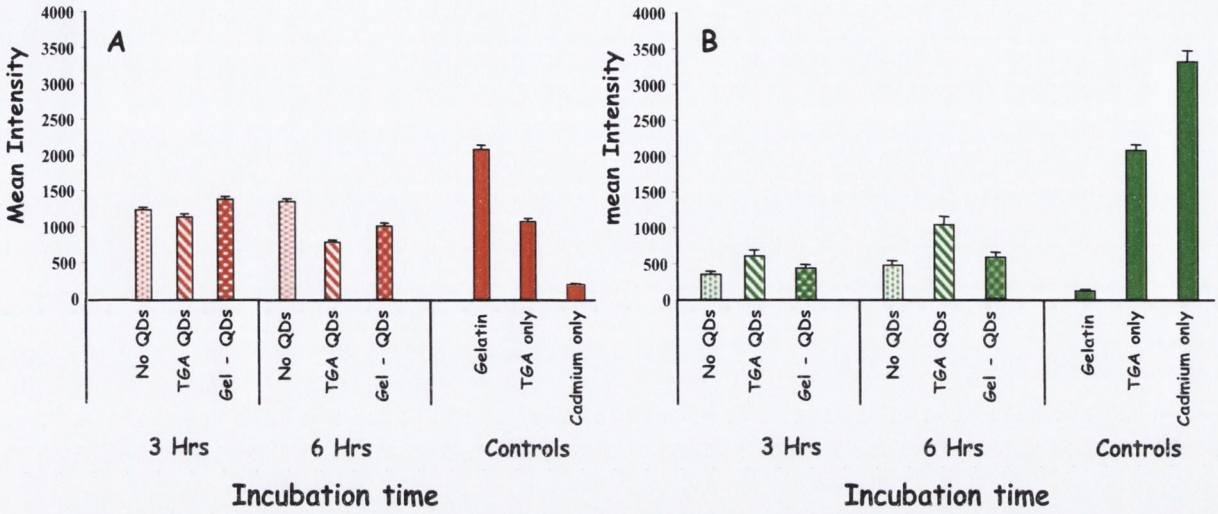


Figure 4.24. a) Histogram illustrating the changes in lysosomal pH with incubation time. Decreases in intensity are indicative of a more basic lysosomal pH while increases are due to acidic pH values. **b)** Histogram illustrating the changes in cell permeability with incubation time. Increases in intensity are indicative of increased cellular permeability.

More dramatic changes in these parameters were noted after 6 hours (Figure 4.24) The TGA QDs showed a marked decrease in intensity which is 50% more substantial than changes due to the gel-TGA-QDs. As expected, the TGA alone, and in particular, the free cadmium in solution showed substantial increases in pH leading to decreased intensity values. The liberation of free cadmium in solution due to UV irradiation has been investigated by Derfus *et al.*, [53] but it seems to have a dependency on dose and cell type. During their investigations into the use of CdSe QDs as potential photosensitisers, Bakolva *et al.* [64] found that lymphocytes were more susceptible to decreased viability than Jurkat cells (white blood cells, used to study T cell leukaemia) and attribute this to a more rapid cadmium influx and induced apoptotic pathways. They also state that Jurkat white blood cells, HeLa cervical cancer cells and breast cancer cells all possess anti-apoptotic mechanisms which render them more resistant to cadmium poisoning. Cell type and their ability to accumulate toxic entities, while still retaining their viability, is very important, but exposure and toxicity due to heavy metals must be analysed and verified throughout any experiment.

Interestingly, in contrast to the negative impact due to cadmium and TGA, gelatin on its own shows an increase in intensity indicating that it generated an environment that was quite favourable for the cells.

Upon analysis of the permeability over 3 hours, initial increases are once again noted to be more substantial for the TGA compared to the gel-TGA-QDs. After 6 hours these changes are quite dramatic and the TGA QDs display an increase in permeability that is approximately 80% greater than changes resulting from the gelatin-QDs. The TGA and cadmium both display significant increases in permeability, while favourable results for cell growth are displayed by the gelatin in solution.

4.7 Conclusions

In conclusion, gelatin has been incorporated in both mechanical mixtures and *in situ* during the preparation of TGA capped CdTe QDs and has, in both instances significantly increased the observed QYs by up to 1.5 times. When added directly to the precursor solution of Cd^{2+} and TGA, it directly impacts the nucleation, growth and photophysical properties. At ratios of 1.75:1 TGA : cadmium, it causes a reduction in the emission wavelengths by encapsulating the individual nucleation centres allowing for a more discrete growth mechanism, while also increasing surface passivation and the rate of radiative recombination. As shown, the gelatin added *in situ* interacts considerable with the QD surface resulting in substantial gains in luminescence efficiency. This surface state interaction is backed up *via* biexponential lifetime decays, which indicate a strong increase in the rate of exciton recombination due to radiative surface states. At lower (1.4:1) ratios of TGA : cadmium, further increases up to 40% QY are possible and reaction yields were increased by effectively increasing the solubility of the cadmium complexes.

Similar emission responses were also observed for MPA stabilised QDs, as smaller QDs were also produced under similar preparatory conditions with increases up to 1.9 times noted in the luminescence responses. To analyse the effect of changing pH and the type of stabiliser, cysteamine was employed. pH values of 6 and later 5.5 were required to solubilise the QDs. No significant changes in growth or emissive response

were noted for this system, indicating that the gelatin does not efficiently act in the same manner within these pH ranges

To evaluate their potential as bioimaging agents, the gel-TGA-QDs were compared to TGA QDs and live THP-1 cells were used as an *in vitro* model to evaluate their uptake. The cultures were analysed using a Cellomics KineticScan® high content screening approach. Both nanocomposites penetrated the cell membrane, illuminating the cytoskeleton of the THP-1 macrophage cells but were excluded from the nucleus. Their distribution within the cells also varied, with the gel-TGA-QDs exhibiting a more agglomerated rather than diffuse cytoplasmic localisation as observed for the TGA QDs.

We have evaluated the biocompatibility and toxicity related phenomena due to the introduction of the QDs and a series of controls including gelatin, cadmium and TGA. Toxicity and cell viability were assessed by analysis of nuclear size, cell permeability and lysosomal pH by a multiparameter cytotoxicity HitKit, which contains a three in one fluorescent dye. Dye response can be directly related to changes within the cellular regions and changes in intensity of emission indicate any perturbations. No changes were recorded in nuclear size as no penetration was observed, but the other toxic responses for the TGA QDs were far higher than those exhibited for the gelatin-QDs. In some cases the gelatin-QDs exhibited up to 80% lower toxicity, assessed *via* an aversion to increased cell permeability and more stable values of the lysosomal pH, than the TGA QDs. Controls of cadmium and TGA also proved highly toxic and quickly induced apoptosis, while adding gelatin to the cell cultures proved beneficial for their general well-being. This reduction in the detrimental effects experienced by the cellular system illustrates the potential importance of gelatin as a co-capping agent for QDs to be used in enhanced biological imaging over extended time periods

These results demonstrate the reduced toxicity for the CdTe QD–gelatin nanocomposites and their potential as bioimaging agents. We believe this approach can be used for the development of other nanoparticle composites with low toxicity. These composites may have a range of potential biomedical applications, including diagnostic recognition and treatment of many diseases.

References

[1] V. L. Colvin, M. C. Schlamp, A. P. Alivisatos, *Nature* **1994**, *370*, 354.

[2] J. Lee, V. C. Sundar, J. R. Heine, M. G. Bawendi., K. F. Jensen, *Adv. Mater.* **2000**, *12*, 1102.

[3] J. S. Steckel, P. Snee, S. Coe-Sullivan, J. P. Zimmer, J. E. Halpert, P. Anikeeva, L-A. Kim, V. Bulovic, M. G. Bawendi, *Angew. Chem. Int. Ed.* **2006**, *45*, 5796.

[4] E. Tekin, P. J. Smith, S. Hoeppener, A. M. J. van den Berg, A. S. Susha, A. L. Rogach, J. Feldmann, U. S. Schubert, *Adv. Fun. Mater.* **2006**, *17*, 23.

[5] V. I. Klimov, A. A. Mikhailovsky, S. Xu, A. Malko, J. A. Hollingsworth, C. A. Leatherdale, H. J. Eisler, M. G. Bawendi, *Science* **2000**, *290*, 314.

[6] N. Gaponik, D. V. Talapin, A. L. Rogach, K. Hoppe, E. V. Shevchenko, A. Kornowski, A. Eychmüller, H. Weller, *J. Phys. Chem. B* **2002**, *106*, 7177.

[7] C. L. Li, N. Murase, *Chem. Lett.* **2005**, *34*, 92.

[8] D. V. Talapin, A. L. Rogach, E. V. Shevchenko, A. Kornowski, M. Haase, H. Weller, *J. Am. Chem. Soc.* **2002**, *124*, 5782.

[9] M. A. Malik, P. O'Brien, N. Revaprasadu, *Chem. Mater.* **2002**, *14*, 2004.

[10] P. Reiss, J. Bleuse, A. Pron, *Nano Lett.* **2002**, *2*, 781.

[11] N. N. Mamedova, N. A. Kotov, A. L. Rogach, J. Studer, *Nano Lett.* **2001**, *1*, 281.

[12] H. Mattoussi, J. M. Mauro, E. R. Goldman, G. P. Anderson, V. C. Sundar, F. V. Mikulec, M. G. Bawendi, *J. Am. Chem. Soc.* **2000**, *122*, 12142.

[13] S. Wang, N. Mamedova, N. A. Kotov, W. Chen, J. Studer, *Nano Lett.* **2002**, *2*, 817.

[14] J. K. Jaiswal, H. Mattoussi, J. M. Mauro, S. M. Simon, *Nat. Biotech.* **2003**, *21*, 47.

[15] Y. Zhang, M. K. So, J. Rao, *Nano Lett.* **2006**, *6*, 1988.

[16] H. Zhang, Z. Cui, Y. Wang, K. Zhang, X. Ji, C. Lü, B. Yang, M. Gao, *Adv. Mater.* **2003**, *15*, 777.

[17] M. R. Lorenz, V. Holzapfel, A. Musyanovych, K. Nothelfer, P. Walther, H. Frank, K. Landfester, H. Schrezenmeier, V. Mailander, *Biomater.* **2006**, *27*, 2820.

[18] S. Zhang, J. Yu, X. Li, W. Tian, *Nanotech.* **2004**, *15*, 1108.

[19] X. Hong, J. Li, M. J. Wang, J. J. Xu, W. Guo, J. H. Li, Y. B. Bai, T. J. Li, *Chem. Mater.* **2004**, *16*, 4022.

[20] C. A. Constantine, K. M. Gattas-Asfura, S. V. Mello, G. Crespo, V. Rastogi, T. C. Cheng, J. J. DeFrank, R. M. Leblanc, *Langmuir* **2003**, *19*, 9863.

[21] S. Jaffar, K. T. Nam, A. Khademhosseini, J. Xing, R. S. Langer, A. M. Belcher, *Nano Lett.* **2004**, *4*, 1421.

[22] V. K. Komarala, Y. P. Rakovich, A. L. Bradley, S. J. Byrne, S. A. Corr, Y. K. Gun'ko, *Nanotech.* **2006**, *17*, 4117.

[23] T. Sugimoto, G. E. Dirige, A. Muramatsu, *J. Colloid Interface Sci.* **1996**, *182*, 444.

[24] L. Xu, K. Chen, H. M. El-Khair, M. Li, X. Huang, *Appl. Surf. Sci.* **2001**, *172*, 84.

[25] A. E. Raevskaya, A. L. Stroyuk, S. Y. Kuchmiy, Y. M. Azhniuk, V. M. Dzhagan, V. O. Yukhymchuk, M. Y. Valakh, *Coll. Surf. A: Physicochem. Eng. Asp.* **2006**, *290*, 304.

[26] A. E. Raevskaya, A. L. Stroyuk, S. Y. Kuchmiy, *J. Colloid Interface Sci.* **2006**, *302*, 133.

[27] H. Zhang, Z. Zhou, B. Yang, M. Y. Gao, *J. Phys. Chem. B* **2003**, *107*, 8.

[28] M. Gao, S. Kirstein, H. Mohwald, A. Rogach, A. Kornowski, A. Eychmüller, H. Weller, *J. Phys. Chem. B* **1998**, *102*, 8360.

[29] I. G. Dance, M. L. Scudder, R. Secomb, *Inorg. Chem.* **1983**, *22*, 1794.

[30] H. Zhang, D. Wang, H. Möhwald, *Angew. Chem. Int. Ed.* **2006**, *45*, 748.

[31] Z. A. Peng, X. Peng, *J. Am. Chem. Soc.* **2001**, *123*, 1389.

[32] Z. A. Peng, X. Peng, *J. Am. Chem. Soc.* **2002**, *124*, 3343.

[33] X. Peng, L. Manna, W. Yang, J. Wickham, E. Scher, A. Kadavanich, A. P. Alivisatos, *Nature* **2000**, *404*, 59.

[34] Q. Pang, L. J. Zhao, Y. Cai, D. P. Nguyen, N. Regnault, N. Wang, S. H. Yang, W. K. Ge, R. Ferreira, G. Bastard, J. N. Wang, *Chem. Mater.* **2005**, *17*, 5263.

[35] D. J. Milliron, S. M. Hughes, Y. Cui, L. Manna, J. Li, L.-W. Wang, A. P. Alivisatos, *Nature* **2004**, *430*, 190.

[36] W. W. Yu, L. H. Qu, W. Z. Guo, X. G. Peng, *Chem. Mater.* **2003**, *15*, 2854.

[37] A. M. Kapitonov, A. P. Stupak, S. V. Gaponenko, E. P. Petrov, A. L. Rogach, A. Eychmüller, *J. Phys. Chem. B* **1999**, *103*, 10109.

[38] L. Qu, W. W. Yu, X. Peng, *Nano Lett.* **2004**, *4*, 465.

[39] R. W. Meulenberg, G. F. Strouse, *J. Phys. Chem. B* **2001**, *105*, 7438.

[40] X. Peng, J. Wickham, A. P. Alivisatos, *J. Am. Chem. Soc.* **1998**, *120*, 5343.

[41] S. J. Byrne, S. A. Corr, T. Y. Rakovich, Y. K. Gun'ko, Y. P. Rakovich, J. F. Donegan, S. Mitchell, Y. Volkov, *J. Mat. Chem.* **2006**, *16*, 2896.

[42] Z. Tang, B. Ozturk, Y. Wang, N. A. Kotov, *J. Phys. Chem. B* **2004**, *108*, 6927.

[43] A. Shavel, N. Gaponik, A. Eychmüller, *J. Phys. Chem. B* **2006**, *110*, 19280.

[44] J. Guo, W. Yang, C. Wang, *J. Phys. Chem. B* **2005**, *109*, 17467.

[45] L. Qu, X. Peng, *J. Am. Chem. Soc.* **2002**, *124*, 2049.

[46] L. Li, H. Qian, N. Fang, J. Ren, *J. Lumin.* **2006**, *116*, 59.

[47] J. O. Winter, N. Gomez, S. Gatzert, C. E. Schmidt, B. A. Korgel, *Colloids Surf. A: Physicochem. Eng. Asp.* **2005**, *254*, 147.

[48] E. J. Holmyard, W. G. Palmer, *Inorganic Chemistry* **1952**, *Dent and Sons*.

[49] M. A. Vairavamurthy, W. S. Goldenberg, S. Ouyang, S. Khalid, *Marine Chem.* **2000**, *70*, 181.

[50] B. Tang, J. Niu, C. Yu, L. Zhuo, J. Ge, *Chem. Comm.* **2005**, 4184.

[51] J. Li, X. Hong, D. Li, K. Zhao, L. Wang, H. Wang, Z. Du, J. Li, Y. Bai, T. Li, *Chem. Comm.* **2004**, 1740.

[52] A. Hoshino, K. Fujioka, T. Oku, M. Suga, Y. F. Sasaki, T. Ohta, M. Yasuhara, K. Suzuki, K. Yamamoto, *Nano Lett.* **2004**, *4*, 2163.

[53] A. M. Derfus, W. C. W. Chan, S. N. Bhatia, *Nano Lett.* **2004**, *4*, 11.

[54] E. Chang, N. Thekkek , W. W. Yu, V. L. Colvin, R. Drezek, *Small* **2006**, *2*, 1412.

[55] A. Shiohara, A. Hoshino, K. Hanaki, K. Suzuki, K. Yamamoto, *Microbiol.Immunol.* **2004**, *48*, 669.

[56] J. Lovrić, H. S. Bazzi, Y. Cuie, G. R. A. Fortin, F. M. Winnik, D. Maysinger., *J. Mol. Med.* **2005**, *83*, 377.

[57] V. A. Sinani, D. S. Koktysh, B. G. Yun, R. L. Matts, T. C. Pappas, M. Motamedi, S. N. Thomas, N. A. Kotov, *Nano Lett.* **2003**, *3*, 1177.

[58] C. Kirchner, T. Liedl, S. Kudera, T. Pellegrino, A. MunozJavier, H. E. Gaub, S. Stolzle, N. Fertig, W. J. Parak, *Nano Lett.* **2005**, *5*, 331.

[59] A. Nel, T. Xia, L. Madler, N. Li, *Science* **2006**, *311*, 622.

[60] K. Boldt, O. T. Bruns, N. Gaponik, A. Eychmüller, *J. Phys. Chem. B* **2006**, *110*, 1959.

[61] J. Ma, C. Ji-Yao, J. Guo, C. C. Wang, W. L. Yang, L. Xu, P. N. Wang, *Nanotech.* **2006**, *17*, 2083.

[62] G. Guo, W. Liu, J. Liang, Z. He, H. Xu, X. Yang, *Mater. Lett.* **2007**, *61*, 1641.

[63] B. P. Aryal, K. P. Neupane, M. G. Sandros, D. E. Benson., *Small* **2006**, *2*, 1159.

[64] R. Bakalova, H. Ohba, Z. Zhelev, T. Nagase, R. Jose, M. Ishikawa, Y. Baba, *Nano Lett.* **2004**, *4*, 1567.

[65] J. Lovrić, S. J. Cho, F. M. Winnik, D. Maysinger, *Chem. Biol.* **2005**, *12*, 1227.

[66] W.-H. Chan, N.-H. Shiao, P.-Z. Lu, *Toxicol. Lett.* **2006**, *167*, 191.

[67] S. T. Selvan, T. T. Tan, J. Y. Ying, *Adv. Mater.* **2005**, *17*, 1620.

[68] T. Franzl, D. S. Koktysh, T. A. Klar, A. L. Rogach, J. Feldmann, N. Gaponik, *Appl. Phys. Lett.* **2004**, *84*, 2904.

[69] M. Kondoh, S. Araragi, K. Sato, M. Higashimoto, M. Takiguchi, M. Sato, *Toxicol.* **2002**, *170*, 111.

[70] D. A. Limaye, Z. A. Shaikh, *Toxicol. Appl. Pharmacol.* **1999**, *154*, 59.

[71] L. E. Rikans, T. Yamano., *J. Biochem. Molec. Tox.* **2000**, *14*, 110.

[72] E. Lopez, S. Figueroa, M. J. Oset-Gasque, M. P. Gonzalez, *Br. J. Pharmacol.* **2003**, *138*, 901.

Chapter 5: Non-steroidal anti-inflammatory drug (NSAID) – QD conjugates

5.1. Introduction

Biological activation and the manipulation of surface terminal groups of QDs is a topic that has been widely explored recently. [1-4] When the QDs are synthesised with various capping groups on the surface such as carboxylic acids or amines, these functionalities can act as a template for the additional construction of novel and exciting moieties. [5-7] One may study the characteristic effects, not only by conventional absorption and luminescence spectroscopy, but also by their potential use in a biologically relevant system.

Examples of such functionalised materials are numerous in biological studies and have been efficiently conjugated to a wide variety of biomolecules in an effort to enhance their biolabelling capabilities and to investigate the mechanism of their cellular interaction. [8-11] Many groups have focussed on this modification of the QD surface after fabrication and have shown that biologically active compounds such as enzymes, [12] antibodies, [13, 14] peptides [15] and oligonucleotides [16, 17] may be attached to the crystallite *via* traditional peptide coupling reactions with subsequent amide bond formation. [8, 13, 18]

This part of the work focussed on the production of novel stabiliser molecules, based on commercially available nonsteroidal anti-inflammatory drugs (NSAIDs) for the synthesis of new CdTe QD nanocomposites. It was hoped that the modification of these molecules, with the availability of a free thiol for QD surface interaction, would lead to the generation of a new class of derivatised CdTe QDs.

One of our main goals was to analyse these nanocomposites in living cells, more specifically THP-1 macrophages. These cells form part of the bodies' autoimmune response and we wanted to conjugate drug molecules which have known effects for such systems. [19-22] We also wished to find out if these NSAID - QD nanocomposites would be stable in a cellular environment and if they could possibly be used as drug delivery agents.

NSAIDs possess anti-inflammatory properties and are the most commonly prescribed drugs (in particular aspirin and ibuprofen) for the treatment of conditions such as arthritis, muscle and back pain. They act by non-selective inhibition of the enzyme cyclooxygenase (COX), which can be present as COX-1, which protects the stomach lining from harsh acids and COX-2, produced during inflammation. Cyclooxygenase actively catalyses the production of prostaglandins and these molecules act as messenger molecules during the inflammation process. [23]

The NSAIDs, ibuprofen and naproxen, were chosen as candidates for conjugation, due to their cost, their fluorescent properties (possible fluorescence resonance energy transfer [FRET] processes) and their potential functionalisation *via* their carboxylic acid group. Previously, ibuprofen was successfully anchored inside the mesoporous channels of silica and on a silica gel surface *via* ester bonds. [24] The use of nanostructured silica allowed for the protection of the drug due to its location inside the pores of the matrix, where it has the potential to be released gradually by the cleavage of the ester bonds by esterases *in vivo*. Our target drug conjugate molecules are shown in Figure 5.1.

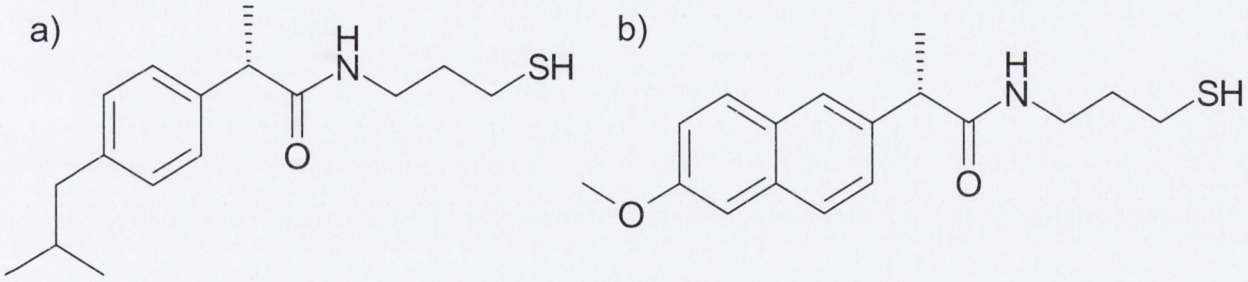


Figure 5.1. **a)** Structure of the ibuprofen hybrid [2-(4-Isobutyl-phenyl)-*N*-(3-mercapto-propyl)-propionamide] and **b)** structure of the naproxen hybrid [*N*-(3-Mercapto-propyl)-2-(6-methoxy-naphthalen-2-yl)-propionamide].

5.1.1 Initial reaction sequence to be employed

The conjugation reaction of a molecule bearing a carboxylic acid group and a free amine to form an amide bond was chosen due to its simplicity and well documented experimental procedure. [11, 13, 25] The direct binding of these molecules to the QD surface is only possible if a thiol group is available. However, the highly reactive thiol group

must be protected in advance of any coupling reactions between free carboxylic acid and amino groups. As such, the disulfide molecule (2,2'-dithiobis(ethylamine) dihydrochloride) was chosen as a linking intermediate between the prospective drug molecule and the QD surface (Figure 5.2). This disulfide allows for the reaction to proceed only at the terminal amine groups and facilitates subsequent reduction of the disulfide bond to generate the free thiol. The thiol is then able to coordinate to the cadmium ions in solution and subsequently be incorporated into the production of QDs.

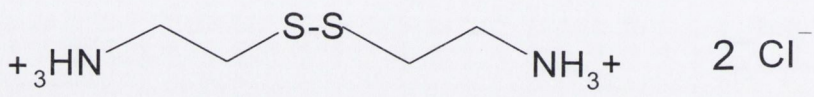
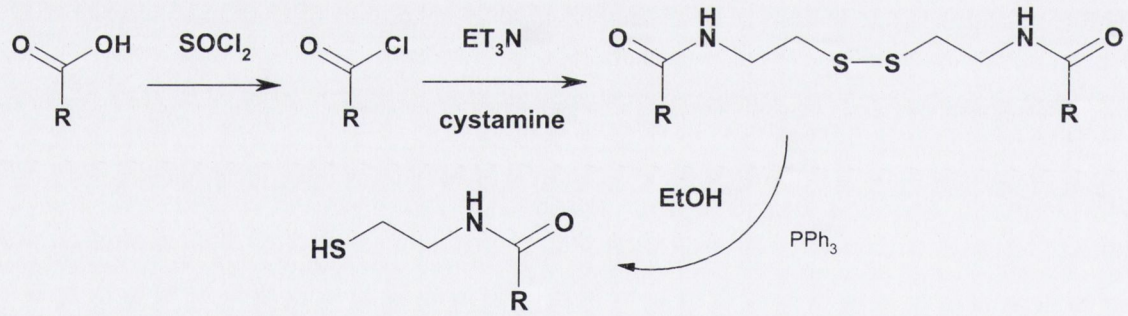


Figure 5.2. Structure of 2,2'-dithiobis(ethylamine) dihydrochloride (cystamine dihydrochloride).

A description of the overall reaction sequence to be employed is illustrated in (Scheme 5.1).



R = ibuprofen, naproxen etc.

Scheme 5.1. Reaction sequence for the chlorination of the carboxylic acid function of a molecule, its reaction with cystamine and the subsequent reduction of the disulfide *via* triphenyl phosphine (PPh_3) to give the free thiol.

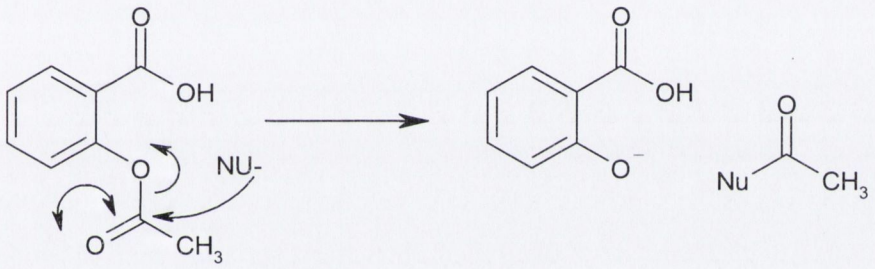
The reaction begins with the generation of the acid chloride from the carboxylic acid by reaction with $SOCl_2$. This acid chloride is then reacted with the two free amines in a 2:1 molar excess. The breaking of the disulfide bond is achieved by reaction with triphenyl phosphine (PPh_3) in ethanol and the free thiol is easily recognisable in TLC by

the addition of 5,5′-Dithiobis(2-nitrobenzoic acid) [DTNB] which generates a bright yellow stain. This new thiol could then be incorporated directly *in situ* into the parent precursor solution for the preparation of new QDs.

5.2 Synthesis of new thiol containing drug conjugates

5.2.1 Synthesis and characterisation of N-(2-Mercaptoethyl)benzamide

Initially, aspirin was chosen as the molecule on which to perform the preliminary studies. This is the most commonly known and most widely used NSAID. However, this proved to be an unsuccessful template due to the lability of the *O*-acetyl group, which prevented selective reaction at the carboxylic acid (Scheme 5.2). Consequently, a different molecule possessing similar properties was required.



Scheme 5.2. Structure of aspirin and the reaction of a nucleophile (Nu^-) illustrating the lability of the *O*-acetyl group.

To avoid the further use of an expensive drug molecule, the first test molecule chosen was benzoyl chloride (Figure 5.3, **a**), as the acid chloride was already present thus eliminating a synthetic step. It could serve as a preliminary test to investigate the feasibility of the synthetic procedure in generating a molecule that could in fact stabilise the CdTe QDs. According to scheme 5.1, excluding the first step, the molecule N-(2-mercaptoethyl)benzamide was successfully synthesised *via* a two step reaction sequence (Figure 5.3 **b**). This compound was characterised by ^1H NMR spectroscopy (400 MHz, $CDCl_3$) (Appendix 5a).

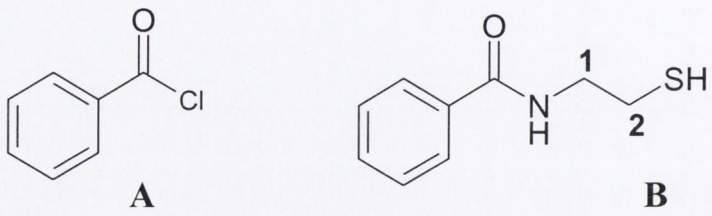


Figure 5.3. **a**) Structure of benzoyl chloride and **b)** N-(2-mercaptoethyl)benzamide.

The ^{1}H NMR spectrum shows a triplet at 1.40 ppm corresponding to the SH proton, two multiplets at 2.76 and 3.61 ppm corresponding to the CH_2 protons closest to the SH (1) and NH (2) respectively. The NH proton peak is seen at 6.94 ppm, and the aromatic protons are seen at 7.40 ppm (meta), 7.49 ppm (para) and 7.79 ppm (ortho).

5.2.2 Synthesis and characterisation of N-(2-Mercaptoethyl)benzamide capped QDs

This compound was produced on a large enough scale to attempt preliminary trials as a novel stabiliser for the CdTe QDs. The same procedure outlined in Chapter 2 for the production of the QDs was applied, except DMF was used as the solvent instead of water. N-(2-mercaptoethyl)benzamide was incorporated into the synthesis and a dark, brown-red coloured solution was produced after heating to reflux. This colour for an aqueous solution of TGA or MPA capped QDs is generally indicative of a sample about to decompose or one that contains poor QDs. As this solution remained stable for several weeks at 4° C, the colour can only be attributed to a poorly passivated QD ensemble with lots of defect states. The QDs were then purified by size selective precipitation using water as a non-solvent. The purified and unpurified samples were characterized by UV-vis absorption (Figure 5.4) and luminescence spectroscopy (Figure 5.5).

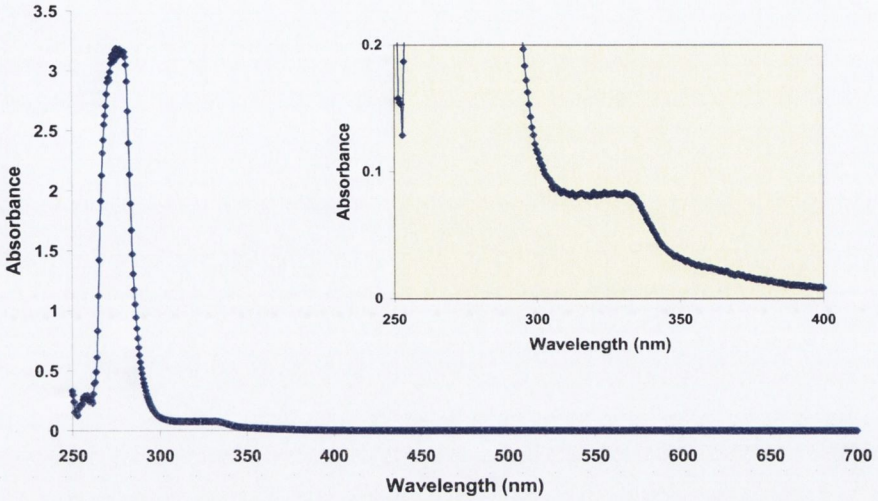


Figure 5.4. UV-vis absorption spectrum of N-(2-mercaptoethyl)benzamide in DMF. Insert: expanded region between 250 & 400 nm.

Figure 5.4 shows the absorption spectrum of N-(2-mercaptoethyl)benzamide in DMF with a peak at 275 nm and shoulder at 330 nm. As shown in Figure 5.5, this molecule possesses a weak fluorescence at 410 nm when excited over a variety of wavelengths.

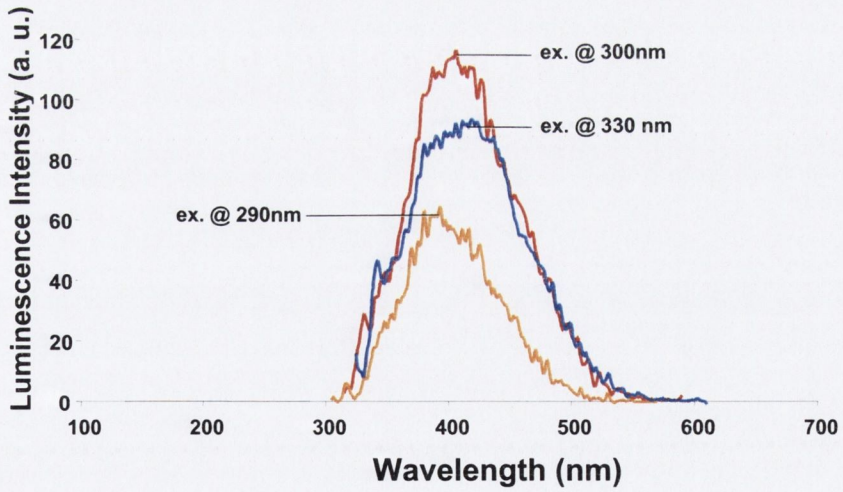


Figure 5.5. Luminescence emission spectra of N-(2-mercaptoethyl)benzamide (λ_{ex} 290, 300 and 330 nm) in DMF.

Following the synthesis of the QDs and incorporation of the N-(2-mercaptoethyl)benzamide molecule, an emission for both the QDs and the free molecule was visible for the crude solution (insert Figure 5.6). The fact that an emission peak inherent to QDs was produced indicates that the thiol does in fact bind to the cadmium rich surface. This binding and surface coverage must not be efficient, as values of the QY were quite poor reaching a maximum of only 4%. This presence of a peak for the N-(2-mercaptoethyl)benzamide in the emission spectrum for the crude, unpurified sample (insert Figure 5.6) indicates that not all of the molecules added to the precursor mixture are incorporated to form a passivating shell. This may be the reason for the poor QY values obtained.

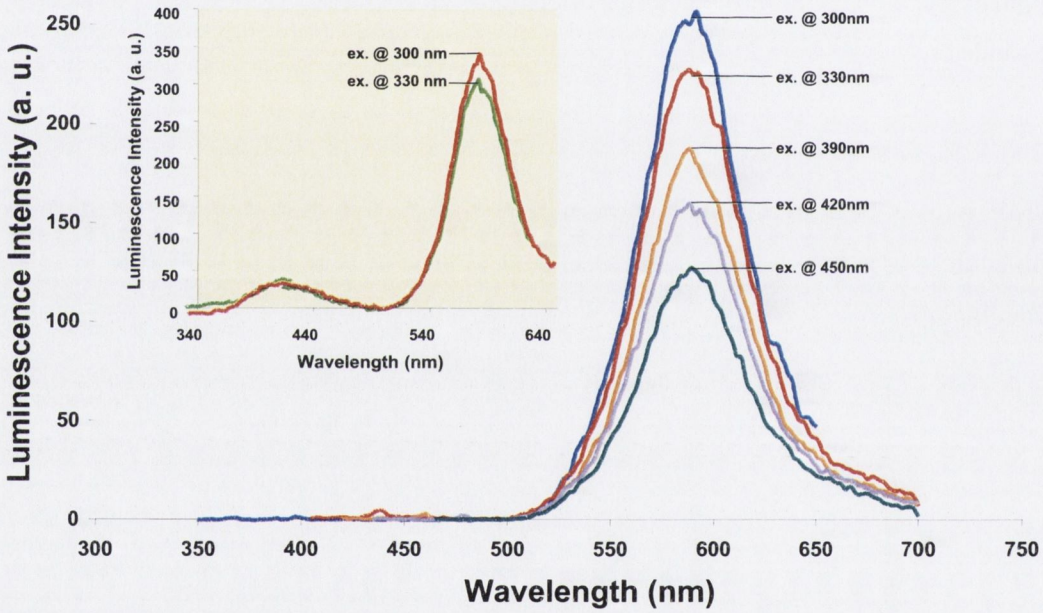


Figure 5.6. Luminescence emission spectra of the purified N-(2-mercaptoethyl)benzamide nanocomposite excited at a variety of wavelengths. **Insert:** Luminescence spectrum of the unpurified sample.

When the sample was purified, the excess unreacted N-(2-mercaptoethyl)benzamide molecules were removed and consequently, the emission band for the free stabiliser molecules is no longer present (Figure 5.6). The QD emission is still visible when excited over a variety of wavelengths. This range incorporates values that

overlap with the absorption spectrum of the N-(2-mercaptoethyl)benzamide and should theoretically also excite the molecule. As no emission is seen, it either must be quenched or transferred to the QDs but as no substantial increases due to potential FRET are observed in the emission intensity this can be ruled out.

In summary, relatively stable but poor quality QDs were produced using N-(2-mercaptoethyl)benzamide as a stabilising agent. However, as one of our goals was to investigate these nanocomposites in biological systems, the distinct lack of water solubility proved problematic to perform any further biological tests. Attempts to re-dissolve the purified fractions in 5% DMSO also failed. As a result, it was decided not to use this procedure on the more expensive and larger naproxen and ibuprofen molecules.

5.3 Synthesis and characterisation of water soluble NSAIDs

5.3.1 Introduction

For the reasons stated above, it was necessary to impart some water solubility on the system. This was achieved by modifying the linker in an effort to increase the hydrophilic nature of the molecule synthesised. Consequently, it was decided to use 2,2′-(ethylenedioxy)diethylamine [amino-PEG] (Figure 5.7), which is a short chain molecule containing oxygen atoms and is capped by terminal amino groups.

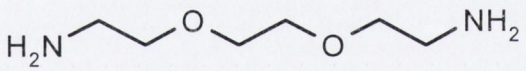
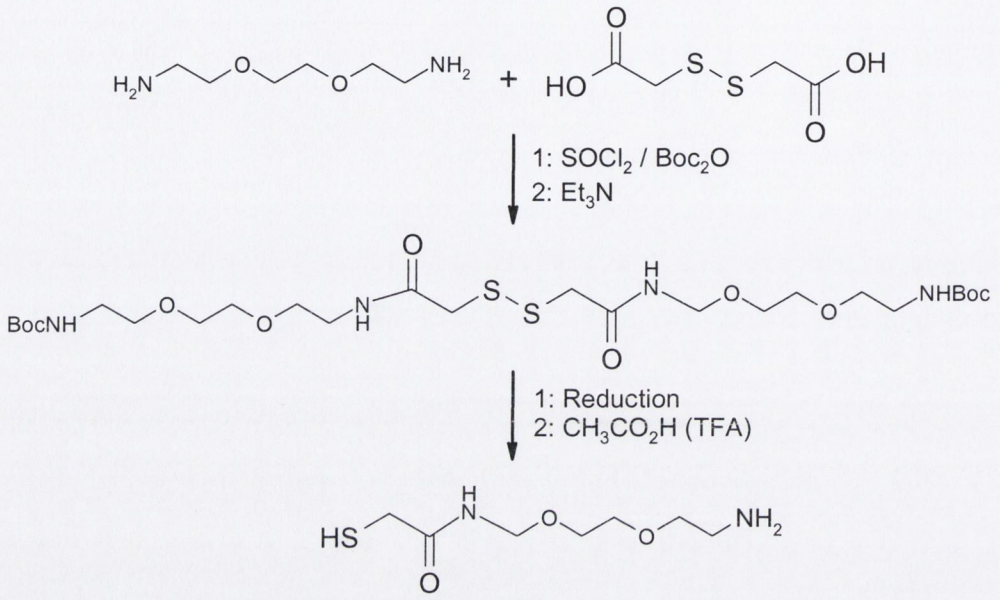


Figure 5.7. Structure of 2,2′-(ethylenedioxy)diethylamine [amino-PEG].

This molecule is readily soluble in water and also possesses two free amino groups which are available for the same sort of coupling reactions described previously (Scheme 5.1). However, there are no sulfur atoms present which could be used for attachment to the QD surface. Therefore, this molecule could only serve as a linker between carboxylic acid capped QDs that have been synthesised and purified and the drug molecule that we wanted to bind.

As this procedure required a significant alteration to the previous synthetic path, it was first investigated if a more appropriate disulfide molecule could be used. 2,2′-dithiodiacetic acid (diTGA), the disulfide of the most common capping agent, TGA, was

reacted with this linker in an effort to generate an extremely water soluble intermediate that possessed a thiol group (Scheme 5.3).



Scheme 5.3. Reaction sequence for conjugation of the amino-PEG with diTGA. $SOCl_2$ is used to generate the acid chloride of the carboxylic acid, Boc_2O (di-*tert*-butyl dicarbonate)is used as a typical protection group for amines. TFA (trifluoracetic acid) is then used to remove the Boc protecting group while the disulfide bond is reduced with PPh_3 to give the free thiol.

The synthesis of this molecule proved unsuccessful and a further investigation of the literature revealed that the relatively acidic nature of the α-proton of the diTGA molecule compromises any reaction and leads to the formation of a variety of by-products. [26] Consequently, it was decided to first conjugate the amino-PEG linker to the drug molecule before binding to the QD surface using the well established 1-ethyl-3-(3-dimethylaminopropyl)-carbodiimide (EDC) coupling method. [9, 11, 13, 25] Synthetic molecular nano-conjugates have previously been developed, such as folic acid coated magnetic nanoparticles, [27] along with modified serotonin, [10] antigen/antibodies, [11, 13] albumin, [8] and proteins [28] bound to QDs. These strategies generally involve EDC coupling or replacement of organic stabilising ligands such as TOPO with thiol containing moieties *via* an exchange mechanism in an effort to improve aqueous solubility or biological activity. In relation to these studies, our aim was to conjugate the

non-steroidal anti-inflammatory drugs (NSAID) naproxen and ibuprofen to the amino-PEG and then bind to the aqueous CdTe QDs.

5.3.2 Spectroscopic characterisation of ibuprofen and naproxen

Ibuprofen and naproxen were chosen primarily since, as mentioned previously, they possess well-defined anti-inflammatory properties [19, 22] and additionally because they display measurable luminescent properties.

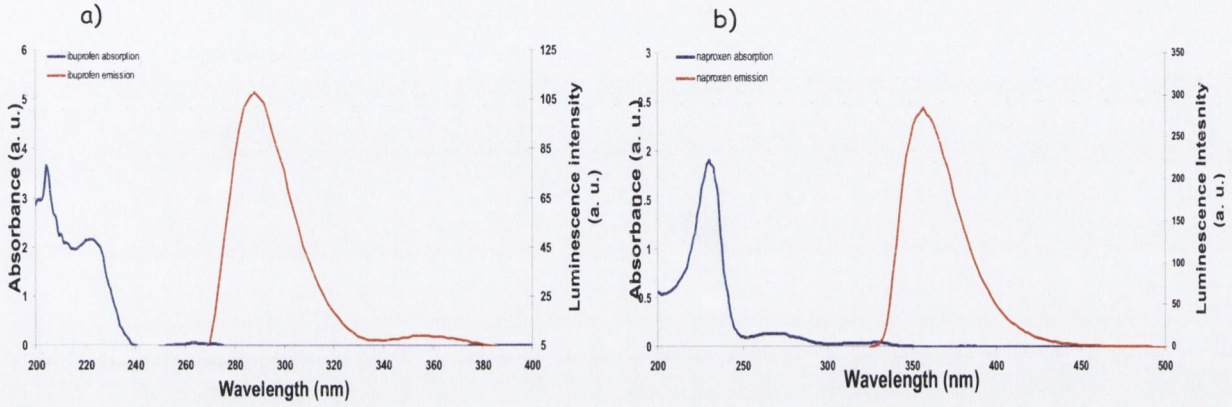


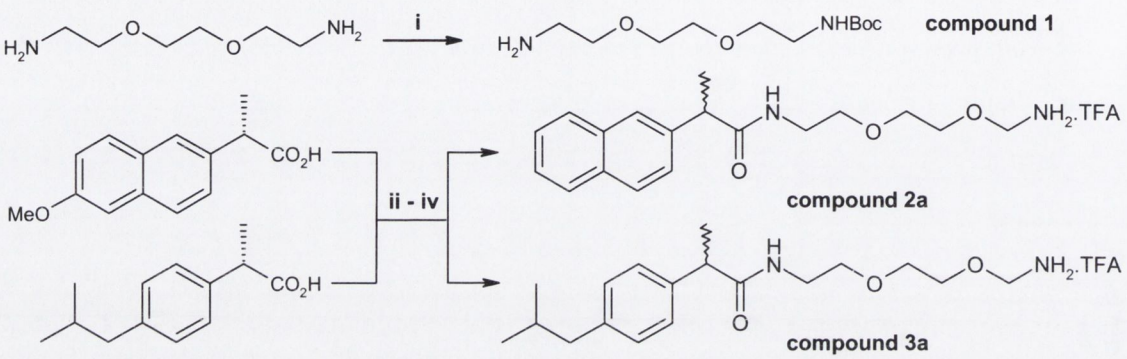
Figure 5.8. a) UV-vis absorption (blue) and luminescence emission spectrum (λ_{ex} 220 nm / λ_{em} 287 nm) [29] (red) of ibuprofen. **b)** UV-vis absorption (blue) and luminescence emission spectrum (λ_{ex} 233 nm / λ_{em} 353 nm) [30] (red) of naproxen. (Spectra taken in water).

Indeed, emission is seen at 356 and 288 nm for the naproxen **(a)** and ibuprofen **(b)** moieties respectively (Figure 5.8). Note, both drugs show emission profiles that do not overlap with that of the QDs, which have emission peaks greater than 500 nm, allowing for the easy identification of any unbound species.

5.3.3 Synthesis of water soluble NSAIDs

Aqueous conjugation of the NSAIDs to TGA capped QDs required the use of a water soluble drug bearing a free amine functionality to facilitate the formation of an amide bond. In order to fulfil these demands, we improved the solubility of the NSAID drug molecules by conjugating them to a 2,2′-(ethylenedioxy)diethylamine linker [amino-PEG] (Figure 5.7). Linking QDs to PEG molecules has previously been used to help alleviate the problem of non-specific binding of the QDs to cells. [2, 3] A three-step

reaction led, reproducibly, to the desired modified drug molecule with acceptable yields of 70%. This short procedure (Scheme 5.4), for a previously unsynthesised intermediate, imparted water solubility on the 'linked' drug molecule while also providing an amino group ready for further conjugation.



i) Boc_2O, dioxane, rt, 80-90%; **ii)** $SOCl_2$, DCM, 40°C; **iii) compound 1,** Et_3N, THF, 0°C to rt, 60-70% over both steps; **iv)** TFA, DCM, 0°C, 90-95%

Scheme 5.4. Synthetic pathway for the Boc protection of 2,2′-(ethylenedioxy)diethylamine (**compound 1**), its reaction with naproxen / ibuprofen chloride and subsequent deprotection to give the TFA salt of the free amine (**compounds 2a** and **3a**).

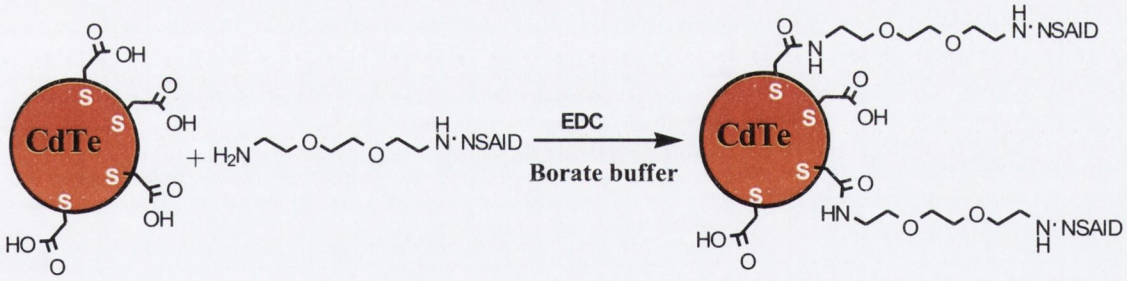
Scheme 5.4 illustrates the reaction pathway for the synthesis of the amino-PEG conjugated NSAID molecules. The first step was the synthesis of {2-[2-(2-amino-ethoxy)-ethoxy}-ethyl}-carbamic acid tert butyl ester [boc-amino-PEG: **compound 1**] *via* the mono Boc [*tert*-butyl carbamate] protection of the 2,2'-(ethylenedioxy)bis-(ethylamine). [31] This was accomplished by reaction of the 6 equivalents of amino-PEG with Boc anhydride (Boc_2O) in dioxane at room temperature. This excess was necessary to facilitate only the mono–protection of one amine group. This compound was charactersed by ^1H and ^{13}C NMR [Appendix 5b].

The next step was the synthesis of *tert*-butyl 2-(2-(2-(2-(6-methoxynaphthalen-2-yl)propanamido)ethoxy)ethoxy)ethylcarbamate [npx-boc-amino-PEG: **compound 2**, this molecule was characterised by ^1H and ^{13}C NMR, see Experimental section] and *tert*-butyl 2-(2-{2-[2-(4-isobutylphenyl)propanamido]ethoxy}ethoxy) ethylcarbamate [ibu-boc-amino-PEG: **compound 3**, this molecule was characterised by ^1H and ^{13}C NMR see Experimental section].

Compound 1 was reacted with the acid chlorides (produced by reaction of ibuprofen / naproxen with $SOCl_2$ in DCM) of the drug to produce **compounds 2** and **3** respectively. The Boc group was removed *via* the addition of TFA (50:50 - TFA:DCM) to give N-2-(2-(2aminoethoxy)ethoxy)ethyl)-2-(6-methoxynaphthalen-2-yl)propanamide, (npx-amino-PEG-NH_2, **compound 2a**) and N-(2-{2-[2-aminoethoxy]ethoxy}ethyl)-2-(4-isobutylphenylpropanamide, (ibu-amino-PEG-NH_2, **compound 3a**), the TFA salts of the new PEG modified NSAIDs (Scheme 5.4).

5.4 Preparation of NSAID CdTe QD conjugates

Following on from the production of the desired water soluble drug molecules, the next step was their conjugation to TGA capped QDs. TGA QDs were prepared according to the published procedure [32] as outlined in Chapter 2. The QD fractions were separated from the parent solution *via* size selective precipitation using isopropanol, re-dissolved in water, purified on a sephadex (G 25) column to remove any remaining unreacted moieties and stored at 4°C. The conjugation between the amino functionality on the modified NSAIDs and the carboxylic acid function of a known concentration of TGA QDs [33] was carried out in a one step reaction using EDC as the coupling agent (Scheme 5.5).



Scheme 5.5. Schematic representation of the conjugation reaction between the water soluble NSAIDs and CdTe QDs (not to scale).

This conjugation reaction was undertaken in borate buffer at pH 7.5 in order to prevent the aggregation of the QDs and a drop in luminescence emission that occurs at low pH values, ie. less than 4. [5] Indeed, some experiments carried out only in millipore water with a substantial excess of EDC·HCl (~ 400 molar equivalents) led to a rapid precipitation of the QDs due the EDC·HCl mediating a drop in pH. A further drop in pH

was also observed under the same conditions on addition of the water soluble NSAIDs as the drug was present as its TFA salt. Furthermore, various experiments carried out with different sizes of QDs and different molar equivalents of EDC and the drug derivatives led, in some cases, to a rapid coagulation of the QDs. These results suggested that the concentrations of the drug and coupling reagent required for the reaction to occur successfully, was highly dependent on the QD size. In our experiments, 3.1 nm sized QDs (λ_{em} 566 nm) [33] were reacted using an optimised coupling reaction with a 25 molar excess of the linked-naproxen and a 100 molar excess of EDC.

Typically, 80 µl of a solution of **compound 2a**, **3a** (0.1g / 5ml buffer) (25 molar excess) was added to 0.25 mL of concentrated QDs. The volume was increased to 2 ml with buffer (final QD concentration ~ 5 x 10^{-5}) (sb28) and the reagents were stirred for 10 minutes. 1 mg of EDC was added to the reaction mixture. The QDs were allowed to react at room temperature for 1 hour and then were stored in the fridge overnight allowing the unreacted EDC to hydrolyse and lose activity. [13] The solution was further purified by sephadex (G-25) chromatography, and a coloured luminescent fraction of approximately 2 ml was collected, filtered through a 0.2 µm filter (to remove any sephadex that may have come through the column) and stored again at 4° C for further characterisation and use.

5.4.1 UV-vis absorption and luminescence emission spectra of the NSAID – QD conjugates

This reaction was studied at various time intervals to monitor the spectroscopic effect that the binding of the NSAIDs had on the QDs. The absorption and luminescence spectra were monitored during reaction, after storage and finally after purification (Figure 5.9 and 5.10).

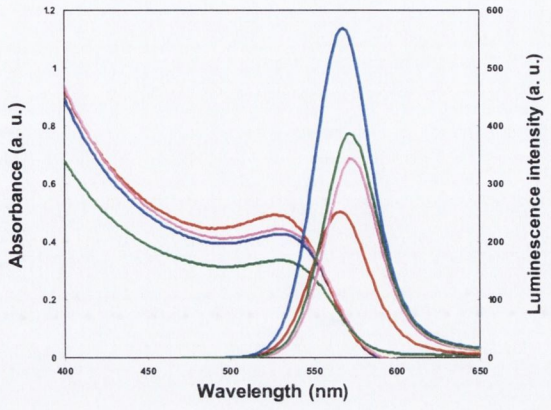


Figure 5.9. UV-vis absorption and luminescence emission spectra (λ_{ex} 450 nm) taken before, during and after the conjugation of npx-amino-PEG-NH_2 to the QDs. [Red line: original QDs, blue line: conjugation reaction after 1 hour, pink line: QDs following storage overnight, green line: QDs following sephadex purification].

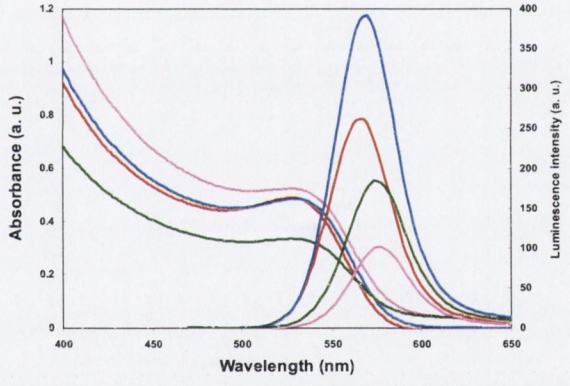


Figure 5.10. UV-vis absorption and luminescence emission spectra (λ_{ex} 450 nm) taken during and after the conjugation of ibu-amino-PEG-NH_2 to the QDs. [Red line: original QDs, blue line: conjugation reaction after 1 hour, pink line: QDs following storage overnight, green line: QDs following purification].

Figures 5.9 and 5.10 show, the UV-vis absorption and emission spectrum (λ_{ex} 450 nm) of the QDs conjugated to **compounds 2a** and **3a** (npx-amino-PEG-NH_2 and ibu-amino-PEG-NH_2) respectively. Upon conjugation of the drug, an initial emission intensity improvement for both conjugates was seen (red lines); however, this was then followed by a decrease after storage and purification (green lines). Coupled to changes in their emission intensities, the samples also displayed a small red shift of 6 nm with

reaction time, which can be attributed to QD interactions and slight aggregation effects within the ensemble. [34] This red shift was more pronounced for the ibu-amino-PEG-NH_2 conjugates.

Nevertheless, the final fluorescence efficiency when purified remained higher for the npx-amino-PEG-NH_2 (QY 27% compared to 20%) but lower for the ibu-amino-PEG-NH_2 (QY 15% compared to 20%). Increases can be accredited to the addition of the hydrophobic drug molecule. This may result in the partial elimination of the surface bound oxygen and water molecules, which can act as potential traps for the surface recombining excitons. As such, their removal enhances radiative recombination and luminescence QY. The decreases witnessed for ibuprofen are possibly due to increased aggregation and precipitation of QDs from solution, which effectively reduces the number of QDs contributing to the emission efficiency.

Throughout the reaction, no discernable changes were noted in the UV-vis absorption spectra indicating that there were no adverse affects to the crystal lattice and any changes in the emission can be attributed to surface interactions of the various reacting species.

5.4.2 Fluorescence lifetime decay analysis

These variations in the luminescence intensity were further corroborated *via* analysis of the lifetime distributions by using time-correlated single photon counting, which displayed an increase in fluorescence lifetime for the naproxen conjugates compared to that of the original QDs (Figure 5.11, Table 5.1).

For all measured luminescence decay curves, samples were excited by 480 nm picosecond pulses and can be successfully simulated using a biexponential function with a shorter lifetime equal to 2–5 ns (band-gap recombination), and a longer one in the range of 18–25 ns (surface recombination). [35-38]

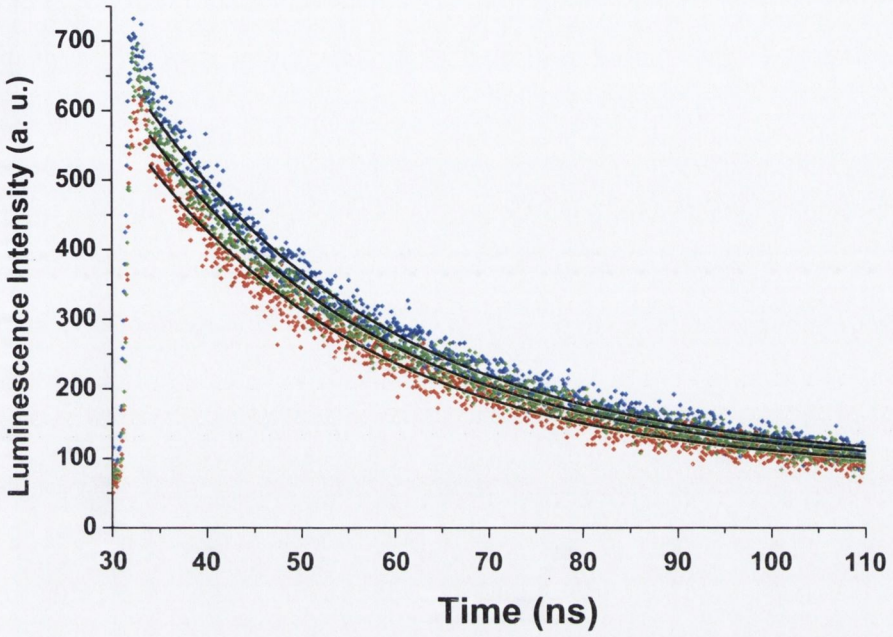


Figure 5.11. Time-dependent luminescence intensity decays for solutions of original TGA-QDs (green line) and the ibuprofen (red line) and naproxen (blue line) QD conjugates. Results of a two-exponential analysis of the decay curves are shown by thick black lines.

Table 5.1. Two exponential fit parameters to the observed luminescence decays (in solution) of original TGA QDs and the npx-amino-PEG-NH_2 and ibu-amino-PEG-NH_2 QD conjugates. The shorter lifetime (τ_1) can be attributed to the intrinsic recombination of populated core states, while the longer lifetime (τ_2) can be associated with the involvement of surface states in the carrier recombination processes. Comparison of the α values gives us an indication of the relative contribution that each part of the radiative lifetime contributes to the average total (τ_{av}).

Sample	τ_1 (ns)	α_1	τ_2 (ns)	α_2	τ_{av} (ns)
Original QDs	2.7	0.60	19.5	0.40	**16.6**
npx-amino-PEG-NH_2 conjugate	3.8	0.46	23.4	0.54	**21.0**
ibu-amino-PEG-NH_2 conjugate	3.1	0.44	18.1	0.56	**15.6**

The data from our time-resolved luminescence measurements imply that conjugation of the NSAID is accompanied by the interaction with trap states of the QDs, i.e. surface impurities with a high electron affinity. The luminescence decay is dominated by two emission components with corresponding lifetimes in the nanosecond time scale (Table 5.1), consistent with a luminescence model that includes multiple emission pathways. [39] This multiexponential behaviour is almost universal in the luminescence dynamics of semiconductor QDs. [39-41] The shorter lifetime can be attributed to the intrinsic recombination of populated core states, [36-38, 42] while the longer lifetime can be associated with the involvement of surface states in carrier recombination processes. [38]

The extremely small size and high surface-to-volume ratio of the QDs imply a strong influence of surface stabilising molecules on their optical spectra. Since the wavefunction of electrons and holes in QDs extends across the particle surface, photoexcited carriers may be easily captured at the surface traps where they recombine non-radiatively. Such a mechanism was proposed to be mainly responsible for the reduced luminescence intensity in CdS QDs [43] and modification of the luminescence decay kinetics due to changes in the surface conditions. [38, 44] Increases in value for the NSAID-QD conjugates and enhanced contributions from the longer lifetime component, clearly indicates that insufficiently passivated surface native defects such as tellurium or cadmium vacancies can be efficiently eliminated upon conjugation, possibly due to the increased steric bulk or hydrophobic nature of the NSAID molecules.

Following the conjugation reaction, the behaviour of the QD conjugates in solution and the increases in luminescence lifetimes were also monitored using fluorescence confocal microscopy (Figure 5.12) The colour-map images give an indication of the average lifetime of the sample, note colour change from a highly green image (shorter lifetime) to a more yellow / yellow orange image (longer lifetime) following conjugation. The QD stability and morphology is outlined by the uniformity of the colour-map distribution.

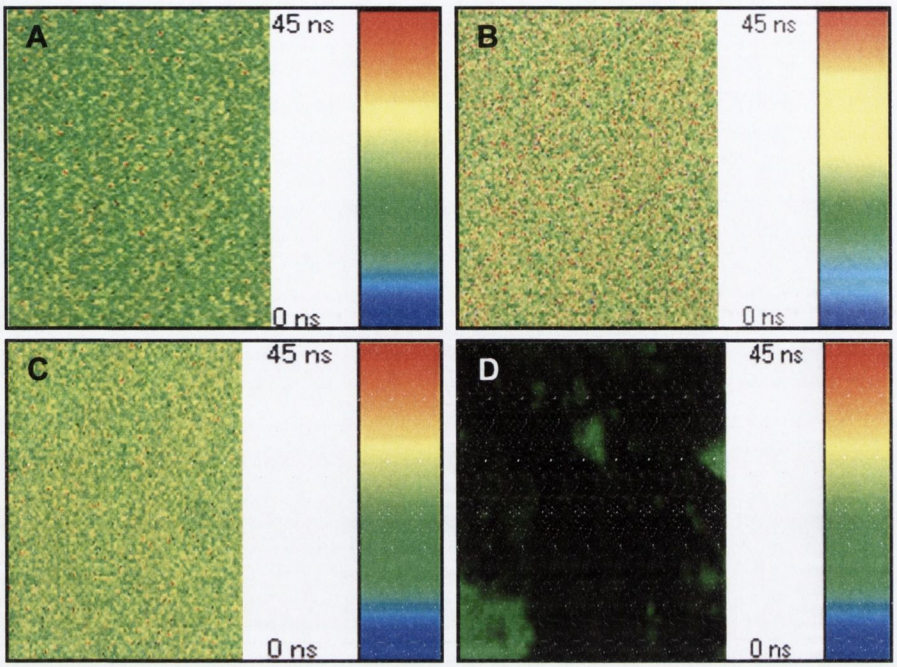


Figure 5.12. Fluorescence lifetime images illustrating the lifetime distribution and uniformity of the NSAID QD samples. **(a)** original CdTe QD solution, **(b)** npx-amino-PEG-NH_2 conjugated QDs, **(c)** ibu-amino-PEG-NH_2 conjugated QDs, **(d)** naproxen QD conjugate solution left in ambient conditions over 48 hours.

Figure 5.12 illustrates the image generated upon analysis of the QD solutions using the Time-Harp, PicoQuant single photon counting apparatus. The lifetime of the species analysed can be verified by colour (as indicated by the right panels on all images) and changes are easily detectable. Clear alterations in the colour-map distribution are clearly seen between all samples. Upon conjugation, the npx-amino-PEG-NH_2 sample shows a distinct shift to longer lifetimes (Table 5.1) and a change in colour indicating the same (Figure 5.12 **b**). A change in lifetime is also noted for the npx-amino-PEG-NH_2 conjugates, which have a lower lifetime and the fluorescent colour map image changes to a lighter shade (Figure 5.12 **c**).

Panel **d** is presented to illustrate that the distribution visualised is highly dependant on the stability of the QD solution. Here, a sample was left out in ambient conditions to initiate decomposition and this is visually reflected in the patchy, agglomerated distribution analysed. This is further evidence that the conjugation of the

NSAID in the appropriate concentrations does not adversely affect the QD stability in solution. Indeed, this agglomeration was witnessed when large excesses of drug were added and QD precipitation was witnessed.

5.4.3 TEM analysis of the NSAID – QD conjugates

In addition to the luminescent confocal images (Figure 5.13), the pictures displayed by TEM analysis show the same string like arrangements for the composites as the original CdTe QDs. This further illustrates that the coupling reaction and the binding of the drug moiety did not significantly alter the morphology of the CdTe QDs (Figure 5.13 **b**).

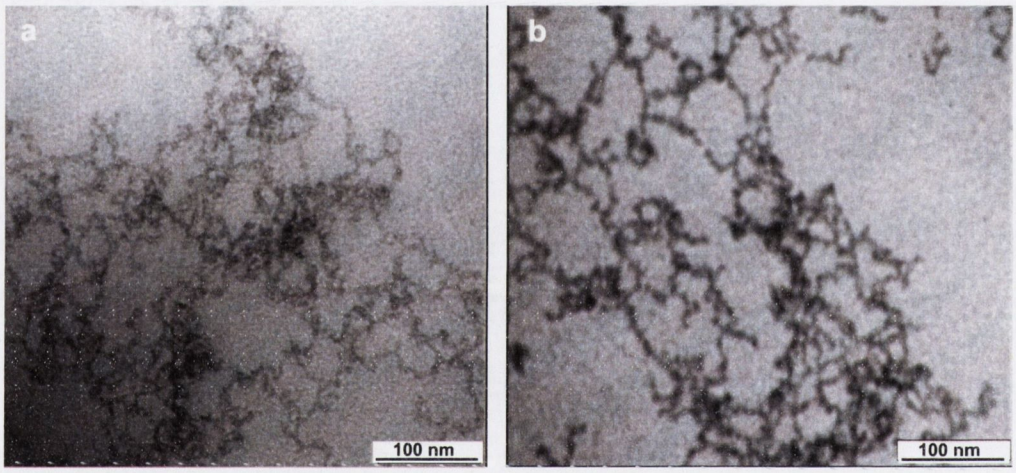


Figure 5.13. TEM images of **a**) original and **b**) NSAID conjugated QDs illustrating that upon conjugation no discernable changes in morphology of the QDs can be seen. (Scale bar = 100 nm for both images).

5.4.4 UV-vis absorption and luminescence emission analysis of the conjugation reaction

To spectroscopically verify the conjugation of the NSAID to the QDs, analysis of the QD solutions before and after conjugation were made. Following purification by sephadex size exclusion chromatography to remove any excess molecules, excitation of the npx-amino-PEG-NH_2 and ibu-amino-PEG-NH_2 QD conjugates gave no visible drug emission peak (Figure 5.14 and 5.15 black lines).

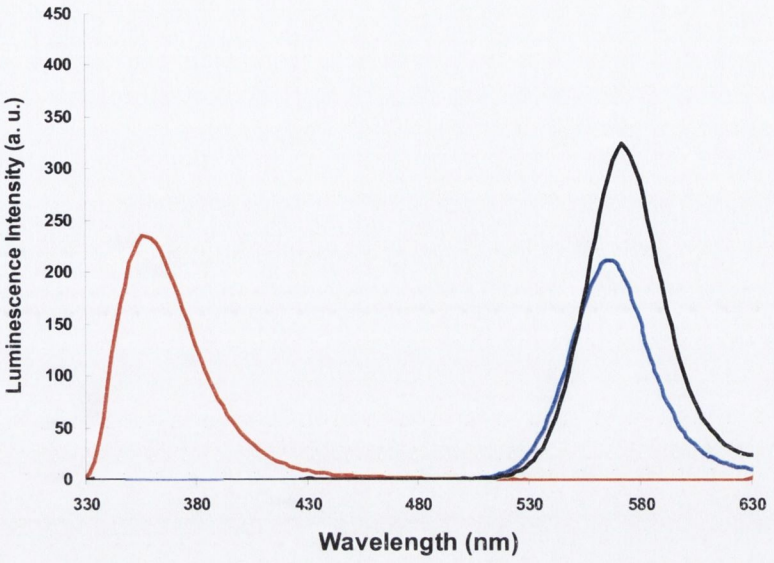


Figure 5.14. Luminescence emission spectra (λ_{ex} 267 nm) of the npx-amino-PEG-NH_2 derivative (red line), the original TGA-QDs (blue line) and the purified npx-amino-PEG-NH_2 QD conjugate (black line).

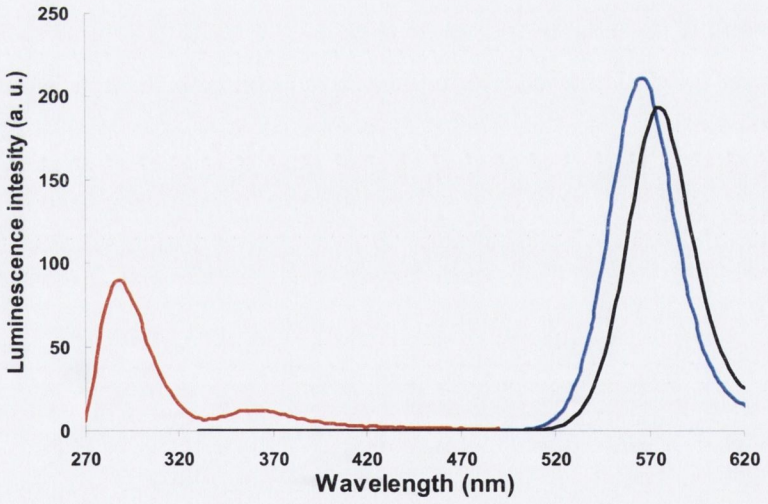


Figure 5.15. Luminescence emission spectra (λ_{ex} 220 nm) of the ibu-amino-PEG-NH_2 derivative (red line), the original TGA-QDs (blue line) and the ibu-amino-PEG-NH_2 QD conjugate (black line).

Figures 5.14 and 5.15 show the emission peaks for the water soluble NSAIDs [naproxen – λ_{em} 356 nm / ibuprofen λ_{em} 288 nm] and the before and after emission

spectra of the npx-amino-PEG-NH_2 and ibu-amino-PEG-NH_2 QD conjugates respectively. Following purification, both the QD emission spectra do not show any residual peak at lower wavenumbers due to any free drug moieties in solution. This proves that all unreacted molecules are successfully removed by sephadex purification and that any bound molecules no longer show emissive properties.

Assuming the effectiveness of the coupling reaction, the binding of the drug moieties resulted in a complete disappearance of the drug luminescence for a purified solution, while the QD luminescence was slightly enhanced. The short length of linker suggests that the observed effect is a result of electron transfer towards the QDs rather than long-range, Förster-type energy transfer processes.

As shown before, there is a slight red shift due to small aggregations with the ensemble. This may be due to interactions between the QDs themselves, [45] possibly caused to the partial removal of the stabilising ligands which can result in the QD surfaces touching and fusing together. [46] These changes do not affect the stability or luminescence properties of the QDs, as noted by TEM and confocal images (Figures 5.12 and 5.13).

In order to investigate the reaction yield for conjugation and uptake of the drug molecules onto the QD surface, the sephadex column was flushed following removal of the desired QD fraction and this residual fraction was analysed for its spectral characteristics (Figure 5.16).

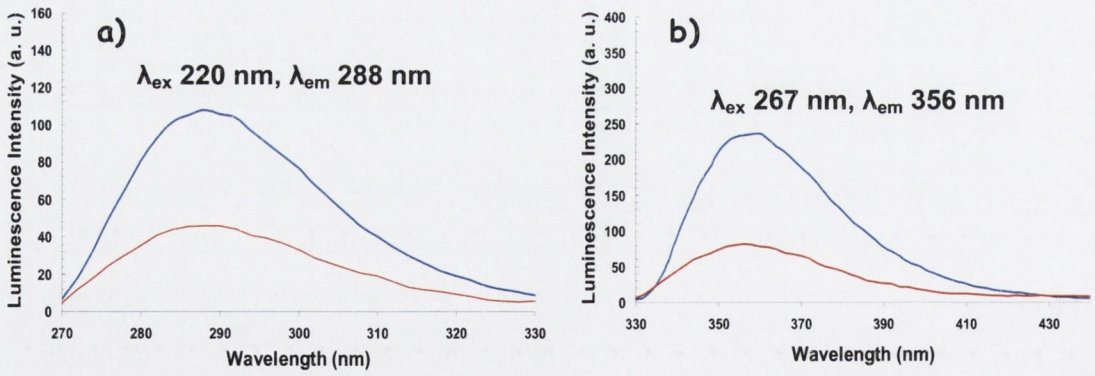


Figure 5.16. Luminescence emission spectra showing the washings from the sephadex columns following conjugation of **a**) ibu-amino-PEG-NH_2 and **b**) npx-amino-PEG-NH_2 to the QDs.

These flushed sephadex fractions showed that with respect to the initial amounts added, 30 - 35 % of the npx-amino-PEG-NH_2 and 40 - 45% of the ibu-amino-PEG-NH_2 moieties still remained unreacted in solution. Thus, even allowing for further experimental error, since there may still be some residual drug molecules present on the sephadex, approximately 50 % of the NSAID moieties added can be assumed to be bound to the QD surface.

These results now raise the question, are the drug conjugates stable or are the NSAIDs easily removed from the surface? As such, we wished to investigate their stability in an aggressive enzymatic medium under criteria designed to mimic the conditions that may be encountered in a biological environment.

5.4.5 Stability of the NSAID conjugates in an enzymatic environment

Consequently, we decided to use the enzyme trypsin, in order to monitor any possible release and stability of the bound NSAID. This enzyme is used to break chemical linkages (ester and peptide bonds) in biological systems and is frequently used to remove cells that have adhered to the bottom of the wells. Thus, 1 mL of a purified QD conjugate solution was mixed in 1 mL of PBS buffer at 37° C with trypsin (10X solution, 5 mg/mL). Fluorescence spectra were taken at different stages (15 minutes, 1 hour and 3 hours) in order to monitor the luminescence evolution of all species present with mixing time (Figure 5.17).

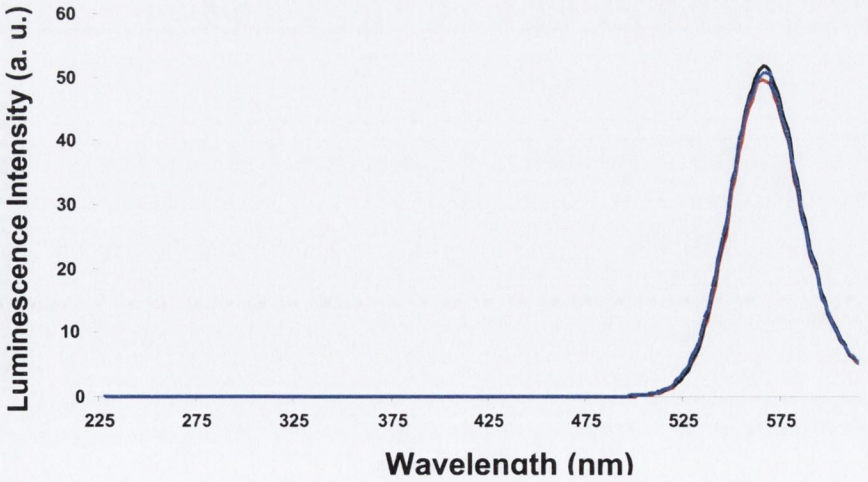


Figure 5.17. Luminescence emission spectrum (λ_{ex} 220 nm) taken after 15, 60 and 180 minutes of mixing the ibu-amino-PEG-NH_2 QD conjugate with trypsin.

Figure 5.17 illustrates the response seen for the ibu-amino-PEG-NH_2 conjugates when mixed with trypsin and excited at 220 nm (ibuprofen absorption). The emission response for the release of the drug was negligible and no discernable change was noted in the QD emission. This could be due to the stability of the nanocomposite or inactivity of the enzyme. Previously, it has been shown that addition of ibu-amino-PEG-NH_2 resulted in a luminescence decreases rather than an increase as seen for npx-amino-PEG-NH_2 composites. This is perhaps an indicator of the stability of the bonds formed upon conjugation of theses nanocomposites to the QDs. Unfortunately, those samples containing ibu-amino-PEG-NH_2 frequently crashed out of solution or became distinctly discoloured. This indicates that these composites are not as stable as their naproxen containing counterparts and as a result, no further testing of these nanocomposites was possible in live cells. Significantly, different results were witnessed for those QDs bound to npx-amino-PEG-NH_2 (Figure 5.18).

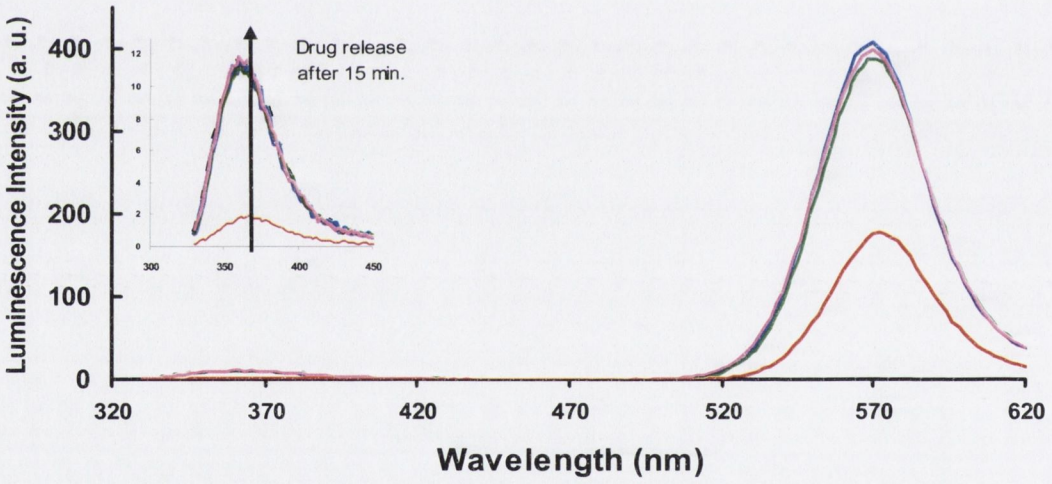


Figure 5.18. Luminescence emission spectra (λ_{ex} 267 nm) of the purified npx-amino-PEG-NH_2 QD conjugate before (red line), 15 min. (green line), 1 hour (blue line) and 3 hours (pink line) after mixing with trypsin (5 mg/mL). [Note, no discernable change in QD emission after the initial increase from 15 minutes of mixing]. **Insert:** blown up section (λ_{em} 356 nm) showing a small increase of the naproxen emission after 15 min of mixing time.

Figure 5.18, shows the luminescence emission due to the npx-amino-PEG-NH_2 QD conjugates. Several variations in emission intensity are noted for both the QDs and

the drug. The QD emission is seen to increase substantially, up to 100% upon addition of the enzyme. This observation differed from previously reported results, where the luminescence of negatively charged QDs mixed with a protein tended to decrease and red shift. [47] However, similar increases due to the interaction of QDs with biomolecules has also been reported. [12, 28] The QD emission increases can be attributed to indirect surface passivation upon interaction of the enzyme with the conjugate and possibly due to expulsion of any adsorbed water and oxygen molecules. Interestingly, there is also an increase of the individual drug emission peak (insert Figure 5.18) which can only be accredited to the breaking of the peptide bond holding the drug to the surface. This release provides further evidence for the binding of the drug to the QD but the peaks minor intensity values indicates that only a small amount of drug is released and that the amide bond is not very labile under these conditions. Indeed, most of the drug must remain bound to the surface indicating that a more specific peptide cleaving enzyme, and possibly a more specific peptide bond formation would be required to efficiently break it.

It is interesting to analyse this behaviour with respect to the ibuprofen containing composites. The only difference between the two composites is the size and structures of the drug molecules. While a single methyl group is present in the naproxen molecule, ibuprofen possesses two methyl groups. This bulky, sterically hindering group may decrease the interaction and binding of the enzyme, thus reducing its mode of action to break the amide bond between the drug and the QD. Finally, after 24 hours, a significant drop in the QD emission intensity was observed for the npx-amino-PEG-NH_2 QDs which was linked to the precipitation of the QDs. Nevertheless, it was also observed that this precipitation cannot be attributed to the degradation of the QDs but instead to their coagulation at the bottom of the sample tube. This deposit was still luminescent when exposed under a UV lamp, indicating that the action of the enzyme over an extended time period resulted in QD aggregation.

Interestingly, when the original TGA QDs were mechanically mixed with the trypsin enzyme and spectroscopically analysed (Figure 5.19), no significant changes, either in the emission wavelength or luminescence intensity were noticed.

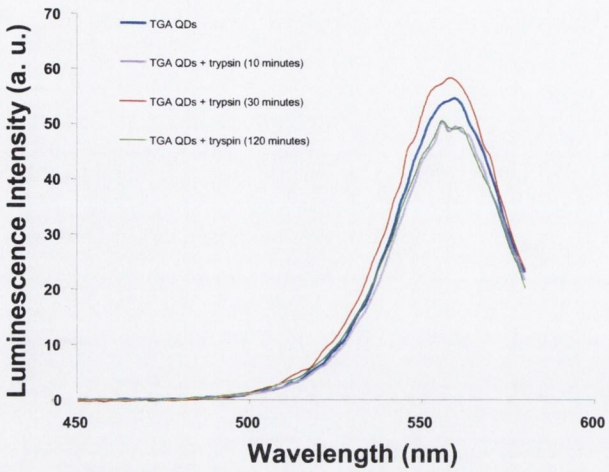


Figure 5.19. Luminescence emission spectra (λ_{ex} 450 nm) of TGA QDs and the trypsin enzyme taken after 0, 10, 30 and 120 minutes.

This discussion is contradictory to increases seen previously (Figure 5.18), which indicates that the interaction of the enzyme with the original QDs differs greatly from that of their NSAID conjugated counterparts. Thus, the presence of a neutral drug molecule on the surface of the QDs could have prevented an electrostatic binding of the enzyme and has altered the way it interacts with the QD surface. This affinity of the enzyme with the QD surface atoms triggers an increase in luminescence emission. This was corroborated by confocal lifetime analysis and can be attributed to the increased surface passivation and the reduced numbers of non-radiative channels available.

5.5 Investigation of the NSAID conjugates in THP-1 cells

To further investigate the stability and possible activity of the NSAID QD conjugates in a live cellular environment, the npx-amino-PEG-NH_2 QD samples were tested with the THP-1 cell line (Figure 5.20). Briefly, CdTe QDs (original and conjugated) were introduced into THP-1 cells and incubated for three hours at 37° C, 5% CO_2. The cells were also counterstained with Hoechst (blue nuclear staining) to improve imaging contrast.

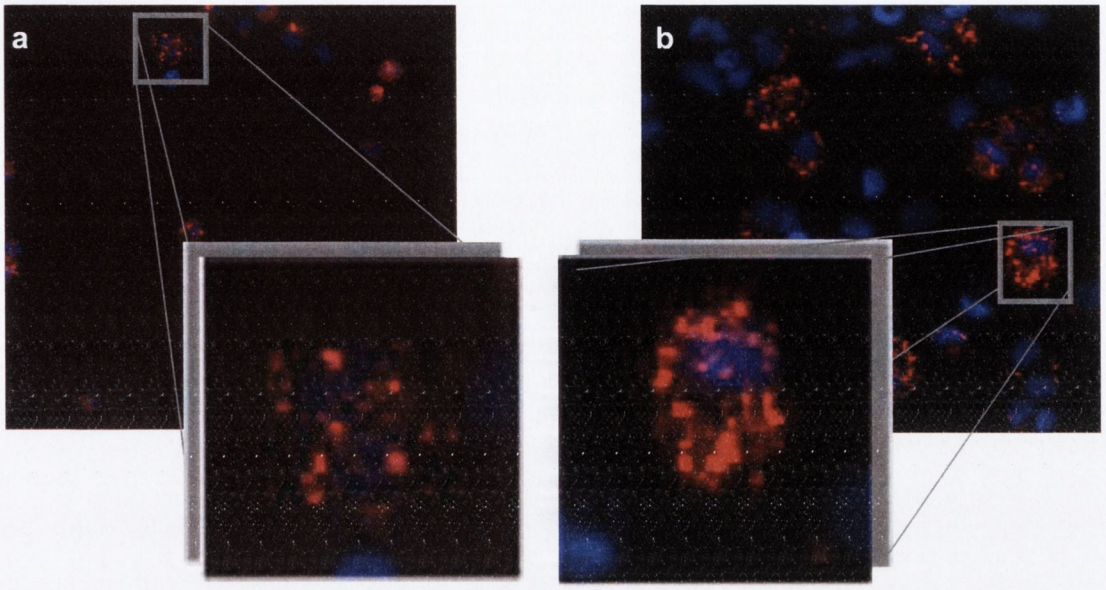


Figure 5.20. Live cell fluorescent images showing the localisation of **a)** naproxen conjugated (λ_{em} 566 nm) QDs onto the outer cellular membrane of THP-1. **b)** More intensely luminescent intra and extra cellular distributions are noted for the original non-conjugated QDs.

The QDs reside mainly on the outside of the cell membrane as indicated by the presence of the QD emission on top of the blue staining of the nucleus). Only the original non conjugated QDs displayed any tendency to partially penetrate the cell surface where QD emission can be seen around the nuclear staining. For both QD systems, a similar surface distribution is noted; however, additional illumination of the cytoplasmic region is also seen for the original QDs (Figure 5.20 **b**). While the intensity and cell uptake of the conjugates was lower that that of their original counterparts, the conjugates did show a strong affinity to the cells following a three-hour incubation period. The QDs are seen to strongly agglomerate on the cell surface in pockets, possibly due to interactions with cell surface receptors. However, the precise nature of this interaction will require further study.

Their lack of membrane penetration can be possibly attributed to their agglomeration upon addition of the cell culture medium. This may render the QDs unable to enter the cells *via* channels or pores within the membrane itself. As has been shown in Chapter 3, the size of the QDs does in fact play a crucial role and perhaps that additional

agglomeration of these nanocomposites prevents them from being sequestered to the cytoplasm.

These experiments have shown, that the drug conjugated QD systems display good cellular localisation for imaging of the THP-1 cell surface over a 3 hour incubation time, confirming their stability in a cellular medium and indicating their potential both as drug delivery and cellular imaging agents.

5.6 Conclusions

We have synthesised and investigated the first NSAID QD conjugates. Our initial strategy to prepare new thiol containing drug based conjugates and to use them as stabilisers for the preparation of novel QDs resulted in nanocomposites with poor solubility in water. Therefore this approach was abandoned and another synthetic strategy based on the carbodiimide coupling of modified drugs to pre-prepared TGA capped QDs was investigated.

Using modified NSAID (ibuprofen and naproxen) molecules with a PEG spacer, nanocomposites with the appropriate stability and solubility in water were produced. The naproxen conjugates showed far more stability than their ibuprofen counterparts and gave particularly interesting results. From this experiment, the naproxen - QD conjugates clearly demonstrated a good stability in an aggressive medium with a noted luminescence enhancement. Upon addition of the enzyme, the conjugates demonstrated a weak release of the drug moiety confirming the presence of bound naproxen to the QD surface. It seems plausible to assume that this release is linked to the amide bond cleavage triggered by the enzyme. Although the amount of drugs released in our experiment was minimal, a further chemical modification of the water soluble linker could lead to a specific enzymatic cleavage. [12]

The NSAID – QDs displayed a localisation on the outer membrane of macrophage THP-1 cells. Despite the lack of cell penetration and some aggregation on the cell surface, these nanocomposites possibly have some potential as drug delivery and cellular imaging agents. However, further research and detailed studies of the enzymatic cleavage mechanisms and intracellular behaviour of the conjugates is necessary to understand their biological behaviour. We believe a similar approach can be used for the

development of other QD-drug conjugates, possibly using ester linkages as their hydrolysis occurs on a faster time-scale to that of amides. This would enable us to better understand the mechanistic pathways of QD-based drug delivery and could possibly help in diagnostic recognition and treatment of many diseases.

References

[1] N. Gaponik, D. V. Talapin, A. L. Rogach, K. Hoppe, E. V. Shevchenko, A. Kornowski, A. Eychmüller, H. Weller, *J. Phys. Chem. B* **2002**, *106*, 7177.

[2] E. L. Bentzen, I. D. Tomlinson, J. Mason, P. Gresch, M. R. Warnement, D. Wright, E. Sanders-Bush, R. Blakely, S. J. Rosenthal, *Biocon. Chem.* **2005**, *16*, 1488.

[3] H. T. Uyeda, I. L. Medintz, J. K. Jaiswal, S. M. Simon, H. Mattoussi, *J. Am. Chem. Soc.* **2005**, *127*, 3870.

[4] S. Pathak, S. K. Choi, N. Arnheim, M. E. Thompson, *J. Am. Chem. Soc.* **2001**, *123*, 4103.

[5] M. Gao, S. Kirstein, H. Mohwald, A. Rogach, A. Kornowski, A. Eychmüller, H. Weller, *J. Phys. Chem. B* **1998**, *102*, 8360.

[6] B. Pan, D. Cui, R. He, F. Gao, Y. Zhang, *Chem. Phys. Lett.* **2006**, *417*, 419.

[7] N. Ma, C. J. Dooley, S. O. Kelley, *J. Am. Chem. Soc.* **2006**.

[8] N. N. Mamedova, N. A. Kotov, A. L. Rogach, J. Studer, *Nano Lett.* **2001**, *1*, 281.

[9] H. Mattoussi, J. M. Mauro, E. R. Goldman, G. P. Anderson, V. C. Sundar, F. V. Mikulec, M. G. Bawendi, *J. Am. Chem. Soc.* **2000**, *122*, 12142.

[10] S. J. Rosenthal, I. Tomlinson, E. M. Adkins, S. Schroeter, S. Adams, L. Swafford, J. McBride, Y. Wang, L. J. DeFelice, R. D. Blakely, *J. Am. Chem. Soc.* **2002**, *124*, 4586.

[11] S. Dwarakanath, J. G. Bruno, A. Shastry, T. Phillips, A. John, A. Kumar, L. D. Stephenson, *Biochem. Biophys. Res. Commun.* **2004**, *325*, 739.

[12] E. Chang, J. S. Miller, J. Sun, W. W. Yu, V. L. Colvin, R. Drezek, J. L. West, *Biochem. Biophys. Res. Comm.* **2005**, *334*, 1317.

[13] S. Wang, N. Mamedova, N. A. Kotov, W. Chen, J. Studer, *Nano Lett.* **2002**, *2*, 817.

[14] E. R. Goldman, E. D. Balighian, H. Mattoussi, M. K. Kuno, J. M. Mauro, P. T. Tran, G. P. Anderson, *J. Am. Chem. Soc.* **2002**, *124*, 6378.

[15] M. E. Akerman, W. C. W. Chan, P. Laakkonen, S. N. Bhatia, E. Ruoslahti, *PNAS* **2002**, *99*, 12617.

[16] G. P. Mitchell, C. A. Mirkin, R. L. Letsinger, *J. Am. Chem. Soc.* **1999**, *121*, 8122.

[17] D. Zhou, J. D. Piper, C. Abell, D. Klenerman, D.-J. Kang, L. Ying, *Chem. Comm.* **2005**, 4807.

[18] A. Schroedter, H. Weller, R. Eritja, W. E. Ford, J. M. Wessels, *Nano Lett.* **2002**, *2*, 1363.

[19] N. J. Lowe, Hensby, C. N., *Karger, Switzerland* **1989**.

[20] K. D. Rainsford, *Taylor & Francis, London* **1999**.

[21] B. L. Furman, *Glasgow : University of Strathclyde* **1983**.

[22] R. N. Dubois, S. B. Abramson, L. Crofford, R. A. Gupta, L. S. Simon, L. B. A. Van De Putte, P. E. Lipsky, *FASEB J.* **1998**, *12*, 1063.

[23] M. G. Malkowski, S. L. Ginell, W. L. Smith, R. M. Garavito, *Science* **2000**, *289*, 1933.

[24] C. Tourne-Peteilh, D. Brunel, S. Begu, B. Chiche, F. Fajula, D. A. Lerner, J.-M. Devoisselle, *New J. Chem.* **2003**, *27*, 1415.

[25] A. Wolcott, D. Gerion, M. Visconte, J. Sun, A. Schwartzberg, S. Chen, J. Z. Zhang, *J. Phys. Chem. B* **2006**, *110*, 5779.

[26] M. Li, R. S. Wu, J. Tsai, S. J. Salamone, *Tet. Lett.* **2002**, *43*, 4861.
[27] Y. Zhang, J. Zhang, *J. Colloid Interface Sci.* **2005**, *283*, 352.
[28] H. Mattoussi, J. M. Mauro, E. R. Goldman, T. M. Green, G. P. Anderson, V. C. Sundar, M. G. Bawendi, *Phys. Stat. Sol. B* **2001**, *224*, 277.
[29] A. Lista, G., M. Palomeque, E., B. Fernández Band, S., *J. Braz. Chem. Soc.* **2006**, *17*, 1428.
[30] W. R. G. Baeyens, M. Vanparys, G. Van der Weken, *Biomed. Chromat.* **1999**, *13*, 145.
[31] R. B. Greenwald, H. Zhao, K. Yang, P. Reddy, A. Martinez, *J. Med. Chem.* **2004**, *47*, 726.
[32] S. J. Byrne, S. A. Corr, T. Y. Rakovich, Y. K. Gun'ko, Y. P. Rakovich, J. F. Donegan, S. Mitchell, Y. Volkov, *J. Mat. Chem.* **2006**, *16*, 2896.
[33] W. W. Yu, L. H. Qu, W. Z. Guo, X. G. Peng, *Chem. Mater.* **2003**, *15*, 2854.
[34] K. Liu, T. A. Schmedake, K. Daneshvar, R. Tsu, *Microelec. J.* **2007**, *38*, 700.
[35] J. Aldana, Y. A. Wang, X. Peng, *J. Am. Chem. Soc.* **2001**, *123*, 8844.
[36] V. I. Klimov, D. W. McBranch, C. A. Leatherdale, M. G. Bawendi, *Phys. Rev. B* **1999**, *60*, 13740.
[37] J. Y. Zhang, X. Y. Wang, M. Xiao, *Opt. Lett.* **2002**, *27*, 1253.
[38] M. G. Bawendi, P. J. Carroll, W. L. Wilson, L. E. Brus, *J. Chem. Phys.* **1992**, *96*, 946.
[39] A. M. Kapitonov, A. P. Stupak, S. V. Gaponenko, E. P. Petrov, A. L. Rogach, A. Eychmüller, *J. Phys. Chem. B* **1999**, *103*, 10109.
[40] S. F. Wuister, I. Swart, F. van Driel, S. G. Hickey, C. de MelloDonega, *Nano Lett.* **2003**, *3*, 503.
[41] X. Wang, L. Qu, J. Zhang, X. Peng, M. Xiao, *Nano Lett.* **2003**, *3*, 1103.
[42] Y. A. Wang, J. J. Li, H. Y. Chen, X. G. Peng, *J. Am. Chem. Soc.* **2002**, *124*, 2293.
[43] L. Spanhel, M. Haase, H. Weller, A. Henglein, *J. Am. Chem. Soc.* **1987**, *109*, 5649.
[44] M. O'Neil, J. Marohn, G. McLendon, *J. Phys. Chem.* **1990**, *94*, 4356.
[45] A. Fischer, L. Anthony, A. D. Compaan, *Appl. Phys. Lett.* **1998**, *72*, 2559.
[46] A. C. Carter, C. E. Bouldin, K. M. Kemner, M. I. Bell, J. C. Woicik, S. A. Majetich, *Phys. Rev. B* **1997**, *55*, 13822.
[47] Z. B. Lin, S. X. Cui, H. Zhang, Q. D. Chen, B. Yang, X. G. Su, J. H. Zhang, Q. H. Jin, *Anal. Biochem.* **2003**, *319*, 239.

Chapter 6: Conclusions, preliminary studies and future work

6.1 Conclusions

In this work we have developed and investigated new CdTe QDs and investigated the production of new QD nanocomposite materials. We have demonstrated, using a statistical study, the conditions required to produce highly luminescent QDs in large quantities and how their properties are influenced by controlling the reagent ratios. These results enabled us to produce QDs and analyse their behaviour over time and also when subjected to irradiation. Analysis of the luminescence lifetimes revealed a biexponential decay, with QY increases dominated by changes in the longer lived component (τ_2) inherent of surface states. Raman studies following irradiation showed the presence of a mixed ternary phase (Cd-S-Te) which caps the surface defects, increasing the rate of radiative recombination. We have demonstrated that ageing and photoetching of QD solutions achieves a significant 3 fold enhancement of the luminescence emission and QY.

One of the main aims of our research was to investigate these QDs in live cellular cultures and we have approached this using several routes. We have studied a series of thiol capped QDs with THP-1 macrophage cells, analysed the varying factors that influenced their uptake and illustrated how they possess the capacity for imaging in biological systems. We have found that both charge and size play a major role, with neutral or positively charged QDs remaining excluded from the cells and only being found around the membrane periphery. A negatively charged surface, facilitated by the presence of a carboxylic acid stabilising moiety, proved ideal for membrane penetration. Both thioglycolic acid (TGA) and mercaptopropionic acid (MPA) stabilised QDs readily entered the cells. Upon accumulation of the QDs, we then found that size is significant factor in their subcellular distribution. The larger 4 nm red QDs were retained primarily in the cytoplasm with some accumulation at the nuclear membrane while only the small 2 nm green QDs penetrated the nuclear membrane, with a distinct accumulation within the nucleolus.

In our work, we have also addressed the important issue of toxicity due to these nanomaterials. The cytotoxicity-induced phenomena due to the presence of both QDs and QD-gelatin composites have been investigated. We successfully prepared "jelly dots" by

introducing the gelatin *in situ* during the preparation of the QDs. It was found that the gelatin had a profound impact on the growth of the QDs and allowed the initial nucleation of the nanoclusters to occur on a more discrete basis. This subsequently altered the growth patterns and allowed for smaller gelatin-QDs to be produced under the same experimental conditions as those without gelatin present. We also discovered that the presence of gelatin substantially increased the QY of the gelatin-QDs, which were up to 1.5 times greater than their non-gelatin counterparts. Therefore, as well as influencing the growth of the QDs, the gelatin also acts as a co-capping agent, effectively stabilising the surface defects and increasing the rate of radiative decay. This was further confirmed by fluorescent lifetime decay analysis.

Most importantly, we also found that the presence of the gelatin also reduced the toxicity of these nanocomposites. We discovered that gel-TGA-QDs were effectively 80% less toxic than non-gelatinated QDs, as assessed by changes in the lysosomal pH and permeability of the THP-1 cells. These results demonstrated the possible use of gelatin or other similar biocompatible polymers as possible toxicity reducing agents for the use of QDs in biological systems.

We have also investigated the conjugation of the QDs with the non-steroidal anti-inflammatory drugs (NSAIDs) ibuprofen and naproxen. We have modified the drug molecules with a small amino PEG (2,2′-(ethylenedioxy)diethylamine) molecule. This imparted water solubility to the drugs and the free amine allowed for the subsequent conjugation of the drugs to the surface carboxylic acid groups of the QDs *via* an EDC coupling reaction. We verified the presence of the drug molecules spectroscopically and analysed the stability of the drug conjugates in an enzymatic environment. The ibuprofen conjugates did not show the same stability as their naproxen counterparts, which demonstrated a small cleavage of the drug. These nanocomposites also displayed a similar distribution when compared to non-conjugated QDs, illustrating that the presence of the drug did not significantly alter their biocompatibility. This work has shown that various drug molecules may be bound to the QDs and opens up the possibility for future studies into the behaviour of these systems and analysis of how altering the linker or bonding changes the biological behaviour.

In conclusion we believe that our work will contribute to the better understanding and future development of various QD systems, particularly with a view to their use as bio-imaging probes.

6.2 Preliminary studies and future work

Our future work will be focused on further studies of the properties of CdTe QDs, the synthesis of novel stabilisers and the interaction and toxicological impact of new QD conjugates with immune and neuron cells. Work will also include investigations into the interface at a nuclear level between the QDs and cells and also their employment in layer by layer systems. Some aspects of this research are discussed below.

6.2.1 Development of novel stabilisers for CdTe QDs

Recently, Maciej Stefanko has synthesised, starting from PEG_{400}, a long chain PEG molecule containing both a thiol and an amino group (Figure 6.1).

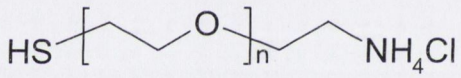


Figure 6.1. Structure of α-mercapto-ω – PEG_{400}.

This molecule possesses both an amino and a thiol function, analogous to cysteamine (Table 3.1), enabling it to bind to the QD surface. This new stabiliser can be used to prepare new positively charged CdTe QDs and investigate their biocompatibility and biological behaviour. In this thesis, we have demonstrated that positively charged QDs do not penetrate into THP-1 cells and the QD remained bound to the outside of the cellular membrane. However, PEG molecules have been used previously to reduce non-specific binding in cells and it would be interesting to investigate if this bio-compatibility can be applied to this QD system. [1, 2] Initial experiments using this molecule as a capping agent showed that the QDs produced were luminescent; however, the solution subsequently became dark and decomposed after storage overnight. Thus, further work will be required to re-synthesis the stabilising molecule and investigate the factors that may lead to the production of highly luminescent, stable and biocompatible positively charged QDs.

Studies will also be conducted into the production of QDs in the presence of a wide range of polymer molecules. This will range from traditional polyelectrolyte molecules such as poly(diallyldimethylammonium chloride [PDDA], poly(sodium4-styrenesolfonate) [PSS] and polyethylene imine [PEI] to various proteins and DNA. Alternating QD capping groups can be used to investigate how charge and surface interactions affect QD growth and behaviour. Initial results have shown that the agglomeration of the QDs due to charge effects is a likely factor in the way they behave in solution. A preliminary experiment was conducted using PEI and TGA QDs to see how a positively charged polyelectrolyte would impact the system. PEI was added *in situ* to a precursor solution containing cadmium and TGA and had a marked effect on the growth and properties of the QDs (Figure 6.2).

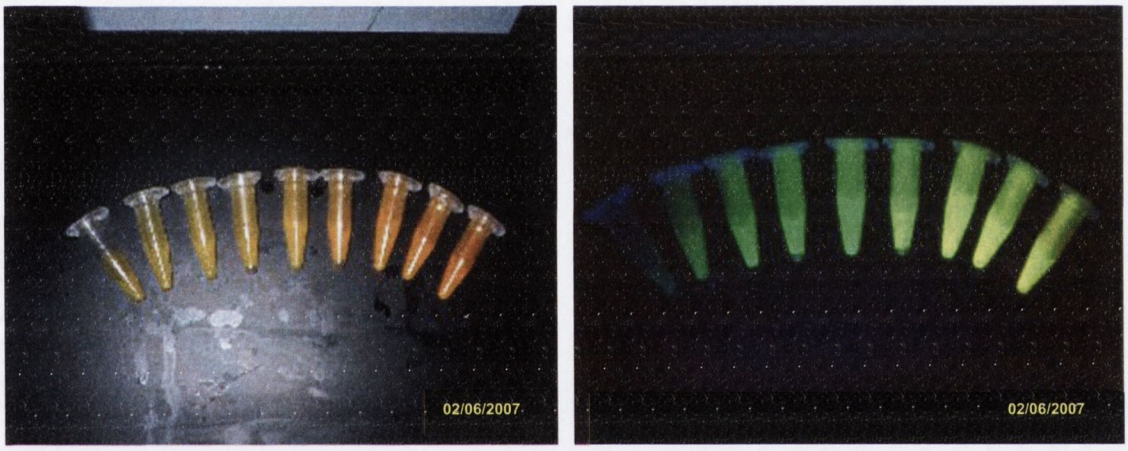


Figure 6.2. Photographs of the fractions (left panel – normal light, right panel – UV light) obtained during the synthesis of TGA QDs in the presence of PEI.

During the synthesis, fractions at various intervals over the course of a day were taken (Figure 6.2). Due to the presence of the PEI, the QDs grew very slowly and after a whole day of heating, the solution colour was orange and not the characteristic red indicative of larger QDs. The spectroscopic data also confirmed the presence of much smaller QDs than we have seen previously for similar time periods of heating (Figure 6.3).

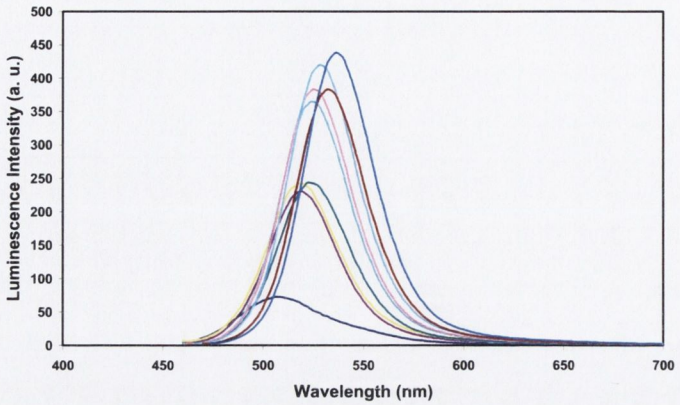


Figure 6.3. Luminescence emission spectra (λ_{ex} 450 nm) taken for each fraction of TGA-PEI QDs analysed.

The emission λ_{max} after one day of heating was 540 nm indicating that the growth of the QDs is hindered by the interaction of the negative TGA and positive PEI. Also, the solutions produced were not stable in water and precipitated rapidly. They were still luminescent however, indicating the integrity of the QDs remained. This preliminary experiment has opened up the possibility of producing extremely small QDs with highly luminescent properties and could allow for their further incorporation into various polyelectrolyte systems.

6.2.2 Investigation of CdTe QDs in neuron cells

Recent advances in nanobiotechnology have demonstrated QDs as novel luminescent biological labels for imaging cellular structures and tracking molecular processes in cells. More recently, in search of new neurotherapeutic and neuroprosthetic strategies, QDs have been explored to manipulate and create active cellular interfaces with nerve cells. [3, 4] Functionalised QDs have been used to track neuron receptors [5] and initiate differentiation. [6] Winter *et al.* [7] investigated directly attaching QDs to nerve cells *via* recognition molecules. Also, Kotov and co-workers demonstrated the excitation of neural cells *via* a sequence of photochemical and charge-transfer reactions on a layer-by-layer assembled QD-polyelectrolyte composite film. [8]

The emergence of QDs for biomedical applications signals the need to understand and manage their cytotoxicity, as this will have major implications for their further use in

nanobiotechnology. [9, 10] For the case of QDs, studies have shown that various factors, such as heavy metal leaching, [11] production processing, [12] surface functionality, [11, 13] size and charge [14, 15] can all be correlated to cytotoxic phenomena. Previously, we have investigated the toxicity of QDs in THP-1 cells and the impact that gelatin has in reducing the toxic effects. [16] In this work, high content screening (HCS) assays were utilised to visualise and analyse the toxicological impact that QDs have on THP-1 cells.

Some current work (in collaboration with Prof. Nicolas Kotov and Edward Chan) also revolves around the further use of HCS to probe the cytotoxicity of TGA capped CdTe QDs in NG108-15 murine neuroblastoma (neuron) cells. These cells can be electrically excited and are used to process and transmit information. They were chosen due to the emerging interest in neuron based nanostructures and also because they are highly susceptible to influence from the surrounding environment. This would give us an early feed back on the detrimental effects induced by the QDs. Initial results have shown that the QDs induce apoptotic responses in a time and dosage dependant manner.

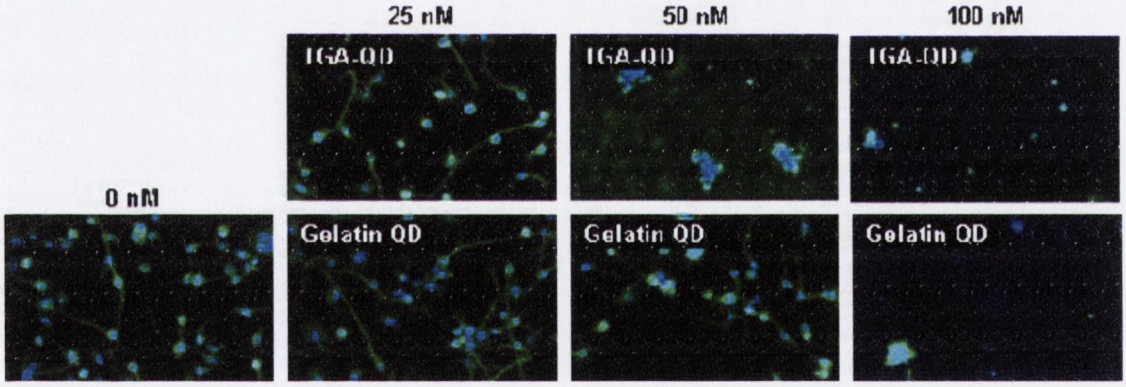


Figure 6.4. Cellomics (HCS) images depicting the changes in neurite outgrowth, due to coincubation of the QD with NG108-15 cells. Cell were incubated with TGA QDs and gel-TGA-QDs at various concentrations for 6 h and induced to differentiate for 4 additional days in low-serum medium. Cells were stained for β-tubulin III (green) and nuclei (blue).

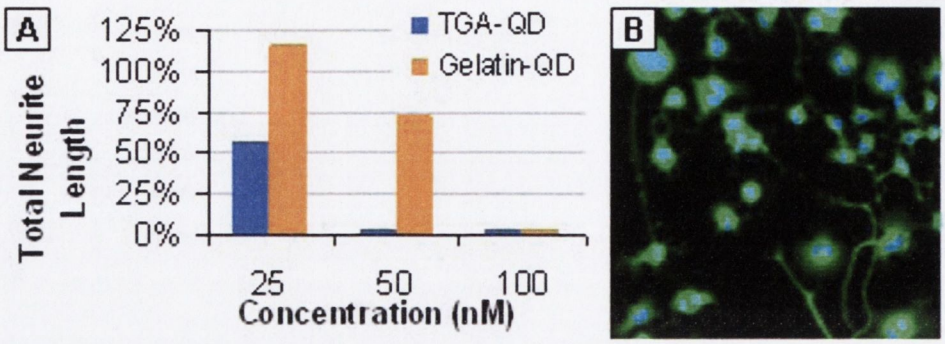


Figure 6.5. (A) Neurite outgrowth was assessed in terms of total neurite length per field. The result is an average of 3 independent experiments and final figures are expressed as percentages relative to the total neurite length per field of the untreated control sample. **(B)** Coloured composite fluorescent image [blue – nucleus, green - neurites] of neurite outgrowth is shown here.

HCS assays of the neurite outgrowth have proven sensitive to both the presence and concentration of the QDs. We have found that gel-TGA-QDs prove more stable and biocompatible than their non gelatin containing counterparts. Their presence in low concentrations does not impact the neurite development as substantially as original TGA QDs and allows for neurite growth to proceed in a manner similar to the control sample.

These findings show that the application of HCS to the study of nanomaterials is not limited to colloidal nanoparticles and cytotoxicity studies. Future work will involve studying the behaviour of cells on nanostructured thin films, as well as the transport and localisation of engineered QDs and nanoparticles in living cells.

6.2.3 Luminescence enhancement in Au / QD layer by layer systems

In collaboration with the school of Physics TCD, there have been investigations into the use of CdTe QDs in polyelectrolyte [PE] multilayers using alternating layers of PDDA and PSS polyelectrolytes. We have found that charge plays a crucial role in determining the emission response of the QDs in layer-by-layer self assembly. 3-mercapto-1, 2-propanediol (neutral charge), thioglycolic acid (negative charge) and cysteamine (positive charge) QDs have all been investigated. For the 3-mercapto-1, 2-propanediol QDs, a 31 fold enhancement in emission intensity and an increase in their

luminescence decay lifetime from 3.74 ns to a maximum of 11.65 ns was witnessed (Figure 6.6).

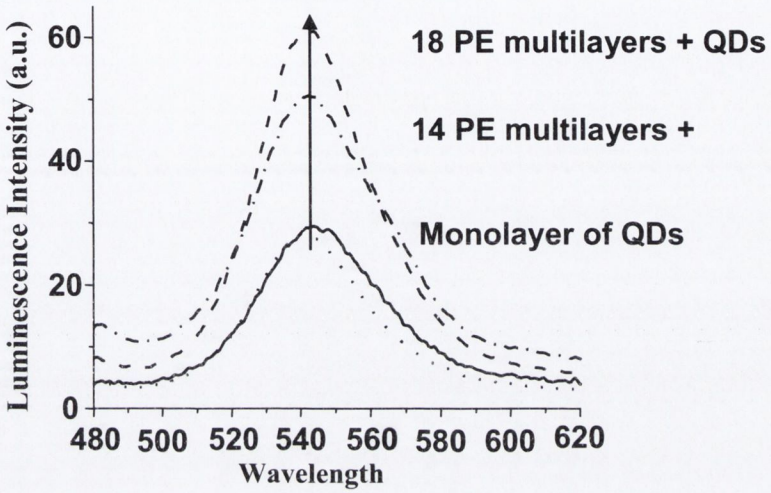


Figure 6.6. Luminescence emission of QDs as a monolayer and embedded in 10 (dots), 14 (dash dots) and 18 (dash) polyelectrolyte multilayers.

These modified emission properties are attributed to the enhanced surface related emission as a result of interaction of the QDs surface with the polyelectrolyte. This occurs as the relatively weak surface charge of MPD stabilised QDs allows significant diffusion to occur. Consequently, the QD surface passivation through interaction with the PE layers produces enhancement of the surface related emission, resulting in an increased quantum yield. Diffusion into the polyelectrolyte multilayers does not occur for the TGA or cysteamine stabilised QDs resulting in their localisation on the outer fringes of the PE multilayers

The observed diffusion of the MPD stabilised QDs shows that QDs can also be easily incorporated into PE multilayers to form composite materials, which will be used as building blocks for the bottom-up self-assembly of nanostructured functional materials making it of potential interest for various applications from photon sources to biological labelling.

This layer-by-layer technique has also been taken further and the use of gold nanoparticle surfaces in conjunction with layers of QDs is currently being investigated. Initial investigations have shown that an increased fluorescence, up to 10 fold, can be

achieved due to surface plasmon (SP) enhancement of the QDs on monolayers of Au nanoparticles. The greatest enhancement was witnessed for QDs red shifted with respect to the plasmon band and spectral overlap determines the magnitude of the enhancement and emission properties of the coupled system. Further work will investigate and analyse any FRET phenomena for this coupled QD – gold nanoparticle system.

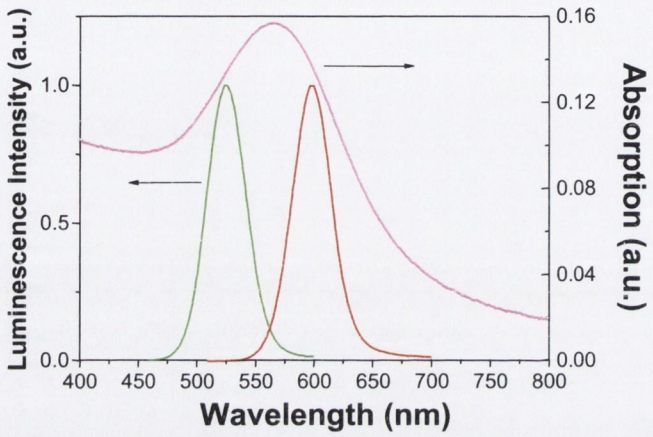


Figure 6.7. UV-vis absorption spectrum of the gold nanoparticles (pink - plasmon band at 565 nm) and the luminescence emission spectra of the donor (green – λ_{em} 525 nm) and acceptor (red – λ_{em} 600 nm) QDs.

For this system, the nanoparticle layers are separated by polyelectrolyte multilayers and initial findings have shown that up to a 4 fold emission enhancement can be seen when the QD emission spectra overlap with the gold plasmon band (Figure 6.8).

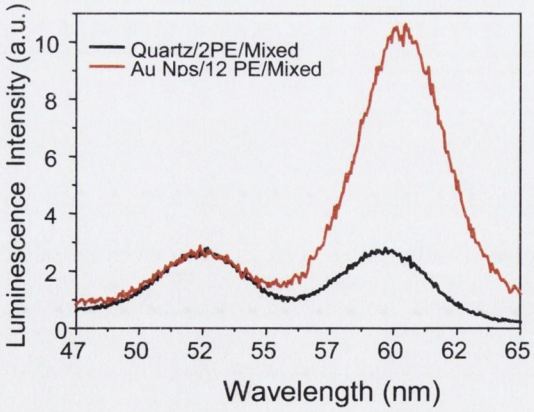


Figure 6.8. Graph of the increases in luminescence emission intensity when QDs are layered on gold nanoparticles.

References

[1] E. L. Bentzen, I. D. Tomlinson, J. Mason, P. Gresch, M. R. Warnement, D. Wright, E. Sanders-Bush, R. Blakely, S. J. Rosenthal, *Biocon. Chem.* **2005**, *16*, 1488.

[2] H. T. Uyeda, I. L. Medintz, J. K. Jaiswal, S. M. Simon, H. Mattoussi, *J. Am. Chem. Soc.* **2005**, *127*, 3870.

[3] N. Gomez, J. O. Winter, F. Shieh, A. E. Saunders, B. A. Korgel, C. E. Schmidt, *Talanta* **2005**, *67*, 462.

[4] S. Pathak, E. Cao, M. C. Davidson, S. Jin, G. A. Silva, *J. Neurosci.* **2006**, *26*, 1893.

[5] M. Dahan, S. Levi, C. Luccardini, P. Rostaing, B. Riveau, A. Triller, *Science* **2003**, *302*, 442.

[6] T. Q. Vu, R. Maddipati, T. A. Blute, B. J. Nehilla, L. Nusblat, T. A. Desai, *Nano Lett.* **2005**, *5*, 603.

[7] J. O. Winter, T. Y. Liu, B. A. Korgel, C. E. Schmidt, *Adv. Mater.* **2001**, *13*, 1673.

[8] T. C. Pappas, W. M. S. Wickramanyake, E. Jan, M. Motamedi, M. Brodwick, N. A. Kotov, *Nano Lett.* **2007**, *7*, 513.

[9] A. Nel, T. Xia, L. Madler, N. Li, *Science* **2006**, *311*, 622.

[10] G. Oberdörster, E. Oberdörster, J. Oberdörster, *Environ. Health Perspec.* **2005**, *113*, 823.

[11] C. Kirchner, T. Liedl, S. Kudera, T. Pellegrino, A. MunozJavier, H. E. Gaub, S. Stolzle, N. Fertig, W. J. Parak, *Nano Lett.* **2005**, *5*, 331.

[12] A. M. Derfus, W. C. W. Chan, S. N. Bhatia, *Nano Lett.* **2004**, *4*, 11.

[13] A. Hoshino, K. Fujioka, T. Oku, M. Suga, Y. F. Sasaki, T. Ohta, M. Yasuhara, K. Suzuki, K. Yamamoto, *Nano Lett.* **2004**, *4*, 2163.

[14] J. Lovrić, H. S. Bazzi, Y. Cuie, G. R. A. Fortin, F. M. Winnik, D. Maysinger *J. Mol. Med.* **2005**, *83*, 377.

[15] W.-H. Chan, N.-H. Shiao, P.-Z. Lu, *Toxicol. Lett.* **2006**, *167*, 191.

[16] S. J. Byrne, Y. Williams, A. Davies, S. A Corr, A. Rakovich, Y. K. Gun'ko, Y. P. Rakovich, J. F. Donegan, Y. Volkov, *Small* **2007**, *3*, 1152.

Chapter 7: Experimental

7.1. General procedures

The synthesis of CdTe QDs and all spectroscopic studies were carried out in Millipore water (18 MΩ.cm). Standard Schlenk techniques and vacuum manifolds were used in the manipulation of air-sensitive solutions. All the compounds were obtained from Sigma-Aldrich (Gillingham), except Aluminium Telluride (Al_2Te_3) which was obtained from Cerac Inc. (Milwaukee) and used without further purification. QD purification was performed *via* size selective precipitation using isopropanol as a non-solvent unless otherwise stated. A Heittich Universal centrifuge 32 machine at 3500 rpm was then used for centrifugation. Further purification was accomplished on size exclusion chromatography [gel Sephadex G-25] (Aldrich).

7.1.1. Instrumental techniques used

UV-Vis absorption spectra were recorded using a Cary 50 UV-Vis spectrophotometer. Fluorescence measurements were performed on a Cary Eclipse spectrophotometer. TEM images were taken on a Hitachi H-7000 at a beam voltage of 100kV. Samples for TEM were prepared by deposition of a 10 μL drop of solution onto a formvar coated 400 mesh carbon grid. The solution was left for 30 minutes before the remaining supernatant was removed with filter paper. HRTEM was only available at certain times and samples had to be sent to Prof. Nicholas Kotov at the University of Michigan for characterisation.

IR spectra (200-4000 cm^{-1}) were recorded by diffuse reflectance in KBr using a Perkin Elmer Spectrum One FT-IR spectrophotometer. Raman spectra were recorded by Dr. Yury Rakovich at room temperature on a Reinshaw 1000 micro-Raman system equipped with a Leica microscope. The 50x-magnifying objective of the microscope focussed a laser beam onto a spot of ~ 1 μm in diameter. Because of the high quantum efficiency of the QDs, resonant Raman spectra were superimposed on a broad luminescence background. This background has been subtracted in all spectra presented in order to show more clearly the Raman signal itself. The excitation wavelength was 514.5 nm from an Ar^+ ion laser and laser power was kept at 0.5 mW to prevent sample heating. An 1800 line/nm gating was used and allowed for a spectral resolution of 1 cm^{-1}.

Each spectrum was averaged over 20 measurements with an accumulation time of 20 seconds and all obtained spectra were fitted using Lorentzian functions.

Fluorescence lifetime decays were measured using a time-correlated single photon counting machine (Time-Harp, PicoQuant). The samples were excited by 480 nm picosecond pulses generated by a PicoQuant, LDH-480 laser head controlled by a PDL-800B driver. The setup was operated at an overall time resolution of approximately 150 ps. Decays were measured to 3000-5000 counts in the peak and reconvoluted using non-linear least squares analysis (FluoFit, PicoQuant), using an equation of the form: $I(t) \propto \sum_i \alpha_i \exp(-t/\tau_i)$, where τ_i is the decay time. The pre-exponential factors α_i, were taken into account by normalisation of the initial point in the decay to unity. The quality of fit was judged in terms of a χ^2 value, with a criteria of less than 1.1 for an acceptable fit and weighted residuals.

^1H and ^{13}C spectra were recorded on a Bruker Advance AC-400 instrument at 400 and 50.3 MHz respectively. Chemical shifts were measured relative to that of $CDCl_3$, δ 7.26 for ^1H and δ 77.16 for ^{13}C. The following abbreviations are used to describe the signal multiplicities: s (singlet), bs (broad singlet), d (doublet), t (triplet), q (quadruplet), sp (septet) and m (multiplet). Chemical shifts are expressed in parts per million and listed as follows: shift in parts per million (multiplicity, integration, coupling and attribution).

Mass spectra (MS) were recorded on a Micromass Time of Flight (oa-TOF) equipped with an electrospray ionisation (ES) interface operated in the positive mode. This method can give either a $M + H^+$ or a $M + Na^+$ signal. PCS (particle sizing) measurements were recorded on a Malvern zetasizer (nano series) machine.

7.1.2. Measurement of the fluorescence Quantum Yield (QY)

The fluorescence QY of the CdTe QDs was measured against a standard of Rhodamine 6G, which has a 95% quantum efficiency. The Rhodamine was standardised to an absorbance value of no more than 0.15 in the region 460 – 480 nm with its overall absorbance kept below 1. The QD solutions were diluted to intersect the Rhodamine absorption typically between 470 – 480 nm. By comparing the integrated areas of the

resultant emission spectra, excited at the intersection wavelength, the fluorescence QY of the CdTe QDs was calculated.

7.1.3. Cell biolabelling experiments

Investigations into the activity and localisation of the QDs within intracellular environments (THP-1 cell) were conducted by Dr. Siobhan Mitchell and Ms Yvonne Williams under the supervision of Dr. Yurii Volkov in the Clinical Medicine Dept. of St. James Hospital Dublin.

The human THP-1 monocyte cell line was obtained from the European Collection of Animal Cell Cultures (ECACC, Salisbury, UK). Cells were grown in RPMI 1640 medium supplemented with 10% heat-inactivated fetal bovine serum (FBS), 2 mM l-glutamine/L, 100 μg penicillin/ml and 100 mg streptomycin/ml, and incubated at 37°C in 5% CO_2. To induce monocyte to macrophage differentiation, THP-1 cells were cultured in the presence of 100 ng/ml PMA for 72 h. Cells were then washed three times with HBSS before use. THP-1 cells were incubated with a 1 in 100 dilution with the quantum dots. Live cell imaging was performed in Lab-Tek chambered coverglass slides (Nunc). Images were acquired by fluorescence microscopy (Nikon Eclipse TE 300) and on the UtraView Live Cell Imager (Nikon Eclipse TE 2000-U) confocal microscopy workstation (Perkin-Elmer Life Sciences, Warrington, UK) (Nikon Eclipse TE 2000-U). Processing was performed using Ultra View LCI.

7.2. Experimental Details for Chapter 2

7.2.1. Preparation of TGA capped CdTe QDs using Al_2Te_3

CdTe QDs were prepared according to published procedure. [1, 2] 100 ml of millipore water (18MΩ.cm) was degassed by heating and then cooling under argon. The solution was further deaerated by bubbling argon for approximately 1 hour. $Cd(ClO_4)_2 \cdot 6H_2O$ (0.737 g, 1.76 mmol) and two molar equivalents of TGA stabiliser (245 μl, 3.51 mmol) were added and the pH was adjusted to 11 for a negatively charged and 6 for a positively charged surface by the addition of a 2M NaOH solution. H_2Te gas, generated from Al_2Te_3 (0.128 g, 0.29 mmol) *via* the dropwise addition of a 0.5M H_2SO_4 solution was bubbled under a slow argon flow for approximately 10 minutes. At that time

the solution changed from clear to an orange/red colour and was optically transparent. This non luminescent solution was then refluxed until the desired emission wavelength, determined *via* luminescence spectroscopy was reached. The solution was then reduced down by rotary evaporation to one fifth the original volume and size selectively precipitated *via* the addition of isopropanol. Upon isopropanol addition the solution went turbid, was stirred and then precipitated out using centrifugation. The resulting fractions were re-dissolved in water and stored at 4° C for further characterisation and use. The solutions were characterised *via* UV-vis absorption and luminescence emission spectroscopy and dried fractions along with the stabiliser were characterised by TEM / HRTEM (Figure 2.5) and IR spectroscopy (Figure 2.6).

IR (KBr, cm^{-1}): thioglycolic acid (TGA): ~ 3000 (br, s) O-H str, 2555 (m) S-H str, 1705 (s) C=O str, 1414 (s) O-H bend, 1286/1193 (s) C-O str.

7.2.2. Preparation of CdTe QDs using Na_2Te

Tellurium powder (0.66g, 5 mmol) was added to a solution of sodium borohydride (0.38g, 10 mmol) made in 10 cm^3 of 2 M NaOH and 50 cm^3 of water. The mixture was heated under reflux for 2 hours and a colour change to purple was noted. A sodium telluride (Na_2Te) slurry was formed after the solution was cooled in ice. The purple liquid was filtered off *via* a cannula and the slurry was washed with ice cold water and then dissolved in water at room temperature. This solution was then added to a $Cd(ClO_4)_2 \cdot 6H_20$ and thiol stabiliser solution with the pH at 11 or 6, adjusted as before. The solution was then heated under reflux to begin nanocrystal formation from the precursors. The size fractions were purified and characterised as stated above.

7.2.3. Statistical analysis

TGA capped CdTe QDs have been prepared according to a 2^2 factorial statistical analysis throughout a series of eight experiments (Figure 2.7) according to the above procedure. The unpurified samples were stored in darkness for a period of 24 hours to allow them to attain thermal equilibrium before the absorption and luminescence spectra

were taken. Room temperature luminescence efficiencies were determined by comparing the QD integrated emission with that of Rhodamine 6G.

7.2.4. Photoetching

50 or 100µl of purified CdTe QDs were diluted with 3 cm^3 millipore water. Solutions of QDs capped by various thiol groups were irradiated with a water filtered, high pressure Mercury (Hg) lamp. The field of irradiation was > 350 nm, but was altered to > 450 nm by use of an optical filter. The solutions were stirred throughout. UV-vis absorption and luminescence emission spectra were taken to monitor any optical effects due to the photoetching process.

7.2.5. Ageing

Freshly prepared but unpurified QD solutions of various stabilisers were diluted and stored at room temperature, in darkness and open to air. 50 or 100µl of the unpurified solutions were diluted with 3 ml of Millipore water. UV-vis absorption and luminescence emission spectra were taken to monitor any optical effects due to the ageing process.

7.3. Experimental Details for Chapter 3

7.3.1. Synthesis and characterisation of CdTe QDs using commercially available thiol stabilisers

CdTe QDs capped with the thiols described in Table 3.1 were synthesised using the same procedure as described in the experimental details of Chapter 2. The thiols and their QD counterparts were analysed spectroscopically (UV-vis absorption and luminescence emission) and a sample after purification was analysed by IR (Appendix 3a-3g).

3-mercapto-1,2-propanediol, (KBr, cm^{-1}): 3321 (s) O-H str, 2924 / 2873 (s) C-H str, 2548 (m) S-H str, 1411 (s) CH_2 bend, 1068 / 1028 (s) C-O str.

mercaptopropionic acid (MPA), (KBr, cm^{-1}): 2954 (m, br) O-H str., 2584 (w) S-H str., 1701 (s) C=O str., 1411 (s) O-H bend, 1245 / 1207 (s) C-O str.

glutathione, (KBr, cm^{-1}): 3241 / 3337 (m) N-H str, 3010 (br, m) O-H str., C-H str., 2522 (m) S-H str, 1715 (s) C=O str, 1593 (s) N-H bend, 1277 / 1243 (s) C-O str., 1074 (m) C-N str.

cysteamine, (KBr, cm^{-1}): 3428 (m) N-H str, 2971 / 2860 (s) C-H str, 2477 (m) S-H str, 1585 (s) N-H bend, 1482 (s) CH_2 bend, 1240 (m) C-N str.

N-acetyl-*L*-cysteine, (KBr, cm^{-1}): 3372 (s) O-H / N-H str, 2547 (m) S-H str, 1716 (s) C=O str, 1587/1532 (s) N-H bend, 1199 - 1300 (s) C-O, C-N str, 1126 (m) C-C str.

***L*-cysteine**, (KBr, cm^{-1}): 3293 (s) N-H str, ~3000 (br, s) O-H str., C-H str., 2522 (m) S-H str, 1743 (s) C=O str, 1603 / 1547 (s) N-H bend, 1393 (m) C-O, 1197 (s) C-N str.

7.3.2 Electrophoresis

A Consort electrophoresis unit set at 70 V, 29 mA and 2 W was used as a power supply. 50 mM TrisHCl [6g Trizma base in 900 ml Millipore water, pH adjusted to 8.1 with 1M HCl and made to 1L] was used as the running buffer (electrolyte solution) and a 0.8% agarose gel [1.6 g agarose in 200 ml Millipore water (18 MΩ)] was used as a separating gel. The agarose was heated to dissolve and then allowed to cool and set in the holding bath.

7.3.3 Live cell experiments

Live cell cultures were prepared and QD samples were analysed as described in section 7.1.3.

7.4. Experimental Details for Chapter 4

7.4.1. Preparation of TGA and gel-TGA-QDs

7.4.1.1. Preparation of gel-TGA-QDs at 1.75 : 1 TGA :Cd ratio

Millipore water (100 ml) was degassed by bubbling argon for approximately 1 hour. $Cd(ClO_4)_2 \cdot 6H_2O$ (3.22 g, 7.68 mmol), TGA (thioglycolic acid) stabiliser (1.24 g, 13.46 mmol, 1.75 molar equivalents) were then added and the pH was adjusted to 11.2 - 11.3 by the addition of a 2 M NaOH solution. For samples containing gelatin, 0.3g was dissolved in 20 ml water by heating gently and added to the reaction mixture. H_2Te gas, generated from the decomposition of Al_2Te_3 (0.56 g, 0.128 mmol) via the drop-wise

addition of a 0.5M H_2SO_4 solution was bubbled through the cadmium / thiol / gelatin solution under a slow argon flow for approximately 10 minutes. The resultant, non-luminescent solution was then heated to reflux and samples were taken and spectroscopically characterised at various time intervals (0 minutes after start of heating and 15, 30, 40, 55, 70, 85, 100, 130 and 160 minutes after start of reflux). The crude mixture was reduced down to one fifth its original volume and sample fractions were precipitated via the addition of isopropanol. Purified samples were stored at 4° C for characterisation in a live cellular environment and toxicity studies.

For experiments with different ratios, the $Cd(ClO_4)_2 \cdot 6H_2O$ concentration was kept constant and the stabiliser quantities were adjusted accordingly. Preparation of gel-TGA-QDs at 1.4 : 1 TGA : Cd ratio [TGA (0.99 g, 10.74 mmol, 1.4 molar equivalents)]. Preparation of gel-MPA-QDs at 1.75 : 1 MPA :Cd ratio [MPA (1.43 g, 13.46 mmol, 1.75 molar equivalents)]. Preparation of gel-MPA-QDs at 1.4 : 1 MPA :Cd ratio [MPA (1.14 g, 10.74 mmol, 1.4 molar equivalents)]. Preparation of gel-cys-QDs at 1.4 : 1 cysteamine :Cd ratio [cysteamine hydrochloride (1.22 g, 10.74 mmol, 1.4 molar equivalents)].

7.4.2 Biological cytotoxicity testing

7.4.2.1 Cell culture

THP-1 monocytic cell line (ECACC, Salisbury, England) was grown in supplemented (10% foetal bovine serum; 2 mM/L L-glutamine; 100 μg/mL penicillin; 100 mg/mL streptomycin) RPMI 1640 media. They were seeded out onto a 96 well microtitre plate at a concentration $2x10^5$ cells/mL in 200 μL/well. The cells were cultured with 100ng/mL PMA, enabling monocyte to macrophage differentiation, for 72 hours, in controlled atmospheric conditions of 37° C, 5% CO_2. Two hours prior to the addition of the QDs, the media was replaced with serum free media.

7.4.2.2 Toxicity assay

Assay protocol:

QDs were diluted 1:50 in complete medium, 100 μl of which replaced 100 μl/well of serum free medium (final dilution 1:100). The QDs were incubated with the cells in controlled atmospheric conditions and analysed after 3 and 6 hours. Each QD sample was

assayed in duplicate for each time point. For controls, cells were also incubated alone or with other variables such as gelatin, thiol or cadmium. A Multiparameter Cytotoxicity 2 HitKit® was utilised for this assay. The dyes from the assay were diluted 1:100 with complete media as per the manufacturer's instructions at 37° C, 5% CO_2 for 30 minutes. The stain was decanted and replaced with 3% paraformaldehyde in MPCT wash buffer (preheated at 37° C) for 15 minutes. The cells were then washed twice with the wash buffer before analysis. The images from the microtitre plates were acquired using the Cellomics KineticScan® (an automated fluorescent microscope) and analysed with the optimised software, Multiparameter Cytoxicity® Bioapplication. The light source was a Hg/Xe white lamp.

Toxicity assay: A commercial kit (multiparameter cytotoxicity 1 HitKit®, Cellomics, PA, USA) was used to monitor the toxic affects induced by the QDs on the cells. The kit contains optimised reagents for simultaneous detection and analysis for the detection of changes in nuclear morphology and size, the cell membrane's permeability status, changes in cell density (number of cells per field) from compound toxicity, and changes induced to the lysosome's pH.

The nucleus (Hoescht / blue) was gated [highlighted] and identified in Channel 1 (blue). Channel 2 (green) was used to measure cell permeability. Any inclusions within a defined radius from the nucleus are gated for measurement of the lysosomal pH in channel 3 (red). Values for the size of the nucleus are in pixel numbers, while the permeability and lysosomal pH are quantified as the average intensity of pixels within the area gated. This kit contains a three-in-one fluorescent dye that stains for nuclei (Hoescht) ($\lambda_{ex/em}$ 350 (± 50) / 460 (± 20) nm) [The assay uses the nuclear stain to identify individual nuclei and thus cell, and measure changes in nuclear size and morphology that are caused by toxic insult], cell permeability ($\lambda_{ex/em}$ 494 (± 40) / 517 (± 20) nm) [healthy cells are nearly impermeable to the dye used in this assay; however after compromising the cell membrane's permeability, the dye stains with a bright green fluorescence] and Lysosomal pH ($\lambda_{ex/em}$ 560 (± 15) / 590 (± 25) nm) [the dye used is a weak base that accumulates in the acidic organelles such as lysosomes and endosomes. A decrease in pH caused by the toxicity of a compound directly correlates to the amount of accumulated

dye and, thus, the fluorescence (red) intensity. Conversely, and increase in pH results in a decrease in staining intensity]. On exposure to toxic compounds cells can respond by exhibiting changes in nuclear size and shape, increased cell permeability and increases in the number in pH. The cytotoxicity assay was performed using High Content Analysis (HCA) in a 96 well format on a well by well and cell by cell basis. The large amount of data obtained ensures robustness of the assay. Also, each assay was performed in duplicate and over two time scales. The complete experiment was repeated with another batch of QDs.

7.5 Experimental Details for Chapter 5

Syntheses of NSAID (Non Steroidal Anti Inflammatory Drug) derivatives were performed in anhydrous solvents under dry and oxygen free argon. The purifications of organic derivatives by column chromatography were carried out using a silica gel 60 (Merck, 60-230 mesh), dichloromethane (DCM), ethyl acetate and methanol (MeOH). The progress of reaction was followed by thin layer chromatography (TLC) on silica plates (Merck, 60F254). The following developing systems were used: UV light at 254nm, ninhydrin (Sigma) and potassium permanganate (Aldrich).

7.5.1 Synthesis of N-(2-Mercaptoethyl)benzamide (Figure 5.4 B)

Benzoyl chloride (3 g, 2.47 ml, 21 mmol), Et_3N (7.5 ml) and 2,2'-Dithiobis(ethylamine) dihydrochloride (2.40 g, 10.6 mmol) were stirred under argon overnight. The disulfide product was worked up with dilute HCl and ether. Purification was performed by flash chromatography (1:1 Hexane/ethyl actetate [H/E]) giving 1.51 g 40% yield of the disulfide derivative. This disulfide (1.5 g, 4.16 mmol) was reduced by reaction with finely ground PPh_3 (1.09 g, 4.76 mmol) under reflux in aqueous methanol (1:9) overnight. The methanol was removed under vacuum. Water and ether were added (~ 30 ml) along with ~ 0.5 g NaOH pellets. The aqueous layer was removed and washed with ether. Dilute HCl was added and the product was extracted with ether. The ether layer was dried over $MgSO_4$ and removed under vacuum, giving 0.805 g, 53% yield of N-(2-Mercaptoethyl)benzamide (Figure 5.4 B). The product was characterized by ^1H NMR spectroscopy (400 MHz, $CDCl_3$) (Appendix 5 a):

N-(2-Mercaptoethyl)benzamide [Structure 5.4 B]: δ (ppm): 1.40 (t, 1H, SH), 2.76 (dt, 2H, $C\underline{H}_2$-SH), 3.61 (dt, 2H, $C\underline{H}_2$-NH), 6.94 (s, 1H, NH), 7.40 and 7.49 (m, 5H, *m&p* Ar-H), 7.79, 2H, *o* Ar-H)

7.5.2 Synthesis of {2-[2-(2-amino-ethoxy)-ethoxy}-ethyl}-carbamic acid tert butyl ester: boc-amino-PEG: compound 1

The synthesis of boc-amino-PEG was conducted as previously described. [3] Boc anhydride (Aldrich) (3 g, 13.7 mmol) in 20 mL of dioxane was added dropwise to a solution of 12 mL (82.3 mmol) of 2,2'-(ethylenedioxy)bis(ethylamine) (Aldrich) in 50 mL dioxane over 5 hours. The reaction mixture was then concentrated under vacuum and the resulting oil was dissolved in 40mL of water and washed 5 times with 50 mL of DCM. The combined organic phases were washed four times with 40 mL of brine and dried over $MgSO_4$. 2.97 g (12 mmol, 87%) of **compound 1** as clear slightly yellow oil was obtained. TLC (DCM/MeOH 8/2, UV and ninhydrin) R_f = 0.36; ^{1}H NMR [Appendix 5 b] ($CDCl_3$) δ 1.41 (s, 9H, Boc), 1.63 (bs, 2H, NH_2), 2.86 (t, 2H, ^3J = 5Hz, CH_2NH_2), 3.29 (m, 2H, CH_2NH), 3.49 and 3.51 (t, 2H, ^3J = 5.1Hz, CH_2O), 3.59 (s, 4H, OCH_2CH_2O), 5.17 (bs, 1H, NH); ^{13}C NMR [Appendix 5 b] ($CDCl_3$) δ 28.6 ($(CH_3)_3C$), 40.5 (CH_2NH), 41.9 (CH_2NH_2), 67.2, 70.4 and 73.5 (CH_2O), 79.4 ($(CH_3)_3C$), 156.1 (CO). ESI-MS, *m/z* 249.18 in agreement with the mass calculated for $[M+H]^+$.

7.5.3 Synthesis of tert-butyl 2-(2-(2-(2-(6-methoxynaphthalen-2-yl) propanamido) ethoxy) ethoxy) ethylcarbamate: (npx-boc-amino-PEG): compound 2

To a solution of Naproxen ((S)-(+)-6-methoxy-2-alpha-methyl-2-naphthalene acetic acid, 2.06 g, 8.95 mmol, Aldrich) in 30 mL of dry DCM, was added thionyl chloride (850 μL, 11.6 mmol, Aldrich). The reaction was stirred under reflux for one hour and then evaporated and dried under vacuum. The yellow solid was then dissolved in dry THF (30 mL) and added dropwise to a solution of **compound 1** (2 g, 8 mmol), NEt_3 (Aldrich, 2.02 mL, 14.1 mmol) in dry THF (30 mL) at 0° C The reaction mixture was then stirred at room temperature for 3 hours, filtered and concentrated under vacuum. The residue was dissolved in DCM (30 mL) and washed three times with an basic aqueous

solution ($NaHCO_3$, 15 mL) then with neutral water (30 mL). The organic layer was dried over $MgSO_4$, filtered and dried under vacuum. The product was further purified by column chromatography (DCM/ethyl acetate 9/1 then DCM/MeOH 95/5) to yield 2.4g (5.2 mmol, 65%) of **2** as a white solid. TLC (DCM/MeOH 9/1, UV and ninhydrin) R_f = 0.44; ^{1}H NMR ($CDCl_3$) δ 1.44 (s, 9H, $(CH_3)_3C$), 1.57 (d, 3H, ^3J = 7.02Hz, CH_3CH), 3.19 (bs, 2H, CH_2NHCOO), 3.33-3.60 (m, 10H, CH_2OCH_2), 3.67 (q, 1H, ^3J = 7.02Hz, $CHCH_3$), 3.91 (s, 3H, OCH_3), 4.94 (bs, 1H, NHCOO), 5.92 (bs, 1H, NHCO), 7.10-7.13 (m, 2H, $CHC(OCH_3)CH$), 7.38 (d, 1H, ^3J = 8.03Hz, $CHC(CH)CH$), 7.67-7.70 (m, 3H, CH). ^{13}C NMR ($CDCl_3$) δ 18.6 ($CHCH_3$), 28.5 ($C(CH_3)_3$), 39.4 (CH_2NHCO), 40.2 (CH_2NHCOO) 47.0 ($CHCH_3$), 55.4 (CH_3O), 69.9,70.1, 70.3 (CH_2OCH_2), 79.3 ($C(CH_3)_3$), 105.6, 119.1, 126.1, 126.4, 127.4, 129.3 (CH), 129.0,133.8, 136.5 (C=C, $C(CHCH_3)$), 156.0 (CH_3OC), 157.7 (NHCOO), 174.4 (NHCO). ESI-MS, *m/z* 483.24 in agreement with the mass calculated for $[M+Na]^+$.

7.5.4 Synthesis of N-2-(2-(2aminoethoxy)ethoxy)ethyl)-2-(6-methoxynaphthalen-2-yl)propanamide:(npx-amino-PEG-NH_2): compound 2a

To a solution of **compound 2** (1.8 g , 3.9 mmol) in 10 mL of dry DCM at 0°C, trifluoroacetic acid (TFA, 10 mL, 130 mmol, Aldrich) was added slowly. The reaction mixture was stirred until disappearance of the protected compound monitored by TLC. After completion of the reaction, the mixture was concentrated and TFA removed by evaporation cycles with DCM/cyclohexane (1/1, v/v). The residue was then dried under vacuum to yield 1.70 g (3.6 mmol, 92%) of **2a** TFA salt as a yellow oil. ^{1}H NMR [Appendix 5c] ($CDCl_3$) δ 1.57 (d, 3H, ^3J = 7.03Hz, CH_3CH), 2.97 (m, 2H, CH_2NH_2), 3.46-3.47 (m, 10H, CH_2OCH_2), 3.79 (q, 1H, ^3J = 7.03Hz, $CHCH_3$), 3.91 (s, 3H, OCH_3), 6.58 (bs, 1H, NH), 7.10-7.15 (m, 2H, $CHC(OCH_3)CH$), 7.31 (m, 1H, $CHC(CH)CH$), 7.65-7.72 (m, 3H, CH). ^{13}C NMR [Appendix 5c] ($CDCl_3$) δ 18.8 ($CHCH_3$), 39.5 (CH_2NH), 42 (CH_2NH_2), 47 ($CHCH_3$), 55.5 (OCH_3), 70, 70.1, 70.3, 73.2 (CH_2OCH_2), 105.7, 119.2, 126.1, 126.5, 127.5, 129.3 (CH), 29.1, 133.8, 136.9 (C=C, $C(CHCH_3)$), 157.8 (CH_3OC), 174.6 (CO). ESI-MS, *m/z* 361.21 in agreement with the mass calculated for $M + H^+$.

7.5.5 Synthesis of tert-butyl 2-(2-{2-[2-(4-isobutylphenyl) propanamido]ethoxy}ethoxy) ethylcarbamate: ibu-boc-amino-PEG-NH_2: compound 3

To a solution of Ibuprofen (S-(+)-2-(4-isobutylphenyl)-propionic acid, 2 g, 9.7 mmol, Fluka) in 20mL of dry DCM was added thionyl chloride (4.25 mL, 58.2 mmol). The solution was stirred under reflux for one hour and then evaporated and dried under vacuum. The pale yellow solid was then dissolved in THF (20 mL) and added dropwise to a solution of **1** (2.4 g, 9.7 mmol) with NEt_3 (3.4 mL, 24 mmol) in dry THF (20 mL) at 0°C. The reaction mixture was then stirred at room temperature until consumption of the chloride compound as monitored by TLC. The residue was dissolved in DCM (30 mL) and washed three times with brine (30 mL) and with neutral water (3x15 mL). The organic layer was dried over $MgSO_4$, filtered and dried under vacuum. The product was further purified by column chromatography (DCM/ethyl acetate 9/1 then DCM/MeOH 95/5) to yield 2g (4.6 mmol, 47%) of **3** as a pale yellow oil. TLC (DCM/MeOH 9/1, UV and ninhydrin) R_f = 0.49; ^{1}H NMR ($CDCl_3$) δ 0.82 (d, 6H, ^{3}J = 6.53Hz, $(CH_3)_2CH$), 1.37 (s, 9H, Boc), 1.41 (d, 3H, ^{3}J = 7.53Hz, CH_3CH), 1.77 (sp, 1H, ^{3}J = 6.53Hz, $(CH_3)_2CH$), 2.37 (d, 2H, ^{3}J = 7.02Hz, $CHCH_2$), 3.21-3.54 (m, 12+1H, CH_2NH, CH_2O, $CHCH_3$), 5.06 (bs, 1H, NHCOO), 6.10 (bs, 1H, NHCO), 7.02 and 7.15 (d, 4H, ^{3}J = 7.53Hz, CHar.). ^{13}C NMR ($CDCl_3$) δ 18.5 (CH_3CH), 22.3 ($(CH_3)_2CH$), 28.3 (CH_3 Boc), 30.1 ($(CH_3)_2CH$), 39.2 (CH_2NH), 40.2 (CH_2NHCOO), 44.9 (CH_2CH), 46.4 (CH_3CH), 69.7 and 70.0 (CH_2OCH_2), 79.1 ($C(CH_3)_3$), 127.2 and 129.3 (CH, Ar) 138.6 and 140.4 (C, Ar), 155.9 (NHCOO), 174.5 (NHCO). ESI-MS, *m/z* 459.28 in agreement with the mass calculated for M +Na^+.

7.5.6 Synthesis of N-(2-{2-[2-aminoethoxy]ethoxy}ethyl)-2-(4-isobutylphenyl propanamide: ibu-amino-PEG-NH_2: compound 3a

The Boc removal procedure is identical as described above with **compound 2a** with 2 g (4.6 mmol) of **compound 3** yielding, after drying, 1.9 g (4.2 mmol, 91%) of **3a,** TFA salt as a pale brown oil. ^{1}H NMR [Appendix 5d] ($CDCl_3$) δ 0.87 (d, 6H, ^{3}J = 6.53Hz, $(CH_3)_2CH$), 1.48 (d, 3H, ^{3}J = 7.03Hz, CH_3CH), 1.79 (sp, 1H, ^{3}J = 6.53Hz, $(CH_3)_2CH$), 2.42 (d, 2H, ^{3}J = 7.03Hz, $CHCH_2$), 3.09 (m, 2H, CH_2NH_2), 3.40 (m, 2H, CH_2NH) 3.48

(m, 6H, CH_2O), 3.63 (m, 3H, CH_2O, $CHCH_3$), 6.50 (bs, 1H, NHCO), 7.11 and 7.16 (d, 4H, ^3J = 8.03Hz, CH Ar.), 7.50 (m, 2H, NH_2). ^{13}C NMR [Appendix 5d] ($CDCl_3$) δ 18.1 (CH_3CH), 22.5 (($CH_3)_2CH$), 30.4 (($CH_3)_2CH$), 39.8 (CH_2NH), 40.1 (CH_2NH_2), 45.1 (CH_2CH), 46.5 (CH_3CH), 66.5, 69.9, 70.1 and 70.4 (CH_2OCH_2), 127.5 and 129.9 (CH, Ar) 137.6 and 141.4 (C, Ar), 174.6 (NHCO). ESI-MS, *m/z* 337.24 in agreement with the mass calculated for $M + H^+$.

7.5.7 Synthesis of NSAID – QD conjugates

Conjugation reactions with QDs (synthesised as described in 7.2.1) were carried out in borate buffer (pH 7.5) with EDC.HCl. NSAID -QD conjugates were purified over a G-25 sephadex column equilibrated in millipore water and filtered with 0.2 μm filters (PAL, Life Sciences). Enzymatic tests were carried out using Trypsin 10X solution from Sigma in PBS 1X buffer at pH 7.4.

7.6 Description of experimental techniques

7.6.1 Fluorescence / Luminescence spectroscopy

Fluorescence / Luminescence spectroscopy measures the quantity of light emitted from a substance upon the absorption of ultraviolet (UV) radiation. When the sample absorbs a photon, electrons are promoted from the ground to a higher vibrational state within the molecules singlet excited electronic state. Collisions with other molecules result in the loss of vibrational energy, until it reaches the lowest state of its excited form. When an electron returns from here to the ground state, a photon is given off. This is known as fluorescence. However, if the spin of the excited state is reversed, *via* intersystem crossing, the molecule may reach an excited triplet state. This state is lower in energy than the singlet excited state and should the electron return to the ground state from here, a different photon is emitted. This is known as phosphorescence. These processes can be visualised with the aid of a Jablonski diagram (Figure 7.1) or for a QD system by Figure 1.1 (see Chapter 1).

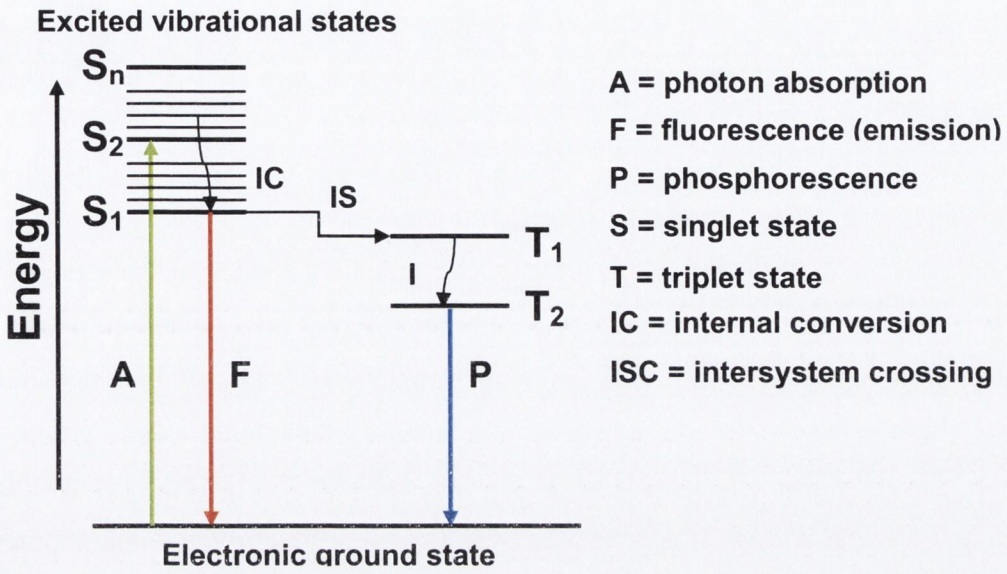


Figure 7.1. Jablonski diagram for an excited molecule showing the possible processes involved in returning to the ground state.

Fluorescence spectra were recorded on a Cary Eclipse spectrophotometer, using quartz cuvettes.

7.6.2 UV-vis absorption spectroscopy

Ultra violet visible (UV-vis) spectroscopy measures the quantity of light (between 400 and 800 nm) of a particular wavelength that is absorbed by a sample. Absorbance [-log (I/I_o)] of light is directly proportional to the path length of the cell used and the concentration of the species under investigation. This is given b the Beer-Lambert Law.

$$A = \varepsilon \, . \, c \, . \, l$$

A = absorbance,

ε = extinction coefficient of the substance (M^{-1} cm^{-1})

c = concentration (M)

l = path length of cell (cm)

The absorption of radiation is characteristic of the material under analysis and different materials absorb at different wavelengths. Absorption leads to the promotion of electrons from one energy level to another. The wavelength (and thus the energy) of the absorbed photon is directly proportional to the energy difference between these levels.

UV-vis spectra were recorded on a Cary 300 scan UV-Vis spectrophotometer, using quartz cuvettes.

7.6.3 Infrared (IR) spectroscopy

Infrared (IR) radiation is electromagnetic radiation greater in wavelength than visible light, but shorter than radio waves. IR spectroscopy investigates the vibrational states within a molecule upon interaction with IR radiation. Bonds within a molecule are not rigid but can be viewed a more spring-like. Within a functional atomic group, each chemical bond vibrates at a characteristic frequency and this is associated with the motion of electrical charge. If an oscillation results in a change in the dipole moment of the molecule, it may then absorb a photon of the same frequency. [4] Thus, if there is a change in dipole moment due to the vibrational excitation of the atomic group it may absorb a photon of the same frequency, generating an IR spectrum characteristic of that atomic group.

Samples for analysis were prepared by mixing with KBr and were subsequently pressed into a disk. IR spectra were recorded on a Perkin Elmer Spectrum One FT-IR spectrophotometer (400 – 4000 cm^{-1})

7.6.4 Raman spectroscopy

When light of energy $h\upsilon_o$ encounters matter (solid, liquid or gas), it may be transmitted, absorbed and emitted or scattered. When a photon has the same energy as the difference between two energy levels within the molecule, absorption and emission may occur. When this is not the case, the photons can be scattered. Most of the light possesses the same wavelength as the incident light (IL); that is, it is elastically scattered resulting in no net change of energy. This is known as Rayleigh scattering. However, a small fraction is shifted in wavelength due to the molecular rotations and vibrations of the molecule resulting in a net change of energy of the photon. This is known as Raman scattering. [5]

Interaction of light with a molecule raises it from a ground state (GS) to a virtual state (VS). The virtual state is a distortion of the electron distribution of the bond in

question by the oscillating electric field of the incident light. It is short lived and the molecule immediately returns back to the ground state, emitting a photon.

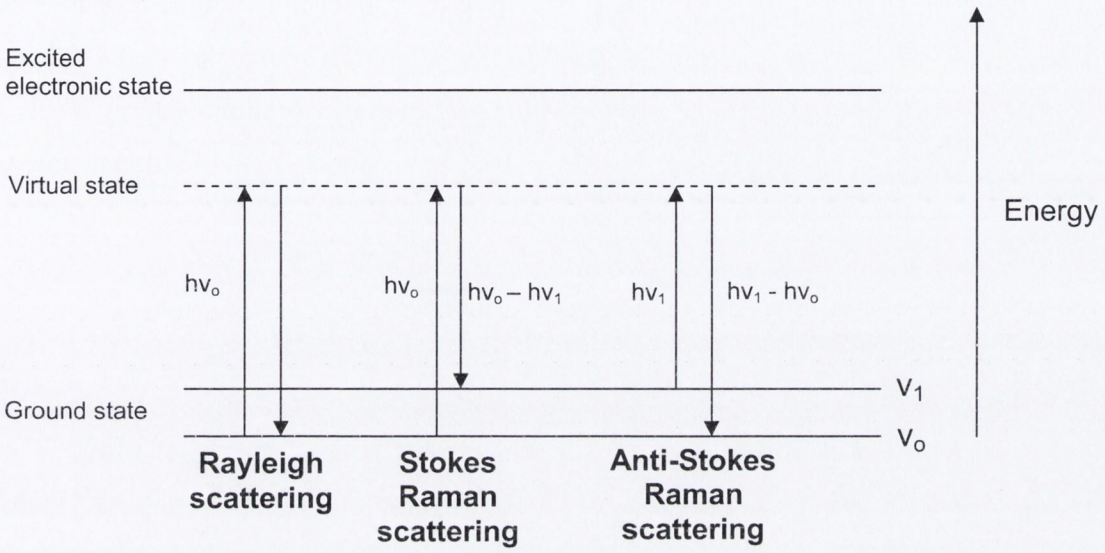


Figure 7.2. Diagram illustrating the possible light scattering events in Raman spectroscopy.

If the molecule, upon interaction with light reaches and returns to the GS from the VS with no change in energy, this is known as Rayleigh scattering. If the molecule returns to a higher vibrational state (v_1), the emitted photon has less energy than the IL, therefore a longer wavelength. This is known as a Stokes Raman shift. If the molecule happens to be in an excited vibrational state (v_1) when the IL is scattered, the photon may gain energy upon returning to the GS leading to an anti-Stokes Raman shift.

The Stokes Raman (SR), anti-Stokes Raman (ASR) are positioned symmetrically about the Rayleigh (R) peak as shown below. [6]

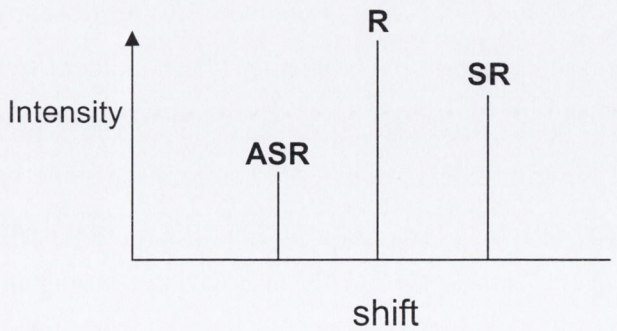


Figure 7.3. Diagram illustrating the Raman shifts due to photon scattering.

Rayleigh scattering is far more likely to occur and it appears with the strongest intensity (only 1 in 10^{10} photons undergo Raman scattering as it is a weak effect) compared to ASR or SR. Raman intensities are proportional to the number of molecules illuminated. Stokes Raman is proportional to the number of molecules in the GS, while anti-Stokes is proportional to the number in the next highest vibrational energy level.

At room temperature (RT), the fraction of molecules in one vibrational state with respect to another is given by a Boltzmann distribution. [7]

$$\mathbf{N_1/N_o = (g_1/g_o)\ exp\ (-(\Delta E)/\ kT)}$$

At RT $N_O > N_1$ which results in the stokes Raman shift being of higher intensity.

Light is an oscillating electric field and when it interacts with the electron cloud of a chemical bond, it can distort this cloud. A measure of the ease of this phenomenon is the polarisability of the bond. This induced dipole moment (μ_{ind}) within the molecule then radiates scattered light with or without changing energy. The strength of the induced polarisability is proportional to the incident electric field (see below) and the degree of polarisability is a function of the type of molecule and can vary as the position of the atoms change.

$\boldsymbol{\mu_{ind} = \alpha\ E.}$ α is the polarisability constant and is characteristic of the particular bond.

Raman spectroscopy is often used in conjunction with IR spectroscopy to build up a complete picture of the vibrational state of a molecule. If the incident light induces a change in dipole moment within the molecule it is said to be IR active, while only a change in polarisability is needed for Raman activity. Therefore the same bonds behave differently when analysed by each technique. For example, the carbonyl stretch is very strongly IR active while weak in Raman, while alkene bonds are strong in Raman but weak in IR. Furthermore, if there is a centre of symmetry present in the molecule a vibration that is active in the IR will be inactive in the Raman and *vice versa*.

7.6.5 Confocal microscopy

Confocal microscopy is a fluorescence based imaging technique that, using point illumination and pinhole detection, can construct a 3-D image of the sample being analysed. A schematic of the apparatus is shown in Figure 7.4.

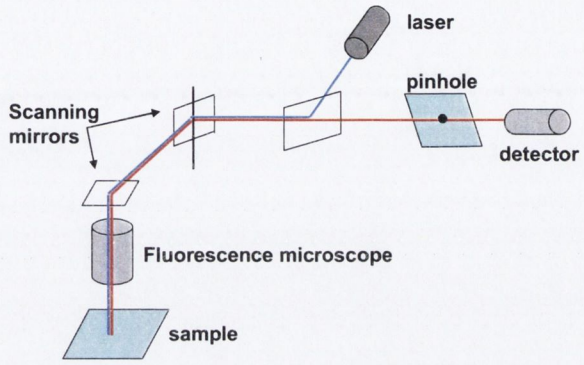


Figure 7.4. Graphical illustration of a confocal microscope setup.

The sample is excited by the fluorescence microscope, whose main feature is the presence of a dichroic mirror which reflects light shorter than a particular wavelength. It allows light of longer wavelength to pass through, enabling the user to only see light emitted by the sample blocking the excitation light. On expanding the setup, the main feature enabling the microscope to image specific regions of the sample is the pinhole. This eliminates any out of focus light and by adjusting the pinhole relative to the lenses the user can focus the incident beam on a point within a specific plane.

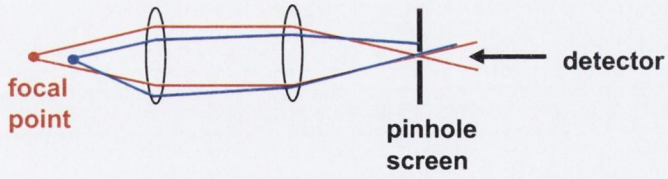


Figure 7.5. Diagram of the pinhole setup in a confocal microscope.

This gives a thin sectioned view of the object under investigation and by moving the pinhole the user may view many different points of focus. Continuous adjustment thus allows many thin sections to be viewed simultaneously enabling a 3-D image of the sample to be generated.

7.6.6 Photon correlation spectroscopy (PCS) / Dynamic light scattering (DLS)

The particle size measured by photon correlation spectroscopy (PCS) / Dynamic light scattering (DLS) is the diameter of the sphere that diffuses at the same speed as the particle being measured. PCS / DLS measures the Brownian motion (the random movement of particles in a liquid due to the bombardment by the molecules that surround them) of the particles and relates this to their size. This is accomplished by illuminating the particles with a laser and analysing the intensity fluctuations or speckle of the scattered light. An important feature is that small particles move more quickly than larger particles and this relationship is defined by the Stokes-Einstein equation.

$$D = kT / 6 \pi r\eta$$

D = diffusion constant, k = Boltzmann constant, T = temperature, f = frictional constant, r = radius, η = solvent viscosity.

Measurement is recorded by measuring the degree of symmetry between two light signals over a period of time. If the particle is stationary, then the correlation between the initial and final signal will be the same, ie equal to 1. However as particles move, so do their light fluctuations. Large particles move slowly, thus the intensity of their speckle patterns will fluctuate slowly. Similarly, for small particles moving quickly their speckle patterns will fluctuate quickly (Figure 7.6).

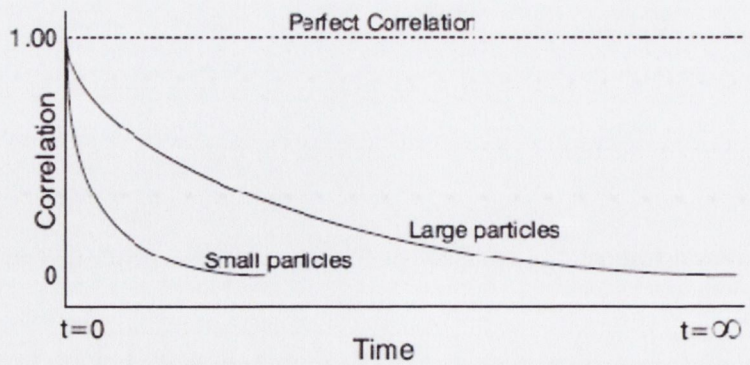


Figure 7.6. Correlation graphs illustrating the difference between small and large particles.

As can be seen from the graph, the rate of decay for the correlation function is proportional to the particle size and clearly, the decay rate for smaller particles is much faster than for larges ones. This data can then be used to generate a distribution plot as shown below.

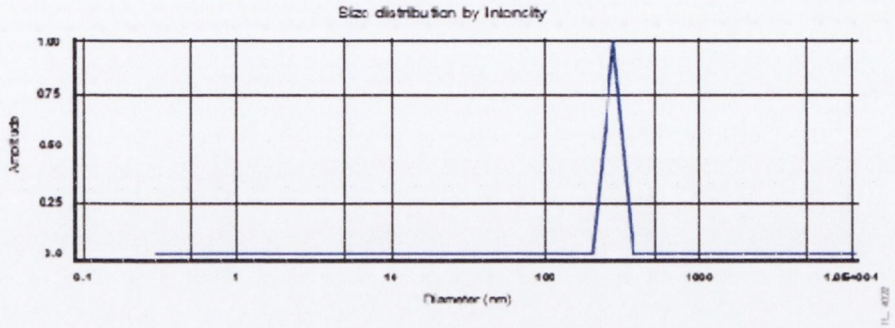


Figure 7.7. Size distribution (by intensity) for a standard sample.

This plot relates the intensity of light scattered to the size of the particle and enables the user to determine particle size within the sample.

7.6.7 Nuclear magnetic resonance (NMR)

When a nucleus is placed in a magnetic field it may absorb (excitation) energy (radiofrequency). The energy ($E = h\upsilon$) of the absorbed radiation is characteristic of the nucleus and its environment. A nucleus may be charged, depending on the population of the subatomic particles (protons (P), neutrons (N) and electrons (E)) and this charge spins on the nuclear axis. This overall spin is important and the number of possible orientations is given by $2I + 1$.

In the absence of a magnetic field, these orientations have equal energy (degenerate) however, upon application of a magnetic field the energy levels split and align either with or against the field (B_o).

In the presence of the magnetic field the populations of the energy levels are given by a Boltzman distribution with a slight excess for the lower energy state.

$$N_\alpha / N_\beta = \exp(\Delta E / kT)$$

Upon absorption of the radiation, the nuclei will flip form the low to the high state. This is called resonance and must be suited by

$$\upsilon = \gamma B_o / 2\Pi$$

υ = frequency of absorbed radiation

γ = magnetogyric ratio

B_o = applied magnetic field

In a static magnetic field a spin ½ nucleus will precess about the field axis at a frequency ω_o (Larmour frequency) analogous to a spinning top. The Larmour frequency is given by the expression [$\omega_o = \gamma B_o$]. As the population of the lower energy state is slightly larger (excess nuclei precessing in α state), this results in a net magnetisation (M_o) in the direction of B_o. [note xy plane rotating at ω_o].

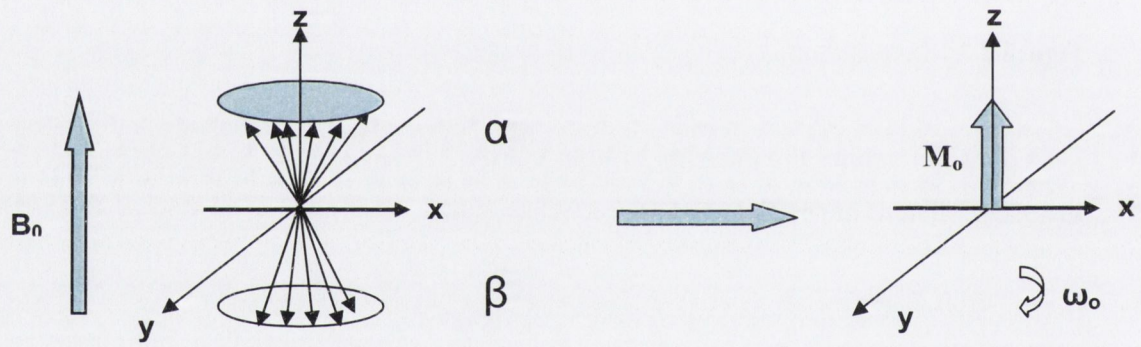


Figure 7.8. Illustration of the rotating planes and the net magnetisation induced upon application of a magnetic field upon a spin ½ nucleus.

M_o is also called the bulk magnetisation vector (BMV). Now to induce electromagnetic radiation, a transmitter coil is used, which generates an oscillating magnetic field (B_1) in the xy plane. B_1 is slit into two counterrotating components, one of which rotates in the same direction as the nucleus which is moving at ω_o around B_o. As the frequency of the radiation is increased, the frequency of B_1 ($+\omega_o$) also increases (ie. no. or rotations increases). Eventually B_1 matches ω_o, and M_o interacts with B_1 tipping M_o into the x-axis – resonance [individual nuclei flip from α to β].

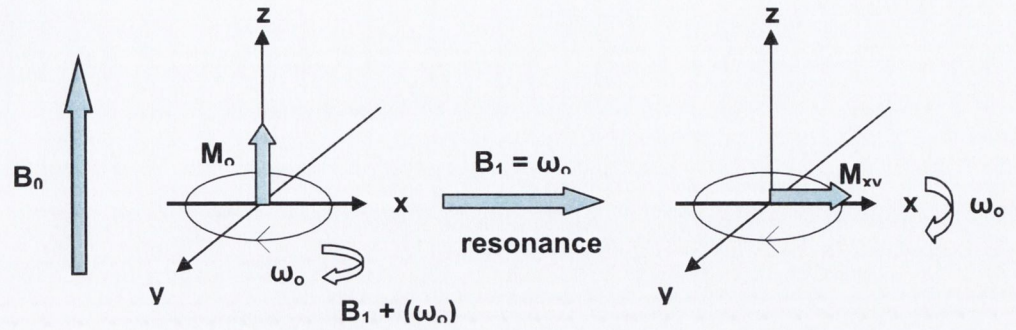


Figure 7.9. Diagram illustrating resonance, the condition where the applied radiofrequency equals the Larmour frequency and the net magnetisation changes plane.

At this stage there are now more nuclei in the β state but upon the removal of B_1 the nuclei return to their previous equilibrium. M_{xy} now returns to M_o but does so in a spiralling motion while still rotating at ω_o. This is referred to as longitudinal relaxation and the time it takes is T_1. The oscillation of M_{xy} returning to M_o generates a current in a receiver coil in the x-axis which is then used to construct a time domain NMR signal. A Fourier Transform is then used to bring the signal from the time domain into the frequency domain and generate the customary spectrum.

7.6.8 Transmission electron microscopy (TEM)

In electron microscopy, a high voltage beam of electrons emitted by a cathode (usually a tungsten filament) is focussed by electrostatic and electromagnetic lenses [condenser lens focuses electrons into narrow beam while aperture lenses focus the beam onto the sample] and bombards a sample to give information about the surface features, composition, lattice planes, size, shape, and distribution. Upon interaction with the sample, those electrons that are transmitted through are refocused through a series of lenses and generate an image on a phosphor screen. A CCD camera can then be used to record an image of the sample.

References

[1] S. J. Byrne, S. A. Corr, T. Y. Rakovich, Y. K. Gun'ko, Y. P. Rakovich, J. F. Donegan, S. Mitchell, Y. Volkov, *J. Mat. Chem.* **2006**, *16*, 2896.

[2] N. Gaponik, D. V. Talapin, A. L. Rogach, K. Hoppe, E. V. Shevchenko, A. Kornowski, A. Eychmüller, H. Weller, *J. Phys. Chem. B* **2002**, *106*, 7177.

[3] M. Braun, X. Camps, O. Vostrowsky, A. Hirsch, E. Endreß, T. M. Bayerl, O. Birkert, G. Gauglitz, G., *Eur. J. Org. Chem.* **2000**, *2000*, 1173.

[4] H. Gunzler, H. U. Gremlich, *IR Spectroscopy* **2002**, *WILEY-VCH*

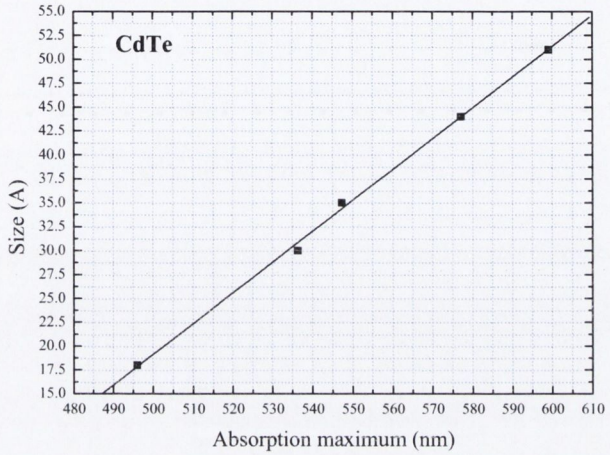
[5] M. J. Pelletier, *Analytical Applications of Raman Spectroscopy* **1999**, *Blackwell Science.*

[6] J. Twardowski, P. Anzenbacher, *Raman and IR spectroscopy in Biology and Chemistry* **1994**, *Ellis Horwood.*

[7] R. L. McCreery, *Raman Spectroscopy for Chemical Analysis* **2000**, *Wiley Interscience.*

Appendices

Appendix 2a: HRTEM sizing data for CdTe QDs correlated to UV-vis absorption maxima (supplied by Dr. Yury Rakovich)

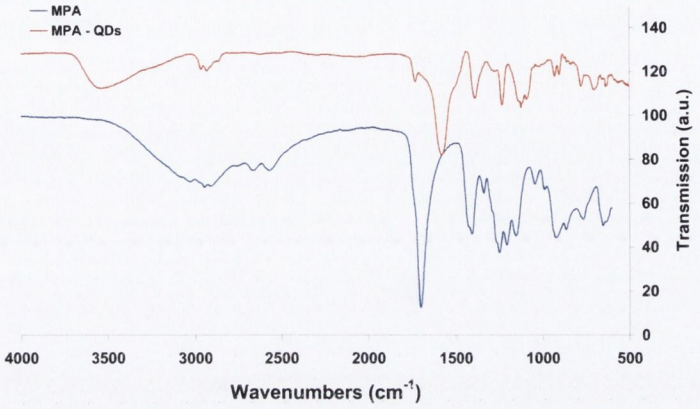


Appendix 3:

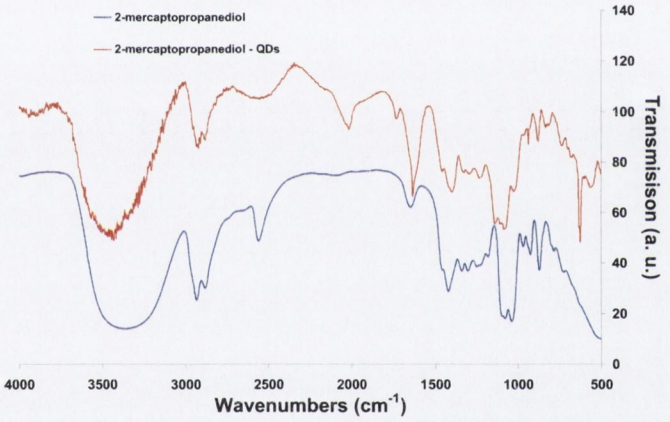
Appendix 3a Table of IR data taken for the QDs capped by the thiols described in Table 3.1

stabiliser	IR bands (cm^{-1})	Assignment
3-mercapto-1,2-propandiol	3321 (s)	O-H str
	2924 / 2873 (s)	C-H str.
	2548 (m)	S-H str.
	1411 (s)	C-H bend
	1028 / 1068 (s)	C-O str.
mercaptopropionic acid (MPA)	2954 (m, broad)	O-H str.
	2584 (w)	S-H str.
	1701 (s)	C=O str.
	1411 (s)	C-H bend
	1245 / 1207 (s)	C-O str.
glutathione	3241 / 3337 (m)	N-H str.
	3010 (br, m)	O-H str, C-H str.
	2522 (m)	S-H str.
	1715 (s)	C=O str.
	1593 (s)	N-H bend
	1277 / 1243 (s)	C-O str.
	1074 (m)	C-N str.
cysteamine	3428 (m)	N-H str.
	2971 / 2860 (s)	C-H str.
	2477 (m)	S-H str.
	1585 (s)	N-H bend
	1482 (s)	C-H bend
	1240 (m)	C-N str.
N-acetyl-*L*-cysteine	3372 (s)	O-H / NH str.
	2547 (m)	S-H str.
	1716 (s)	C=O str.
	1578 (s)	} N-H bend
	1532 (s)	
	1199-1300 (s)	C-O, C-N str.
	1126 (s)	C-C str.
***L*-cysteine**	3293 (s)	NH str.
	~3000 (s, broad)	O-H str., C-H str.
	2522 (m)	S-H str.
	1743 (s)	C=O str.
	1603 (s)	} N-H bend
	1547 (s)	
	1393 (m)	C-O str.
	1197 (s)	C-N str.

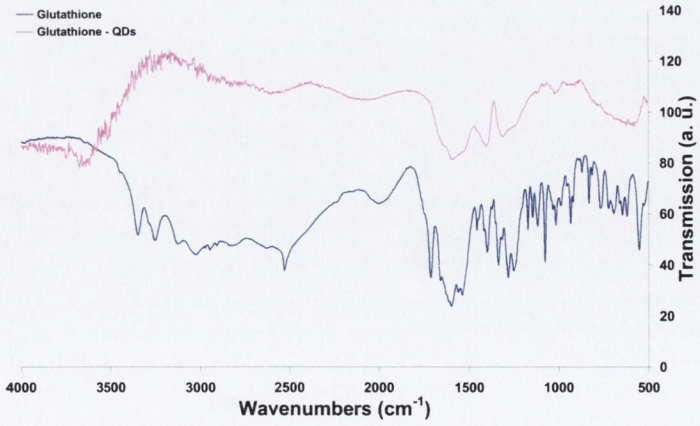
Appendix 3b: IR spectra of mercaptopropionic acid (MPA) – QDs



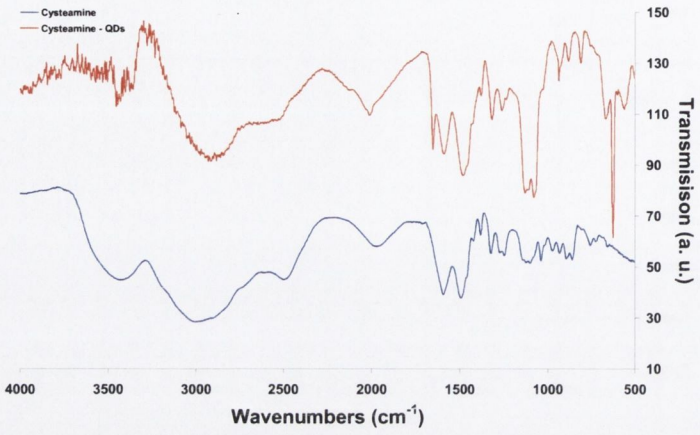
Appendix 3c: IR spectra of 3-mercapto-1,2-propandiol – QDs



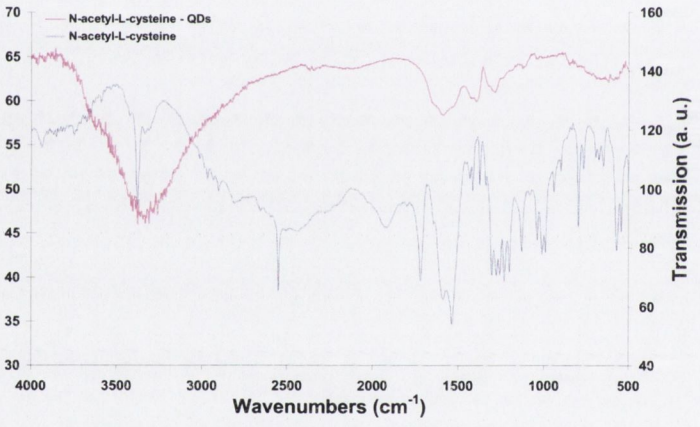
Appendix 3d: IR spectra of glutathione – QDs



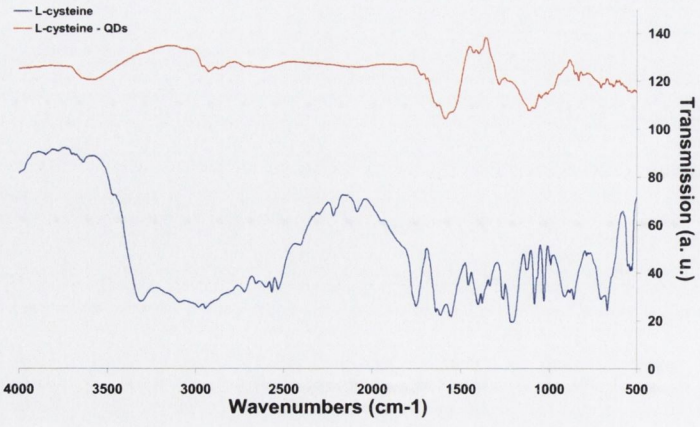
Appendix 3e: IR spectra of cysteamine – QDs



Appendix 3f: IR spectra of N-acetyl-*L*-cysteine – QDs

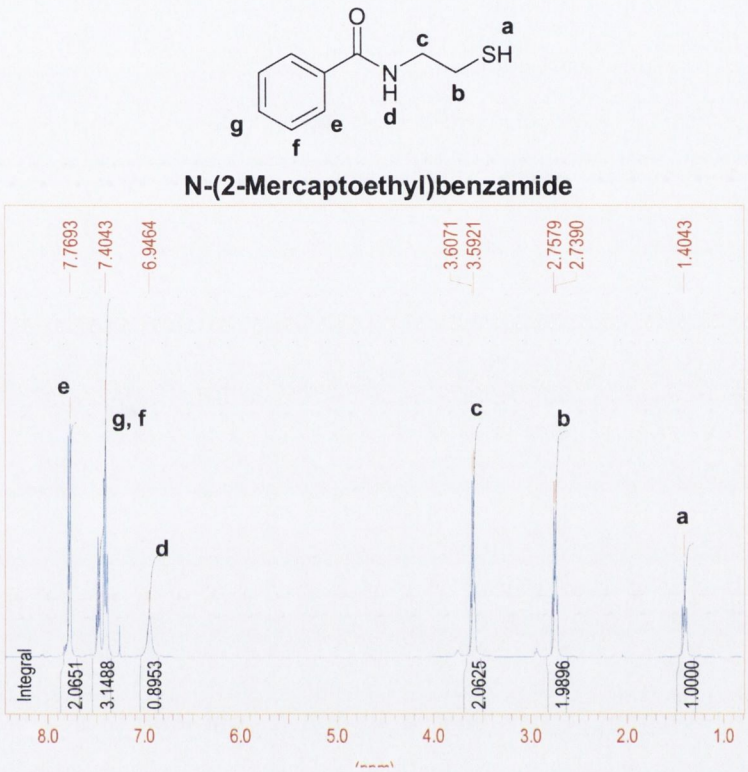


Appendix 3g: IR spectra of *L*-cysteine – QDs

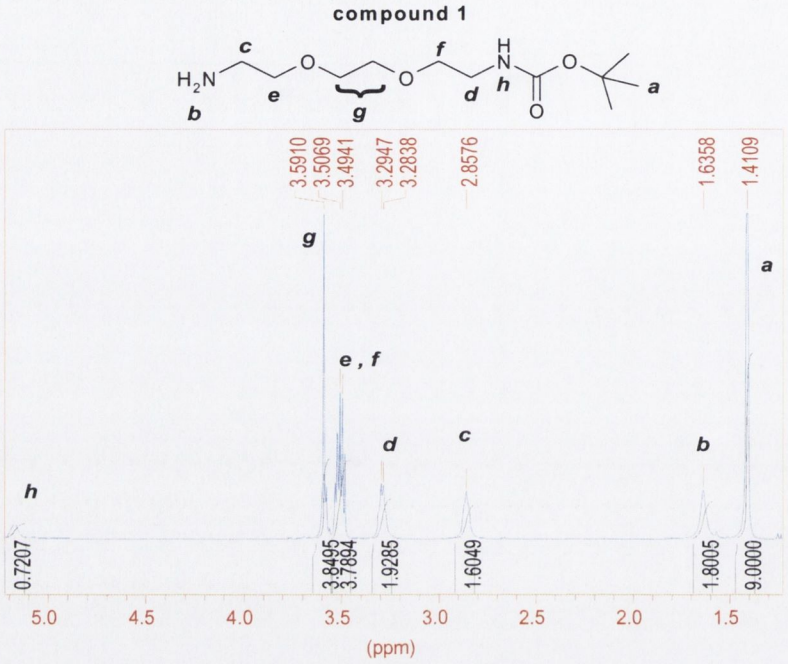


Appendix 5:

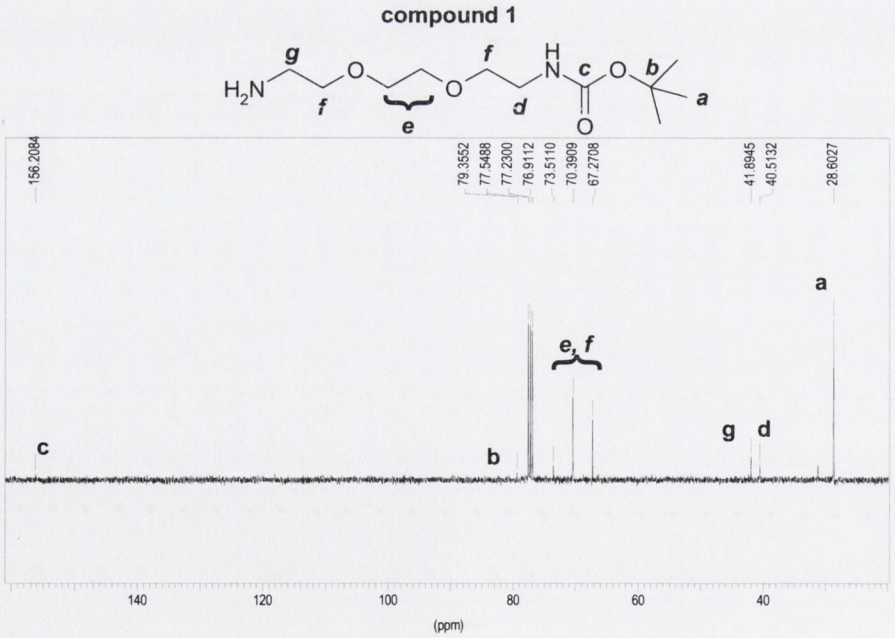
Appendix 5a: ^{1}H spectrum of N-(2-Mercaptoethyl)benzamide (Figure 5.4 B)



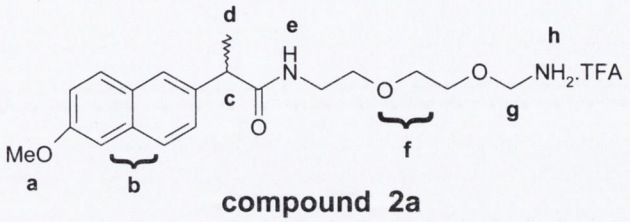
Appendix 5b: ^{1}H spectrum of 2-[2-(2-amino-ethoxy)-ethoxy}-ethyl}-carbamic acid tert butyl ester] (boc-amino-PEG): **compound 1**



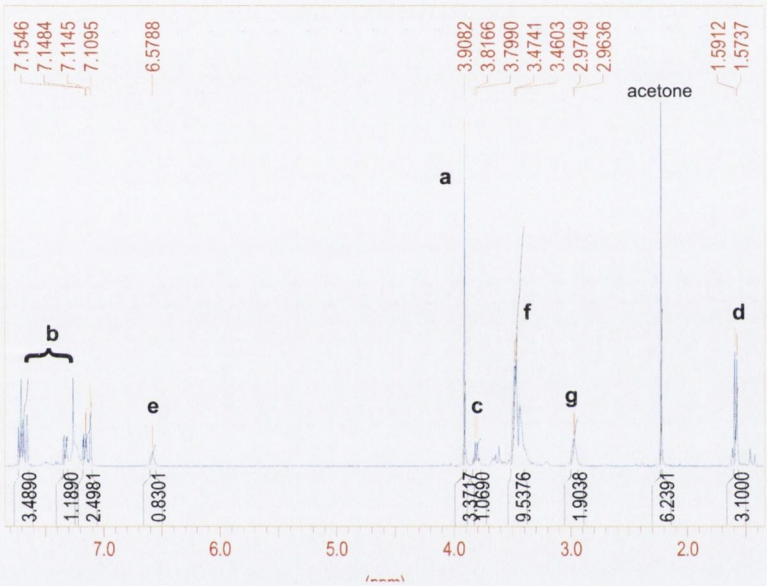
Appendix 5b: ^{13}C spectrum of 2-[2-(2-amino-ethoxy)-ethoxy}-ethyl}-carbamic acid tert butyl ester] (boc-amino-PEG): **compound 1**



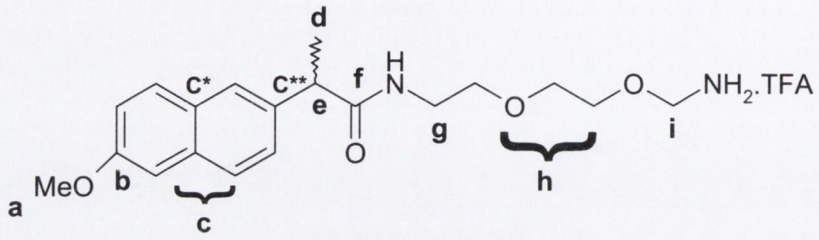
Appendix 5c: ^{1}H spectrum of N- 2-(2-(2aminoethoxy)ethoxy)ethyl)-2-(6-methoxynaphthalen-2-yl)propanamide: (npx-amino-PEG-NH_2): **compound 2a**



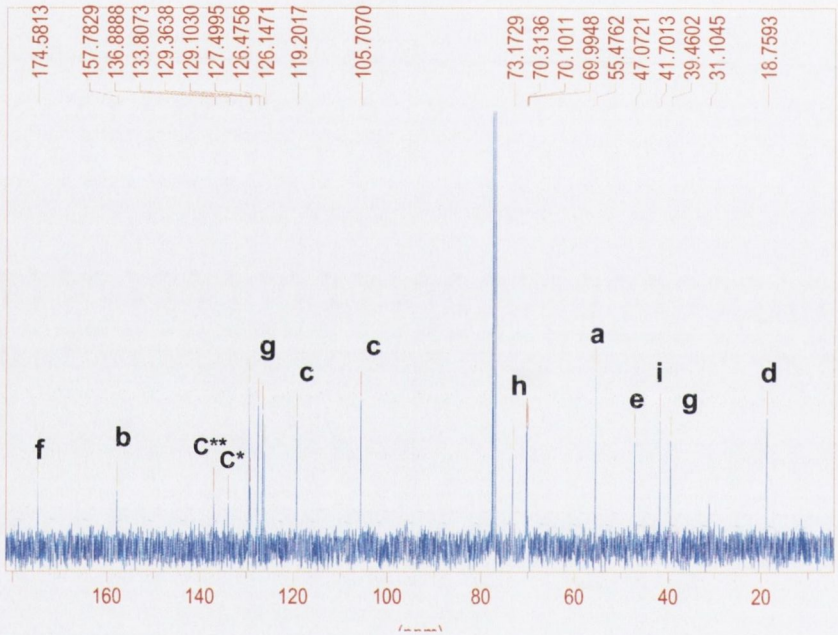
compound 2a



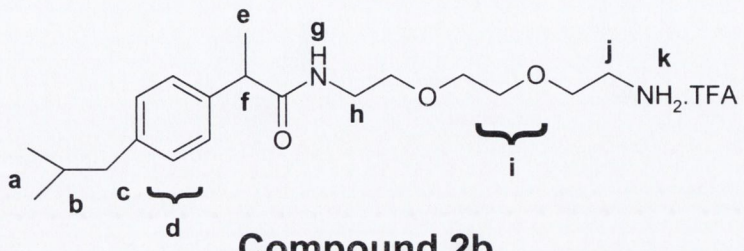
Appendix 5c: ^{13}C spectrum of N- 2-(2-(2aminoethoxy)ethoxy)ethyl)-2-(6-methoxynaphthalen-2-yl)propanamide: (npx-amino-PEG-NH_2): **compound 2a**



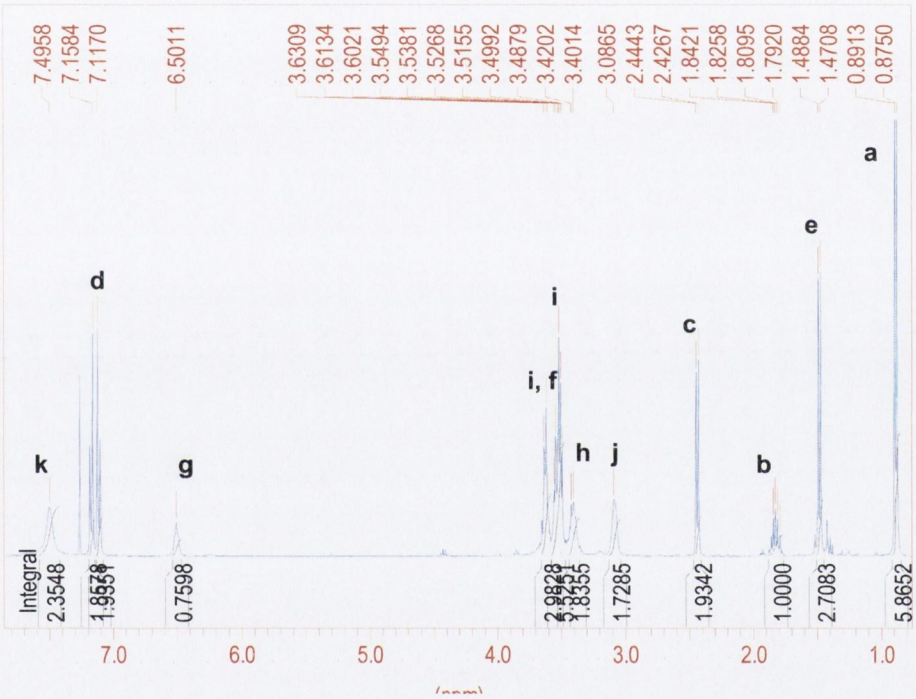
compound 2a



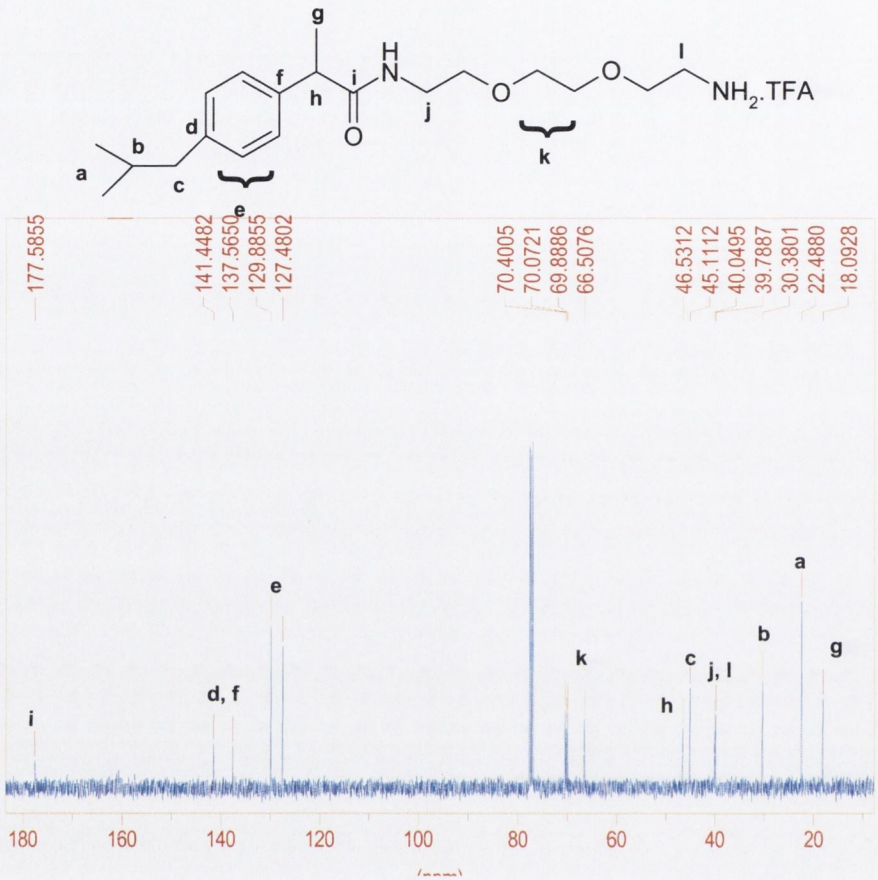
Appendix 5d: ^{1}H spectrum of N-(2-{2-[2-aminoethoxy]ethoxy}ethyl)-2-(4-isobutylphenyl propanamide: ibu-amino-PEG-NH_2: **compound 3a**



Compound 2b



Appendix 5d: ^{13}C spectrum of N-(2-{2-[2-aminoethoxy]ethoxy}ethyl)-2-(4-isobutylphenyl propanamide: ibu-amino-PEG-NH_2: **compound 3a**



List of Publications

"Jelly dots" Synthesis and cytotoxicity studies of CdTe quantum dot - gelatin nanocomposites

S. J. Byrne, Y. Williams, A. Davies, S. A. Corr, Y. K. Gun'ko, A. Rakovich, Y. P. Rakovich, J. F. Donegan , Y. Volkov, *Small* **2007**, *3*, 1152.

Synthesis, Characterisation, and Biological Studies of CdTe Quantum Dot – Naproxen Conjugates

S. J. Byrne, B. le Bon, S. A. Corr, M. Stefanko, C. O´Connor, Y. K. Gun'ko, Y. P. Rakovich, J. F. Donegan, Y. Williams, Y. Volkov, P. Evans, *ChemMedChem* **2007**, *2*, 183.

Optimisation of the synthesis and modification of CdTe quantum dots for enhanced live cell imaging

S. J. Byrne, S. A. Corr, T. Y. Rakovich, Y. K. Gun'ko, Y. P. Rakovich, J. F. Donegan, S. Mitchell, Y. Volkov, *J. Mater. Chem.* **2006**, *28*, 2896.

Preparation and biological investigation of luminescent water soluble CdTe nanoparticles

S. J. Byrne, C. M. O'Driscoll, S. A. Corr, Y. K. Gun'ko, S. Mitchell, Y. Volkov, *Proc. SPIE* **2005**, *129*, 2842.

High content analysis of differential uptake and subcellular distribution selectivity of CdTe Quantum Dots in human macrophages and non-phagocytic cell types

S. Mitchell, A. Davis, Y. Williams, D. Kelleher, R. Moore, Y. Gun'ko, S. Byrne, Y. Rakovich, J. Donegan, I. Nabiev, A. Sukhanova, D. Cottell, N. Gaponik, A. Rogach, Y. Volkov, *Nano Lett.* **2007**, submitted.

Off-resonance surface plasmon enhanced spontaneous emission from CdTe quantum dots

V. K. Komarala, Y. P. Rakovich, A. L. Bradley, S. J. Byrne, Y. K. Gun'ko, N. Gaponik, A. Eychmüller, *App. Phys. Lett.* **2006**, *89*, 253118.

Emission properties of colloidal quantum dots on polyelectrolyte multilayers

V. K. Komarala, Y. P. Rakovich, A. L. Bradley, S. J. Byrne, S. A. Corr, Y. K. Gun'ko, *Nanotech.* **2006**, *17*, 4117.

New two in one magnetic fluorescent nanocomposites

S. A. Corr, Y. K. Gun'ko, S. J. Byrne, A. P. Douvalis, M. Venkatesan, R. D. Gunning, Proc. SPIE **2005**, *71*, 2842.

Magnetic nanoparticle assemblies on denatured DNA show unusual magnetic relaxivity and potential applications for MRI

S. J. Byrne, S. A. Corr, Y. K. Gun'ko, J. M. Kelly, D. F. Brougham, S. Ghosh, *Chem. Comm.*, **2004**, *22*, 2560.